Co-rotational beam elements in instability problems

by

Jean-Marc Battini

Department of Mechanics

January 2002
Technical Reports from
Royal Institute of Technology
Department of Mechanics
SE-100 44 Stockholm, Sweden



To Amra

Abstract

The purpose of the work presented in this thesis is to implement co-rotational beam elements and branch-switching procedures in order to analyse elastic and elastoplastic instability problems.

For the 2D beam elements, the co-rotational framework is taken from Crisfield [23]. The main objective is to compare three different local elasto-plastic elements.

The 3D co-rotational formulation is based on the work of Pacoste and Eriksson [73], with new items concerning the parameterisation of the finite rotations, the definition of the local frame, the inclusion of warping effects through the introduction of a seventh nodal degree of freedom and the consideration of rigid links. Different types of local formulations are considered, including or not warping effects. It is shown that at least some degree of non-linearity must be introduced in the local strain definition in order to obtain correct results for certain classes of problems. Within the present approach any cross-section can be modelled, and particularly, the centroid and shear center are not necessarily coincident.

Plasticity is introduced via a von Mises material with isotropic hardening. Numerical integration over the cross-section is performed. At each integration point, the constitutive equations are solved by including interaction between the normal and shear stresses.

Concerning instabilities, a new numerical method for the direct computation of elastic critical points is proposed. This is based on a minimal augmentation procedure as developed by Eriksson [32–34]. In elasto-plasticity, a literature survey, mainly concerned with theoretical aspects is first presented. The objective is to get a complete comprehension of the phenomena and to give a basis for the two branch-switching procedures presented in this thesis.

A large number of examples are used in order to assess the performances of the elements and the path-following procedures.

Keywords: instability, co-rotational method, branch-switching, beam element, warping, plastic buckling, post-bifurcation.

List of papers

The work presented in this thesis is based on 6 papers and a licentiate thesis according to the list below. The correspondence between the chapters of this manuscript and these previous publications is given in Section 1.2.

Journal papers

J.-M. Battini and C. Pacoste

Co-rotational beam elements with warping effects in instability problems Accepted by Computer Methods in Applied Mechanics and Engineering

J.-M. Battini and C. Pacoste

Plastic instability of beam structures using co-rotational elements Submitted to Computer Methods in Applied Mechanics and Engineering

J.-M. Battini, C. Pacoste and A. Eriksson

Minimal augmentation procedure for the direct computation of critical points Submitted to Computer Methods in Applied Mechanics and Engineering

Conference papers

C. Pacoste, J.-M. Battini and A. Eriksson

Parameterisation of rotations in co-rotational elements Proceedings Euromech 2000, Metz

J.-M. Battini and C. Pacoste

Eléments poutres co-rotationels avec gauchissement

Proceedings CSMA 5ème colloque national en calcul des structures, Giens 2001

C. Pacoste and J.-M. Battini

Calcul des chemins d'équilibres post-critiques

Proceedings CSMA 5ème colloque national en calcul des structures, Giens 2001

Licentiate thesis: J.-M. Battini

Plastic instability analysis of plane frames using a co-rotational approach Department of Structural Engineering, KTH, Stockholm 1999

Preface

The research reported in the present thesis was carried out first at the Department of Structural Engineering and later at the Department of Mechanics, at the Royal Institute of Technology in Stockholm.

The work was initiated by Associate Professor Costin Pacoste and conducted under his supervision.

This project was financed by KTH and partially by the Swedish Research Council for Engineering Sciences (TFR).

First of all, I want to express my gratitude to my supervisor *Costin Pacoste* for his encouragement, valuable advice and for always having time for discussions. I want particularly to thank him for continuing to help me during the writing of this manuscript and the preparation of the defence, although he had resigned his position at KTH in October 2001.

I also wish to thank Professor Anders Eriksson for reviewing the manuscript of this thesis, providing valuable comments for improvement, and specially for accepting to present me to the doctoral examination.

I am also grateful to *Gunnar Tibert* who helped me with the LaTex code and spent several hours in proof reading this manuscript.

Finally, I would like to thank Amra for her love and support.

Stockholm, December 2001

Jean-Marc Battini

Contents

\mathbf{A}	bstra	ct		V
Li	st of	paper	'S	vii
\mathbf{P}_{1}	refac	e		ix
1	Intr	oduct	ion	1
	1.1	Aims	and scope	2
	1.2	Gener	al structure	4
2	Plas	stic ins	stabilities – review	7
	2.1	Simple	e models	8
		2.1.1	Shanley's column	8
		2.1.2	Hutchinson's model	11
	2.2	Hill's	criterion of uniqueness	16
		2.2.1	Linear comparison solid	17
	2.3	Euler	beam analysis	18
		2.3.1	Elastic case	19
		2.3.2	Reduced versus tangent modulus load	19
		2.3.3	Theoretical plastic analysis	22
	2.4	Discre	etised systems	27
		2.4.1	Constitutive framework and discretised rate problem	28
		2.4.2	Tangent comparison solid	30
		2.4.3	Bifurcation and stability	30
		2 1 1	Energy approach	39

3	2D	beam	element formulation	35
	3.1	Co-ro	tational framework	36
		3.1.1	Beam kinematics	37
		3.1.2	Virtual displacements	38
		3.1.3	Internal forces	39
		3.1.4	Tangent stiffness matrix	39
	3.2	Local	linear Bernoulli element	40
		3.2.1	Definition	40
		3.2.2	Gauss integration	41
		3.2.3	Local internal forces	41
		3.2.4	Local tangent stiffness matrix	42
		3.2.5	Constitutive equations	43
	3.3	Local	shallow arch Bernoulli element	43
		3.3.1	Definition	43
		3.3.2	Local internal forces	43
		3.3.3	Local tangent stiffness matrix	44
	3.4	Local	linear Timoshenko element	46
		3.4.1	Definition	46
		3.4.2	Local internal forces	46
		3.4.3	Local tangent stiffness matrix	47
		3.4.4	Constitutive equations	47
1	3D	hoom	element formulation	55
4				
	4.1		neterisation of finite 3D rotations	
		4.1.1	Rotational vector	
		4.1.2	Incremental rotation vector	
	4.2	Co-ro	tational framework	59
		4.2.1	Coordinate systems, beam kinematics	
		4.2.2	Change of variables $\delta \bar{\theta} \longrightarrow \delta \bar{\theta} \dots \dots \dots \dots$	63
		4.2.3	Change of variables $\delta \mathbf{p}_a \longrightarrow \delta \mathbf{p}_a^g \dots \dots \dots \dots$	64

		4.2.4	Eccentric nodes, rigid links	70
		4.2.5	Finite rotation parameters	71
		4.2.6	Formulation with warping	73
	4.3	Local	element formulation in elasticity	74
		4.3.1	Local beam kinematics, strain energy	75
		4.3.2	Element types	79
		4.3.3	Beams with thin-walled or open cross-sections	79
		4.3.4	Beams with solid or closed cross-sections	80
	4.4	Local	element formulation in elasto-plasticity	80
		4.4.1	Strain definition	81
		4.4.2	Finite element formulation	82
		4.4.3	Beams with thin-walled or open cross-sections	82
		4.4.4	Beams with solid or closed cross-section	84
	4.5	Applie	ed loads	85
		4.5.1	Eccentric forces	85
		4.5.2	External moments	85
5	Pat	h follo	wing techniques	87
	5.1	Non-c	ritical equilibrium path	88
		5.1.1	Procedure at the structural level	88
		5.1.2	Procedures at the element level	90
	5.2	Direct	computation of elastic critical points	91
		5.2.1	Classical approach	91
		5.2.2	Alternative extended system	92
		5.2.3	Modified algorithm	94
		5.2.4	Initialisation	95
	5.3	Branc	h-switching in elasto-plasticity	97
		5.3.1	Mode injection method	97
		532	Minimisation procedure	98

6	2D (examples in elasto-plasticity	101
	6.1	Example 1: cantilever beam	101
	6.2	Example 2: Lee's frame	103
	6.3	Example 3: Euler beam	107
	6.4	Example 4: asymmetrical frame	112
	6.5	Example 5: toggle frame	114
7	3D (examples in elasticity	117
	7.1	Example 1, deployable ring	117
	7.2	Example 2, helical beam	119
	7.3	Example 3, right angle frame	120
	7.4	Example 4, non-linear torsion	122
	7.5	Example 5, channel-section beam	123
	7.6	Example 6, torsional buckling	124
	7.7	Example 7, lateral torsional buckling	126
	7.8	Example 8, lateral buckling of a cantilever	127
	7.9	Example 9, lateral buckling with warping	130
	7.10	Example 10, L frame	130
8	Elas	etic isolation – examples	133
	8.1	Example 1, 2D clamped arch	133
	8.2	Example 2, 2D simply supported arch	134
	8.3	Example 3, 2D shallow arch	136
	8.4	Example 4, deep circular arch	137
	8.5	Example 5, narrow cantilever	138
	8.6	Example 6, L frame	139
	8.7	Example 7, cable hockling	141
	8.8	Example 8, spatial frame	142
9	3D (examples in elasto-plasticity	145
	9.1	Example 1, channel-section beam	145

	9.2	Example 2, framed dome	146
	9.3	Example 3, lateral buckling of an I beam	150
	9.4	Example 4, lateral buckling of a T cantilever	152
	9.5	Example 5, buckling by torsion and flexure	156
10	Con	clusions and future research	161
	10.1	Conclusions	161
	10.2	Future research	163
Bi	bliog	raphy	165
\mathbf{A}	3D	elastic local formulation	173
	A.1	t3d element	173
	A.2	tw3d element	174
	A.3	b3d element	174
	A.4	bw3d element	175
В	War	rping function	177
	B.1	Basic equations	177
	B.2	Saint-Venant torsion	178
	В.3	Determination of the warping function	178
	B.4	Cross-section quantities	180

Chapter 1

Introduction

The analysis of structural instabilities is an important part of the design process in civil, mechanical and aeronautical engineering. Despite the great interest surrounding these problems, most of commercial finite elements codes can model such phenomena only partially. As a matter of fact, in these programs bifurcation loads are often calculated through a linearised buckling analysis, which may give inaccurate results in certain cases. Concerning post-bifurcation paths, these are often studied by introducing small initial imperfections. In addition to the difficulties related to the choice of the form and the magnitude of these imperfections, such an approach removes the bifurcation and does not allow a complete physical understanding.

However, an accurate evaluation of bifurcation points is necessary for two different purposes. First, these points define critical conditions for the functionality of structures. Second, in order to get a complete description of the instability, secondary paths must be computed using perfect structures. This requires on one hand a procedure for detecting and isolating bifurcation points along fundamental paths, and, on the other hand, a procedure for performing branch-switching to secondary paths. One of the purposes of this thesis is to develop such procedures for elastic and elasto-plastic cases.

Most of the work done about instability concerns elastic structures under quasi-static loading. The reason is that the analysis of such problems requires the introduction of geometrical non-linearities which, in itself, is a rather complicated task to work with. However, the assumption that the structure behaves elastically up to the bifurcation point may not always hold. If some part of the structure develops prebuckling plastic deformations, then the analysis of the instability must include both geometrical and material non-linearities.

Stability analysis of inelastic structures is complicated by the fact that the principle of minimum potential energy, which is the basic tool for the stability analysis of elastic structures, cannot be applied. This is due to the dissipation of energy inherent in plastic deformations. Consequently, the theory developed by Koiter or the more refined catastrophe theory, which proposes a classification of the critical points as well as methods to investigate post-bifurcation paths and imperfection sensitivity aspects, cannot be applied. In fact, the irreversibility of plastic deforma-

tions produces new phenomena. While in elasticity bifurcation occurs at isolated critical points and is characterised by a loss of stability on the fundamental path, in plasticity, bifurcation along the fundamental path may occur at a continuous range of equilibrium points.

Although that the first comprehensive description of this phenomenon has been given in 1947 by Shanley [88], the complete description of bifurcation and instability in time-independent plasticity was mostly developed in the two last decades. The absence until recent years of such a theoretical basis and the complexity of the problem explain why most of the books about stability of structures treat plastic instabilities only superficially or even not at all. It explains also why so little numerical research has been performed concerning the topic. Most of the work with finite elements concern elastic structures and often under quasi-static evolutions.

Naturally, finite beam elements are very common: a huge amount of research has been carried out within this topic and commercial codes propose often several elements which include both geometrical and material non-linearities. However, two problems remain. The first one concerns warping effects which are usually not included in non-linear formulations; if they are considered, it is often by assuming bi-symmetric cross-sections. The second problem is related to plastic instability problems in the sense that most of elements are too crude to model correctly such phenomena. As an example, it will be shown in this thesis that elements which neglect hardening or use yield criteria expressed in function of stress resultants cannot be used. In fact, concerning beam elements, attempts to correctly model plastic bifurcation problems and compute post-bifurcation paths are not very common in literature. Thus another purpose of this thesis is to develop efficient non-linear beam elements which can include warping effects for arbitrary cross-sections and which are accurate enough in order to model elastic and elasto-plastic instability problems.

In this context, the co-rotational approach has generated an increased amount of interest in the last decade. However, most of the work done on co-rotational beam elements concern trivial cross-sections, as rectangular ones. It appears then interesting to investigate the co-rotational approach in order to introduce warping effects and arbitrary cross-sections.

1.1 Aims and scope

An important research concerning numerical stability analysis of elastic structures under quasi-static loading has been carried out in the last years by the Structural Mechanics Group at KTH. Based on a co-rotational approach and under the assumption of small deformations, efficient beam [72,73] and shell elements [59,68,71] have been developed in order to model large displacements problems in general and stability problems in particular. At the same time, advanced path-following methods [30–34,65] including branch-switching procedures and parameter sensitivity analyses (fold lines) have been implemented. An incursion into dynamics [37] has also been performed.

The first aim of this thesis was to introduce material non-linearity in this previous work and to investigate how the co-rotational beam elements and the path-following procedures have to be modified in order to account for plastic deformations. For this purpose, the co-rotational approach is well suited since it leads to an artificial separation of the material and geometrical non-linearities. Consequently, only local internal force vectors and tangent stiffness matrices need to be modified.

The work first focused on 2D beam elements. Three local elasto-plastic formulations have been developed and tested. Based on the Bernoulli assumption, the first two local elements use a linear and a shallow arch local strain definition, respectively. The third element is based on the Timoshenko assumption with linear interpolations.

Concerning path following aspects, two methods of branch-switching in elastoplasticity have been implemented. In the first one, branch-switching is operated by using as predictor the eigenvector associated to the negative eigenvalue at the bifurcation point. In the second one, introduced by Petryk [76–81], an energy approach is used to select automatically the stable post-bifurcation path.

Before dealing with numerical aspects, a literature review on plastic instabilities was carried out. The first objective was to get a complete picture of the physical phenomena involved, and thus enable a correct numerical modelling. For that, the models of Shanley and Hutchinson have been carefully analysed. The second objective was to get the theoretical background for the two branch-switching procedures. This background has been provided by the works of Hill [45] and Petryk [76–81].

This work constitutes the Licentiate Thesis, *Plastic instability analysis of plane frames using a co-rotational approach* [5], presented by the author in June 1999.

The second aim of this thesis was to further develop the 3D beam elements developed by Pacoste and Eriksson [73] and also to incorporate material non-linearity. With respect to this previous publication, the new items concerning the co-rotational framework are a new definition of the local frame, the use of the spatial form of the incremental rotational vector to parameterise finite rotations, the inclusion of warping effects through the introduction of a seventh nodal degree of freedom and the consideration of rigid links. As regard the local formulation, a systematic study of partly non-linear expressions for beam deformations has been carried out and it has been shown that some degree of non-linearity must be introduced in the local strain definition in order to obtain correct results for certain problems involving torsional effects.

With these improvements, the elements presented in this thesis can be used to model any problems involving large displacements and rotations, under the assumption of small strains. In addition, arbitrary beam cross-sections can be considered and particularly, the centroid and shear center are not necessarily coincident, as it is often assumed in non-linear beam elements.

The third aim of this thesis was to adapt the work of Eriksson [32–34] about fold line algorithms and develop a new procedure for the direct computation of elastic critical points. Compared to the classical approach of Wriggers et al. [104, 105], two main

modifications have been introduced. First, following Eriksson [32–34], the condition of criticality is expressed by a scalar equation instead of a vectorial one. Next, the present procedure does not use exclusively the extended system obtained from the equilibrium equations and the criticality condition, but also introduces intermediate iterations based purely on equilibrium equations under load or displacement control.

Finally, concerning the modelling of inelastic instabilities, the choice between an incremental flow plastic theory and a total strain or deformation theory must be discussed. As a matter of fact, experimental results have paradoxically but persistently shown that the deformation theory is superior to the flow one in predicting plastic buckling loads for certain problems, e.g. the inelastic axial-torsional buckling of cruciform columns. However, contrary to the flow theory which relates the increment of plastic strains to the stresses so that the plastic strains depend on the loading history, the deformation theory relates the total plastic strains to the stresses and the plastic strains are independent of the loading history. Consequently, the deformation theory cannot describe phenomena associated with loading and unloading from the yield surface. In fact, this theory is restricted to the particular type of stress history known as proportional loadings [11] in which the components of the stress tensor increase in constant ratio to each other. This assumption is not respected in many cases and particularly it makes the study of secondary paths impossible. For this reason, and despite the previously mentioned paradox, an incremental flow theory has been adopted in this thesis, and a von Mises material with isotropic hardening has been taken. Two additional arguments against the deformation theory is its lack of physical ground and the difficulty of finding numerical examples in the literature.

1.2 General structure

To get an overview of the general structure of this thesis, the contents of the chapters are presented in the following.

In Chapter 2, a review on plastic instabilities is presented. As mentioned before, both physical and theoretical aspects are emphasised. Since a lot of work has been done on it, a special section is devoted to the plastic buckling of the Euler beam.

In Chapter 3, internal force vectors and tangent stiffness matrices for three elastoplastic 2D beam elements are derived. An important part is devoted to the resolution of the constitutive equations for the Timoshenko element.

In Chapter 4, a complete description of the co-rotational framework for 3D beam elements is presented. Several local formulations in elasticity, including or not warping effects and based on Timoshenko or Bernoulli assumptions are discussed. Plasticity is further included in the local formulation of the Timoshenko elements.

In Chapter 5, path following techniques are developed. First, the procedure used to compute non-critical paths is presented, both at structural and element levels. Then, the new algorithm for the direct computation of elastic critical points and the

two branch-switching methods in elasto-plasticity are explained in detail.

In Chapter 6, five 2D numerical examples in elasto-plasticity are studied in order to assess the performances of the branch-switching procedures and the 2D elements.

In Chapter 7, ten 3D numerical examples are presented in order to assess the performances of the elastic elements. Several examples are devoted to the parameterisation of finite rotations.

In Chapter 8, eight numerical examples are studied in order to compare the convergence properties of the new algorithm for the direct computation of elastic critical points with the classical approach of Wriggers et al. [104, 105]

In Chapter 9, five 3D numerical examples in elasto-plasticity are used in order to assess the performances of the elements and the branch-switching procedures.

In Chapter 10, conclusions and directions for future research are presented.

Correspondence with previous publications

Chapters 2 and 3 are reproduced from [5] with some minor modifications. In Chapter 4, the description of the co-rotational framework and the elastic local formulation are taken from [6], while the plastic local formulation is taken from [9]. Minors modifications have been introduced and particularly, the evaluations of matrices \mathbf{G} and \mathbf{K}_g in Section 4.2.3 are extended. In Chapter 5, Section 5.2 is taken from [8], while Section 5.3 is taken from [9]. The numerical examples in Chapter 6 are similar to the ones published in [5]; However, some modifications have been introduced, e.g. the implementation of the minimisation procedure. Chapters 7 and 8 correspond to the sections headed "Numerical examples" in [6] and [8], respectively. Chapter 9 corresponds mainly to the section headed "Numerical examples" in [9]; the only difference is that the two 2D examples presented in [9] are not reproduced.

Chapter 2

Plastic instabilities – review

Historically, plastic buckling of columns has been studied since the early works of Considère [20] (1891) and von Karman [102] (1910). The issue under consideration at that time was the determination of the maximal load that columns can support. Despite considerable efforts in the following decades, this apparently simple problem did not receive a comprehensive solution until the work of Shanley [88] (1947). Based on experimental results, Shanley showed that the plastic bifurcation of a perfect column occurs at the so-called tangent modulus load and is characterised by the apparition of a zone of elastic unloading. Moreover, by using a very simple model of the column, consisting of two rigid parts connected with two springs, Shanley was able to give a correct qualitative description of the phenomenon of plastic bifurcation and outlined the existence of a continuous range of bifurcation points. The most interesting feature of Shanley's model lies in its simplicity: with very simple mathematics a complete solution to the problem can be obtained. An improved model, where the two rigid parts are connected by a continuous range of springs was introduced by Hutchinson [49] (1973). This model has been used to study theoretically and numerically imperfection sensitivity and secondary postbifurcation paths in plastic buckling problems.

Based on the study of Shanley's model, one very important difference between elastic and plastic bifurcations becomes apparent: in elasticity, bifurcation occurs at isolated critical points and is characterised by a loss of stability on the fundamental path; in plasticity, a continuous range of stable bifurcation points along the fundamental path may occur.

Despite its significant phenomenological insights, the work of Shanley remains limited in scope. Its conclusions are essentially restricted to the plastic buckling of compressed columns. The first theoretical general approach to bifurcation and stability in elasto-plastic solids was given by Hill [45] (1959). By taking into account the change in geometry during the deformation process, Hill derived criteria for the uniqueness and stability of a solution and introduced the notion of linear comparison solid. However, several problems remained. On the theoretical side, one important question is how to interpret the stability of the points along the fundamental path beyond the first bifurcation point since these points have no apparent physical mean-

ing. On the numerical side the notion of linear comparison solid does not lend itself to a direct implementation which would result in a reliable numerical procedure to calculate the lowest bifurcation point.

Within the framework of an energetic approach, Petryk [76–81] proposed a solution to these two problems by introducing the notions of tangent comparison solid and stability of a deformation path. His results, obtained by assuming a discretisation of the structure and the symmetry of the constitutive moduli give a complete theoretical description of the phenomenon and can be considered as a generalisation of the conclusions obtained with Shanley's model. Furthermore, they are the basis for the numerical branch-switching procedures used in this thesis.

It should be noted here that an energetic approach to Hill's criteria was also given by Nguyen [62,63] in 1987. This theory, which has also applications in fracture and friction mechanics, will not be investigated in this thesis.

Following this brief introduction, the remainder of this chapter is organised in four parts. The first part is a review of the work done on the simple models introduced by Shanley and Hutchinson. The second part presents the criterion of uniqueness and the notion of linear comparison solid introduced by Hill. As an application, the theoretical analysis of the plastic buckling of the Euler beam is presented in the third part. In this context, emphasis is given to the study of the secondary post-bifurcation path. Finally, based on the work of Petryk, the last part presents a complete theoretical approach to instability problems in time-independent plasticity in the context of discrete structures.

2.1 Simple models

Two simple models are presented and analysed in this section. The first one originates from Shanley. Its study is interesting for several purposes. From a pedagogical point of view, Shanley's column is the simplest structure presenting plastic bifurcation and can be studied with very easy mathematics. From a historical point of view, the work done by Shanley in 1947 gives the first correct description of the problem. The second model has been introduced by Hutchinson in 1973 and has been investigated later by several authors. Its study generates qualitative conclusions about the effects of both geometrical and material non-linearities on post-bifurcation behaviour.

2.1.1 Shanley's column

In his famous article, Shanley [88] studied a model (cf. Figure 2.1) consisting of a rigid \perp frame loaded by a vertical downward force P. The frame is maintained in equilibrium by two springs k_1 and k_2 . The stiffness of the springs is either E or E_t , depending on whether plastic deformation occurs. The system has two degrees of freedom, z and θ . A linearised study is performed.

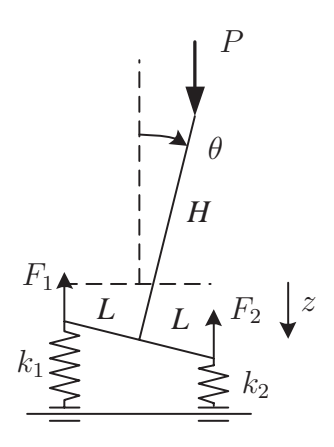


Figure 2.1: Shanley's column.

Equilibrium equations

The equilibrium equations are

$$P = F_1 + F_2 (2.1a)$$

$$P H \theta = (F_2 - F_1) L \tag{2.1b}$$

where F_1 and F_2 are the forces in the springs given by

$$F_1 = k_1 \left(z - L \, \theta \right) \tag{2.2a}$$

$$F_2 = k_2 \left(z + L \, \theta \right) \tag{2.2b}$$

which finally gives

$$P = (k_1 + k_2) z + (k_2 - k_1) L \theta$$
 (2.3a)

$$(k_1 + k_2) (H z - L^2) \theta = (k_2 - k_1) L z$$
 (2.3b)

By differentiation the following rate equations are obtained

$$\dot{P} = (k_1 + k_2) \dot{z} + (k_2 - k_1) L \dot{\theta}$$
(2.4a)

$$P = (k_1 + k_2) z + (k_2 - k_1) L \theta$$

$$(k_1 + k_2) \left[(H z - L^2) \dot{\theta} + H \theta \dot{z} \right] = (k_2 - k_1) L \dot{z}$$
(2.4a)

Fundamental path

The fundamental path is defined by

$$\theta = 0$$
 $k_1 = k_2 = E$ $P = 2 E z$ in the elastic range $\theta = 0$ $k_1 = k_2 = E_t$ $P = 2 E_t z$ in the plastic range (2.5)

Bifurcation paths

The possibility of bifurcation from the fundamental path with $\dot{\theta} > 0$ is now investigated. Since a linearised analysis is performed, only the initial tangent of the post-bifurcation paths is possible to evaluate. Consequently, the angle θ is set to 0. Two trivial cases can easily be found if $k_1 = k_2$. Equation (2.4b) is then reduced to

$$(Hz - L^2)\dot{\theta} = 0 \tag{2.6}$$

and bifurcation is possible if

$$z = \frac{L^2}{H} \tag{2.7}$$

which by taking account of (2.3a) gives as bifurcation loads

$$P_e = \frac{2L^2}{H}E$$
 if $k_1 = k_2 = E$
 $P_t = \frac{2L^2}{H}E_t$ if $k_1 = k_2 = E_t$ (2.8)

where P_e is the elastic buckling load and P_t is the tangent modulus load.

Other solutions are searched by assuming

$$k_1 = E \qquad k_2 = E_t \tag{2.9}$$

which implies

$$\dot{F}_1 < 0 \qquad \dot{F}_2 > 0 \tag{2.10}$$

and therefore, from (2.2a) and (2.2b)

$$-L\dot{\theta} < \dot{z} < L\dot{\theta} \tag{2.11}$$

Equation (2.4b) can be rewritten as

$$\dot{z} = \frac{E + E_t}{E - E_t} \left(1 - \frac{H}{L^2} z \right) L \dot{\theta} \tag{2.12}$$

Introducing equation (2.12) in (2.4a), and taking (2.3a) into account gives

$$\dot{P} = (P_r - P) \frac{H}{L} \frac{E + E_t}{E - E_t} \dot{\theta} \tag{2.13}$$

where

$$P_r = \frac{2L^2}{H}E_r$$
 $E_r = \frac{2EE_t}{E+E_t}$ (2.14)

 P_r is the reduced modulus load and E_r is the reduced modulus.

By using (2.12) and (2.3a) the conditions (2.11) provide after some work

$$P_t < P < P_e \tag{2.15}$$

Conclusions

From the equations (2.13) and (2.15), it can be concluded that there is a continuous range of bifurcation loads between P_t and P_e . Moreover, the initial tangent of the post-bifurcation path is positive at P_t , negative at P_e , and range monotonically between P_t and P_e with a horizontal tangent at P_r . These results are represented in Figure 2.2.

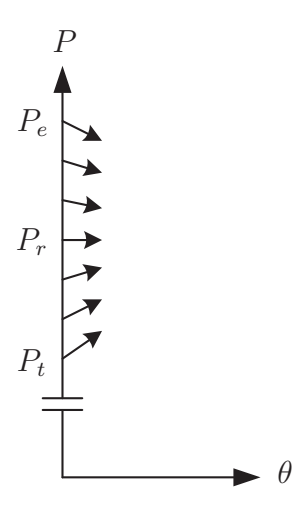


Figure 2.2: Linearised analysis of Shanley's column.

Three remarks concerning the study of this model should be mentioned [87]:

- The infinite number of bifurcations does not come from the non-linearity of the stress—strain relation but from the irreversible character of the process: a strain configuration can correspond to an infinite number of stress configurations, corresponding to different histories of the loading.
- The stability aspect will be studied in details in the following sections. However, it can be inferred intuitively that the fundamental path will be stable in a dynamical sense up to P_r (upward tangent) and unstable after (downward tangent).
- The conditions (2.10) assume that both springs are plasticised $(k_1 = k_2 = E_t)$ before the load reaches P_t . If P_Y is the yield limit of the springs and if $P_t < P_Y$, then the bifurcations between P_t and P_Y do not exist.

2.1.2 Hutchinson's model

The model introduced by Hutchinson [48–50] and shown in Figure 2.3 differs from the previous one in that the \perp frame is supported by a continuous distribution of springs. Imperfections are represented by an initial rotation $\bar{\theta}$ from the vertical in the unloaded state. Linearised analysis is performed once again and geometrical non-linearities are artificially introduced through a horizontal non-linear spring which develops a force $F(\theta) = k L^2 \theta^2$ (k > 0).

This model has been studied with two different elasto-plastic laws as shown in Figure 2.4. The first law is the classical bilinear one while the second is of Ramberg-Osgood type defined by the equation

$$\frac{\varepsilon}{\varepsilon_Y} = \frac{\sigma}{\sigma_Y} + \alpha \left(\frac{\sigma}{\sigma_Y}\right)^n \tag{2.16}$$

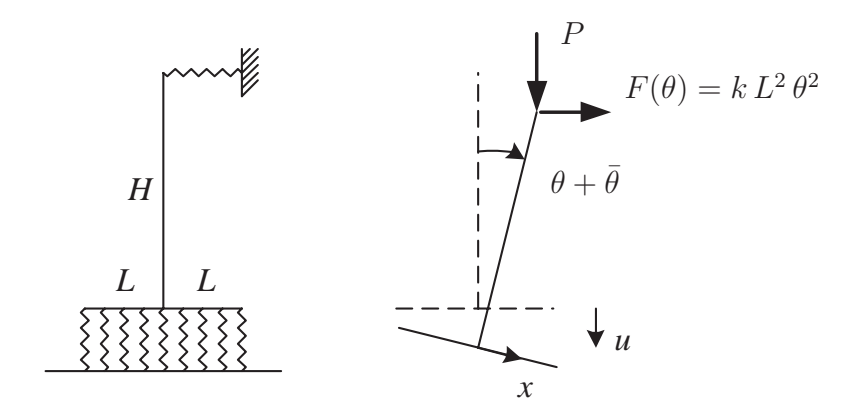


Figure 2.3: Hutchinson's continuous model of Shanley's column.

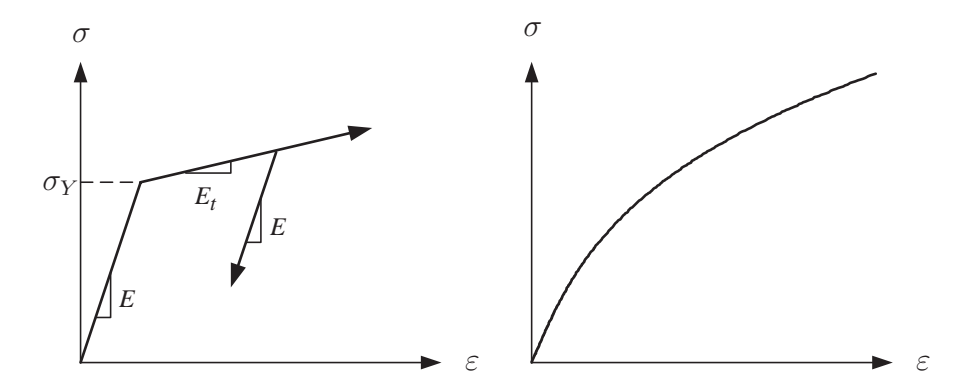


Figure 2.4: Bilinear and Ramberg-Osgood ($\alpha = 0.2, n = 3$) elasto-plastic laws.

Equilibrium equations

The linearised equilibrium equations are

$$P = \int_{-L}^{L} \sigma \, \mathrm{d}x \tag{2.17}$$

$$P H \left(\theta + \bar{\theta}\right) + F H = \int_{-L}^{L} \sigma x \, dx \qquad (2.18)$$

with

$$\varepsilon = u + x \,\theta \tag{2.19}$$

and

$$\dot{\sigma} = E_t \dot{\varepsilon}$$
 for plastic loading $\dot{\sigma} = E \dot{\varepsilon}$ for elastic unloading or within the elastic range (2.20)

A review of some results found in literature is presented below.

Continuous range of bifurcation points

The purpose of the study performed by Cimetière, Elkoulani and Léger [18] was to prove mathematically the results obtained by Shanley on the basis of the two springs model, i.e. every point within the interval $[P_t, P_e]$ where $P_t = \frac{2L^3}{3H}E_t$ and $P_e = \frac{2L^3}{3H}E$ is a bifurcation point while no bifurcation points are present outside this interval. In this study, a constant value of E_t was adopted and geometrical non-linearities were neglected (k = 0). The results, adapted from [18], are shown in Figure 2.5.

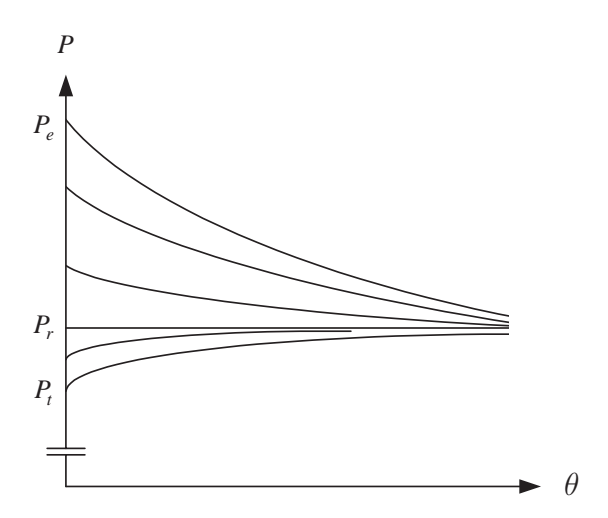


Figure 2.5: Bifurcation diagram for $E/E_t = 5$.

Imperfection analysis

Hutchinson [48, 50] calculated numerically the post-buckling path in the case of a Ramberg-Osgood model with $\alpha=0.2$ and n=3. The results (adapted from [48]) with and without imperfections are shown in Figure 2.6. The imperfect paths are obtained for $\bar{\theta}=0.001$. The imperfect structure gives equilibrium paths which tend to the path branching at P_t when $\bar{\theta}$ tends to 0. This suggests that a perfect model will bifurcate at P_t , and therefore, only the path branching at P_t needs to be investigated. The other post-bifurcation paths do not have any physical meaning. Su and Lu [94] studied the case with constant E_t and k>0 and found similar results.

Asymptotic expressions

The curves shown in Figure 2.6 present a maximum point for relatively small values of θ . Hutchinson calculated asymptotic expressions for the stable portion of the post-bifurcation path and then deduced expressions for the maximum load. For the structure without imperfection, he obtained expansions in the form

$$P = P_t + \lambda_1 \,\theta + \lambda_2 \,\theta^{3/2} + \lambda_3 \,\theta^2 + \dots \tag{2.21}$$

The difference from similar expressions obtained using Koiter's theory for elastic structures (cf. e.g. [96]) is the presence of a term $\lambda_2 \theta^{3/2}$, which comes from the apparition of a growing elastic unloading zone at bifurcation. However, it has to be emphasised that such expressions are only valid for sufficiently small values of θ .

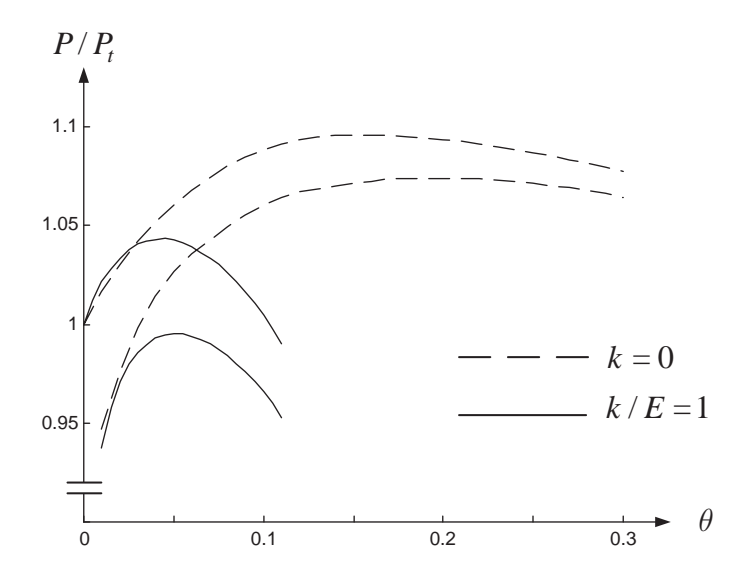


Figure 2.6: Post-buckling behaviour and imperfection sensitivity in the case of a Ramberg-Osgood relation (H/L=1).

Hutchinson compared these asymptotic expansions with numerical calculations and found that good accuracy is preserved until the maximal load only in the case of strong geometrical non-linearity (k/E=1). Van der Heijden [99] proposed a different method to calculate more accurate asymptotic expansions, but strong divergence from numerical simulations were still observed for cases without strong geometrical non-linearity.

Combination of geometrical and material non-linearities

An analysis without linearisation (and thus without a horizontal spring) was proposed by Cimetière and Léger [19]. A better description of the model is needed and the two cases shown in Figure 2.7 were studied. In case (a) the springs are tied at their bottom and free to move along the x-axis at their top. In case (b) the contrary applies.

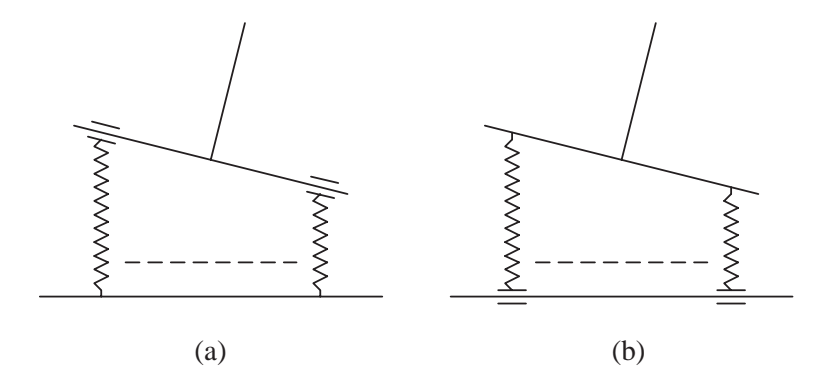


Figure 2.7: Models with non-linear geometry.

In case (a), equations (2.19) and (2.18) are replaced by

$$\varepsilon = u + x \, \tan \theta \tag{2.22}$$

$$PH \sin \theta = \int_{-L}^{L} \frac{\sigma}{\cos^2 \theta} x \, dx \qquad (2.23)$$

while in case (b) they are replaced by

$$\varepsilon = u + x \sin \theta \tag{2.24}$$

$$PH \sin \theta = \int_{-L}^{L} x \, \sigma \cos \theta \, \mathrm{d}x \tag{2.25}$$

The models have been tested with a bilinear elastic-plastic law, without geometrical imperfections. The numerical results for case (a) show a monotonically increasing post-bifurcation curve. In case (b), the bifurcated branch can be either monotonically strictly increasing or it can present a maximum, depending on the ratio E_t/E .

The conclusions presented in [19] are now summarised.

The cumulative effects of geometrical and material non-linearities are difficult to study without numerical simulations, e.g. different ratios E_t/E in the bilinear elastic-plastic law or different exponents n in the Ramberg-Osgood relation can lead to different qualitative solutions (cf. also [61]).

With respect to the effects of material non-linearities, it can be concluded by comparing Figures 2.5 and 2.6 that the decreasing stiffness of the material in the plastic range (Ramberg-Osgood law) has destabilising effects.

The geometrical non-linearity can have both stabilising or destabilising effects. The differences in the post-buckling paths of the cases investigated can be partly understood by considering only geometrical non-linearity. Four models have been studied:

- model 1: linearised equations without geometrical imperfections
- model 2: linearised equations with geometrical imperfections
- model 3: non-linearised equations, case (a)
- model 4: non-linearised equations, case (b)

The elastic post-buckling paths for these models are shown in Figure 2.8. It can be concluded that an unstable elastic post-critical curve accentuates the possibility of occurrence of a maximum point and a stable one accentuates the possibility of a monotonic path.

Moreover, in the vicinity of the bifurcation, material non-linearity prevails over the geometric one and a stable path is always obtained. More detailed conclusions cannot be derived.

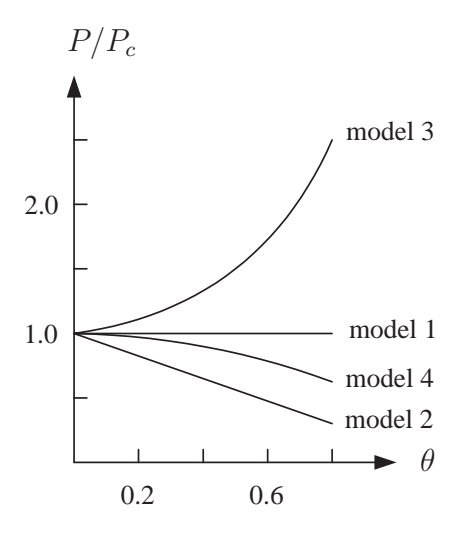


Figure 2.8: Elastic post-buckling of the studied models.

2.2 Hill's criterion of uniqueness

This section presents the theoretical results, due to Hill [45], concerning uniqueness of the solution of an elastic-plastic deformation.

A general solid body subjected to a quasi-static loading defined by the parameter λ is considered. The general boundary-value problem in elastic-plastic deformation can be defined as follow: at a generic stage in the loading process, the current shape of the body and the internal stress distribution are supposed to have been determined already, together with the existing state of hardening and mechanical properties in general. The incremental changes in all these variables have now to be calculated for a further infinitesimal variation $\dot{\lambda}$ of the loading parameter. The question of the uniqueness of the solution is then set.

The differentiation of the principle of virtual work can be written in the form

$$\int_{v} \dot{N}_{ij} \, \delta u_{j,i} \, \mathrm{d}v = \int_{v} \dot{b}_{j} \, \delta u_{j} \, \mathrm{d}v + \int_{s} \dot{T}_{j} \, \delta u_{j} \, \mathrm{d}s \tag{2.26}$$

where T_j are the surface tractions applied on the surface s and b_j are the body forces. N_{ij} are the nominal stresses, i.e. the stresses acting in the current configuration on an infinitesimal surface element in the reference configuration. δu_j is a kinematically admissible virtual displacement.

Two different incremental solutions, \dot{u}_j and \dot{u}_j^* , are considered. By taking as virtual displacement

$$\delta u_j = \dot{u}_j - \dot{u}_j^* = \Delta u_j \tag{2.27}$$

the following equation is obtained

$$\int_{v} \dot{N}_{ij} \left(\Delta u_{j} \right),_{i} dv = \int_{v} \dot{b}_{j} \Delta u_{j} dv + \int_{s} \dot{T}_{j} \Delta u_{j} ds \qquad (2.28)$$

Equation (2.28) must hold also if \dot{u}_j and \dot{u}_j^* are interchanged, that is, if \dot{N}_{ij} , \dot{b}_j and \dot{T}_j are replaced by \dot{N}_{ij}^* , \dot{b}_j^* , and \dot{T}_j^* . Subtracting these two equalities and introducing the notations

$$\Delta \dot{N}_{ij} = \dot{N}_{ij} - \dot{N}_{ij}^* \quad \Delta \dot{b}_j = \dot{b}_j - \dot{b}_i^* \quad \Delta \dot{T}_j = \dot{T}_j - \dot{T}_i^*$$
 (2.29)

gives

$$\int_{v} \Delta \dot{N}_{ij} \left(\Delta u_{j} \right),_{i} dv = \int_{v} \Delta \dot{b}_{j} \Delta u_{j} dv + \int_{s} \Delta \dot{T}_{j} \Delta u_{j} ds \qquad (2.30)$$

The loading is assumed conservative, which means that T_j and b_j are only depending on λ , which further implies $\dot{T}_j = \dot{T}_j^*$ and $\dot{b}_j = \dot{b}_j^*$. Equation (2.30) is then reduced to

$$H = \int_{v} \Delta \dot{N}_{ij} \left(\Delta u_{j} \right),_{i} dv = 0$$
(2.31)

Hence, according to Hill, uniqueness of the solution is ensured if

$$H = \int_{\mathcal{V}} \Delta \dot{N}_{ij} \left(\Delta u_j \right),_i \, \mathrm{d}v > 0 \tag{2.32}$$

for every kinematically admissible Δu_i .

2.2.1 Linear comparison solid

The criterion defined in equation (2.32) is difficult to apply in practical problems. By introducing the notion of linear comparison solid, Hill proposed a second criterion which is easier to handle. A fictitious solid having the same configuration and stresses under the current loading as the real one, but a different incremental constitutive law is considered. Namely, at each material point, the fictitious solid is assumed as incrementally linear with the constitutive relationship

$$\dot{N}_{ij} = C_{ijkl}^L u_{l,k} \tag{2.33}$$

By using the notations in (2.27) and (2.29), the modulus C_{ijkl}^L is chosen such that

$$\Delta \dot{N}_{ij} \left(\Delta u_j\right)_{,i} \geq C_{ijkl}^L \left(\Delta u_j\right)_{,i} \left(\Delta u_l\right)_{,k} \tag{2.34}$$

for every pair of incremental solutions \dot{u}_j and \dot{u}_j^* .

The following functional F is then defined

$$F = \int_{v} C_{ijkl}^{L} (\Delta u_j)_{,i} (\Delta u_l)_{,k} dv$$
 (2.35)

From (2.31) and (2.34), it can be concluded that

$$H \ge F \tag{2.36}$$

and by using (2.32), the criterion of uniqueness can be expressed as

$$F = \int_{v} C_{ijkl}^{L} \left(\Delta u_{j} \right),_{i} \left(\Delta u_{l} \right),_{k} dv > 0$$

$$(2.37)$$

for every kinematically admissible Δu_i .

The problem related to equation (2.37) lies in choosing the optimal linear comparison solid so that the difference between F and H is as small as possible. An example of such a choice is given in Section 2.3.3.

2.3 Euler beam analysis

The purpose of this section is to present a review of the different works done on the plastic buckling of a pin-ended column based on the Bernoulli plane beam assumptions. After presenting the elastic case and the two classical theories of the tangent and reduced modulus load, a theoretical analysis is performed, starting from Hill's criterion of uniqueness. A post-bifurcation analysis is also presented.

The column, see Figure 2.9, has a circular cross-section. It is assumed thick enough so that elastic buckling is prohibited, but slender enough so that beam theory can still be applied. The model adopted is based on a *shallow arch* strain formulation which, under Bernoulli hypothesis, is defined by

$$\varepsilon = u' + \frac{1}{2}(v')^2 - yv'' \tag{2.38}$$

where a prime denotes differentiation with respect to x.

A bilinear elastic-plastic law is considered.

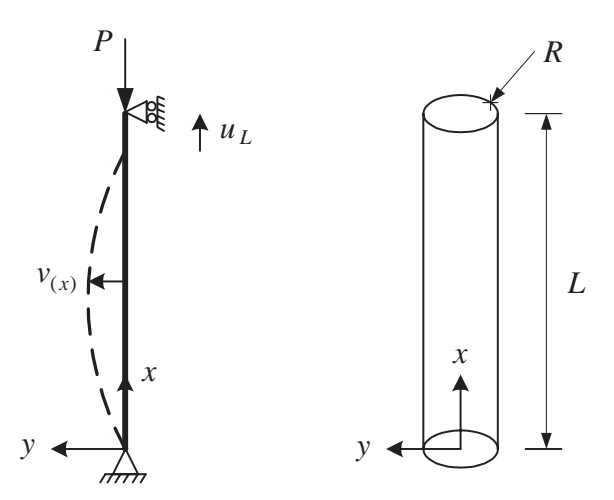


Figure 2.9: Simply supported column with circular cross-section.

2.3.1 Elastic case

The elastic buckling analysis is performed by using the principle of virtual work

$$\int_{v} \sigma \, \delta \varepsilon \, \mathrm{d}v = -P \, \delta u_{L} \tag{2.39}$$

If the beam is inextensible, equation (2.38) gives

$$u' + \frac{1}{2}(v')^2 = 0 (2.40)$$

and therefore

$$\delta u_L = \int_L \delta u' = -\int_L v' \, \delta v' \, \mathrm{d}x \tag{2.41}$$

Equations (2.38), (2.40) and (2.41) are introduced in (2.39). After some work, the second order terms give the classical Euler equation

$$E I v'' + P v = 0 (2.42)$$

The solution is given by

$$P_e = \frac{\pi^2 E I}{L^2} = \frac{\pi^3 E R^4}{4 L^2} \tag{2.43}$$

The eigenmode associated with P_e is

$$v = R \sin\left(\frac{\pi x}{L}\right) \tag{2.44}$$

and the related strains are

$$\varepsilon = \frac{\pi^2}{L^2} R y \sin\left(\frac{\pi x}{L}\right) \tag{2.45}$$

Equation (2.42) can also be derived by using a linear strain theory and by writing the equilibrium equations in the deformed configuration. This analysis, based on a shallow arch strain definition, is usually called *linearised buckling* or *Euler buckling*. It gives the right critical load, but the post-bifurcation path obtained is the horizontal line $P = P_e$, while the exact one is an upward parabola [29,72].

2.3.2 Reduced versus tangent modulus load

These two theories based on linearised buckling assumption were in concurrence until Shanley showed that a perfect column begins to bend at the tangent modulus load P_t . Shanley's results are based on experiments and on the assumption that a column behaves qualitatively in the same way as the discrete model he introduced. The theoretical rigorous proof requires Hill's criterion of uniqueness and will be described in the next section.

Apart from the historical aspect, the interest in presenting these two theories lies in the physical description of the buckling phenomenon. Moreover, although the theory of the reduced modulus load P_r is not correct, this load corresponds to the limit of stability along the fundamental path and has therefore a theoretical importance (cf. Section 2.4.3)

In order to simplify the calculations, a column with a rectangular cross-section (A = b h) is considered.

Reduced modulus load

It is assumed that the column remains straight while the axial load is increased beyond the yield point, after which the column bends, or tries to bend, at a constant compressive force. The problem is then the same as for Euler's theory, i.e. to determine deformed configurations which are in equilibrium. The calculations based on Figure 2.10 are summarised below.

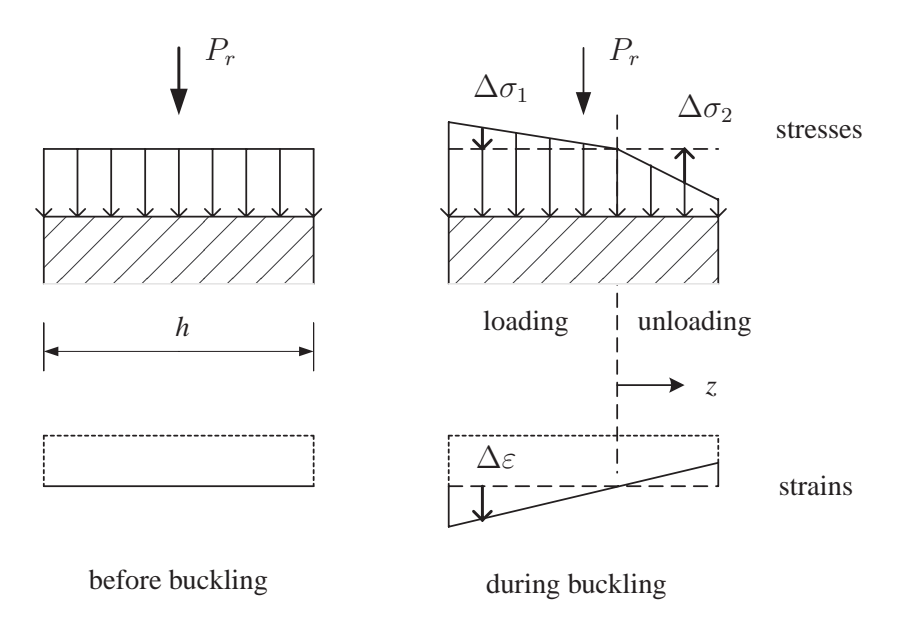


Figure 2.10: Reduced modulus load assumptions.

$$\Delta \sigma_1 = E_t \Delta \varepsilon$$
 in the loading area $\Delta \sigma_2 = E \Delta \varepsilon$ in the unloading area (2.46)

Buckling occurs at a constant axial load, which implies

$$\int_{A} \Delta \sigma = 0 \tag{2.47}$$

Equation (2.47) gives the position of the z axis as function of the moduli E and E_t . The bending moment is then calculated according to

$$M = \int_{A} z \,\Delta\sigma \tag{2.48}$$

which gives

$$M = E_r I/\rho \tag{2.49}$$

with

$$E_r = \left[\frac{1}{2} \left(E^{-1/2} + E_t^{-1/2} \right) \right]^{-2} \tag{2.50}$$

 E_r is called the reduced modulus and depends on the shape of the cross-section.

By introducing the classical equations

$$M = -P y$$
 $1/\rho = y''$ (2.51)

the following differential equation is obtained

$$E_r I y'' + P y = 0 (2.52)$$

By similarity with Euler equation, the solution is given by

$$P_{cr} = P_r = \frac{\pi^2}{L^2} E_r I \tag{2.53}$$

This result is valid under the assumption that the column is plasticised at P_r , i.e. if $P_r > A \sigma_Y$ (σ_Y is yield limit defined in Figure 2.4).

Tangent modulus load

Actually, the column is free to bend at any time. There is nothing to prevent it from bending simultaneously with increasing axial load. The tangent modulus load theory assumes that the column remains straight until the critical load P_t is reached and that an infinitesimal lateral deflection occurs when applying an infinitesimal increment load ΔP in such a way that the tensile strain caused by the deflection is compensated by the axial shortening due to ΔP . Then there is no unloading point in the cross-section (cf. Figure 2.11) and $\Delta \sigma = E_t \Delta \varepsilon$ still applies everywhere. The analysis is therefore the same as in the elastic case by replacing E by E_t . The solution (Euler) is

$$P_t + \Delta P = \frac{\pi^2}{L^2} E_t I \tag{2.54}$$

If ΔP is assumed infinitesimal, the critical load is obtained as

$$P_{cr} = P_t = \frac{\pi^2}{L^2} E_t I \tag{2.55}$$

This result assumes also that the column is plasticised at P_t , i.e. $P_t > A \sigma_Y$.

Remark

This approach presents a paradox. There is no elastic unloading and E_t applies everywhere. Therefore, according to Euler's theory of buckling, the load cannot

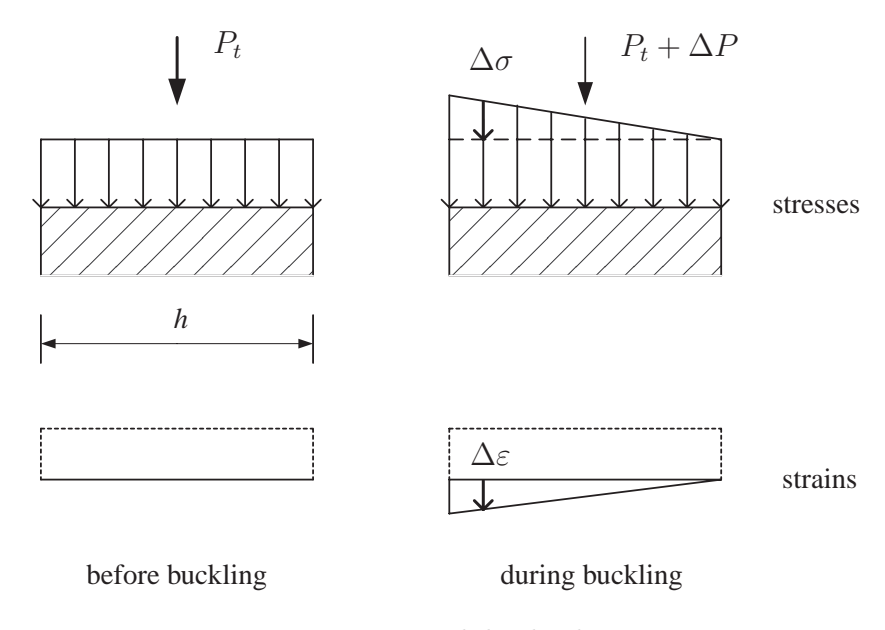


Figure 2.11: Tangent modulus load assumptions.

exceed P_t , which is inconsistent with the application of ΔP . This paradox was explained first by Shanley [88]. By measuring the strain distribution in a column test, he showed that bending in a perfect column begins at the tangent modulus load P_t with one line of non-loading (in case of a column with rectangular cross-section). After that, a further increase of the load is supported by the apparition of a zone of elastic unloading. This zone expands when the load increases as shown in Figure 2.12.

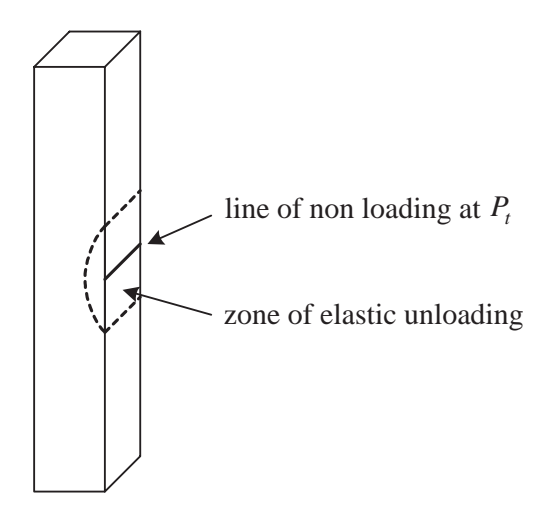


Figure 2.12: Zone of elastic unloading in a column with rectangular cross-section.

2.3.3 Theoretical plastic analysis

This analysis can be seen as an application of the concepts presented in Section 2.2. In addition, based on the work done by Hutchinson [49, 50], a study of the post-bifurcation path is performed.

The beam is assumed uniformly compressed beyond the plastic limit $(P > \sigma_Y \pi R^2)$. The problem is to determine whether it is possible to obtain a bifurcation when an infinitesimal load increment ΔP is applied. The incremental changes of the fundamental solution are denoted by $\Delta \sigma_f$ and $\Delta \varepsilon_f$ while those of the bifurcated solution are denoted by $\Delta \sigma_b$ and $\Delta \varepsilon_b$ with ε defined according to equation (2.38).

The difference between these two solutions is denoted by

$$\Delta \varepsilon = \Delta \varepsilon_b - \Delta \varepsilon_f \qquad \Delta \sigma = \Delta \sigma_b - \Delta \sigma_f \tag{2.56}$$

The function H, defined in (2.31), can be rewritten as

$$H = \int_{v} \Delta \sigma \, \Delta \varepsilon \, \mathrm{d}v \tag{2.57}$$

At P the whole beam is plasticised since the fundamental path is a pure axial compression. The linear comparison operator C_{ijkl}^L defined in Section 2.2 is taken as

$$C_{ijkl}^L = E_t$$

Hence, the function F(2.35) can be rewritten as

$$F = \int_{v} E_t \, \Delta \varepsilon^2 \, \mathrm{d}v \tag{2.58}$$

For this particular problem, the relation $F \leq H$ (2.36) can easily be proved as follow

$$H - F = \int_{v} T \, \mathrm{d}v \tag{2.59}$$

with

$$T = (\Delta \sigma - E_t \Delta \varepsilon) \Delta \varepsilon$$

= $[(\Delta \sigma_b - \Delta \sigma_f) - E_t (\Delta \varepsilon_b - \Delta \varepsilon_f)] (\Delta \varepsilon_b - \Delta \varepsilon_f)$ (2.60)

Depending on the sign of $\Delta \varepsilon_b$ and $\Delta \varepsilon_f$, T can take the following values

•
$$\Delta \varepsilon_b \leq 0$$
 $\Delta \varepsilon_f \leq 0$ \rightarrow $\Delta \sigma_b = E_t \Delta \varepsilon_b$ $\Delta \sigma_f = E_t \Delta \varepsilon_f$ \rightarrow $T = 0$

•
$$\Delta \varepsilon_b \leq 0$$
 $\Delta \varepsilon_f \geq 0$ \rightarrow $\Delta \sigma_b = E_t \, \Delta \varepsilon_b$ $\Delta \sigma_f = E \, \Delta \varepsilon_f$
 \rightarrow $T = (E_t - E) \, \Delta \varepsilon_f \, (\Delta \varepsilon_b - \Delta \varepsilon_f) \geq 0$ $(E_t < E)$

•
$$\Delta \varepsilon_b \ge 0$$
 $\Delta \varepsilon_f \ge 0$ \rightarrow $\Delta \sigma_b = E \, \Delta \varepsilon_b$ $\Delta \sigma_f = E \, \Delta \varepsilon_f$
 \rightarrow $T = (E - E_t) (\Delta \varepsilon_b - \Delta \varepsilon_f)^2 \ge 0$

•
$$\Delta \varepsilon_b \ge 0$$
 $\Delta \varepsilon_f \le 0$ \rightarrow $\Delta \sigma_b = E \, \Delta \varepsilon_b$ $\Delta \sigma_f = E_t \, \Delta \varepsilon_f$
 \rightarrow $T = (E - E_t) \, (\Delta \varepsilon_b - \Delta \varepsilon_f) \, \Delta \varepsilon_b \ge 0$

This shows that $T \geq 0$ always applies and therefore $H - F \geq 0$.

Bifurcation load

Let P_c be the lowest value for which the condition F=0 is satisfied. The solution of the variational principle $\delta F=0$ is given in Section 2.3.1. The only modification required is the replacement of E by E_t . Hence, the critical load is

$$P_c = \frac{\pi^2 E_t I}{L^2} = \frac{\pi^3 E_t R^4}{4L^2} = P_t \tag{2.61}$$

and the associated eigenmode is defined by

$$\stackrel{(1)}{v} = R \sin\left(\frac{\pi x}{L}\right) \qquad \stackrel{(1)}{\varepsilon} = \frac{\pi^2}{L^2} R y \sin\left(\frac{\pi x}{L}\right) \tag{2.62}$$

Equation (2.61) confirms that the lowest bifurcation occurs at the tangent modulus load P_t as it was originally shown by Shanley.

Initial tangent

A bifurcated solution is searched as a linear combination of the fundamental path and the eigenmode of the elastic comparison solid

$$\Delta \varepsilon_b - \Delta \varepsilon_f = \xi \stackrel{(1)}{\varepsilon} \tag{2.63}$$

with ξ denoting the amplitude of the eigenmode defined by (2.62) which is taken as the independent variable in the post-buckling expansion. With (2.63) F=0, but not H, unless both $\Delta \varepsilon_b$ and $\Delta \varepsilon_f$ have the property that no elastic unloading occurs at any point in the column. The load ratio λ and its incremental variation $\Delta \lambda$ are introduced as

$$\lambda = \frac{P}{P_c} \tag{2.64}$$

$$\Delta \lambda = \lambda - \lambda_c = \lambda_1 \xi \qquad (\lambda_c = 1) \tag{2.65}$$

If λ_1 has to represent the initial tangent to the bifurcated path, a differential form of equations (2.63) and (2.65) can be obtained by the following transformations

$$\frac{\Delta\varepsilon_b}{\xi} - \frac{\Delta\varepsilon_f}{\xi} = \stackrel{(1)}{\varepsilon} \qquad \frac{\Delta\lambda}{\xi} = \lambda_1 \tag{2.66}$$

When $\xi \to 0$, equations (2.66) give

$$\overset{\circ}{\varepsilon}_{b} = \overset{\circ}{\varepsilon}_{f} + \overset{(1)}{\varepsilon} = \lambda_{1} \overset{\prime}{\varepsilon}_{f} + \overset{(1)}{\varepsilon} \tag{2.67}$$

with

$$\stackrel{\circ}{()} = \frac{\partial ()}{\partial \xi} \qquad \stackrel{\prime}{()} = \frac{\partial ()}{\partial \lambda} \Big|_{\lambda_c} \tag{2.68}$$

For the column

$$\varepsilon_f = \frac{\sigma_f}{E_t} = \frac{-\lambda P_c}{\pi R^2 E_t} \quad \to \quad \varepsilon_f = \frac{-\pi^2 R^2}{4 L^2} \tag{2.69}$$

Equations (2.67) and (2.69) give

$$\stackrel{\circ}{\varepsilon}_b = \frac{\pi^2 R^2}{L^2} \left[-\frac{\lambda_1}{4} + \frac{y}{R} \sin\left(\frac{\pi x}{L}\right) \right]$$
 (2.70)

By taking λ_1 large enough it is obviously possible to obtain

$$\stackrel{\circ}{\varepsilon}_b < 0$$
 (2.71)

everywhere in the column so that no elastic unloading occurs, which further implies H=0. The problem is to determine which value(s) of λ_1 can be solution to the boundary-value problem. For this purpose, the slope for the elastic comparison solid at bifurcation is denoted by λ_1^{he} . Euler analysis gives $\lambda_1^{he}=0$. Then λ_1^{he} is such that

$$-\frac{\lambda_1^{he}}{4} + \frac{y}{R}\sin\left(\frac{\pi x}{L}\right) > 0 \tag{2.72}$$

in some part of the column and therefore¹

$$\lambda_1^{he} < \lambda_1 \tag{2.73}$$

It can then be inferred that the initial slope of the elastic-plastic solid λ_1 must be the smallest value consistent with (2.71). The reason for this is that if λ_1 were larger, then by continuity there would be some range of positive ξ where $\stackrel{\circ}{\varepsilon}_b$ would be lower than zero everywhere. Consequently, the behaviour of the elastic-plastic solid would initially coincide with that of the comparison solid so that $\lambda_1^{he} = \lambda_1$. However, this possibility is contradicted by (2.73) which implies that λ_1 is the smallest value such that

$$\forall x \in [0; L] \text{ and } y \in [-R; R] \quad \stackrel{\circ}{\varepsilon}_b = \frac{\pi^2 R^2}{L^2} \left[-\frac{\lambda_1}{4} + \frac{y}{R} \sin\left(\frac{\pi x}{L}\right) \right] \le 0 \quad (2.74)$$

The solution is then

$$\lambda_1 = 4 \tag{2.75}$$

and one point of non-loading ($\stackrel{\circ}{\varepsilon}_b = 0$) is obtained at x = L/2 and y = R. This argumentation proves that a zone of elastic unloading spreads from this point after the bifurcation.

Post-bifurcation path

By performing a perturbation expansion of λ about the bifurcation point, Hutchinson calculated an expression for the post-bifurcation path under the form

$$\lambda = 1 + 4\xi + \lambda_2 \xi^{1+\beta} \tag{2.76}$$

¹The inequality (2.73) is verified in most of the common elastic-plastic problems.

This approach is similar to that developed in Section 2.1.2 for the \perp model. Here, λ_2 and β are determined by an approximation of the lowest order non-vanishing terms in the equation of virtual work (2.39), which gives

$$\lambda_2 = -6.337 \left(\frac{E_t}{E - E_t}\right)^{1/3} \qquad \beta = \frac{1}{3}$$
 (2.77)

The analysis which leads to the above expression is rather lengthy and will not be described here. It can be noted that Hutchinson showed that the second term of the perturbation expansion comes essentially from the apparition and expansion of the zone of elastic unloading. The same result was also obtained using a different method by Leger and Potier-Ferry [58]. Using the expression (2.76), an estimation of the maximal load can be calculated as

$$\lambda_{\text{max}} = 1 + 0.106 \, \frac{E - E_t}{E_t} \qquad \xi_{\text{max}} = 0.106 \, \frac{E - E_t}{E_t}$$
 (2.78)

In the case of a rectangular cross-section, the same analysis leads to

$$\lambda = 1 + 3\xi + \lambda_2 \xi^{7/5}$$
 $\lambda_2 = -5.003 \left(\frac{E_t}{E - E_t}\right)^{2/5}$ (2.79)

Remark 1: Contrary to the elastic case, the post-buckling path in the plastic range depends on the geometry of the cross-section. It comes from the growth of the elastic unloading zone which depends on the shape of the cross-section (cf. Figure 2.13).

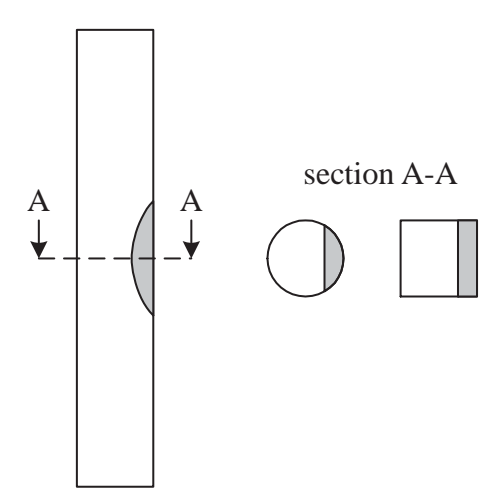


Figure 2.13: Zone of elastic unloading for circular and rectangular cross-sections.

According to the author's opinion, the two following remarks about expressions (2.76) and (2.79) can be stated.

Remark 2: The strain assumption (2.38) is to crude to represent correctly the elastic post-bifurcation. This study is therefore based on the assumption that in the vicinity of the post-bifurcation path material non-linearity prevails over the geometrical one. However it is not known how far this assumption is valid and especially if it is still valid when the maximal load is reached. The results presented

in Section 2.1.2 suggest that geometrical non-linearity influences the post-bifurcation path in the plastic range and therefore the value of the maximal load.

Remark 3: The expressions (2.76) and (2.79) are only valid for small values of ξ , but it is not known how large ξ can be. They may diverge from the correct path before the occurrence of the maximal load and therefore the estimations of the maximal load may not be correct. In the case of a rectangular cross-section, Cheng [16], using a different approach, calculated the following term in the expansion

$$\lambda = 1 + 3\xi + \lambda_2 \xi^{7/5} + \lambda_3 \xi^{9/5}$$
 $\lambda_3 = 2.207 \left(\frac{E_t}{E - E_t}\right)^{4/5}$ (2.80)

The expressions (2.79) and (2.80) are plotted in Figure 2.14. Here again, it is not known how far the expression (2.80) is valid. It is not certain that the addition of another term in the expansion will increase the accuracy of the maximal load. The unusual high values of $\lambda_{\text{max}} (\approx 2)$ and $\xi_{\text{max}} (\approx 1.8)$ suggest that (2.80) diverges from the correct path before the occurrence of the maximal load.

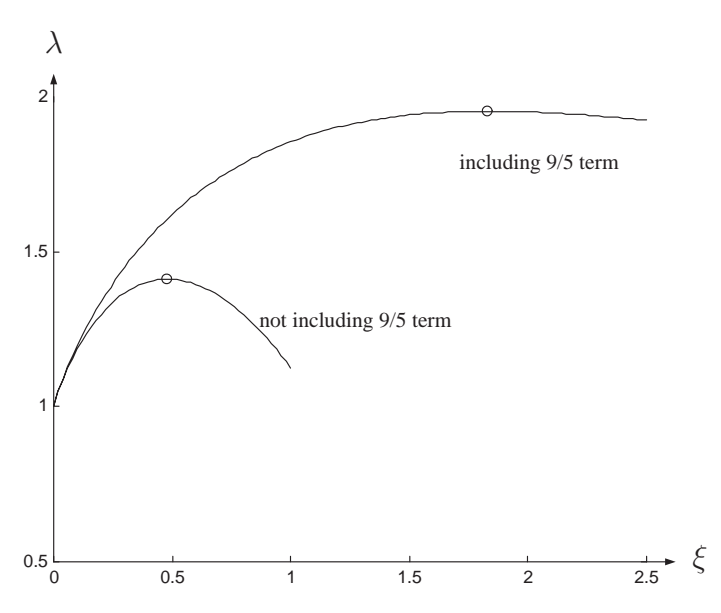


Figure 2.14: Post-critical paths according to (2.79) and (2.80) with $E_t/E = 0.2$

2.4 Discretised systems

In the light of the application presented in the last section two fundamental questions remain. The first one concerns the choice of the constitutive moduli in the elastic comparison solid. Until now, no method has been proposed to find a comparison solid which does not overestimate the range of non-uniqueness and gives by eigenvalue analysis the lowest bifurcation point. For the Euler beam it has only been shown that taking E_t as elastic comparison modulus everywhere in the beam, works. This choice is rather intuitive since the fundamental solution is a uniform plastic compression. However, in a finite element context this choice is not obvi-

ous, especially in cases where the fundamental solution is more complicated than a uniformly compressed state.

The second question concerns the existence of an infinite number of secondary postcritical paths. In the last section, only the secondary path branching at P_t has been studied. The essential question in a numerical context is then whether it is worthwhile to determinate the other secondary paths. An additional question refers to the nature of the fundamental path beyond P_t . On one hand imperfection analyses (cf. e.g. Section 2.1.2) suggest that only the first secondary path has a physical meaning. However, on the other hand, the points along the fundamental path are stable up to P_r .

The answers to these questions have been given by Petryk [76–81]. This work, which is summarised in this section, gives a complete theoretical description of the phenomenon of bifurcation and instability in time-independent plasticity. The notions of uniqueness and stability of the solutions to the boundary-value problem in elastic-plastic deformation are discussed and an energy interpretation is given. Moreover, this work gives the theoretical basis for the two numerical branch switching procedures presented in Section 5.3.

The theory developed by Petryk is based on the assumptions that the problem has been spatially discretised and that the constitutive moduli are symmetric.

2.4.1 Constitutive framework and discretised rate problem

A time-independent elastic-plastic material is considered. The constitutive equation between the rate of stresses and strains is expressed in the form

$$\dot{\mathbf{S}} = \mathbf{C}(\dot{\mathbf{F}}, \mathcal{H}) \cdot \dot{\mathbf{F}} \qquad \mathbf{C} = \frac{\partial \dot{\mathbf{S}}}{\partial \dot{\mathbf{F}}}$$
 (2.81)

where S is the first Piola-Kirchoff stress tensor (i.e. the transpose of the nominal stress tensor) and F is the deformation gradient. The symbol \mathcal{H} represents the influence of the deformation history.

It is assumed that relation (2.81) admits a potential $U(\dot{\mathbf{F}}, \mathcal{H})$ so that

$$\dot{\mathbf{S}} = \frac{\partial U}{\partial \dot{\mathbf{F}}} \qquad \mathbf{C} = \frac{\partial^2 U}{\partial \dot{\mathbf{F}} \partial \dot{\mathbf{F}}}$$
 (2.82)

which is equivalent to imposing that the instantaneous modulus C is symmetric.

The problem is supposed spatially discretised. The velocity fields ${\bf v}$ are then restricted to having the classical form

$$v(\xi) = \phi_{\alpha}(\xi) v_{\alpha} \qquad \alpha = 1, ..., N$$
 (2.83)

where ξ are the position vectors in the reference configuration, ϕ_{α} the shape functions and v_{α} the velocities of the nodal degrees of freedom. In the same way, the

displacements \mathbf{u} and the velocity variations \mathbf{w} are given by

$$u(\xi) = \phi_{\alpha}(\xi) u_{\alpha} \qquad \alpha = 1, ..., N$$

$$w(\xi) = \phi_{\alpha}(\xi) w_{\alpha} \qquad \alpha = 1, ..., N$$
(2.84)

The numeration of the shape functions is chosen such that the boundary conditions give prescribed values $v_{\alpha} = \bar{v}_{\alpha}$ and $w_{\alpha} = 0$ for $\alpha = M + 1, ..., N$.

By assuming a conservative loading, components of the prescribed load vector are given, in the rate form, by

$$\dot{P}_{\alpha} = \int_{v} \dot{\mathbf{b}} \,\phi_{\alpha} \,\mathrm{d}v + \int_{s} \dot{\mathbf{T}} \,\phi_{\alpha} \,\mathrm{d}s \qquad \alpha = 1, ..., M \tag{2.85}$$

and the rates of the internal forces are given by

$$\dot{Q}_{\alpha}\left(\tilde{\mathbf{v}}\right) = \int_{v} \dot{\mathbf{S}}\left(\nabla \mathbf{v}\right) \cdot \nabla \phi_{\alpha} \, \mathrm{d}v \qquad \alpha = 1, ..., N$$
(2.86)

where a tilde over a symbol denotes a spatial field defined over the body volume in the reference configuration.

The equilibrium equations of the first order problem in velocities are

$$\dot{Q}_{\alpha}\left(\tilde{\mathbf{v}}\right) = \dot{P}_{\alpha} \qquad \alpha = 1, ..., M$$
 (2.87)

The components of the tangent stiffness matrix are defined by

$$K_{\alpha\beta}\left(\tilde{\mathbf{v}}\right) = \frac{\partial \dot{Q}_{\alpha}\left(\tilde{\mathbf{v}}\right)}{\partial v_{\beta}} = \int_{v} \nabla \phi_{\alpha} \cdot \mathbf{C}\left(\nabla \mathbf{v}\right) \cdot \nabla \phi_{\beta} \, \mathrm{d}v \tag{2.88}$$

which allows the reformulation of the equilibrium equations (2.87) as

$$K_{\alpha\beta}\left(\tilde{\mathbf{v}}\right) v_{\beta} = \dot{P}_{\alpha} \qquad \alpha = 1, ..., M$$
 (2.89)

From (2.82) and (2.88), it follows that **K** is symmetric, i.e. $K_{\alpha\beta} = K_{\beta\alpha}$.

Since the existence of a potential U is assumed, a functional J can be defined as

$$J(\tilde{\mathbf{v}}) = \int_{v} U(\nabla \mathbf{v}) \, dv - \sum_{\alpha=1}^{M} \dot{P}_{\alpha} v_{\alpha} = \frac{1}{2} K_{\alpha\beta}(\tilde{\mathbf{v}}) v_{\beta} v_{\alpha} - \sum_{\alpha=1}^{M} \dot{P}_{\alpha} v_{\alpha}$$
(2.90)

The equations (2.87) or (2.89) can then be given the variational formulation

$$\frac{\partial J\left(\tilde{\mathbf{v}}\right)}{\partial v_{\alpha}} = 0 \qquad \alpha = 1, ..., M \tag{2.91}$$

From (2.90), the tangent stiffness matrix can also be expressed as

$$K_{\alpha\beta}\left(\tilde{\mathbf{v}}\right) = \frac{\partial^{2} J\left(\tilde{\mathbf{v}}\right)}{\partial v_{\alpha} \partial v_{\beta}} \tag{2.92}$$

2.4.2 Tangent comparison solid

The theory developed by Hill (cf. Section 2.2) does not require any solution to be known in advance. However, in practice a fundamental solution is known and the optimal choice for the linear comparison solid can be determined from the fundamental solution, as explained in the following.

The elastic operator is C_{ijkl}^e . Where the yield condition is satisfied, the elasto-plastic operator is C_{ijkl}^e in case of elastic unloading, and C_{ijkl}^p in case of plastic loading. The linear comparison operator C_{ijkl}^L is defined by

$$C_{ijkl}^L = C_{ijkl}^p (2.93)$$

at every point in the body where the yield condition is currently satisfied, independent of the case (plastic loading or elastic unloading) concerned, and by

$$C_{ijkl}^L = C_{ijkl}^e \tag{2.94}$$

at every point where the stresses lie within the yield surface. With this choice, it can be proved that the condition (2.34) is respected for elastic-plastic material with smooth yield surface.

In other words, the actual tangent moduli of the fundamental solution is taken as linear comparison solid. For this reason Petryk introduced the notion of tangent comparison solid.

It can be noted that in the analysis of Euler beam in Section 2.3.3, $C_{ijkl}^L = E_t$ has been assumed, which actually corresponds to the tangent comparison solid.

2.4.3 Bifurcation and stability

Directional stability of an equilibrium state

The notion of stability is often referred to the definition given by Liapunov. Roughly speaking, an equilibrium state is stable if after applying a small perturbation at constant loading, the damped structure returns to the previous equilibrium state. For elastic-plastic structures, this cannot be expected in general. Moreover, even if the equilibrium state after perturbation is very close to the original one, there is no guarantee that the continuation of the loading process will not give divergence between the two paths. To avoid this problem, Petryk proposed a different definition of stability of an equilibrium state: "an equilibrium configuration is said to be stable if the distance from that configuration in any dynamic motion caused by a disturbance can be made as small as we please if a measure of the disturbance itself is sufficiently small." He introduced a restriction to this definition by considering that the perturbed motion from the equilibrium state is such that variations of the direction of the velocity field is negligible. In that restrictive sense, he introduced the notion of directional stability.

Under these assumptions, it can be proved that an equilibrium state is directionally stable if

$$\dot{Q}_{\alpha}(\tilde{\mathbf{w}}) \ w_{\alpha} > 0 \qquad \text{for every } \tilde{\mathbf{w}} \neq 0$$
 (2.95)

Uniqueness of the solution

It is supposed that a fundamental solution $\tilde{\mathbf{v}}_f$ to the equation (2.87) is known. The respective tangent stiffness matrix is denoted \mathbf{K}_f . Petryk has shown that if the condition (2.95) is respected, uniqueness of the solution is ensured if $\tilde{\mathbf{v}}_f$ assigns to J a strict and absolute minimum value, i.e. if

$$J(\tilde{\mathbf{v}}_f) < J(\tilde{\mathbf{v}})$$
 for every admissible $\tilde{\mathbf{v}}$ (2.96)

By using equations (2.91) and (2.92) and the condition (2.96), it can be concluded that uniqueness of the solution is ensured as long as \mathbf{K}_f is positive definite. This result can also be obtained from Hill's criterion of uniqueness. The definition of the tangent comparison solid allows to use results for elastic structures. Therefore equation (2.37) ensures uniqueness of the solution as long as \mathbf{K}_f is positive definite.

This criterion holds for elastic-plastic materials obeying the normality flow rule relative to a smooth yield surface. This is the case for the von Mises material which will be used in the numerical applications. Petryk proposed a less restrictive condition

$$\dot{\mathbf{S}}_f \cdot \dot{\mathbf{F}} - \dot{\mathbf{S}} \cdot \dot{\mathbf{F}}_f \ge 0$$
 for every admissible $\dot{\mathbf{F}}$ (2.97)

where $\dot{\mathbf{S}} = \mathbf{C} \,\dot{\mathbf{F}}$. For the applications in this thesis, this condition does not need to be further investigated.

Continuous range of bifurcation

The question investigated here is to determine what happens beyond the first bifurcation point when the tangent stiffness matrix \mathbf{K}_f ceases to be positive definite. It is possible that on the secondary post-bifurcation path the tangent stiffness matrix becomes positive definite again. This is due to the local elastic unloading which starts at the bifurcation (cf. e.g. the case of the Euler beam in Section 2.3). In that case, uniqueness of the solution is guaranteed and the secondary path can be treated exactly in the same way as the fundamental path before bifurcation.

The situation is different on the fundamental path where \mathbf{K}_f becomes indefinite after the first bifurcation point. If the condition (2.95) fails at the same point where \mathbf{K}_f becomes indefinite then this critical point is a limit point. If the condition (2.95) is still valid beyond the first critical point, it can be shown that there is a bifurcation at every point on the fundamental path along which \mathbf{K}_f is indefinite and the condition (2.95) holds. This defines a continuous range of bifurcation points along the fundamental path. It has to be noted that every point within this interval is stable in a dynamical sense. These results, illustrated in Figure 2.15, can be seen as a generalisation of the results obtained for Shanley's column, i.e., along the fundamental path every point within the interval $[P_t, P_r]$ is a bifurcation point and is stable in the dynamical sense.

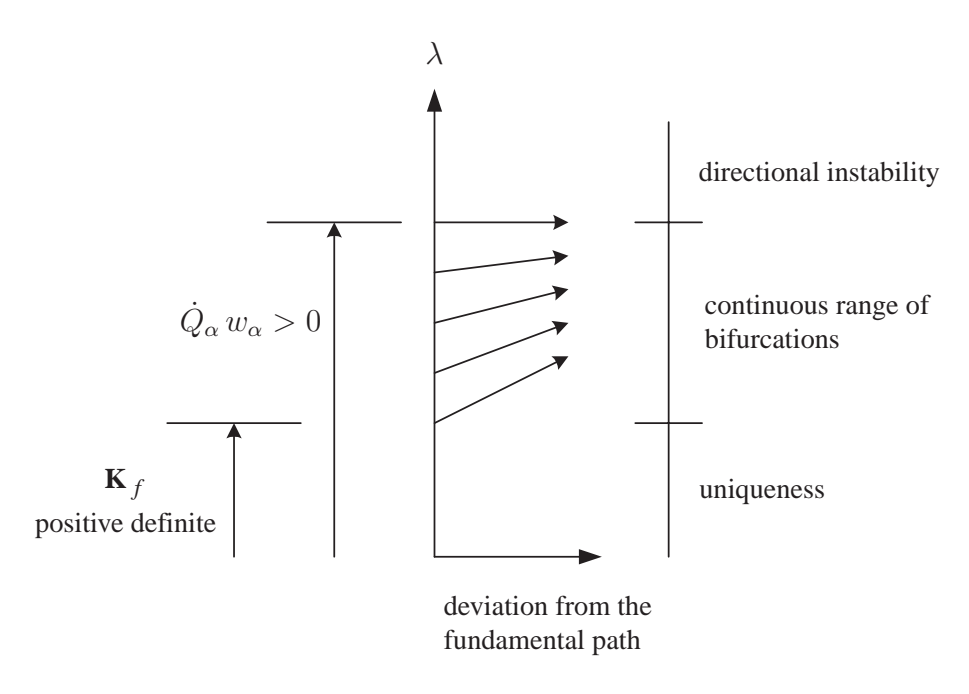


Figure 2.15: Schematic illustration of the results of Section 2.4.3.

2.4.4 Energy approach

Instability of a deformation path

The case of a continuous range of bifurcation points is considered. The question investigated here is to determine among all these possible paths which ones are realisable in a physical sense. The response can be found by introducing small imperfections: when the imperfections tend to zero, the equilibrium paths obtained tend to the secondary path branching out at the lowest bifurcation point. This proves that only this secondary path has a physical meaning. A probabilistic approach gives the same result: if at a bifurcation point both paths (fundamental and secondary) have comparable chances to be followed, then, due to the infinite number of bifurcation points, any segment of the fundamental path has zero probability to be followed. Therefore it can be concluded that beyond the first bifurcation point, the fundamental path, even if each equilibrium point along it is stable in a dynamical sense, has no physical meaning and can be considered as unstable. The notion of stability introduced here does not concern any more an equilibrium point but a deformation path: a deformation path is said to be unstable if it cannot be followed in a physical sense.

Energy interpretation

The purpose of this section is to give an energy interpretation of the notion of instability of a deformation path.

The deformation work in the body during a deformation process is expressed as

$$W = \int_0^t Q_\alpha \, v_\alpha \, \mathrm{d}\tau \tag{2.98}$$

The potential energy of the loading is expressed as

$$\Omega = -\sum_{\alpha=1}^{M} P_{\alpha} u_{\alpha} \tag{2.99}$$

The energy functional is then defined by

$$E = W + \Omega \tag{2.100}$$

An increment of the value of E can be interpreted as the amount of external energy which has to be supplied to the system consisting of the body and the loading in order to produce the deformation increment.

By time derivation, it can be shown that \dot{E} is independent of $\tilde{\mathbf{v}}$, i.e.

$$\dot{E}\left(\tilde{\mathbf{v}}\right) = \text{constant}$$
 (2.101)

and that if $\tilde{\mathbf{v}}_1$ and $\tilde{\mathbf{v}}_2$ are two admissible velocity fields at the equilibrium state

$$\frac{1}{2}\ddot{E}\left(\tilde{\mathbf{v}}_{1}\right) - \frac{1}{2}\ddot{E}\left(\tilde{\mathbf{v}}_{2}\right) = J\left(\tilde{\mathbf{v}}_{1}\right) - J\left(\tilde{\mathbf{v}}_{2}\right) \tag{2.102}$$

where J is the functional defined in equation (2.90). Hence, the variational principle (2.91) can be equivalently written as

$$\delta \ddot{E}(\tilde{\mathbf{v}}, \tilde{\mathbf{w}}) = 0$$
 for every admissible $\tilde{\mathbf{w}} \neq 0$ (2.103)

The following criterion of path instability is then adopted: along a stable deformation path, the deformation increment must minimise the value of the increment of the energy functional E. This can be related to the physical hypothesis that the real deformation path minimises the energy consumption. By using (2.101), the solution $\tilde{\mathbf{v}}_1$ is therefore stable in an energy sense if

$$\ddot{E}\left(\tilde{\mathbf{v}}_{1}\right) < \ddot{E}\left(\tilde{\mathbf{v}}\right)$$
 for every admissible $\tilde{\mathbf{v}}$ (2.104)

which, from (2.102) can be rewritten as

$$J(\tilde{\mathbf{v}}_1) < J(\tilde{\mathbf{v}})$$
 for every admissible $\tilde{\mathbf{v}}$ (2.105)

By comparing (2.96) and (2.105) it can be concluded that the fundamental solution $\tilde{\mathbf{v}}_f$ is stable as long as the uniqueness of the solution is guaranteed. Beyond the first bifurcation point the tangent matrix \mathbf{K}_f becomes indefinite along the fundamental path. Therefore, from (2.92), the fundamental solution $\tilde{\mathbf{v}}_f$ does no longer minimise \ddot{E} and the solution becomes unstable in the energy sense. It can be proved that another solution which minimises \ddot{E} exists as long as the condition (2.95) holds.

As a conclusion, it has been shown that the definition of stability in an energy sense (minimisation of the consumption of energy) proposed by Petryk is equivalent to the notion of stability of a deformation path given in the previous section. Consequently, the fundamental path $\tilde{\mathbf{v}}_f$ becomes unstable exactly when the tangent stiffness matrix \mathbf{K}_f becomes indefinite.

Chapter 3

2D beam element formulation

In this chapter, internal forces and tangent stiffness matrices for three plane beam elements are derived. All of them are based on the same co-rotational approach, and differ by the strain definition used in the local co-rotational coordinate system. Based on the Bernoulli assumption, the first two elements use a linear and a shallow arch strain definition, respectively. The third element is based on the Timoshenko assumption with linear interpolations for the displacements.

Co-rotational formulation

The co-rotational approach, viewed as an alternative way of deriving efficient non-linear finite elements, has generated an increased amount of interest in the last decade [22, 23, 25, 35, 47, 53, 64, 72, 73, 83, 84, 95]. The main idea in this context is to decompose the motion of the element into rigid body and pure deformational parts, through the use of a local coordinate system (x_l, z_l) , see Figure 3.1, which continuously rotates and translates with the element. The motion of the element from the original undeformed configuration to the actual deformed one can thus be split in two steps. The first one is a rigid rotation and translation of the element. The second step consists of a deformation in the local coordinate system. Assuming that the length of the element is properly chosen, the deformational part of the motion is always small relative to the local axes. Consequently, the local deformations can be expressed with a low order of non-linearity. It must however be emphasised that this low-order non-linearity is only apparent as the geometrical non-linearity is included in the motion of the local coordinate system.

The main advantage of a co-rotational approach is that it leads to an artificial separation of the material and geometrical non-linearities when a linear strain definition in the local coordinate system is used (which is the case for the first and third elements developed in this chapter): plastic deformations occur in the local coordinate system where geometrical linearity is assumed; geometrical non-linearity is only present during the rigid rotation and translation of the undeformed beam. This leads to very simple expressions for the local internal force vector and tangent stiffness matrix. Even when a low-order geometrical non-linearity is included in the strain definition (which is the case of the second element), the expressions for the local internal force vector and tangent stiffness matrix are still very simple.

Constitutive equations

The assumption of small strains but large displacements and rotations, is adopted. Therefore, constitutive elasto-plastic equations based on an additive strain decomposition can be used. In this thesis, a von Mises material with isotropic constant hardening is considered. The reason for this choice has already been discussed in Section 1.1. For the Timoshenko element, interaction between the normal and the shear stress is considered and the constitutive equations are derived from the ones under plane stress conditions by introducing the beam hypothesis.

Resultant forces against Gauss integration

The computation of the local internal forces and stiffness matrix involves several integrations over the element. With respect to integration over a cross-section, two approaches can be considered: the layered and non-layered ones [67].

The non-layered method is based on plastic equations at the section level. This means that the yield criterion is defined as a function of the internal forces. Such functions can be found in [1,56,89] for rectangular and bi-symmetric cross-sections. However, these functions are only approximations of the plastic flow rules. Moreover, they do not model the propagation of plastification and they consider perfect elasto-plastic material models without hardening. For the Bernoulli assumption, Crisfield [24] proposes a function which takes into account the propagation of the plastification, but without considering hardening. Another problem with this approach is the practical impossibility to derive functions for arbitrary cross-sections.

As shown in Chapter 2 for the case of the Euler beam, a growing zone of elastic unloading is developing after bifurcation. Furthermore, the bifurcation point and the nature of the post-bifurcation path are dependent on the hardening. It seems therefore impossible to study plastic instability problems with a non-layered approach. This method, though efficient from a computational point of view, is limited to quick and approximate analyses.

In the layered approach, numerical Gauss integration is performed through the cross-section which means that the plastic rate equations are solved at each Gauss point. A relatively high number of Gauss points is needed in order to model correctly the growing of the elastic unloading zone (case of the Euler beam) and obtain an accurate post-bifurcation path. As alternative to Gauss integration, the Lobatto rule could also be considered. This procedure has the advantage of taking integration points on the surface. However, if a sufficient number of points is taken, both methods give almost the same numerical results.

3.1 Co-rotational framework

The purpose of this section is to derive relations between the local and global expressions of the internal force vector and tangent stiffness matrix. This presentation is mainly taken from Crisfield [23].

3.1.1 Beam kinematics

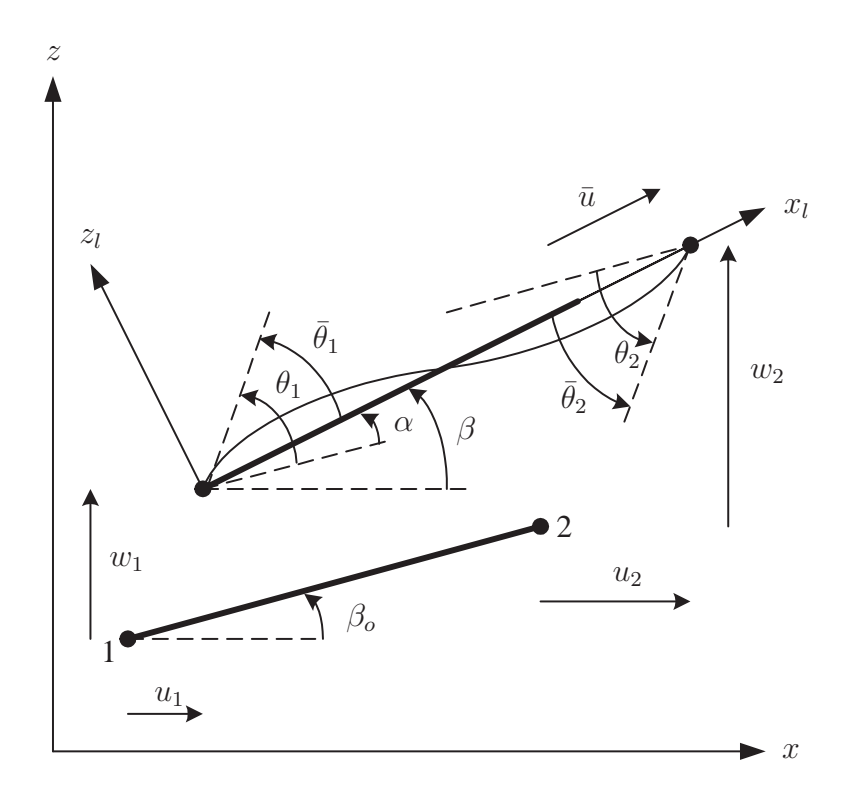


Figure 3.1: Co-rotational formulation: beam kinematics.

The notations used in this section are defined in Figure 3.1. The coordinates for the nodes 1 and 2 in the global coordinate system (x, z) are (x_1, z_1) and (x_2, z_2) . The vector of global displacements is defined by

$$\mathbf{p}_g = \begin{bmatrix} u_1 & w_1 & \theta_1 & u_2 & w_2 & \theta_2 \end{bmatrix}^{\mathrm{T}} \tag{3.1}$$

The vector of local displacements is defined by

$$\mathbf{p}_{l} = \begin{bmatrix} \bar{u} & \bar{\theta}_{1} & \bar{\theta}_{2} \end{bmatrix}^{\mathrm{T}} \tag{3.2}$$

The components of \mathbf{p}_l can be computed according to

$$\bar{u} = l_n - l_o \tag{3.3a}$$

$$\bar{\theta}_1 = \theta_1 - \alpha \tag{3.3b}$$

$$\bar{\theta}_2 = \theta_2 - \alpha \tag{3.3c}$$

In the above equations l_o and l_n denote the initial and current lengths of the element

$$l_o = \left[\left(x_2 - x_1 \right)^2 + \left(z_2 - z_1 \right)^2 \right]^{1/2} \tag{3.4}$$

$$l_n = \left[(x_2 + u_2 - x_1 - u_1)^2 + (z_2 + w_2 - z_1 - w_1)^2 \right]^{1/2}$$
 (3.5)

and α denotes the rigid rotation which can be computed as

$$\sin \alpha = c_o s - s_o c \tag{3.6a}$$

$$\cos \alpha = c_o c + s_o s \tag{3.6b}$$

with

$$c_o = \cos \beta_o = \frac{1}{l_o} (x_2 - x_1)$$
 (3.7a)

$$s_o = \sin \beta_o = \frac{1}{l_o} (z_2 - z_1)$$
 (3.7b)

$$c = \cos \beta = \frac{1}{l_n} (x_2 + u_2 - x_1 - u_1)$$
 (3.7c)

$$s = \sin \beta = \frac{1}{l_n} (z_2 + w_2 - z_1 - w_1)$$
(3.7d)

Then, provided that $|\alpha| < \pi$, α is given by

$$\alpha = \sin^{-1}(\sin \alpha) \quad \text{if } \sin \alpha \ge 0 \text{ and } \cos \alpha \ge 0$$

$$\alpha = \cos^{-1}(\cos \alpha) \quad \text{if } \sin \alpha \ge 0 \text{ and } \cos \alpha < 0$$

$$\alpha = \sin^{-1}(\sin \alpha) \quad \text{if } \sin \alpha < 0 \text{ and } \cos \alpha \ge 0$$

$$\alpha = -\cos^{-1}(\cos \alpha) \quad \text{if } \sin \alpha < 0 \text{ and } \cos \alpha < 0$$

$$(3.8)$$

3.1.2 Virtual displacements

The virtual local displacements are obtained through differentiation of equations (3.3)

$$\delta \bar{u} = c \left(\delta u_2 - \delta u_1 \right) + s \left(\delta w_2 - \delta w_1 \right) = \begin{bmatrix} -c & -s & 0 & c & s & 0 \end{bmatrix} \delta \mathbf{p}_q \tag{3.9a}$$

$$\delta\bar{\theta}_1 = \delta\theta_1 - \delta\alpha = \delta\theta_1 - \delta\beta \qquad (\alpha = \beta - \beta_o) \tag{3.9b}$$

$$\delta\bar{\theta}_2 = \delta\theta_2 - \delta\alpha = \delta\theta_2 - \delta\beta \tag{3.9c}$$

Further, $\delta\beta$ can be calculated by differentiation of (3.7d)

$$\delta\beta = \frac{1}{c \, l_n^2} \left[(\delta w_2 - \delta w_1) \, l_n - (z_2 + w_2 - z_1 - w_1) \, \delta l_n \right] \tag{3.10}$$

where $\delta l_n = \delta \bar{u}$ is given by (3.9a). Using (3.7d), the expression of $\delta \beta$ becomes

$$\delta\beta = \frac{1}{c l_n} \left[(\delta w_2 - \delta w_1) - s c \left(\delta u_2 - \delta u_1 \right) - s^2 \left(\delta w_2 - \delta w_1 \right) \right]$$
(3.11)

which, after simplifications gives

$$\delta\beta = \frac{1}{l_n} \begin{bmatrix} s & -c & 0 & -s & c & 0 \end{bmatrix} \delta \mathbf{p}_g \tag{3.12}$$

Hence, the transformation matrix **B**, defined by

$$\delta \mathbf{p}_l = \mathbf{B} \, \delta \mathbf{p}_g \tag{3.13}$$

is given by

$$\mathbf{B} = \begin{bmatrix} -c & -s & 0 & c & s & 0 \\ -s/l_n & c/l_n & 1 & s/l_n & -c/l_n & 0 \\ -s/l_n & c/l_n & 0 & s/l_n & -c/l_n & 1 \end{bmatrix}$$
(3.14)

3.1.3 Internal forces

The relation between the local internal force vector \mathbf{f}_l and the global one \mathbf{f}_g is obtained by equating the virtual work in both the local and global systems

$$V = \delta \mathbf{p}_{q}^{\mathrm{T}} \mathbf{f}_{q} = \delta \mathbf{p}_{l}^{\mathrm{T}} \mathbf{f}_{l} = \delta \mathbf{p}_{q}^{\mathrm{T}} \mathbf{B}^{\mathrm{T}} \mathbf{f}_{l}$$
(3.15)

Equation (3.15) must apply for any arbitrary $\delta \mathbf{p}_g$, and hence the global internal force vector \mathbf{f}_g is given by

$$\mathbf{f}_q = \mathbf{B}^{\mathrm{T}} \,\mathbf{f}_l \tag{3.16}$$

in which the local internal force vector $\mathbf{f}_l = \begin{bmatrix} N & M_1 & M_2 \end{bmatrix}^T$ depends on the element definition and will be calculated in the following sections.

3.1.4 Tangent stiffness matrix

The global tangent stiffness matrix \mathbf{K}_q defined by

$$\delta \mathbf{f}_{g} = \mathbf{K}_{g} \, \delta \mathbf{p}_{g} \tag{3.17}$$

is obtained by differentiation of (3.16)

$$\delta \mathbf{f}_{a} = \mathbf{B}^{\mathrm{T}} \, \delta \mathbf{f}_{l} + N \, \delta \mathbf{b}_{1} + M_{1} \, \delta \mathbf{b}_{2} + M_{2} \, \delta \mathbf{b}_{3}$$

$$(3.18)$$

where \mathbf{b}_2 , for example, is the second column of \mathbf{B}^{T} .

The following notations are introduced

$$\mathbf{r} = \begin{bmatrix} -c & -s & 0 & c & s & 0 \end{bmatrix}^{\mathrm{T}} \tag{3.19}$$

$$\mathbf{z} = \begin{bmatrix} s & -c & 0 & -s & c & 0 \end{bmatrix}^{\mathrm{T}} \tag{3.20}$$

which by differentiation gives

$$\delta \mathbf{r} = \mathbf{z} \,\delta \beta \tag{3.21a}$$

$$\delta \mathbf{z} = -\mathbf{r} \,\delta \beta \tag{3.21b}$$

Equations (3.9a) and (3.12) can be rewritten as

$$\delta \bar{u} = \delta l_n = \mathbf{r}^{\mathrm{T}} \, \delta \mathbf{p}_q \tag{3.22a}$$

$$\delta \beta = \frac{\mathbf{z}^{\mathrm{T}}}{l_n} \delta \mathbf{p}_g \tag{3.22b}$$

With these notations

$$\mathbf{b}_1 = \mathbf{r} \tag{3.23a}$$

$$\mathbf{b}_2 = \begin{bmatrix} 0 & 0 & 1 & 0 & 0 & 0 \end{bmatrix}^{\mathrm{T}} - \frac{\mathbf{z}}{l_n} \tag{3.23b}$$

$$\mathbf{b}_3 = \begin{bmatrix} 0 & 0 & 0 & 0 & 0 & 1 \end{bmatrix}^{\mathrm{T}} - \frac{\mathbf{z}}{l_n} \tag{3.23c}$$

which by differentiation gives

$$\delta \mathbf{b}_1 = \delta \mathbf{r} = \frac{\mathbf{z} \, \mathbf{z}^{\mathrm{T}}}{l_n} \, \delta \mathbf{p}_g \tag{3.24a}$$

$$\delta \mathbf{b}_{2} = \delta \mathbf{b}_{3} = -\frac{\delta \mathbf{z}}{l_{n}} + \frac{\mathbf{z} \, \delta l_{n}}{l_{n}^{2}} = \frac{1}{l_{n}^{2}} \left(\mathbf{r} \, \mathbf{z}^{\mathrm{T}} + \mathbf{z} \, \mathbf{r}^{\mathrm{T}} \right) \delta \mathbf{p}_{g}$$
(3.24b)

The first term in equation (3.18) is computed by introducing the local tangent stiffness matrix \mathbf{K}_l , which depends on the element definition and will be calculated in the following sections.

$$\delta \mathbf{f}_l = \mathbf{K}_l \, \delta \mathbf{p}_l = \mathbf{K}_l \, \mathbf{B} \, \delta \mathbf{p}_q \tag{3.25}$$

Finally, from (3.17), (3.18), (3.24a), (3.24b) and (3.25), the expression of the global tangent stiffness matrix becomes

$$\mathbf{K}_{g} = \mathbf{B}^{\mathrm{T}} \mathbf{K}_{l} \mathbf{B} + \frac{\mathbf{z} \mathbf{z}^{\mathrm{T}}}{l_{n}} N + \frac{1}{l_{n}^{2}} \left(\mathbf{r} \mathbf{z}^{\mathrm{T}} + \mathbf{z} \mathbf{r}^{\mathrm{T}} \right) \left(M_{1} + M_{2} \right)$$
(3.26)

Equations (3.16) and (3.26) give the relations between the local values of the internal forces \mathbf{f}_l and tangent stiffness matrix \mathbf{K}_l and the global ones, \mathbf{f}_g and \mathbf{K}_g . These relations are independent on the local element definition and are therefore available for all three elements developed in the following sections. This approach is different from the one adopted by Crisfield [23] where different local displacements definitions where used, leading to different relations between the local and global values.

The purpose of the following sections is to calculate the local internal force vector \mathbf{f}_l and tangent stiffness matrix \mathbf{K}_l for the three elements.

3.2 Local linear Bernoulli element

3.2.1 Definition

This element is based on the classical linear beam theory, using a linear interpolation for the axial displacement u and a cubic one for the vertical displacement w.

$$u = \frac{x}{L}\bar{u} \tag{3.27a}$$

$$w = x \left(1 - \frac{x}{L}\right)^2 \bar{\theta}_1 + \frac{x^2}{L} \left(\frac{x}{L} - 1\right) \bar{\theta}_2 \tag{3.27b}$$

According to the Bernoulli assumption, the curvature k and strain ε are defined by

$$k = \frac{\partial^2 w}{\partial x^2} = \left(-\frac{4}{L} + 6\frac{x}{L^2}\right)\bar{\theta}_1 + \left(-\frac{2}{L} + 6\frac{x}{L^2}\right)\bar{\theta}_2 \tag{3.28a}$$

$$\varepsilon = \frac{\partial u}{\partial x} - kz = \frac{\bar{u}}{L} + z \left[\left(\frac{4}{L} - 6 \frac{x}{L^2} \right) \bar{\theta}_1 + \left(\frac{2}{L} - 6 \frac{x}{L^2} \right) \bar{\theta}_2 \right]$$
(3.28b)

3.2.2 Gauss integration

Because of the non-linear relation between ε and σ , it is not possible to derive analytical expressions for the internal forces and the local tangent stiffness matrix and a Gauss quadrature has to be adopted. The number of Gauss points per section has already been discussed: two cases, with seven and fifteen points are considered. The number of sections, i.e. the number of Gauss points along the beam axis is taken as two in order to obtain the exact solution for the elastic case (the elastic strain energy defined by $\Phi = \frac{1}{2} \int_v E \varepsilon^2 dv$ is a polynomial of second order in x and therefore is exactly evaluated using a two points Gauss integration). Taking more points along the beam axis would of course increase the precision in the elasto-plastic case, but at some computational cost.

The position (and weight) of the Gauss points are within 0 < x < L

$$x_1 = \frac{L}{2} \left(1 - \frac{1}{\sqrt{3}} \right) \quad \left(\frac{L}{2} \right) \qquad x_2 = \frac{L}{2} \left(1 + \frac{1}{\sqrt{3}} \right) \quad \left(\frac{L}{2} \right) \tag{3.29}$$

3.2.3 Local internal forces

The local internal forces are calculated by using the theorem of virtual work

$$V = \int_{v} \sigma \, \delta \varepsilon \, dv = N \, \delta \bar{u} + M_1 \, \delta \bar{\theta}_1 + M_2 \, \delta \bar{\theta}_2$$
 (3.30)

which by introducing (3.28b) gives

$$V = \int_{v} \sigma \left[\frac{\delta \bar{u}}{L} + z \left(\frac{4}{L} - 6 \frac{x}{L^{2}} \right) \delta \bar{\theta}_{1} + z \left(\frac{2}{L} - 6 \frac{x}{L^{2}} \right) \delta \bar{\theta}_{2} \right] dv$$
 (3.31)

Equation (3.30) must apply for every $(\delta \bar{u}, \delta \bar{\theta}_1, \delta \bar{\theta}_2)$ and hence the local internal forces are given by

$$N = \int_{v} \frac{\sigma}{L} \, \mathrm{d}v \tag{3.32a}$$

$$M_1 = \int_v \sigma z \left(\frac{4}{L} - 6\frac{x}{L^2}\right) dv \tag{3.32b}$$

$$M_2 = \int_v \sigma z \left(\frac{2}{L} - 6\frac{x}{L^2}\right) dv \tag{3.32c}$$

Using a two points Gauss integration gives

$$N = \frac{1}{2} \left[\int_{A_1} \sigma \, dA_1 + \int_{A_2} \sigma \, dA_2 \right]$$
 (3.33a)

$$M_1 = \frac{\sqrt{3} + 1}{2} \int_{A_1} \sigma z \, dA_1 + \frac{1 - \sqrt{3}}{2} \int_{A_2} \sigma z \, dA_2$$
 (3.33b)

$$M_2 = \frac{\sqrt{3} - 1}{2} \int_{A_1} \sigma z \, dA_1 - \frac{\sqrt{3} + 1}{2} \int_{A_2} \sigma z \, dA_2$$
 (3.33c)

3.2.4 Local tangent stiffness matrix

Differentiation of σ gives

$$\delta\sigma = \hat{E}\,\delta\varepsilon = \hat{E}\left[\frac{\delta\bar{u}}{L} + z\left(\frac{4}{L} - 6\,\frac{x}{L^2}\right)\delta\bar{\theta}_1 + z\left(\frac{2}{L} - 6\,\frac{x}{L^2}\right)\delta\bar{\theta}_2\right] \tag{3.34}$$

where $\hat{E} = E$ in the elastic range and $\hat{E} = E_t$ in the plastic range. The local tangent stiffness matrix \mathbf{K}_l is obtained by differentiation of equations (3.32)

$$\delta N = \frac{1}{L} \int_{v} \delta \sigma \, \mathrm{d}v \tag{3.35a}$$

$$\delta M_1 = \int_v \delta \sigma \, z \left(\frac{4}{L} - 6 \, \frac{x}{L^2} \right) dv \tag{3.35b}$$

$$\delta M_2 = \int_v \delta \sigma \, z \left(\frac{2}{L} - 6 \, \frac{x}{L^2} \right) \, \mathrm{d}v \tag{3.35c}$$

which from (3.34) gives

$$K_{l_{11}} = \frac{\partial N}{\partial \bar{u}} = \frac{1}{L^2} \int_{v} \hat{E} \, \mathrm{d}v \tag{3.36a}$$

$$K_{l_{22}} = \frac{\partial M_1}{\partial \bar{\theta}_1} = \int_v z^2 \left(\frac{4}{L} - 6\frac{x}{L^2}\right)^2 dv \tag{3.36b}$$

$$K_{l_{33}} = \frac{\partial M_2}{\partial \bar{\theta}_2} = \int_v z^2 \left(\frac{2}{L} - 6\frac{x}{L^2}\right)^2 dv$$
 (3.36c)

$$K_{l_{12}} = K_{l_{21}} = \frac{\partial N}{\partial \bar{\theta}_1} = \frac{\partial M_1}{\partial \bar{u}} = \frac{1}{L} \int_{v} \hat{E} z \left(\frac{4}{L} - 6 \frac{x}{L^2} \right) dv$$
 (3.36d)

$$K_{l_{13}} = K_{l_{31}} = \frac{\partial N}{\partial \bar{\theta}_2} = \frac{\partial M_2}{\partial \bar{u}} = \frac{1}{L} \int_v \hat{E} z \left(\frac{2}{L} - 6\frac{x}{L^2}\right) dv$$
 (3.36e)

$$K_{l_{23}} = K_{l_{32}} = \frac{\partial M_1}{\partial \bar{\theta}_2} = \frac{\partial M_2}{\partial \bar{\theta}_1} = \int_v \hat{E} z^2 \left(\frac{4}{L} - 6\frac{x}{L^2}\right) \left(\frac{2}{L} - 6\frac{x}{L^2}\right) dv$$
 (3.36f)

Finally, by using a two points Gauss integration

$$K_{l_{11}} = \frac{1}{2L} \left[\int_{A_1} \hat{E} \, dA_1 + \int_{A_2} \hat{E} \, dA_2 \right]$$
 (3.37a)

$$K_{l_{22}} = \frac{\left(\sqrt{3} + 1\right)^2}{2L} \int_{A_1} \hat{E} z^2 dA_1 + \frac{\left(\sqrt{3} - 1\right)^2}{2L} \int_{A_2} \hat{E} z^2 dA_2$$
 (3.37b)

$$K_{l_{33}} = \frac{\left(\sqrt{3} - 1\right)^2}{2L} \int_{A_1} \hat{E} z^2 dA_1 + \frac{\left(\sqrt{3} + 1\right)^2}{2L} \int_{A_2} \hat{E} z^2 dA_2$$
 (3.37c)

$$K_{l_{12}} = \frac{\sqrt{3} + 1}{2L} \int_{A_1} \hat{E} z \, dA_1 + \frac{1 - \sqrt{3}}{2L} \int_{A_2} \hat{E} z \, dA_2$$
 (3.37d)

$$K_{l_{13}} = \frac{\sqrt{3} - 1}{2L} \int_{A_1} \hat{E} z \, dA_1 - \frac{\sqrt{3} + 1}{2L} \int_{A_2} \hat{E} z \, dA_2$$
 (3.37e)

$$K_{l_{23}} = \frac{1}{L} \int_{A_1} \hat{E} z^2 dA_1 + \frac{1}{L} \int_{A_2} \hat{E} z^2 dA_2$$
 (3.37f)

3.2.5 Constitutive equations

A bilinear strain–stress relation, see Figure 3.2, with an isotropic hardening is adopted. This model presents a constant modulus E_t in the plastic range, and therefore the influence of the decreasing of E_t , cf. Section 2.1.2, cannot be studied.

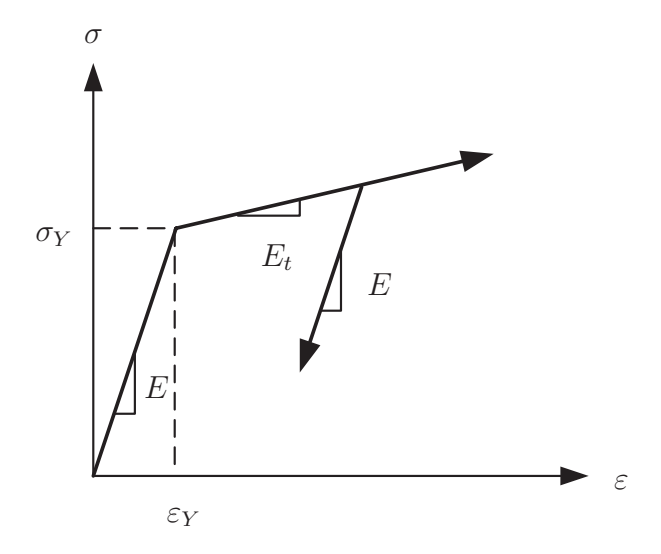


Figure 3.2: Bilinear elastic-plastic law.

3.3 Local shallow arch Bernoulli element

3.3.1 Definition

The second element uses a shallow arch definition for the local strain, according to

$$\varepsilon = \varepsilon_f - kz = \frac{1}{L} \int_L \left[\frac{\partial u}{\partial x} + \frac{1}{2} \left(\frac{\partial w}{\partial x} \right)^2 \right] dx - kz$$
 (3.38)

In (3.38), an averaged measure for the axial strain is introduced in order to avoid membrane locking. Using the same definition of the curvature and the same interpolations as in Section 3.2.1, gives

$$\varepsilon = \frac{\bar{u}}{L} + \frac{1}{15}\bar{\theta}_1^2 - \frac{1}{30}\bar{\theta}_1\bar{\theta}_2 + \frac{1}{15}\bar{\theta}_2^2 + z\left[\left(\frac{4}{L} - 6\frac{x}{L^2}\right)\bar{\theta}_1 + \left(\frac{2}{L} - 6\frac{x}{L^2}\right)\bar{\theta}_2\right]$$
(3.39)

For the same reason as in Section 3.2.2, a two points Gauss integration along the beam axis is adopted.

3.3.2 Local internal forces

As before, the local internal forces are computed using the theorem of virtual work

$$V = \int_{v} \sigma \, \delta \varepsilon \, dv = N \, \delta \bar{u} + M_1 \, \delta \bar{\theta}_1 + M_2 \, \delta \bar{\theta}_2 \tag{3.40}$$

with $\delta \varepsilon$ evaluated from (3.39)

$$\delta \varepsilon = \frac{\delta \bar{u}}{L} + \frac{2}{15} \bar{\theta}_1 \, \delta \bar{\theta}_1 - \frac{1}{30} \bar{\theta}_1 \, \delta \bar{\theta}_2 - \frac{1}{30} \bar{\theta}_2 \, \delta \bar{\theta}_1 + \frac{2}{15} \bar{\theta}_2 \, \delta \bar{\theta}_2$$

$$+ z \left[\left(\frac{4}{L} - 6 \frac{x}{L^2} \right) \delta \bar{\theta}_1 + \left(\frac{2}{L} - 6 \frac{x}{L^2} \right) \delta \bar{\theta}_2 \right]$$
(3.41)

Hence

$$N = \int_{v} \frac{\sigma}{L} \, \mathrm{d}v \tag{3.42a}$$

$$M_{1} = \left(\frac{2}{15}\bar{\theta}_{1} - \frac{1}{30}\bar{\theta}_{2}\right) \int_{v} \sigma \,dv + \int_{v} \sigma \,z \left(\frac{4}{L} - 6\frac{x}{L^{2}}\right) dv \tag{3.42b}$$

$$M_2 = \left(\frac{2}{15}\,\bar{\theta}_2 - \frac{1}{30}\,\bar{\theta}_1\right) \int_v \sigma \,dv + \int_v \sigma \,z \left(\frac{2}{L} - 6\,\frac{x}{L^2}\right) dv \tag{3.42c}$$

which, using a two points Gauss integration, gives

$$N = \frac{1}{2} \left[\int_{A_1} \sigma \, dA_1 + \int_{A_2} \sigma \, dA_2 \right]$$
 (3.43a)

$$M_{1} = \frac{L}{2} \left(\frac{2}{15} \bar{\theta}_{1} - \frac{1}{30} \bar{\theta}_{2} \right) \left[\int_{A_{1}} \sigma \, dA_{1} + \int_{A_{2}} \sigma \, dA_{2} \right] + \frac{\sqrt{3} + 1}{2} \int_{A_{1}} \sigma \, z \, dA_{1} + \frac{1 - \sqrt{3}}{2} \int_{A_{2}} \sigma \, z \, dA_{2}$$

$$(3.43b)$$

$$M_{2} = \frac{L}{2} \left(\frac{2}{15} \bar{\theta}_{2} - \frac{1}{30} \bar{\theta}_{1} \right) \left[\int_{A_{1}} \sigma \, dA_{1} + \int_{A_{2}} \sigma \, dA_{2} \right] + \frac{\sqrt{3} - 1}{2} \int_{A_{1}} \sigma \, z \, dA_{1} - \frac{\sqrt{3} + 1}{2} \int_{A_{2}} \sigma \, z \, dA_{2}$$

$$(3.43c)$$

3.3.3 Local tangent stiffness matrix

The local tangent stiffness matrix is calculated by differentiation of (3.42).

$$\delta N = \frac{1}{L} \int_{v} \delta \sigma \, \mathrm{d}v \tag{3.44a}$$

$$\delta M_1 = \left(\frac{2}{15}\delta\bar{\theta}_1 - \frac{1}{30}\delta\bar{\theta}_2\right) \int_v \sigma \,dv + \left(\frac{2}{15}\bar{\theta}_1 - \frac{1}{30}\bar{\theta}_2\right) \int_v \delta\sigma \,dv + \int_v \delta\sigma \,z \left(\frac{4}{L} - 6\frac{x}{L^2}\right) dv$$
(3.44b)

$$\delta M_2 = \left(\frac{2}{15}\delta\bar{\theta}_2 - \frac{1}{30}\delta\bar{\theta}_1\right) \int_v \sigma \,dv + \left(\frac{2}{15}\bar{\theta}_2 - \frac{1}{30}\bar{\theta}_1\right) \int_v \delta\sigma \,dv + \int_v \delta\sigma \,z \left(\frac{2}{L} - 6\frac{x}{L^2}\right) dv$$
(3.44c)

with $\delta \sigma = \hat{E} \, \delta \varepsilon$ and $\delta \varepsilon$ given in (3.41). Using a two points Gauss rule, the local tangent stiffness matrix is evaluated as

$$K_{l_{11}} = \frac{\partial N}{\partial \bar{u}} = \frac{1}{2L} \left[\int_{A_1} \hat{E} \, dA_1 + \int_{A_2} \hat{E} \, dA_2 \right]$$

$$K_{l_{12}} = \frac{\partial N}{\partial \bar{\theta}_1} = \frac{1}{2} \left(\frac{2}{15} \, \bar{\theta}_1 - \frac{1}{30} \, \bar{\theta}_2 \right) \left[\int_{A_1} \hat{E} \, dA_1 + \int_{A_2} \hat{E} \, dA_2 \right]$$

$$+ \frac{\sqrt{3} + 1}{2L} \int_{A_1} \hat{E} z \, dA_1 + \frac{1 - \sqrt{3}}{2L} \int_{A_2} \hat{E} z \, dA_2$$

$$K_{l_{13}} = \frac{\partial N}{\partial \bar{\theta}_2} = \frac{1}{2} \left(\frac{2}{15} \, \bar{\theta}_2 - \frac{1}{30} \, \bar{\theta}_1 \right) \left[\int_{A_1} \hat{E} \, dA_1 + \int_{A_2} \hat{E} \, dA_2 \right]$$

$$+ \frac{\sqrt{3} - 1}{2L} \int_{A_1} \hat{E} z \, dA_1 - \frac{\sqrt{3} + 1}{2L} \int_{A_2} \hat{E} z \, dA_2$$

$$K_{l_{22}} = \frac{\partial M_1}{\partial \bar{\theta}_1} = \frac{1}{2} L \left(\frac{2}{15} \, \bar{\theta}_1 - \frac{1}{30} \, \bar{\theta}_2 \right)^2 \left[\int_{A_1} \hat{E} \, dA_1 + \int_{A_2} \hat{E} \, dA_2 \right]$$

$$+ \left(\frac{2}{15} \, \bar{\theta}_1 - \frac{1}{30} \, \bar{\theta}_2 \right) \left[\left(\sqrt{3} + 1 \right) \int_{A_1} \hat{E} z \, dA_1 + \left(1 - \sqrt{3} \right) \int_{A_2} \hat{E} z \, dA_2 \right]$$

$$+ \frac{\left(\sqrt{3} + 1 \right)^2}{2L} \int_{A_1} \hat{E} z^2 \, dA_1 + \frac{\left(\sqrt{3} - 1 \right)^2}{2L} \int_{A_2} \hat{E} z^2 \, dA_2$$

$$+ \frac{L}{15} \left[\int_{A_1} \sigma \, dA_1 + \int_{A_2} \sigma \, dA_2 \right]$$

$$K_{l_{33}} = \frac{\partial M_2}{\partial \bar{\theta}_2} = \frac{1}{2} L \left(\frac{2}{15} \, \bar{\theta}_2 - \frac{1}{30} \, \bar{\theta}_1 \right)^2 \left[\int_{A_1} \hat{E} \, dA_1 + \int_{A_2} \hat{E} \, dA_2 \right]$$

$$K_{l_{33}} = \frac{\partial M_2}{\partial \bar{\theta}_2} = \frac{1}{2} L \left(\frac{2}{15} \bar{\theta}_2 - \frac{1}{30} \bar{\theta}_1 \right)^2 \left[\int_{A_1} \hat{E} \, dA_1 + \int_{A_2} \hat{E} \, dA_2 \right]$$

$$+ \left(\frac{2}{15} \bar{\theta}_2 - \frac{1}{30} \bar{\theta}_1 \right) \left[\left(\sqrt{3} - 1 \right) \int_{A_1} \hat{E} z \, dA_1 - \left(\sqrt{3} + 1 \right) \int_{A_2} \hat{E} z \, dA_2 \right]$$

$$+ \frac{\left(\sqrt{3} - 1 \right)^2}{2 L} \int_{A_1} \hat{E} z^2 \, dA_1 + \frac{\left(\sqrt{3} + 1 \right)^2}{2 L} \int_{A_2} \hat{E} z^2 \, dA_2$$

$$+ \frac{L}{15} \left[\int_{A_1} \sigma \, dA_1 + \int_{A_2} \sigma \, dA_2 \right]$$

$$(3.45e)$$

$$K_{l_{23}} = \frac{\partial M_1}{\partial \bar{\theta}_2} = \frac{1}{2} L \left(\frac{2}{15} \bar{\theta}_1 - \frac{1}{30} \bar{\theta}_2 \right) \left(\frac{2}{15} \bar{\theta}_2 - \frac{1}{30} \bar{\theta}_1 \right) \left[\int_{A_1} \hat{E} \, dA_1 + \int_{A_2} \hat{E} \, dA_2 \right]$$

$$+ \left[\frac{\sqrt{3} - 1}{2} \left(\frac{2}{15} \bar{\theta}_1 - \frac{1}{30} \bar{\theta}_2 \right) + \frac{\sqrt{3} + 1}{2} \left(\frac{2}{15} \bar{\theta}_2 - \frac{1}{30} \bar{\theta}_1 \right) \right] \int_{A_1} \hat{E} z \, dA_1$$

$$- \left[\frac{\sqrt{3} + 1}{2} \left(\frac{2}{15} \bar{\theta}_1 - \frac{1}{30} \bar{\theta}_2 \right) + \frac{\sqrt{3} - 1}{2} \left(\frac{2}{15} \bar{\theta}_2 - \frac{1}{30} \bar{\theta}_1 \right) \right] \int_{A_2} \hat{E} z \, dA_2$$

$$+ \frac{1}{L} \left[\int_{A_1} \hat{E} z^2 \, dA_1 + \int_{A_2} \hat{E} z^2 \, dA_2 \right] - \frac{L}{60} \left[\int_{A_1} \sigma \, dA_1 + \int_{A_2} \sigma \, dA_2 \right]$$

$$(3.45f)$$

$$K_{l_{21}} = K_{l_{12}} K_{l_{31}} = K_{l_{13}} K_{l_{32}} = K_{l_{23}} (3.45g)$$

Constitutive equations

The same elastic-plastic model as for the previous element is used.

3.4 Local linear Timoshenko element

3.4.1 Definition

A classical two noded Timoshenko beam element is defined with linear interpolations for u, w and θ in the local co-rotational coordinate system.

$$u = \frac{x}{L}\bar{u} \tag{3.46a}$$

$$w = 0 (3.46b)$$

$$\theta = \left(1 - \frac{x}{L}\right)\bar{\theta}_1 + \frac{x}{L}\bar{\theta}_2 \tag{3.46c}$$

The curvature k, shear deformation γ and strain ε are defined by

$$k = \frac{\partial \theta}{\partial x} = \frac{\bar{\theta}_2 - \bar{\theta}_1}{L} \tag{3.47a}$$

$$\gamma = \frac{\partial w}{\partial x} - \theta = -\left(1 - \frac{x}{L}\right)\bar{\theta}_1 - \frac{x}{L}\bar{\theta}_2 \tag{3.47b}$$

$$\varepsilon = \frac{\partial u}{\partial x} - k z = \frac{\bar{u}}{L} - \frac{\bar{\theta}_2 - \bar{\theta}_1}{L} z \tag{3.47c}$$

3.4.2 Local internal forces

The local internal forces are here also calculated by using the theorem of virtual work, which, taking account of the shear deformation can be expressed as

$$V = \int_{v} (\sigma \, \delta \varepsilon + \tau \, \delta \gamma) \, dv = N \, \delta \bar{u} + M_1 \, \delta \bar{\theta}_1 + M_2 \, \delta \bar{\theta}_2$$
 (3.48)

Further, $\delta \varepsilon$ and $\delta \gamma$ are calculated by differentiation of (3.47b-c) which gives

$$V = \int_{\mathbb{R}} \left\{ \frac{\sigma}{L} \left[\delta \bar{u} - z \left(\delta \bar{\theta}_2 - \delta \bar{\theta}_1 \right) \right] - \tau \left[\left(1 - \frac{x}{L} \right) \delta \bar{\theta}_1 + \frac{x}{L} \delta \bar{\theta}_2 \right] \right\} dv$$
 (3.49)

Using a one point Gauss integration in order to avoid shear locking, the local internal forces are computed from (3.48) and (3.49) as

$$N = \int_{v} \frac{\sigma}{L} \, \mathrm{d}v = \int_{A} \sigma \, \mathrm{d}A \tag{3.50a}$$

$$M_1 = \int_v \left(\frac{\sigma}{L} z - \frac{\tau}{2}\right) dv = \int_A \sigma z dA - \frac{L}{2} \int_A \tau dA$$
 (3.50b)

$$M_2 = \int_v \left(-\frac{\sigma}{L} z - \frac{\tau}{2} \right) dv = -\int_A \sigma z dA - \frac{L}{2} \int_A \tau dA$$
 (3.50c)

3.4.3 Local tangent stiffness matrix

The consistent tangent operator defined by

$$\begin{bmatrix} \dot{\sigma} \\ \dot{\tau} \end{bmatrix} = \begin{bmatrix} C_{ct1} & C_{ct3} \\ C_{ct3} & C_{ct2} \end{bmatrix} \begin{bmatrix} \dot{\varepsilon} \\ \dot{\gamma} \end{bmatrix}$$
 (3.51)

will be calculated in Section 3.4.4. Equation (3.51) can be rewritten as

$$\delta\sigma = C_{ct1}\,\delta\varepsilon + C_{ct3}\,\delta\gamma\tag{3.52a}$$

$$\delta\tau = C_{ct3}\,\delta\varepsilon + C_{ct2}\,\delta\gamma\tag{3.52b}$$

which, by using (3.47b-c) gives

$$\delta\sigma = \frac{C_{ct1}}{L} \left(\delta \bar{u} + z \delta \bar{\theta}_1 - z \delta \bar{\theta}_2 \right) - \frac{C_{ct3}}{2} \left(\delta \bar{\theta}_1 + \delta \bar{\theta}_2 \right)$$
(3.53a)

$$\delta \tau = \frac{C_{ct3}}{L} \left(\delta \bar{u} + z \delta \bar{\theta}_1 - z \delta \bar{\theta}_2 \right) - \frac{C_{ct2}}{2} \left(\delta \bar{\theta}_1 + \delta \bar{\theta}_2 \right)$$
(3.53b)

Differentiation of (3.50) gives

$$\delta N = \int_{A} \delta \sigma \, \mathrm{d}A \tag{3.54a}$$

$$\delta M_1 = \int_A \delta \sigma \, z \, dA - \frac{L}{2} \int_A \delta \tau \, dA \qquad (3.54b)$$

$$\delta M_2 = -\int_A \delta \sigma \, z \, \mathrm{d}A - \frac{L}{2} \int_A \delta \tau \, \mathrm{d}A \tag{3.54c}$$

Finally, from (3.53) and (3.54), the local tangent stiffness matrix is

$$K_{l_{11}} = \frac{\partial N}{\partial \bar{u}} = \frac{1}{L} \int_{A} C_{ct1} \, \mathrm{d}A$$
 (3.55a)

$$K_{l_{22}} = \frac{\partial M_1}{\partial \bar{\theta}_1} = \frac{1}{L} \int_A C_{ct1} z^2 dA - \int_A C_{ct3} z dA + \frac{L}{4} \int_A C_{ct2} dA$$
 (3.55b)

$$K_{l_{33}} = \frac{\partial M_2}{\partial \bar{\theta}_2} = \frac{1}{L} \int_A C_{ct1} z^2 dA + \int_A C_{ct3} z dA + \frac{L}{4} \int_A C_{ct2} dA$$
 (3.55c)

$$K_{l_{12}} = K_{l_{21}} = \frac{\partial N}{\partial \bar{\theta}_1} = \frac{1}{L} \int_A C_{ct1} z \, dA - \frac{1}{2} \int_A C_{ct3} \, dA$$
 (3.55d)

$$K_{l_{13}} = K_{l_{31}} = \frac{\partial N}{\partial \bar{\theta}_2} = -\frac{1}{L} \int_A C_{ct1} z \, dA - \frac{1}{2} \int_A C_{ct3} \, dA$$
 (3.55e)

$$K_{l_{23}} = K_{l_{32}} = \frac{\partial M_1}{\partial \bar{\theta}_2} = -\frac{1}{L} \int_A C_{ct1} z^2 dA + \frac{L}{4} \int_A C_{ct2} dA$$
 (3.55f)

3.4.4 Constitutive equations

The plastic rate equations for the Timoshenko beam are more complicated, since two strains (ε, γ) and two stresses (σ, τ) are involved. Many different algorithms exist

to integrate these equations. The simplest one is the forward-Euler scheme, which avoids iteration at the Gauss point level. However, even if sub-incrementation is used, the forward-Euler scheme does not give stresses which lie on the yield surface. Another method to get an explicit integration is to assume a constant strain direction (i.e. proportional loading) at each increment [75, 85]. However, this assumption, based on the deformation theory of plasticity [11], is too restrictive for stability problems. Another argument against this method is the implicit violation of the plastic flow rules.

Among the iterative procedures (see e.g. [66]), the most popular one is the backward-Euler scheme. It takes a simple form in case of the von Mises yield criterion (which is adopted here) and it allows the generation of a consistent tangent operator which maintains the quadratic convergence of the Newton-Raphson method used at the structure level. Consistent tangent matrices can also be derived from other implicit algorithms such as the mid-point rule, but this requires the computation of the contact point when the initial stresses lie inside the yield surface. For all these reasons, the backward-Euler scheme has been adopted.

Plane beam equations

The relations for the plane beam are derived from the von Mises material with isotropic hardening under plane stress conditions [23] by setting

$$\sigma_z = 0 \tag{3.56}$$

The von Mises yield function is

$$f = \left(\sigma_x^2 + 3\tau_{xz}^2\right)^{1/2} - \sigma_o\left(\varepsilon_{ps}\right) = \sigma_e - \sigma_o\left(\varepsilon_{ps}\right) \tag{3.57}$$

with

$$\varepsilon_{ps} = \int \dot{\varepsilon}_{ps} \, dt \qquad \dot{\varepsilon}_{ps} = \frac{2}{\sqrt{3}} \left(\dot{\varepsilon}_{px}^2 + \dot{\varepsilon}_{pz}^2 + \dot{\varepsilon}_{px}\dot{\varepsilon}_{px} + \dot{\gamma}_{pxz}^2 / 4 \right) = \dot{\lambda}$$
 (3.58)

The hardening parameter H is calculated from the uniaxial stress strain law

$$H = \frac{\partial \sigma_o}{\partial \varepsilon_{ps}} = \frac{E_t}{1 - E_t/E} \tag{3.59}$$

which gives

$$\sigma_o = \sigma_Y + H \,\varepsilon_{ps} \tag{3.60}$$

where σ_Y is the yield stress. The Prandtl-Reuss flow rules associated to (3.57) are

$$\dot{\boldsymbol{\varepsilon}}_{p} = \begin{bmatrix} \dot{\varepsilon}_{px} \\ \dot{\varepsilon}_{pz} \\ \dot{\gamma}_{pxz} \end{bmatrix} = \dot{\lambda} \frac{\partial f}{\partial \boldsymbol{\sigma}} = \dot{\lambda} \, \mathbf{a} = \frac{\dot{\lambda}}{2 \, \sigma_{e}} \begin{bmatrix} 2 \, \sigma_{x} \\ -\sigma_{x} \\ 6 \, \tau_{xz} \end{bmatrix}$$
(3.61)

The stress changes are related to the strain changes via

$$\dot{\boldsymbol{\sigma}} = \mathbf{C} \left(\dot{\boldsymbol{\varepsilon}} - \dot{\boldsymbol{\varepsilon}}_p \right) = \mathbf{C} \left(\dot{\boldsymbol{\varepsilon}} - \dot{\lambda} \, \mathbf{a} \right) \tag{3.62}$$

where

$$\mathbf{C} = \frac{E}{1 - \nu^2} \begin{bmatrix} 1 & \nu & 0 \\ \nu & 1 & 0 \\ 0 & 0 & (1 - \nu)/2 \end{bmatrix} \quad \dot{\boldsymbol{\sigma}} = \begin{bmatrix} \dot{\sigma}_x \\ \dot{\sigma}_z \\ \dot{\tau}_{xz} \end{bmatrix} \quad \dot{\boldsymbol{\varepsilon}} = \begin{bmatrix} \dot{\varepsilon}_x \\ \dot{\varepsilon}_z \\ \dot{\gamma}_{xz} \end{bmatrix}$$
(3.63)

By assuming that the stresses must remain on the yield surface in case of plastic loading $(\dot{\lambda} > 0)$, it is obtained

$$\dot{f} = \frac{\partial f^{\mathrm{T}}}{\partial \boldsymbol{\sigma}} \dot{\boldsymbol{\sigma}} + \frac{\partial f}{\partial \sigma_o} \frac{\partial \sigma_o}{\partial \varepsilon_{ps}} \dot{\varepsilon}_{ps} = \mathbf{a}^{\mathrm{T}} \dot{\boldsymbol{\sigma}} - H \dot{\lambda} = 0$$
 (3.64)

which by using (3.62) gives

$$\dot{\lambda} = \frac{\mathbf{a}^{\mathrm{T}} \mathbf{C} \dot{\boldsymbol{\varepsilon}}}{\mathbf{a}^{\mathrm{T}} \mathbf{C} \mathbf{a} + H} \tag{3.65}$$

Since $\dot{\sigma}_z = 0$, the second equation of (3.62) gives

$$\dot{\varepsilon}_z = -\nu \,\dot{\varepsilon}_x + \frac{\dot{\lambda} \,\sigma_x}{\sigma_e} \left(\nu - \frac{1}{2}\right) \tag{3.66}$$

which by introduction in the first and third equations of (3.62) gives

$$\dot{\sigma}_x = E\left(\dot{\varepsilon}_x - \frac{\sigma_x}{\sigma_e}\dot{\lambda}\right) \qquad \dot{\tau}_{xz} = G\left(\dot{\gamma}_{xz} - \frac{3\,\tau_{xz}}{\sigma_e}\dot{\lambda}\right) \tag{3.67}$$

Substitution of equations (3.66) and (3.67) in (3.65) gives after some algebra

$$\dot{\lambda} = \frac{\sigma_e \left(E \, \sigma_x \, \dot{\varepsilon}_x + 3 \, G \, \tau_{xz} \, \dot{\gamma}_{xz} \right)}{\left(E \, \sigma_x^2 + 9 \, G \, \tau_{xz}^2 \right) + H \, \sigma_e^2} \tag{3.68}$$

Finally, introducing (3.65) in (3.62) gives

$$\dot{\boldsymbol{\sigma}} = \mathbf{C}_t \, \dot{\boldsymbol{\varepsilon}} = \mathbf{C} \left(\mathbf{I} - \frac{\mathbf{a} \, \mathbf{a}^{\mathrm{T}} \, \mathbf{C}}{\mathbf{a}^{\mathrm{T}} \, \mathbf{C} \, \mathbf{a} + H} \right) \dot{\boldsymbol{\varepsilon}}$$
(3.69)

where \mathbf{C}_t is the tangent operator.

The backward-Euler algorithm shown in Figure 3.3 consists in applying an elastic forward step (AB) followed by a return mapping (BC) on the yield surface.

$$\sigma_C = \sigma_B - \Delta \lambda \mathbf{C} \mathbf{a}_C = \sigma_A + \mathbf{C} \Delta \varepsilon - \Delta \lambda \mathbf{C} \mathbf{a}_C$$
 (3.70)

The vector \mathbf{a}_C is normal to the yield surface at C, which is not known and therefore an iterative procedure must be used.

Since $\sigma_{zC} = \sigma_{zA} = 0$, the second equation of (3.70) gives

$$\Delta \varepsilon_z = -\nu \, \Delta \varepsilon_x + \frac{\Delta \lambda \, \sigma_{xC}}{2 \, \sigma_{eC}} \left(2\nu - 1 \right) \tag{3.71}$$

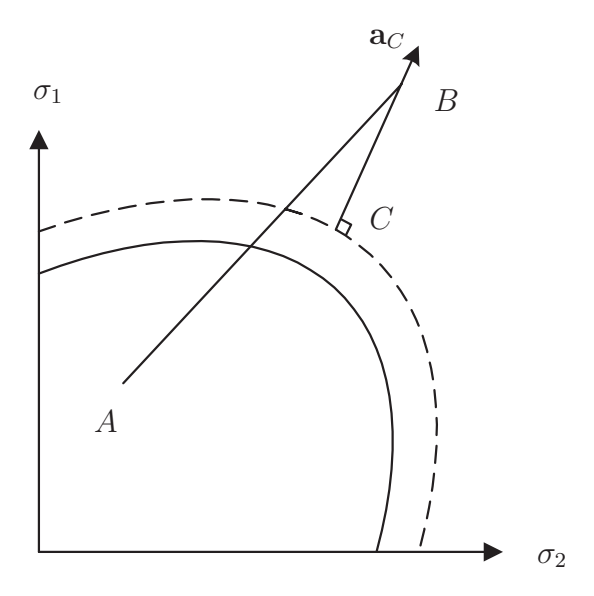


Figure 3.3: Backward-Euler scheme.

which, by substitution into the first and third equations, gives after some algebra

$$\sigma_{xC} - \sigma_{xA} = E\left(\Delta \varepsilon_x - \frac{\sigma_{xC}}{\sigma_{eC}} \Delta \lambda\right)$$
 (3.72a)

$$\tau_{xzC} - \tau_{xzA} = G\left(\Delta \gamma_{xz} - \frac{3 G \tau_{xzC}}{\sigma_{eC}} \Delta \lambda\right)$$
 (3.72b)

By introducing the notations

$$\sigma = \sigma_x \qquad \tau = \tau_{xz} \qquad \varepsilon = \varepsilon_x \qquad \gamma = \gamma_{xz}$$
 (3.73)

and new definitions for $C, \sigma, \varepsilon, a$

$$\mathbf{C} = \begin{bmatrix} E & 0 \\ 0 & G \end{bmatrix} \qquad \boldsymbol{\sigma} = \begin{bmatrix} \sigma \\ \tau \end{bmatrix} \qquad \boldsymbol{\varepsilon} = \begin{bmatrix} \varepsilon \\ \gamma \end{bmatrix}$$
 (3.74)

equations (3.61), (3.67), (3.68) and (3.72) can be combined and rewritten as

$$\dot{\boldsymbol{\varepsilon}}_p = \dot{\lambda} \, \mathbf{a} = \frac{\dot{\lambda}}{\sigma_e} \begin{bmatrix} \sigma \\ 3\tau \end{bmatrix} \tag{3.75}$$

$$\dot{\boldsymbol{\sigma}} = \mathbf{C} \left(\dot{\boldsymbol{\varepsilon}} - \dot{\boldsymbol{\varepsilon}}_p \right) = \mathbf{C} \left(\dot{\boldsymbol{\varepsilon}} - \dot{\lambda} \,\mathbf{a} \right) \tag{3.76}$$

$$\dot{\lambda} = \frac{\mathbf{a}^{\mathrm{T}} \,\mathbf{C} \,\dot{\boldsymbol{\varepsilon}}}{\mathbf{a}^{\mathrm{T}} \,\mathbf{C} \,\mathbf{a} + H} \tag{3.77}$$

$$\sigma_C = \sigma_B - \Delta \lambda \mathbf{C} \mathbf{a}_C = \sigma_A + \mathbf{C} \Delta \varepsilon - \Delta \lambda \mathbf{C} \mathbf{a}_C$$
 (3.78)

It is therefore proved by comparing (3.62), (3.65) and (3.70) with (3.76), (3.77) and (3.78) that the equations for the plane beam can be written in the same form as

those under plane stress conditions. It can be noted that the elastic forward step in the backward-Euler scheme does not give $\sigma_{zB} = 0$, but the equation (3.78) proves that σ_{zB} does not need to be calculated. A similar procedure is adopted in [23] to derive equations under plane stress condition from the three-dimensional case.

Backward-Euler scheme

The algorithm of the backward-Euler scheme is taken from [23], with the notations introduced at the end of the previous section.

The first estimation of σ_C is calculated with

$$\sigma_C = \sigma_B - \Delta \lambda \mathbf{C} \mathbf{a}_B = \sigma_A + \mathbf{C} \Delta \varepsilon - \Delta \lambda \mathbf{C} \mathbf{a}_B$$
 (3.79)

where \mathbf{a}_B is calculated from (3.75) and $\Delta\lambda$ is determined from a first order Taylor expansion of the yield function around point B

$$f = f_B + \frac{\partial f^{\mathrm{T}}}{\partial \boldsymbol{\sigma}} \Delta \boldsymbol{\sigma}_B + \frac{\partial f}{\partial \sigma_o} \frac{\partial \sigma_o}{\partial \varepsilon_{ps}} \Delta \varepsilon_{ps} = f_B + \mathbf{a}_B^{\mathrm{T}} \Delta \boldsymbol{\sigma}_B - H \Delta \lambda$$
 (3.80)

 $\Delta \sigma_B$ is then calculated from (3.76) as

$$\Delta \boldsymbol{\sigma}_B = \mathbf{C} \left(\Delta \boldsymbol{\varepsilon} - \Delta \lambda \, \mathbf{a}_B \right) \tag{3.81}$$

with $\Delta \varepsilon = \mathbf{0}$ since the total strain has already been applied in the elastic step (AB). Introducing (3.81) in (3.80) and setting f = 0 gives

$$\Delta \lambda = \frac{f_B}{\mathbf{a}_B^{\mathrm{T}} \mathbf{C} \, \mathbf{a}_B + H} \tag{3.82}$$

Equation (3.79) gives stresses which do not satisfy the yield function since the normal at B is not the same as the normal at the final position C.

The iterative process is performed by introducing the vector \mathbf{r} defined by the difference between the current stresses and the backward-Euler ones

$$\mathbf{r} = \boldsymbol{\sigma}_C - (\boldsymbol{\sigma}_B - \Delta \lambda \, \mathbf{C} \, \mathbf{a}_C) \tag{3.83}$$

A truncated Taylor expansion of (3.83) gives

$$\mathbf{r} = \mathbf{r}_o + \dot{\boldsymbol{\sigma}} + \dot{\lambda} \mathbf{C} \mathbf{a} + \Delta \lambda \mathbf{C} \frac{\partial \mathbf{a}}{\partial \boldsymbol{\sigma}} \dot{\boldsymbol{\sigma}}$$
 (3.84)

where

$$\frac{\partial \mathbf{a}}{\partial \boldsymbol{\sigma}} = \frac{\partial^2 f}{\partial \boldsymbol{\sigma}^2} = \frac{3}{\sigma_e^3} \begin{bmatrix} \tau^2 & -\sigma\tau \\ -\sigma\tau & \sigma^2 \end{bmatrix}$$
(3.85)

and $\dot{\boldsymbol{\sigma}}$ is the change in $\boldsymbol{\sigma}_C$ and λ is the change in $\Delta\lambda$. The subscript C is from now dropped in order to simplify the notations (all the notations without subscripts refer to C). Setting \mathbf{r} to zero in (3.84) gives

$$\dot{\boldsymbol{\sigma}} = -\left(\mathbf{I} + \Delta\lambda \mathbf{C} \frac{\partial \mathbf{a}}{\partial \boldsymbol{\sigma}}\right)^{-1} \left(\mathbf{r}_o + \dot{\lambda} \mathbf{C} \mathbf{a}\right) = -\mathbf{Q}^{-1} \left(\mathbf{r}_o + \dot{\lambda} \mathbf{C} \mathbf{a}\right)$$
(3.86)

A truncated Taylor expansion of the yield function at C gives

$$f = f_o + \frac{\partial f^{\mathrm{T}}}{\partial \boldsymbol{\sigma}} \dot{\boldsymbol{\sigma}} + \frac{\partial f}{\partial \sigma_o} \frac{\partial \sigma_o}{\partial \varepsilon_{ps}} \dot{\varepsilon}_{ps} = f_o + \mathbf{a}^{\mathrm{T}} \dot{\boldsymbol{\sigma}} - H \dot{\lambda}$$
(3.87)

further, setting f = 0 and using (3.86) gives

$$\dot{\lambda} = \frac{f_o - \mathbf{a}^{\mathrm{T}} \mathbf{Q}^{-1} \mathbf{r}_o}{\mathbf{a}^{\mathrm{T}} \mathbf{Q}^{-1} \mathbf{C} \mathbf{a} + H}$$
(3.88)

The backward-Euler scheme is summarised by a flowchart in Figure 3.4.

Consistent tangent operator

The tangent operator C_t defined in equation (3.69) assumes infinitesimal strain and stress changes. However, in order to eliminate numerical elastic unloading, a path-independent strategy [28] is adopted. This means that at each iteration, the strain changes are calculated with reference to the beginning of the increment (last equilibrium state) and not with reference to the last iteration. This is the reason why the use of C_t leads to low convergence rates for the Newton-Raphson method at the structural level, unless the increments are infinitesimal. In order to maintain the quadratic convergence inherent in the Newton-Raphson method, a tangent operator C_{ct} , consistent with the backward-Euler scheme is derived. The concept of consistent tangent operator has been first introduced by Simo and Taylor [90,91] and then used by several authors. The derivation presented here follows [23].

Differentiation of (3.78) gives (subscript C is dropped)

$$\dot{\boldsymbol{\sigma}} = \mathbf{C}\,\dot{\boldsymbol{\varepsilon}} - \dot{\lambda}\,\mathbf{C}\,\mathbf{a} - \Delta\lambda\,\mathbf{C}\,\frac{\partial\mathbf{a}}{\partial\boldsymbol{\sigma}}\,\dot{\boldsymbol{\sigma}} \tag{3.89}$$

where the last term in equation (3.89) is omitted in the derivation of the standard tangent operator. From (3.89), it is obtained

$$\dot{\boldsymbol{\sigma}} = \left(\mathbf{I} + \Delta \lambda \, \mathbf{C} \, \frac{\partial \mathbf{a}}{\partial \boldsymbol{\sigma}}\right)^{-1} \mathbf{C} \left(\dot{\boldsymbol{\varepsilon}} - \dot{\lambda} \, \mathbf{a}\right) = \mathbf{R} \left(\dot{\boldsymbol{\varepsilon}} - \dot{\lambda} \, \mathbf{a}\right) \tag{3.90}$$

The stresses must remain on the yield surface, which, from (3.64), gives

$$\dot{f} = \mathbf{a}^{\mathrm{T}} \,\dot{\boldsymbol{\sigma}} - H \,\dot{\lambda} = \mathbf{a}^{\mathrm{T}} + \mathbf{R} \left(\dot{\boldsymbol{\varepsilon}} - \dot{\lambda} \,\mathbf{a} \right) - H \,\dot{\lambda} = 0 \tag{3.91}$$

and hence

$$\dot{\lambda} = \frac{\mathbf{a}^{\mathrm{T}} \mathbf{R} \dot{\boldsymbol{\varepsilon}}}{\mathbf{a}^{\mathrm{T}} \mathbf{R} \mathbf{a} + H} \tag{3.92}$$

Introducing (3.92) in (3.90) finally gives

$$\dot{\boldsymbol{\sigma}} = \mathbf{C}_{ct} \, \dot{\boldsymbol{\varepsilon}} = \mathbf{R} \left(\mathbf{I} - \frac{\mathbf{a} \, \mathbf{a}^{\mathrm{T}} \, \mathbf{R}}{\mathbf{a}^{\mathrm{T}} \, \mathbf{R} \, \mathbf{a} + H} \right) \dot{\boldsymbol{\varepsilon}}$$
(3.93)

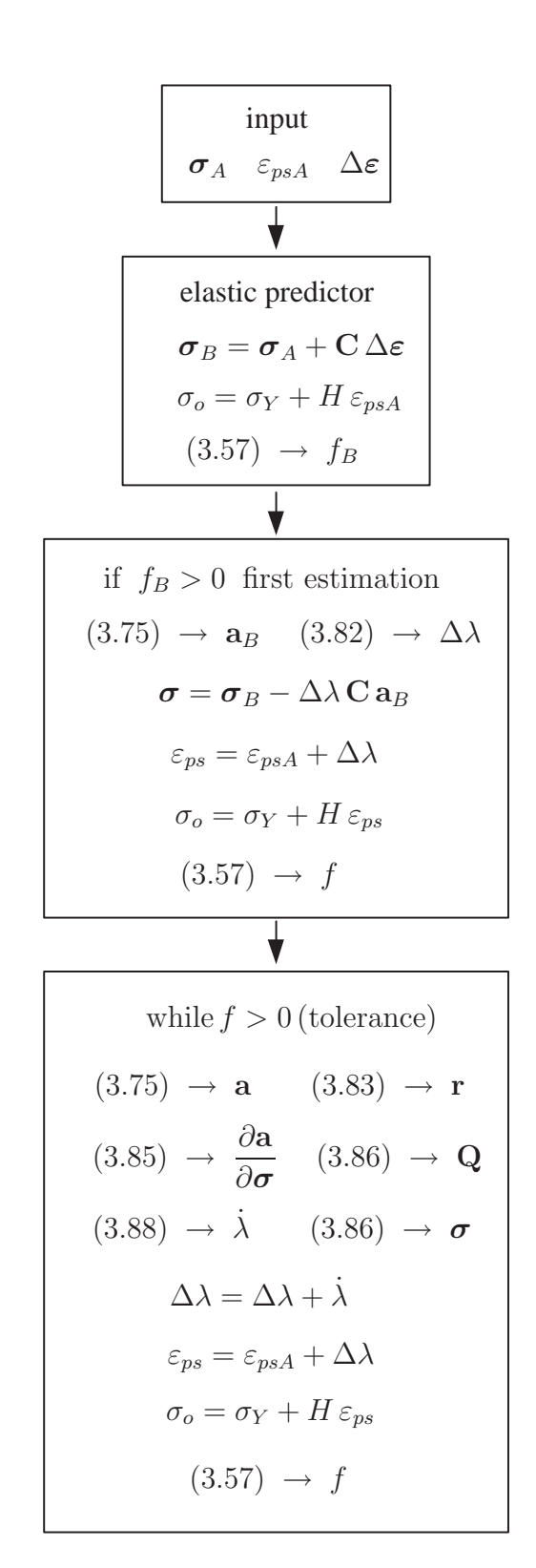


Figure 3.4: Backward-Euler algorithm.

Chapter 4

3D beam element formulation

As for the 2D case, the main idea of the co-rotational approach in 3D [22,23,25,35,47,53,64,72,73,83,84,95] is to decompose the motion of the element into rigid body and pure deformational parts, through the use of a reference system which continuously rotates and translates with the element. The deformational response is captured at the level of the local reference frame, whereas the geometric non-linearity induced by the large rigid-body motion, is incorporated in the transformation matrices relating local and global quantities. Assuming the pure deformation part to be small, a linear theory can be used from the onset in the local system. As pointed out by Haugen and Felippa in their review of the topic [43,44], the main benefit of such an assumption is the possibility to reuse existing high-performance linear elements.

In order to fully exploit this possibility, Rankin and co-workers [64,83,84] introduced the so called "element independent co-rotational formulation". The definition of the element resorts to several changes of variables from the local frame to the global one. This is done through the use of a projector matrix which relates the variations of the local displacements to the variations of the global ones, by extracting the rigid body modes from the latter. A very similar line of work was adopted by Pacoste and Eriksson [73] and will also be followed in this chapter. With respect to the cited reference, several improvements have been introduced.

The first one concerns the co-rotational framework. A different definition of the local coordinate system is adopted. Besides, the number of local displacements is kept to seven (one translation and six rotations) and therefore, the projector matrix is never explicitly computed. Instead, only certain block components in this matrix are evaluated and used directly in the expressions of the internal force vector and tangent stiffness in global coordinates. The objective here was to obtain a formulation which is more efficient from a computational point of view. Rigid links and eccentric forces are also introduced.

The second one is related to the parameterisation of finite 3D rotations. Thus, in [73] a 3-parameter representation based on the so-called "rotational vector", is used. The main advantage here is that the rotational variables become additive and the necessity of a special updating procedure is avoided. However, this parameterisation can not be retained globally [51,73] as the magnitude of the rotational vector must be

restricted to values less than 2π . In order to overcome this inconvenience, a different possibility is explored in the present work. Essentially it amounts to using a vector like parameterisation but this time within each increment. Using the terminology in [51], this alternative is based on the spatial form of the incremental rotation vector. Additive updates will still apply but this time only within an increment at the level of the iterative corrections.

The third improvement is related to warping effects which are introduced by adding a seventh degree of freedom at each node of the element. With respect to [64,73], this requires an adaptation of the co-rotational framework.

As already mentioned, the main feature of the adopted co-rotational formulation is its independence on the assumptions used to derive the internal forces and tangent stiffness in local coordinates. This means that for elements with the same number of nodes and degrees of freedom the co-rotational framework is the same. Using this property, different local formulations can be tested and compared. In many instances, see e.g. [22, 43, 44, 64, 73], a linear strain definition is adopted in the local system. However, as the numerical applications will demonstrate, such a choice will lead to incorrect results for certain classes of problems, especially when the torsional effects are important. For this reason a different approach is advocated in this work. At the level of the local frame, the kinematic description proposed by Gruttmann et al. [41] is adopted and used to construct a consistent second order approximation to the Green-Lagrange strains. Various possibilities to simplify the resulting expressions are further discussed and tested in numerical examples.

The organisation of this chapter is as follows. Section 4.1 discusses some aspects related to the parameterisation of finite 3D rotations, whereas the general co-rotational framework for a two node beam element is introduced in Section 4.2. Section 4.3 is devoted to the local element formulation in elasticity. Several local elements, based on Timoshenko and Bernoulli assumptions and including or not warping effects are presented. Based on the same strain assumptions as in elasticity, elasto-plastic local Timoshenko elements are derived in Section 4.4. Finally, Section 4.5 addresses certain issues related to the applied external forces, e.g. rigid eccentricities, definition of external moments.

4.1 Parameterisation of finite 3D rotations

One of the central issues in the development of a non-linear beam element is the treatment of finite 3D rotations. In general, finite rotations are represented through an orthogonal tensor \mathbf{R} which is an element of the SO(3) rotation group. Its coordinate representation is a 3×3 orthogonal matrix involving nine components. However, owing to its orthonormality, it can be described in terms of only three independent parameters. One alternative in this context, is based on the so-called "rotational vector" [51,68,72,73], defined by

$$\Psi = \mathbf{u}\,\psi\tag{4.1}$$

The geometrical significance of the above definition is the following: any finite rotation can be represented by a unique rotation with an angle ψ about an axis defined by the unit vector **u**. The magnitude of ψ is given by

$$\psi = \sqrt{\Psi_1^2 + \Psi_2^2 + \Psi_3^2} \tag{4.2}$$

where Ψ_i , (i = 1, 2, 3) are the components of Ψ . In terms of Ψ , the orthogonal matrix \mathbf{R} admits the following representation

$$\mathbf{R} = \mathbf{I} + \frac{\sin \psi}{\psi} \,\tilde{\mathbf{\Psi}} + \frac{1}{2} \left[\frac{\sin(\psi/2)}{\psi/2} \right]^2 \tilde{\mathbf{\Psi}}^2 \tag{4.3}$$

Here, as in the sequel, a tilde denotes the skew-symmetric matrix obtained with the components of the corresponding vector, whereas \mathbf{I} denotes a 3×3 identity matrix. If the trigonometric functions in the above equation are expanded in Taylor series, \mathbf{R} can be written as

$$\mathbf{R} = \mathbf{I} + \tilde{\mathbf{\Psi}} + \frac{1}{2}\tilde{\mathbf{\Psi}}^2 + \dots = \exp(\tilde{\mathbf{\Psi}})$$
 (4.4)

Following the notations introduced in Figure 4.1, \mathbf{R}_o is a rotation operator which maps the orthogonal cartesian frame \mathbf{e}_i into the orthonormal frame \mathbf{t}_i , which implies $\mathbf{t}_i = \mathbf{R}_o \mathbf{e}_i$, (i = 1, 2, 3). An incremental rotation which carries the moving frame \mathbf{t}_i

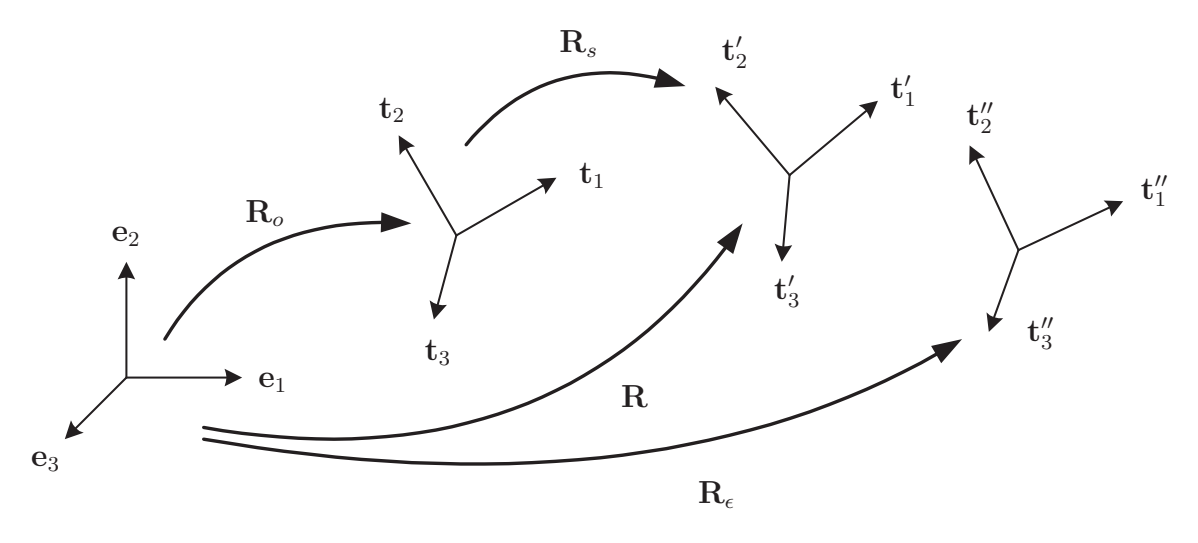


Figure 4.1: Parameterisation of finite 3D rotations.

into a new position \mathbf{t}_i' can be expressed through a spatial rotation Θ which is viewed as a rotation applied to \mathbf{t}_i

$$\mathbf{t}_{i}' = \mathbf{R} \, \mathbf{e}_{i} = \mathbf{R}_{s} \, \mathbf{R}_{o} \, \mathbf{e}_{i} \qquad \mathbf{R}_{s} = \exp(\tilde{\boldsymbol{\Theta}})$$
 (4.5)

or through a material rotation \mathbf{W} , which is viewed as a rotation applied to the material frame \mathbf{e}_i

$$\mathbf{t}'_i = \mathbf{R} \, \mathbf{e}_i = \mathbf{R}_o \, \mathbf{R}_m \, \mathbf{e}_i \qquad \mathbf{R}_m = \exp(\tilde{\mathbf{W}})$$
 (4.6)

In the terminology of Argyris [1], the sequence of rotation in equation (4.5) is denoted as "rotation around follower axes", i.e. axes rotated by the previous rotation in the sequence, whereas the sequence described in equation (4.6) is denoted as "rotation around fixed axes", i.e. the rotation axes remain fixed but the rotation sequence itself is inverted. The relationship connecting the spatial Θ and material W incremental rotation vectors is thus given by

$$\mathbf{\Theta} = \mathbf{R}_o \, \mathbf{W} \tag{4.7}$$

Let now consider an infinitesimal rotation which carries the frame \mathbf{t}'_i into \mathbf{t}''_i , such that $\mathbf{t}''_i = \mathbf{R}_{\epsilon} \mathbf{e}_i$, (i = 1, 2, 3). Using the same dualism as above, admissible variations $\delta \mathbf{R}$ are computed as

$$\delta \mathbf{R} = \frac{d}{d\epsilon} [\mathbf{R}_{\epsilon}]_{\epsilon=0} = \frac{d}{d\epsilon} \left(\exp(\epsilon \,\tilde{\boldsymbol{\theta}}) \,\mathbf{R} \right)_{\epsilon=0} = \delta \tilde{\boldsymbol{\theta}} \,\mathbf{R}$$

$$= \frac{d}{d\epsilon} (\mathbf{R} \, \exp(\epsilon \,\tilde{\boldsymbol{\omega}}))_{\epsilon=0} = \mathbf{R} \,\delta \tilde{\boldsymbol{\omega}}$$
(4.8)

where $\delta \tilde{\boldsymbol{\omega}}$ denotes material and $\delta \tilde{\boldsymbol{\theta}}$ spatial angular variations, i.e. infinitesimal rotations superimposed onto the existing \mathbf{R} . As defined in the above equation, the parameterisation of admissible variations $\delta \mathbf{R}$ is largely independent of the technique used to parameterise \mathbf{R} itself. In order to obtain a consistent parameterisation, $\delta \boldsymbol{\theta}$ (or alternatively $\delta \boldsymbol{\omega}$) must be projected onto the parameter space adopted for \mathbf{R} . This issue will be addressed in the remainder of this subsection, for the types of parameterisation adopted in this work.

4.1.1 Rotational vector

Considering the spatial form of equation (4.8), admissible variations $\delta \Psi$ which lead to the same perturbed matrix \mathbf{R}_{ϵ} are found from

$$\mathbf{R}_{\epsilon} = \exp(\tilde{\mathbf{\Psi}}_{\epsilon}) = \exp(\epsilon \,\delta \tilde{\boldsymbol{\theta}}) \,\mathbf{R} \tag{4.9}$$

where $\Psi_{\epsilon} = \Psi + \epsilon \, \delta \Psi$. Taking into account that $\mathbf{R} = \exp(\tilde{\Psi})$, this leads to

$$\exp(\epsilon \,\delta \tilde{\boldsymbol{\theta}}) = \exp(\tilde{\boldsymbol{\Psi}}_{\epsilon}) \, \exp(-\tilde{\boldsymbol{\Psi}}) \tag{4.10}$$

Using the formula for compound rotations in terms of the rotational pseudo-vector (i.e. Rodrigues parameters) and differentiating with respect to ϵ , gives

$$\delta \boldsymbol{\theta} = \mathbf{T}_s(\boldsymbol{\Psi}) \, \delta \boldsymbol{\Psi} \tag{4.11}$$

with

$$\mathbf{T}_s(\mathbf{\Psi}) = \frac{\sin \psi}{\psi} \mathbf{I} + \left(1 - \frac{\sin \psi}{\psi}\right) \mathbf{u} \mathbf{u}^{\mathrm{T}} + \frac{1}{2} \left(\frac{\sin(\psi/2)}{(\psi/2)}\right)^2 \tilde{\mathbf{\Psi}}$$
(4.12)

Similar equations involving material angular variations $\delta \omega$ can be easily derived by noting that $\delta \theta = \mathbf{R} \delta \omega$. For details concerning the above derivation the interested reader is referred to [51,72].

In connection with the linear operator T_s it should also be noted that

$$\det(\mathbf{T}_s) = \frac{2(1 - \cos\psi)}{\psi^2} \tag{4.13}$$

which shows that the corresponding mapping ceases to be a bijection for $\psi = 2k\pi$, k = 1, 2, ... [51,72]. Avoiding these points, the inverse mapping is well defined as

$$\delta \mathbf{\Psi} = \mathbf{T}_{s}^{-1}(\mathbf{\Psi}) \,\delta \boldsymbol{\theta} \tag{4.14}$$

with

$$\mathbf{T}_s^{-1} = \frac{(\psi/2)}{\tan(\psi/2)} \mathbf{I} + \left(1 - \frac{(\psi/2)}{\tan(\psi/2)}\right) \mathbf{u} \mathbf{u}^{\mathrm{T}} - \frac{1}{2} \tilde{\boldsymbol{\Psi}}$$
(4.15)

4.1.2 Incremental rotation vector

Considering equation (4.5), admissible variations $\delta \Theta$ which lead to the same perturbed matrix \mathbf{R}_{ϵ} are found from

$$\mathbf{R}_{\epsilon} = \exp(\tilde{\mathbf{\Theta}}_{\epsilon}) \,\mathbf{R}_{o} = \exp(\epsilon \,\delta \tilde{\boldsymbol{\theta}}) \,\mathbf{R} \tag{4.16}$$

where $\Theta_{\epsilon} = \Theta + \epsilon \delta \Theta$. Taking equation (4.5) into account leads to

$$\exp(\epsilon \,\delta \tilde{\boldsymbol{\theta}}) = \exp(\tilde{\boldsymbol{\Theta}}_{\epsilon}) \exp(-\tilde{\boldsymbol{\Theta}}) \tag{4.17}$$

Following a procedure entirely similar to the one used in the preceding subsection (for details see [51]) leads to

$$\delta \boldsymbol{\theta} = \mathbf{T}_s(\boldsymbol{\Theta}) \, \delta \boldsymbol{\Theta} \tag{4.18}$$

Note that a similar relation connecting $\delta \omega$ and δW can also be obtained. This issue however will not be further utilised in this thesis.

4.2 Co-rotational framework

The objective of this section is to define the co-rotational framework for a two node beam element. The central idea in this context is to introduce a local coordinate system which continuously rotates and translates with the element. With respect to the moving frame, local (deformational) displacements \mathbf{p}_l are defined by extracting the rigid body modes from the global displacements \mathbf{p}_g^g . The local displacements are expressed as functions of the global ones, i.e.

$$\mathbf{p}_{l} = \mathbf{p}_{l} \left(\mathbf{p}_{q}^{g} \right) \tag{4.19}$$

and used in order to compute the internal force vector \mathbf{f}_l and tangent stiffness matrix \mathbf{K}_l in local coordinates. Note that \mathbf{f}_l and \mathbf{K}_l depend only on the definition of the local strains and not on the particular form of equation (4.19).

The expression of the internal force vector in global coordinates \mathbf{f}_g , can be obtained by equating the internal virtual work in both the global and local systems

$$V = \delta \mathbf{p}_l^{\mathrm{T}} \mathbf{f}_l = \delta \mathbf{p}_q^{g \mathrm{T}} \mathbf{f}_q \tag{4.20}$$

Using equation (4.19), the connection between the variations of local and global displacements is obtained as

$$\delta \mathbf{p}_l = \mathbf{B} \, \delta \mathbf{p}_a^g \tag{4.21}$$

which, upon substitution into (4.20), provides the result of interest

$$\mathbf{f}_{q} = \mathbf{B}^{\mathrm{T}} \,\mathbf{f}_{l} \tag{4.22}$$

The expression of the tangent stiffness matrix in global coordinates \mathbf{K}_g , is obtained by taking the variations of equation (4.22), which gives

$$\mathbf{K}_{g} = \mathbf{B}^{\mathrm{T}} \mathbf{K}_{l} \mathbf{B} + \frac{\partial \mathbf{B}}{\partial \mathbf{p}_{g}^{g}} : \mathbf{f}_{l}$$

$$(4.23)$$

The second term on the right-hand side of the above equation is the so-called "geometric" stiffness, with the symbol ":" used to denote a contraction.

In equations (4.22) and (4.23), **B** and $\partial \mathbf{B}/\partial \mathbf{p}_g^g$ play the role of transformation matrices required in order to re-express \mathbf{f}_l and \mathbf{K}_l in global coordinates. These matrices, which actually define the co-rotational framework, depend on the non-linear functions in equation (4.19) and thus on the choice of the local coordinate system. However, they are independent of the particular strain definition used in order to derive \mathbf{f}_l and \mathbf{K}_l . Consequently, various co-rotational elements defined using different local strain assumptions but the same type of local coordinate system will share the same transformation matrices, i.e. the co-rotational formulation is "element independent" [64]. Using this property, various local assumptions can be placed at the core of the co-rotational formulation and tested for efficiency and accuracy. The issues pertaining to the development of a specific form for the local internal forces \mathbf{f}_l and tangent stiffness \mathbf{K}_l will however be addressed in the following sections.

The remainder of this section will instead focus on the definition of the co-rotational framework. The approach put forth follows mainly [64, 73]. Thus, the change of variables (4.19) and subsequently the definition of the transformation matrices in equations (4.22) and (4.23) are performed by extracting the rigid body modes from the variations of the global displacements.

4.2.1 Coordinate systems, beam kinematics

The definition of the co-rotational two node beam element described in this section, involves several reference systems. First (see Figure 4.2), a global reference system defined by the triad of unit orthogonal vectors \mathbf{e}_{α} , $\alpha = 1, 2, 3$. Second, a local system which continuously rotates and translates with the element. The orthonormal basis

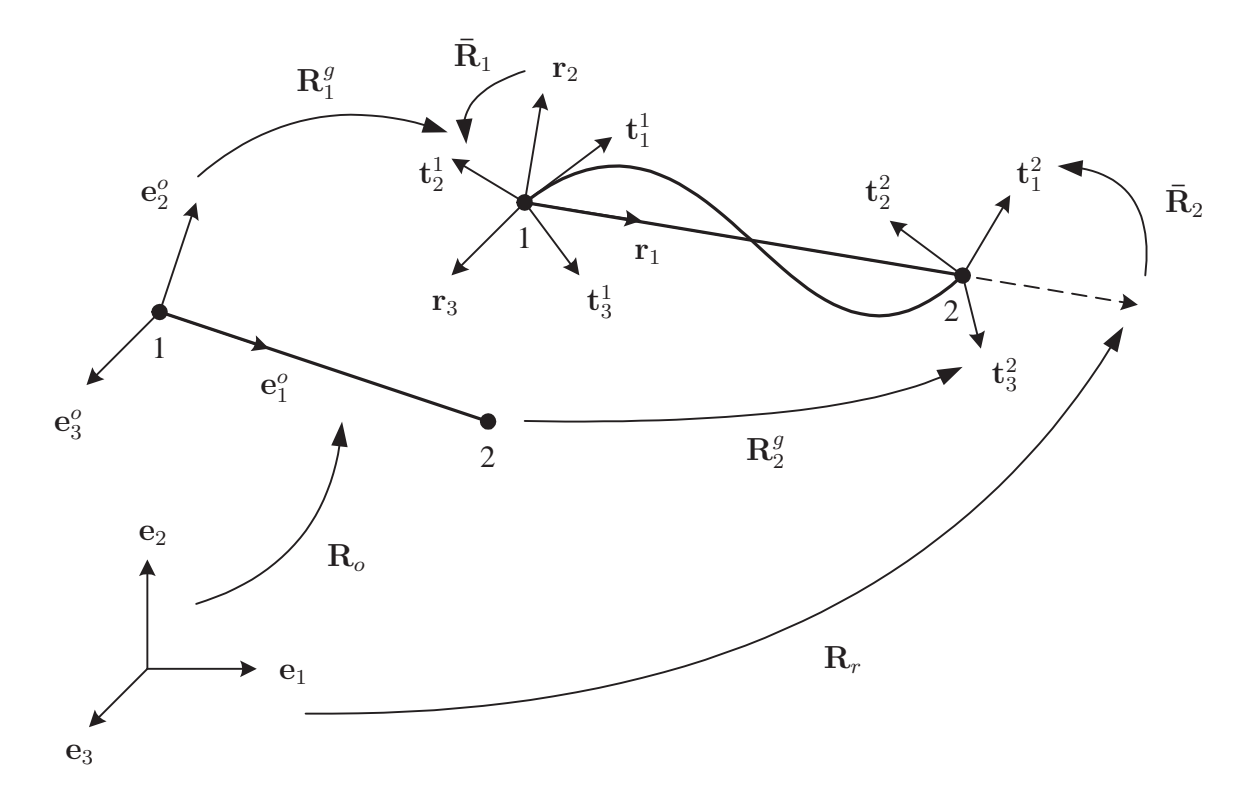


Figure 4.2: Beam kinematics and coordinate systems.

vectors of the local system are denoted by \mathbf{r}_{α} , $\alpha = 1, 2, 3$. In the initial (undeformed) configuration, the local system is defined by the orthonormal triad \mathbf{e}_{α}^{o} . In addition, \mathbf{t}_{α}^{1} and \mathbf{t}_{α}^{2} , $\alpha = 1, 2, 3$, denote two unit triads rigidly attached to nodes 1 and 2.

According to the main idea of the co-rotational formulation, the motion of the element from the initial to the final deformed configuration is split into a rigid body component and a deformational part. The rigid body component consists of a rigid translation and rotation of the local element frame. The origin of the local system is taken at node one and thus the rigid translation is defined by \mathbf{u}_1^g , i.e. the translation at node 1. Here as in the sequel, the superscript g indicates quantities expressed in the global reference system.

The rigid rotation is such that the new orientation of the local reference system is defined by an orthogonal matrix \mathbf{R}_r , given by

$$\mathbf{R}_r = [\mathbf{r}_1 \ \mathbf{r}_2 \ \mathbf{r}_3] \tag{4.24}$$

The first coordinate axis of the local system is defined by the line connecting nodes 1 and 2 of the element. Consequently, \mathbf{r}_1 is given by

$$\mathbf{r}_{1} = \frac{\mathbf{x}_{2}^{g} + \mathbf{u}_{2}^{g} - \mathbf{x}_{1}^{g} - \mathbf{u}_{1}^{g}}{l_{n}}$$
(4.25)

with \mathbf{x}_i^g , i = 1, 2 denoting the nodal coordinates in the initial undeformed configuration and l_n denoting the current length of the beam, i.e.

$$l_n = \|\mathbf{x}_2^g + \mathbf{u}_2^g - \mathbf{x}_1^g - \mathbf{u}_1^g\| \tag{4.26}$$

The remaining two axes are determined with the help of an auxiliary vector \mathbf{q} . In the initial configuration \mathbf{q} is directed along the local \mathbf{e}_2^o direction, whereas in the deformed configuration its orientation is obtained from

$$\mathbf{q} = \frac{1}{2} (\mathbf{q}_1 + \mathbf{q}_2) \qquad \mathbf{q}_i = \mathbf{R}_i^g \mathbf{R}_o [0 \ 1 \ 0]^{\mathrm{T}} \qquad i = 1, 2$$
 (4.27)

where \mathbf{R}_1^g and \mathbf{R}_2^g are the orthogonal matrices used to specify the orientation of the nodal triads \mathbf{t}_{α}^1 and \mathbf{t}_{α}^2 respectively, and \mathbf{R}_o specifies the orientation of the local frame in the initial configuration, i.e. $\mathbf{R}_o = [\mathbf{e}_1^o \mathbf{e}_2^o \mathbf{e}_3^o]$. The unit vectors \mathbf{r}_2 and \mathbf{r}_3 are then computed by the vector products

$$\mathbf{r}_3 = \frac{\mathbf{r}_1 \times \mathbf{q}}{\|\mathbf{r}_1 \times \mathbf{q}\|} \qquad \mathbf{r}_2 = \mathbf{r}_3 \times \mathbf{r}_1 \tag{4.28}$$

and the orthogonal matrix \mathbf{R}_r in equation (4.24) is completely determined.

The rigid motion previously described, is accompanied by local deformational displacements with respect to the local element axes. In this context, due to the particular choice of the local system, the local translations at node 1 will be zero. Moreover, at node 2, the only non zero component is the translation along \mathbf{r}_1 . This can easily be evaluated according to

$$\bar{u} = l_n - l_o \tag{4.29}$$

with l_o denoting the length of the beam in the original undeformed configuration. Here as in the sequel, an overbar denotes a deformational kinematic quantity.

The global rotations at node i can be expressed in terms of the rotation of the local axes, defined by \mathbf{R}_r , followed by a local rotation relative to these axes; this is defined by the orthogonal matrix $\bar{\mathbf{R}}_i$. Using the terminology of Section 4.1, the latter should be viewed as a material rotation. Consequently, the orientation of the nodal triad \mathbf{t}_{α}^i can be obtained by means of the product $\mathbf{R}_r \bar{\mathbf{R}}_i$. On the other hand, (see Figure 4.2) this orientation can also be obtained through the product $\mathbf{R}_i^g \mathbf{R}_o$, which gives

$$\bar{\mathbf{R}}_i = \mathbf{R}_r^{\mathrm{T}} \, \mathbf{R}_i^g \, \mathbf{R}_o \qquad i = 1, 2 \tag{4.30}$$

The local rotations are then evaluated from

$$\bar{\boldsymbol{\vartheta}}_i = \log\left(\bar{\mathbf{R}}_i\right) \qquad i = 1, 2$$
 (4.31)

The explicit form of equation (4.19) is thus completely specified through equations (4.29), (4.30) and (4.31), with \mathbf{p}_l given by

$$\mathbf{p}_{l} = \begin{bmatrix} \bar{u} & \bar{\boldsymbol{\vartheta}}_{1}^{\mathrm{T}} & \bar{\boldsymbol{\vartheta}}_{2}^{\mathrm{T}} \end{bmatrix}^{\mathrm{T}} \tag{4.32}$$

Correspondingly, the local internal force vector is given by

$$\mathbf{f}_l = \begin{bmatrix} n & \mathbf{m}_1^{\mathrm{T}} & \mathbf{m}_2^{\mathrm{T}} \end{bmatrix}^{\mathrm{T}} \tag{4.33}$$

where n denotes the axial force whereas \mathbf{m}_1 and \mathbf{m}_2 denote the moments at nodes 1 and 2, respectively.

The next step will then be to determine the transformation matrix \mathbf{B} in equation (4.21). This matrix relates the variations of the local displacements

$$\delta \mathbf{p}_{l} = \left[\delta \bar{u} \ \delta \bar{\boldsymbol{\vartheta}}_{1}^{\mathrm{T}} \ \delta \bar{\boldsymbol{\vartheta}}_{2}^{\mathrm{T}} \right]^{\mathrm{T}} \tag{4.34}$$

to their global counterparts

$$\delta \mathbf{p}_{g}^{g} = \left[\delta \mathbf{u}_{1}^{g \, \mathrm{T}} \ \delta \boldsymbol{\theta}_{1}^{g \, \mathrm{T}} \ \delta \mathbf{u}_{2}^{g \, \mathrm{T}} \ \delta \boldsymbol{\theta}_{2}^{g \, \mathrm{T}} \right]^{\mathrm{T}}$$
(4.35)

with $\delta \theta_i^g$, i = 1, 2 denoting spatial angular variations as defined in (4.8). The expression of **B**, and subsequently the transformations in equations (4.22) and (4.23) are derived using a sequence of two changes of variables, as described in the following subsections.

4.2.2 Change of variables $\delta \bar{\theta} \longrightarrow \delta \bar{\theta}$

The general procedure for evaluating the transformation matrix **B** involves the variations of equations (4.29) and (4.30). Referring to (4.30), admissible variations $\delta \bar{\mathbf{R}}_i$, i = 1, 2 are computed – cf. equation (4.8) – according to

$$\delta \bar{\mathbf{R}}_i = \delta \tilde{\bar{\boldsymbol{\theta}}}_i \bar{\mathbf{R}}_i \tag{4.36}$$

The angular variations $\delta \bar{\theta}_i$ involved in the above equation, are of a different nature than $\delta \bar{\vartheta}_i$ as defined in (4.31). A change of variables from $\delta \bar{\vartheta}_i$ to $\delta \bar{\theta}_i$ is thus required. In order to construct such a change of variables, using equations (4.14), (4.31) and (4.36), $\delta \bar{\theta}_i$ and $\delta \bar{\vartheta}_i$ are connected by

$$\delta \bar{\boldsymbol{\vartheta}} = \mathbf{T}_s^{-1}(\bar{\boldsymbol{\vartheta}}) \, \delta \bar{\boldsymbol{\theta}} \tag{4.37}$$

which, by introducing the notation

$$\delta \mathbf{p}_{a} = \begin{bmatrix} \delta \bar{u} & \delta \bar{\boldsymbol{\theta}}_{1}^{\mathrm{T}} & \delta \bar{\boldsymbol{\theta}}_{2}^{\mathrm{T}} \end{bmatrix}^{\mathrm{T}}$$

$$(4.38)$$

gives

$$\delta \mathbf{p}_{l} = \mathbf{B}_{a} \, \delta \mathbf{p}_{a} \qquad \mathbf{B}_{a} = \begin{bmatrix} 1 & \mathbf{0}_{1,3} & \mathbf{0}_{1,3} \\ \mathbf{0}_{3,1} & \mathbf{T}_{s}^{-1}(\bar{\boldsymbol{\vartheta}}_{1}) & \mathbf{0} \\ \mathbf{0}_{3,1} & \mathbf{0} & \mathbf{T}_{s}^{-1}(\bar{\boldsymbol{\vartheta}}_{2}) \end{bmatrix}$$
(4.39)

Here, as in the sequel $\mathbf{0}_{i,j}$ denotes an $i \times j$ zero matrix. For a 3×3 zero matrix the notation $\mathbf{0}$ is however used.

Further, a virtual work equation gives

$$\mathbf{f}_a = \mathbf{B}_a^{\mathrm{T}} \mathbf{f}_I \tag{4.40}$$

with \mathbf{f}_a denoting the internal force vector consistent with $\delta \mathbf{p}_a$. The corresponding transformation for the local tangent stiffness matrices, i.e. \mathbf{K}_l and \mathbf{K}_a , is obtained by taking the variations of (4.40)

$$\delta \mathbf{f}_a = \mathbf{B}_a^{\mathrm{T}} \, \delta \mathbf{f}_l + \delta \mathbf{B}_a^{\mathrm{T}} \, \mathbf{f}_l \tag{4.41}$$

where, by definition

$$\delta \mathbf{f}_l = \mathbf{K}_l \, \delta \mathbf{p}_l \qquad \delta \mathbf{f}_a = \mathbf{K}_a \, \delta \mathbf{p}_a \tag{4.42}$$

Using equations (4.39), (4.41) and (4.42) gives the required transformation

$$\mathbf{K}_{a} = \mathbf{B}_{a}^{\mathrm{T}} \mathbf{K}_{l} \mathbf{B}_{a} + \mathbf{K}_{h} \qquad \mathbf{K}_{h} = \begin{bmatrix} 0 & \mathbf{0}_{1,3} & \mathbf{0}_{1,3} \\ \mathbf{0}_{3,1} & \mathbf{K}_{h1} & \mathbf{0} \\ \mathbf{0}_{3,1} & \mathbf{0} & \mathbf{K}_{h2} \end{bmatrix}$$
(4.43)

The expressions of \mathbf{K}_{h1} and \mathbf{K}_{h2} are computed from

$$\frac{\partial}{\partial \bar{\boldsymbol{\theta}}} \left[\mathbf{T}_{s}^{-\mathrm{T}} \mathbf{v} \right] = \frac{\partial}{\partial \bar{\boldsymbol{\theta}}} \left[\mathbf{T}_{s}^{-\mathrm{T}} \mathbf{v} \right] \frac{\partial \bar{\boldsymbol{\theta}}}{\partial \bar{\boldsymbol{\theta}}} = \frac{\partial}{\partial \bar{\boldsymbol{\theta}}} \left[\mathbf{T}_{s}^{-\mathrm{T}} \mathbf{v} \right] \mathbf{T}_{s}^{-1} \tag{4.44}$$

with the vector \mathbf{v} maintained constant during differentiation. Using (4.14) gives after some algebra

$$\frac{\partial}{\partial \bar{\boldsymbol{\theta}}} \left[\mathbf{T}_{s}^{-\mathrm{T}} \mathbf{v} \right] = \left[\eta \left[\bar{\boldsymbol{\vartheta}} \, \mathbf{v}^{\mathrm{T}} - 2 \, \mathbf{v} \, \bar{\boldsymbol{\vartheta}}^{\mathrm{T}} + \left(\bar{\boldsymbol{\vartheta}}^{\mathrm{T}} \cdot \mathbf{v} \right) \mathbf{I} \right] + \mu \, \tilde{\bar{\boldsymbol{\vartheta}}}^{2} \left[\mathbf{v} \, \bar{\boldsymbol{\vartheta}}^{\mathrm{T}} \right] - \frac{1}{2} \tilde{\mathbf{v}} \right] \mathbf{T}_{s}^{-1} (\bar{\boldsymbol{\vartheta}}) \quad (4.45)$$

with the coefficients η and μ given by

$$\eta = \frac{2\sin\alpha - \alpha(1 + \cos\alpha)}{2\alpha^2\sin\alpha} \quad \mu = \frac{\alpha(\alpha + \sin\alpha) - 8\sin^2(\alpha/2)}{4\alpha^4\sin^2(\alpha/2)} \quad \alpha = \|\bar{\boldsymbol{\vartheta}}\| \quad (4.46)$$

Thus, \mathbf{K}_{hi} , i = 1, 2 are evaluated from equation (4.45) with $\mathbf{\bar{\vartheta}} = \mathbf{\bar{\vartheta}}_i$ and $\mathbf{v} = \mathbf{m}_i$, with \mathbf{m}_i as defined in (4.33).

Finally, it should be mentioned that, at least for small increments, $\bar{\boldsymbol{\vartheta}}$ is a small quantity. Consequently, $\mathbf{T}_s^{-1}(\bar{\boldsymbol{\vartheta}})$ is close to identity. For this reason, the transformation described by equations (4.40) and (4.43) is often omitted in the formulation of co-rotational elements (cf. e.g. [22]). The numerical tests performed in [73] showed that this omission has scarcely any effect on the correctness of the results, although it has an impact on the convergence properties of the element.

4.2.3 Change of variables $\delta \mathbf{p}_a \longrightarrow \delta \mathbf{p}_a^g$

The second step of the variable change involves $\delta \mathbf{p}_a$ and $\delta \mathbf{p}_g^g$, as defined in equations (4.38) and (4.35), respectively.

Referring first to the local axial translation \bar{u} , the variations of equation (4.29) give

$$\delta \bar{u} = \delta l_n = \mathbf{r} \, \delta \mathbf{p}_q^g \qquad \mathbf{r} = \begin{bmatrix} -\mathbf{r}_1^{\mathrm{T}} & \mathbf{0}_{1,3} & \mathbf{r}_1^{\mathrm{T}} & \mathbf{0}_{1,3} \end{bmatrix}$$
(4.47)

For the rotational terms, the variations of equation (4.30) are needed

$$\delta \bar{\mathbf{R}}_i = \delta \mathbf{R}_r^{\mathrm{T}} \mathbf{R}_i^g \mathbf{R}_o + \mathbf{R}_r^{\mathrm{T}} \delta \mathbf{R}_i^g \mathbf{R}_o \tag{4.48}$$

where $\delta \bar{\mathbf{R}}_i$ is defined in (4.36) whereas $\delta \mathbf{R}_i^g$ and $\delta \mathbf{R}_r$ are computed using the spatial form of equation (4.8), i.e.

$$\delta \mathbf{R}_{i}^{g} = \delta \tilde{\boldsymbol{\theta}}_{i}^{g} \mathbf{R}_{i}^{g} \qquad \delta \mathbf{R}_{r} = \delta \tilde{\boldsymbol{\theta}}_{r}^{g} \mathbf{R}_{r} \tag{4.49}$$

 $\delta \mathbf{R}_r^{\mathrm{T}}$ is calculated from the orthogonality condition $\mathbf{R}_r \mathbf{R}_r^{\mathrm{T}} = \mathbf{I}$ which, by differentiation and introduction of (4.49) gives

$$\delta \mathbf{R}_r \, \mathbf{R}_r^{\mathrm{T}} + \mathbf{R}_r \, \delta \mathbf{R}_r^{\mathrm{T}} = 0 \tag{4.50a}$$

$$\delta \tilde{\boldsymbol{\theta}}_r^g \mathbf{R}_r \mathbf{R}_r^{\mathrm{T}} + \mathbf{R}_r \delta \mathbf{R}_r^{\mathrm{T}} = 0 \tag{4.50b}$$

and then

$$\delta \mathbf{R}_r^{\mathrm{T}} = -\mathbf{R}_r^{\mathrm{T}} \, \delta \tilde{\boldsymbol{\theta}}_r^{g} \tag{4.51}$$

Using (4.36), (4.49) and (4.51), equation (4.48) can be rewritten as

$$\delta \tilde{\boldsymbol{\theta}}_{i} \, \bar{\mathbf{R}}_{i} = -\mathbf{R}_{r}^{\mathrm{T}} \, \delta \tilde{\boldsymbol{\theta}}_{r}^{g} \, \mathbf{R}_{i}^{g} \, \mathbf{R}_{o} + \mathbf{R}_{r}^{\mathrm{T}} \, \delta \tilde{\boldsymbol{\theta}}_{i}^{g} \, \mathbf{R}_{i}^{g} \, \mathbf{R}_{o}$$

$$= -\mathbf{R}_{r}^{\mathrm{T}} \, \delta \tilde{\boldsymbol{\theta}}_{r}^{g} \, \mathbf{R}_{r} \, \mathbf{R}_{r}^{\mathrm{T}} \, \mathbf{R}_{i}^{g} \, \mathbf{R}_{o} + \mathbf{R}_{r}^{\mathrm{T}} \, \delta \tilde{\boldsymbol{\theta}}_{i}^{g} \, \mathbf{R}_{r} \, \mathbf{R}_{r}^{\mathrm{T}} \, \mathbf{R}_{i}^{g} \, \mathbf{R}_{o}$$

$$= (\delta \tilde{\boldsymbol{\theta}}_{i}^{e} - \delta \tilde{\boldsymbol{\theta}}_{r}^{e}) \, \bar{\mathbf{R}}_{i}$$

$$(4.52)$$

where use has been made of equation (4.30) and of the fact that \mathbf{R}_r transforms a vector and a tensor from global to local coordinates according to

$$\mathbf{x}^e = \mathbf{R}_r^{\mathrm{T}} \mathbf{x}^g \qquad \tilde{\mathbf{x}}^e = \mathbf{R}_r^{\mathrm{T}} \tilde{\mathbf{x}}^g \mathbf{R}_r \tag{4.53}$$

Thus, equation (4.52) gives

$$\delta \bar{\boldsymbol{\theta}}_i = \delta \boldsymbol{\theta}_i^e - \delta \boldsymbol{\theta}_r^e \qquad i = 1, 2 \tag{4.54}$$

Further, let

$$\delta \mathbf{p}_{g}^{e} = \mathbf{E}^{T} \delta \mathbf{p}_{g}^{g} \qquad \mathbf{E} = \begin{bmatrix} \mathbf{R}_{r} & \mathbf{0} & \mathbf{0} & \mathbf{0} \\ \mathbf{0} & \mathbf{R}_{r} & \mathbf{0} & \mathbf{0} \\ \mathbf{0} & \mathbf{0} & \mathbf{R}_{r} & \mathbf{0} \\ \mathbf{0} & \mathbf{0} & \mathbf{0} & \mathbf{R}_{r} \end{bmatrix}$$
(4.55)

Then, using the chain rule, $\delta \bar{\theta}_i$ is evaluated as

$$\delta \bar{\boldsymbol{\theta}}_{i} = \frac{\partial \bar{\boldsymbol{\theta}}_{i}}{\partial \mathbf{p}_{g}^{e}} \frac{\partial \mathbf{p}_{g}^{e}}{\partial \mathbf{p}_{g}^{g}} \delta \mathbf{p}_{g}^{g} = \frac{\partial \bar{\boldsymbol{\theta}}_{i}}{\partial \mathbf{p}_{g}^{e}} \mathbf{E}^{\mathrm{T}} \delta \mathbf{p}_{g}^{g} \qquad i = 1, 2$$

$$(4.56)$$

Substituting from equation (4.54) gives

$$\begin{bmatrix} \delta \bar{\boldsymbol{\theta}}_1 \\ \delta \bar{\boldsymbol{\theta}}_2 \end{bmatrix} = \begin{pmatrix} \begin{bmatrix} \mathbf{0} & \mathbf{I} & \mathbf{0} & \mathbf{0} \\ \mathbf{0} & \mathbf{0} & \mathbf{0} & \mathbf{I} \end{bmatrix} - \begin{bmatrix} \mathbf{G}^{\mathrm{T}} \\ \mathbf{G}^{\mathrm{T}} \end{bmatrix} \end{pmatrix} \mathbf{E}^{\mathrm{T}} \delta \mathbf{p}_g^g = \mathbf{P} \mathbf{E}^{\mathrm{T}} \delta \mathbf{p}_g^g$$
(4.57)

where the matrix G is defined by

$$\mathbf{G} = \frac{\partial \boldsymbol{\theta}_r^e}{\partial \mathbf{p}_q^e} \tag{4.58}$$

Hence, from (4.47) and (4.57), the connection between $\delta \mathbf{p}_a$ and $\delta \mathbf{p}_g^g$ is given by

$$\delta \mathbf{p}_a = \mathbf{B}_g \, \delta \mathbf{p}_g^g \qquad \mathbf{B}_g = \begin{bmatrix} \mathbf{r} \\ \mathbf{P} \, \mathbf{E}^{\mathrm{T}} \end{bmatrix}$$
 (4.59)

Expression of G

The expression of G is obtained from (4.49) which can be rewritten as

$$\delta \tilde{\boldsymbol{\theta}}_r^g = \delta \mathbf{R}_r \, \mathbf{R}_r^{\mathrm{T}} \tag{4.60}$$

and after the transformation (4.53) as

$$\delta \tilde{\boldsymbol{\theta}}_r^e = \mathbf{R}_r^{\mathrm{T}} \delta \mathbf{R}_r \tag{4.61}$$

From (4.24) and the above equation, it can easily be found that

$$\delta \boldsymbol{\theta}_{r}^{e} = \begin{bmatrix} \delta \theta_{r_{1}}^{e} \\ \delta \theta_{r_{2}}^{e} \\ \delta \theta_{r_{3}}^{e} \end{bmatrix} = \begin{bmatrix} -\mathbf{r}_{2}^{\mathrm{T}} \, \delta \mathbf{r}_{3} \\ -\mathbf{r}_{3}^{\mathrm{T}} \, \delta \mathbf{r}_{1} \\ \mathbf{r}_{2}^{\mathrm{T}} \, \delta \mathbf{r}_{1} \end{bmatrix}$$
(4.62)

Introducing the notation $\mathbf{u}_{i}^{g} = \left[u_{i1}^{g} \ u_{i2}^{g} \ u_{i3}^{g}\right]^{\mathrm{T}} (i=1,2)$, differentiation of (4.25) gives

$$\delta \mathbf{r}_{1}^{g} = \frac{1}{l_{n}} \left[\mathbf{I} - \mathbf{r}_{1} \mathbf{r}_{1}^{\mathrm{T}} \right] \begin{bmatrix} \delta u_{21}^{g} - \delta u_{11}^{g} \\ \delta u_{22}^{g} - \delta u_{12}^{g} \\ \delta u_{23}^{g} - \delta u_{13}^{g} \end{bmatrix}$$
(4.63)

and after transformation (4.53) in the local coordinate system, it is obtained

$$\delta \mathbf{r}_{1}^{e} = \frac{1}{l_{n}} \begin{bmatrix} \delta u_{21}^{e} - \delta u_{11}^{e} \\ \delta u_{22}^{e} - \delta u_{12}^{e} \\ \delta u_{23}^{e} - \delta u_{13}^{e} \end{bmatrix}$$
(4.64)

Hence, since the local expressions of \mathbf{r}_2 and \mathbf{r}_3 are $\begin{bmatrix} 0 & 1 & 0 \end{bmatrix}^T$ and $\begin{bmatrix} 0 & 0 & 1 \end{bmatrix}^T$, equation (4.62) gives

$$\delta\theta_{r_2}^e = \frac{1}{l_n} \left(\delta u_{13}^e - \delta u_{23}^e \right) \tag{4.65a}$$

$$\delta\theta_{r_3}^e = \frac{1}{l_n} \left(\delta u_{22}^e - \delta u_{12}^e \right) \tag{4.65b}$$

The evaluation of $\delta\theta_{r_1}^e$ is more complicated and can be performed as follows. Differentiation of (4.27) gives

$$\delta \mathbf{q} = \frac{1}{2} (\delta \mathbf{R}_1^g + \delta \mathbf{R}_2^g) \mathbf{R}_o [0 \ 1 \ 0]^{\mathrm{T}}$$

$$= \frac{1}{2} (\delta \tilde{\boldsymbol{\theta}}_1^g \mathbf{R}_1^g + \delta \tilde{\boldsymbol{\theta}}_2^g \mathbf{R}_2^g) \mathbf{R}_o [0 \ 1 \ 0]^{\mathrm{T}}$$

$$= \frac{1}{2} (\delta \tilde{\boldsymbol{\theta}}_1^g \mathbf{q}_1 + \delta \tilde{\boldsymbol{\theta}}_2^g \mathbf{q}_2)$$

$$(4.66)$$

The local expressions of the vectors \mathbf{q} , \mathbf{q}_1 and \mathbf{q}_2 are denoted by

$$\mathbf{R}_r^{\mathrm{T}} \mathbf{q} = \begin{bmatrix} q_1 \\ q_2 \\ 0 \end{bmatrix} \qquad \mathbf{R}_r^{\mathrm{T}} \mathbf{q}_1 = \begin{bmatrix} q_{11} \\ q_{12} \\ q_{13} \end{bmatrix} \qquad \mathbf{R}_r^{\mathrm{T}} \mathbf{q}_2 = \begin{bmatrix} q_{21} \\ q_{22} \\ q_{23} \end{bmatrix}$$
(4.67)

The last coordinate of $\mathbf{R}_r^{\mathrm{T}} \mathbf{q}$ is zero since \mathbf{q} is perpendicular to \mathbf{r}_3 .

The local expression of $\delta \mathbf{q}$ can be deduced from equation (4.66) as

$$\delta \mathbf{q}^{e} = \frac{1}{2} \delta \tilde{\boldsymbol{\theta}}_{1}^{e} \begin{bmatrix} q_{11} \\ q_{12} \\ q_{13} \end{bmatrix} + \frac{1}{2} \delta \tilde{\boldsymbol{\theta}}_{2}^{e} \begin{bmatrix} q_{21} \\ q_{22} \\ q_{23} \end{bmatrix}$$
(4.68)

which after calculation gives

$$\delta \mathbf{q}^{e} = \frac{1}{2} \begin{bmatrix} -q_{12} \delta \theta_{13}^{e} + q_{13} \delta \theta_{12}^{e} - q_{22} \delta \theta_{23}^{e} + q_{23} \delta \theta_{22}^{e} \\ +q_{11} \delta \theta_{13}^{e} - q_{13} \delta \theta_{11}^{e} + q_{21} \delta \theta_{23}^{e} - q_{23} \delta \theta_{21}^{e} \\ -q_{11} \delta \theta_{12}^{e} + q_{12} \delta \theta_{11}^{e} - q_{21} \delta \theta_{22}^{e} + q_{22} \delta \theta_{21}^{e} \end{bmatrix}$$
(4.69)

The following notations are introduced

$$\eta = \frac{q_1}{q_2} \qquad \eta_{11} = \frac{q_{11}}{q_2} \qquad \eta_{12} = \frac{q_{12}}{q_2} \qquad \eta_{21} = \frac{q_{21}}{q_2} \qquad \eta_{22} = \frac{q_{22}}{q_2}$$
(4.70)

The differentiation of \mathbf{r}_3 is calculated from its definition (4.28). By noting that $\|\mathbf{r}_1 \times \mathbf{q}\| = q_2$, the first line of equation (4.62) can be rewritten as

$$\delta\theta_{r_1}^e = -\frac{\mathbf{r}_2^{\mathrm{T}}}{q_2} \delta\mathbf{r}_1^e \times \mathbf{q} - \frac{\mathbf{r}_2^{\mathrm{T}}}{q_2} \mathbf{r}_1 \times \delta\mathbf{q}^e - \delta\left(\frac{1}{q_2}\right) \mathbf{r}_2^{\mathrm{T}} \left(\mathbf{r}_1 \times \mathbf{q}\right)$$
(4.71)

The last term in the above equation is zero. The two others terms can be evaluated from equations (4.64), (4.67) and (4.69). The result, after some work, is

$$\delta\theta_{r_1}^e = \frac{\eta}{l_n} \left(\delta w_1^e - \delta w_2^e \right) - \frac{\eta_{11}}{2} \, \delta\theta_{12}^e + \frac{\eta_{12}}{2} \, \delta\theta_{11}^e - \frac{\eta_{21}}{2} \, \delta\theta_{22}^e + \frac{\eta_{22}}{2} \, \delta\theta_{21}^e \tag{4.72}$$

Finally, the expression for the matrix G is

$$\mathbf{G}^{\mathrm{T}} = \begin{bmatrix} 0 & 0 & \frac{\eta}{l_n} & \frac{\eta_{12}}{2} & -\frac{\eta_{11}}{2} & 0 & 0 & 0 & -\frac{\eta}{l_n} & \frac{\eta_{22}}{2} & -\frac{\eta_{21}}{2} & 0 \\ 0 & 0 & \frac{1}{l_n} & 0 & 0 & 0 & 0 & -\frac{1}{l_n} & 0 & 0 & 0 \\ 0 & -\frac{1}{l_n} & 0 & 0 & 0 & 0 & \frac{1}{l_n} & 0 & 0 & 0 & 0 \end{bmatrix}$$
(4.73)

Internal forces

Using (4.59), the internal force vector in global coordinates is computed as

$$\mathbf{f}_g = \mathbf{B}_g^{\mathrm{T}} \, \mathbf{f}_a \tag{4.74}$$

Note that, according to the sequence of variable changes previously defined, the matrix \mathbf{B} in equation (4.21) is explicitly given by the product $\mathbf{B}_a \mathbf{B}_q$.

Tangent stiffness matrix

Differentiation of (4.74) gives

$$\delta \mathbf{f}_{g} = \mathbf{B}_{g}^{\mathrm{T}} \mathbf{K}_{a} \mathbf{B}_{g} \delta \mathbf{p}_{g}^{g} + \delta \mathbf{r}^{\mathrm{T}} f_{a_{1}} + \delta (\mathbf{E} \mathbf{P}^{\mathrm{T}}) \mathbf{m}$$
(4.75)

with

$$\mathbf{m} = \begin{bmatrix} f_{a_2} & f_{a_3} & f_{a_4} & f_{a_5} & f_{a_6} & f_{a_7} \end{bmatrix}^{\mathrm{T}}$$
 (4.76)

where f_{a_i} , i = 1, 7 denotes the *i*-th component of the vector \mathbf{f}_a .

From (4.47) and (4.63), it can easily be derived that

$$\delta \mathbf{r}^{\mathrm{T}} = \mathbf{D} \, \delta \mathbf{p}_{g}^{g} \qquad \mathbf{D} = \begin{bmatrix} \mathbf{D}_{3} & \mathbf{0} & -\mathbf{D}_{3} & \mathbf{0} \\ \mathbf{0} & \mathbf{0} & \mathbf{0} & \mathbf{0} \\ -\mathbf{D}_{3} & \mathbf{0} & \mathbf{D}_{3} & \mathbf{0} \\ \mathbf{0} & \mathbf{0} & \mathbf{0} & \mathbf{0} \end{bmatrix} \qquad \mathbf{D}_{3} = \frac{1}{l_{n}} (\mathbf{I} - \mathbf{r}_{1} \, \mathbf{r}_{1}^{\mathrm{T}}) \quad (4.77)$$

The last term in expression (4.75) is evaluated from

$$\delta(\mathbf{E}\,\mathbf{P}^{\mathrm{T}})\,\mathbf{m} = \delta\mathbf{E}\,\mathbf{P}^{\mathrm{T}}\,\mathbf{m} + \mathbf{E}\,\delta\mathbf{P}^{\mathrm{T}}\,\mathbf{m} \tag{4.78}$$

By introducing

$$\mathbf{P}^{\mathrm{T}} \mathbf{m} = \begin{bmatrix} \mathbf{n}_1 \\ \mathbf{m}_1 \\ \mathbf{n}_2 \\ \mathbf{m}_2 \end{bmatrix} \tag{4.79}$$

and using (4.55) and (4.61), the first term in (4.78) can be expressed as

$$\delta \mathbf{E} \, \mathbf{P}^{\mathrm{T}} \, \mathbf{m} = \begin{bmatrix} \mathbf{R}_{r} \, \delta \tilde{\boldsymbol{\theta}}_{r}^{e} & \mathbf{0} & \mathbf{0} & \mathbf{0} \\ \mathbf{0} & \mathbf{R}_{r} \, \delta \tilde{\boldsymbol{\theta}}_{r}^{e} & \mathbf{0} & \mathbf{0} \\ \mathbf{0} & \mathbf{0} & \mathbf{R}_{r} \, \delta \tilde{\boldsymbol{\theta}}_{r}^{e} & \mathbf{0} \\ \mathbf{0} & \mathbf{0} & \mathbf{0} & \mathbf{R}_{r} \, \delta \tilde{\boldsymbol{\theta}}_{r}^{e} \end{bmatrix} \begin{bmatrix} \mathbf{n}_{1} \\ \mathbf{m}_{1} \\ \mathbf{n}_{2} \\ \mathbf{m}_{2} \end{bmatrix} = \mathbf{E} \begin{bmatrix} \delta \tilde{\boldsymbol{\theta}}_{r}^{e} \, \mathbf{n}_{1} \\ \delta \tilde{\boldsymbol{\theta}}_{r}^{e} \, \mathbf{m}_{1} \\ \delta \tilde{\boldsymbol{\theta}}_{r}^{e} \, \mathbf{n}_{2} \\ \delta \tilde{\boldsymbol{\theta}}_{r}^{e} \, \mathbf{m}_{2} \end{bmatrix}$$

$$(4.80)$$

which, using the relation

$$\tilde{\mathbf{a}}\,\mathbf{b} = -\tilde{\mathbf{b}}\,\mathbf{a}\tag{4.81}$$

gives

$$\delta \mathbf{E} \, \mathbf{P}^{\mathrm{T}} \, \mathbf{m} = -\mathbf{E} \, \mathbf{Q} \, \delta \boldsymbol{\theta}_{r}^{e} \qquad \mathbf{Q} = \begin{bmatrix} \tilde{\mathbf{n}}_{1} \\ \tilde{\mathbf{m}}_{1} \\ \tilde{\mathbf{n}}_{2} \\ \tilde{\mathbf{m}}_{2} \end{bmatrix}$$
(4.82)

Then, by using (4.58), it is obtained

$$\delta \mathbf{E} \mathbf{P}^{\mathrm{T}} \mathbf{m} = -\mathbf{E} \mathbf{Q} \mathbf{G}^{\mathrm{T}} \mathbf{E}^{\mathrm{T}} \delta \mathbf{p}_{q}^{g}$$
(4.83)

The calculation of the second term of (4.78) requires the value of $\delta \mathbf{P}^{\mathrm{T}}$ which can be obtained by introducing the matrix \mathbf{A} such as

and by noting that

$$\mathbf{A}^{\mathrm{T}}\mathbf{G} = \mathbf{I} \tag{4.85}$$

Differentiation of the above equation gives

$$\delta \mathbf{A}^{\mathrm{T}} \mathbf{G} + \mathbf{A}^{\mathrm{T}} \delta \mathbf{G} = \mathbf{0} \tag{4.86}$$

and hence

$$\delta \mathbf{G} = -\mathbf{A}^{-\mathrm{T}} \, \delta \mathbf{A}^{\mathrm{T}} \, \mathbf{G} = -\mathbf{G} \, \delta \mathbf{A}^{\mathrm{T}} \, \mathbf{G} \tag{4.87}$$

Further, using the definition of \mathbf{P} in (4.57) gives

$$\delta \mathbf{P} = -\mathbf{C}\,\delta \mathbf{G}^{\mathrm{T}} \qquad \mathbf{C} = \begin{bmatrix} \mathbf{I} \\ \mathbf{I} \end{bmatrix} \tag{4.88}$$

which can be rewritten as

$$\delta \mathbf{P}^{\mathrm{T}} = -\delta \mathbf{G} \, \mathbf{C}^{\mathrm{T}} = \mathbf{G} \, \delta \mathbf{A}^{\mathrm{T}} \, \mathbf{G} \, \mathbf{C}^{\mathrm{T}}$$
(4.89)

Then, the second term of (4.78) becomes

$$\mathbf{E}\,\delta\mathbf{P}^{\mathrm{T}}\,\mathbf{m} = \mathbf{E}\,\mathbf{G}\,\delta\mathbf{A}^{\mathrm{T}}\,\mathbf{G}\,\mathbf{C}^{\mathrm{T}}\,\mathbf{m} \tag{4.90}$$

which can be simplified after symbolic matrix multiplications as

$$\mathbf{E}\,\delta\mathbf{P}^{\mathrm{T}}\,\mathbf{m} = \mathbf{E}\,\mathbf{G}\,\mathbf{a}\,\delta l_{n} \tag{4.91}$$

with

$$\mathbf{a} = \begin{bmatrix} 0 \\ \frac{\eta}{l_n} (f_{a_2} + f_{a_5}) - \frac{1}{l_n} (f_{a_3} + f_{a_6}) \\ \frac{1}{l_n} (f_{a_4} + f_{a_7}) \end{bmatrix}$$
(4.92)

Introducing (4.47) in (4.91) gives

$$\mathbf{E}\,\delta\mathbf{P}^{\mathrm{T}}\,\mathbf{m} = \mathbf{E}\,\mathbf{G}\,\mathbf{a}\,\mathbf{r}\,\delta\mathbf{p}_{a}^{g} \tag{4.93}$$

Finally, from equations (4.75), (4.78), (4.83) and (4.93) the expression of the global tangent stiffness matrix is

$$\mathbf{K}_{g} = \mathbf{B}_{g}^{\mathrm{T}} \, \mathbf{K}_{a} \, \mathbf{B}_{g} + \mathbf{K}_{m} \qquad \mathbf{K}_{m} = \mathbf{D} \, f_{a_{1}} - \mathbf{E} \, \mathbf{Q} \, \mathbf{G}^{\mathrm{T}} \, \mathbf{E}^{\mathrm{T}} + \mathbf{E} \, \mathbf{G} \, \mathbf{a} \, \mathbf{r}$$
(4.94)

Note that the tangent stiffness matrix as given by equation (4.94), is not symmetric. However, as shown in [64], it can be symmetrised without losing quadratic convergence unless concentrated moments are applied on the structure.

4.2.4 Eccentric nodes, rigid links

A beam element is defined such that node 1 is rigidly linked to another node I of the structure. Mathematically this can be expressed as

$$\mathbf{x}_{\mathrm{I}}^{g} = \mathbf{x}_{1}^{g} + \mathbf{v}_{o} \tag{4.95}$$

where \mathbf{x}_1^g and \mathbf{x}_I^g denote the position vectors of nodes 1 and I in the original undeformed configuration whereas \mathbf{v}_o denotes an eccentricity vector. Since the link is assumed as rigid, the magnitude of the eccentricity vector will not change during the deformation of the structure. The connection between the displacements at the two nodes 1 and I can then be expressed as

$$\mathbf{u}_{\mathrm{I}}^{g} = \mathbf{u}_{\mathrm{I}}^{g} + (\mathbf{R}_{\mathrm{I}}^{g} - \mathbf{I}) \mathbf{v}_{o} \qquad \mathbf{R}_{\mathrm{I}}^{g} = \mathbf{R}_{\mathrm{I}}^{g} \tag{4.96}$$

The modelling of a rigid link will thus require a change of variables from \mathbf{u}_{1}^{g} to \mathbf{u}_{1}^{g} . Taking the variations of equation (4.96), and using (4.81), gives

$$\delta \mathbf{u}_{1}^{g} = \delta \mathbf{u}_{1}^{g} + \delta \mathbf{R}_{1}^{g} \mathbf{v}_{o} = \delta \mathbf{u}_{1}^{g} + \delta \tilde{\boldsymbol{\theta}}_{1}^{g} \mathbf{R}_{1}^{g} \mathbf{v}_{o} = \delta \mathbf{u}_{1}^{g} - \tilde{\mathbf{v}} \, \delta \boldsymbol{\theta}_{1}^{g}$$

$$(4.97)$$

with

$$\mathbf{v} = \mathbf{R}_1^g \, \mathbf{v}_o \tag{4.98}$$

which, by introducing the notation

$$\delta \mathbf{p}_{ec}^{g} = \begin{bmatrix} \delta \mathbf{u}_{1}^{g T} & \delta \boldsymbol{\theta}_{1}^{g T} & \delta \mathbf{u}_{2}^{g T} & \delta \boldsymbol{\theta}_{2}^{g T} \end{bmatrix}^{T}$$

$$(4.99)$$

leads to

$$\delta \mathbf{p}_{g}^{g} = \mathbf{B}_{ec} \, \delta \mathbf{p}_{ec}^{g} \qquad \mathbf{B}_{ec} = \begin{bmatrix} \mathbf{I} & \tilde{\mathbf{v}} & \mathbf{0} & \mathbf{0} \\ \mathbf{0} & \mathbf{I} & \mathbf{0} & \mathbf{0} \\ \mathbf{0} & \mathbf{0} & \mathbf{I} & \mathbf{0} \\ \mathbf{0} & \mathbf{0} & \mathbf{0} & \mathbf{I} \end{bmatrix}$$
(4.100)

with $\delta \mathbf{p}_g^g$ as defined in equation (4.35). The internal force vector \mathbf{f}_{ec} and tangent stiffness matrix \mathbf{K}_{ec} consistent with $\delta \mathbf{p}_{ec}^g$ are then given by

$$\mathbf{f}_{ec} = \mathbf{B}_{ec}^{\mathrm{T}} \mathbf{f}_{g} \qquad \mathbf{K}_{ec} = \mathbf{B}_{ec}^{\mathrm{T}} \mathbf{K}_{g} \mathbf{B}_{ec} + \mathbf{K}_{n}$$
 (4.101)

The matrix \mathbf{K}_n is calculated by

$$\mathbf{K}_{n} \, \delta \mathbf{p}_{ec}^{g} = \delta(\mathbf{B}_{ec}^{\mathrm{T}}) \, \mathbf{f}_{g} = \begin{bmatrix} \mathbf{0}_{3,1} \\ -\delta \tilde{\mathbf{v}} \, \mathbf{n} \\ \mathbf{0}_{3,1} \\ \mathbf{0}_{3,1} \end{bmatrix} = \begin{bmatrix} \mathbf{0}_{3,1} \\ \tilde{\mathbf{n}} \, \delta \tilde{\boldsymbol{\theta}}_{1}^{g} \, \mathbf{v} \\ \mathbf{0}_{3,1} \\ \mathbf{0}_{3,1} \end{bmatrix} = \begin{bmatrix} \mathbf{0}_{3,1} \\ -\tilde{\mathbf{n}} \, \tilde{\mathbf{v}} \, \delta \boldsymbol{\theta}_{1}^{g} \\ \mathbf{0}_{3,1} \\ \mathbf{0}_{3,1} \end{bmatrix}$$

$$= \begin{bmatrix} \mathbf{0} & \mathbf{0} & \mathbf{0} & \mathbf{0} \\ \mathbf{0} & -\tilde{\mathbf{n}} \, \tilde{\mathbf{v}} & \mathbf{0} & \mathbf{0} \\ \mathbf{0} & \mathbf{0} & \mathbf{0} & \mathbf{0} \\ \mathbf{0} & \mathbf{0} & \mathbf{0} & \mathbf{0} \end{bmatrix} \delta \mathbf{p}_{ec}^{g}$$

$$(4.102)$$

with $\mathbf{n} = [f_{g_1} f_{g_2} f_{g_3}]^{\mathrm{T}}$, $f_{g_i} i = 1, 12$ denotes the *i*-th component of the vector \mathbf{f}_q .

4.2.5 Finite rotation parameters

The global internal force vector \mathbf{f}_g and tangent stiffness matrix \mathbf{K}_g computed according to equations (4.74) and (4.94) are consistent with spatial angular variations $\delta \boldsymbol{\theta}^g$ of the type defined in the first of equations (4.8). Consequently, for a certain node of the structure, the updating of the rotation matrix at each iteration step would have to be done according to

$$\mathbf{R}_{n}^{g} = \exp(\delta \tilde{\boldsymbol{\theta}}^{g}) \, \mathbf{R}_{o}^{g} \tag{4.103}$$

where the subscripts n and o denote quantities corresponding to the "new" and "old" configurations, respectively. Note that in this case the parameterisation of \mathbf{R}^g is largely independent on the technique used to parameterise its admissible variations. Using the terminology in [51], this alternative will be denoted as "intrinsic" parameterisation of 3D rotations.

In addition to the "intrinsic" parameterisation, two alternatives are explored in the present work. The first one is based on the rotation vector Ψ^g , i.e. a 3-parameter representation, cf. (4.3). In this case, the rotational variables are additive and the necessity of a special updating procedure is avoided. The second alternative is based on the spatial form of the incremental rotation vector Θ^g , cf. (4.5) [51,68]. The rotational variables are still additive, but this time only within an increment at the level of the iterative corrections. Corresponding to these two choices, additional changes of variables from $\delta\theta^g$ to $\delta\Psi^g$ or alternatively from $\delta\theta^g$ to $\delta\Theta^g$, must be introduced. These changes of variables are defined in the remainder of this subsection.

It should be noted here that in the context of multi-parametric analyses of instability problems, additive variables, at least at the level of iterative corrections, are essential for an efficient implementation of fold line evaluation algorithms [68, 71]. In the context of dynamical problems and Newmark time-stepping schemes, an excellent discussion on the relative merits of the different alternatives is presented in [51].

Change of variables: $\delta \theta^g \longrightarrow \delta \Psi^g$

For the purposes of this subsection, let \mathbf{p}_r^g denote the following vector of global nodal displacements

$$\mathbf{p}_r^g = \begin{bmatrix} \mathbf{u}_1^{g \, \mathrm{T}} & \mathbf{\Psi}_1^{g \, \mathrm{T}} & \mathbf{u}_2^{g \, \mathrm{T}} & \mathbf{\Psi}_2^{g \, \mathrm{T}} \end{bmatrix}^{\mathrm{T}}$$
(4.104)

where Ψ_i^g denotes the rotational vector at node *i*. The change to the new kinematic variables in \mathbf{p}_r^g requires the connection between $\delta \mathbf{p}_g^g$ as defined in (4.35) and $\delta \mathbf{p}_r^g$. This connection can be easily constructed using (4.11)

$$\delta \mathbf{p}_{g}^{g} = \mathbf{B}_{r} \, \delta \mathbf{p}_{r}^{g} \qquad \mathbf{B}_{r} = \begin{bmatrix} \mathbf{I} & \mathbf{0} & \mathbf{0} & \mathbf{0} \\ \mathbf{0} & \mathbf{T}_{s}(\mathbf{\Psi}_{1}^{g}) & \mathbf{0} & \mathbf{0} \\ \mathbf{0} & \mathbf{0} & \mathbf{I} & \mathbf{0} \\ \mathbf{0} & \mathbf{0} & \mathbf{0} & \mathbf{T}_{s}(\mathbf{\Psi}_{2}^{g}) \end{bmatrix}$$
(4.105)

The global internal force vector \mathbf{f}_r and tangent stiffness matrix \mathbf{K}_r , consistent with \mathbf{p}_r^g , are then given by

$$\mathbf{f}_r = \mathbf{B}_r^{\mathrm{T}} \mathbf{f}_g \qquad \mathbf{K}_r = \mathbf{B}_r^{\mathrm{T}} \mathbf{K}_g \mathbf{B}_r + \mathbf{K}_v$$
 (4.106)

where

$$\mathbf{K}_{v} = \begin{bmatrix} 0 & 0 & 0 & 0 \\ 0 & \mathbf{K}_{v1} & 0 & 0 \\ 0 & 0 & 0 & 0 \\ 0 & 0 & 0 & \mathbf{K}_{v2} \end{bmatrix}$$
(4.107)

The expressions of \mathbf{K}_{v1} and \mathbf{K}_{v2} are obtained from

$$\frac{\partial}{\partial \Psi} [\mathbf{T}_{s}^{\mathrm{T}} \mathbf{v}] = -\left(\frac{\sin \psi}{\psi} - \left(\frac{\sin(\psi/2)}{(\psi/2)}\right)^{2}\right) (\mathbf{u} \times \mathbf{v}) \mathbf{u}^{\mathrm{T}} + \frac{1}{2} \left(\frac{\sin(\psi/2)}{(\psi/2)}\right)^{2} \tilde{\mathbf{v}}
+ \left(\cos \psi - \frac{\sin \psi}{\psi}\right) \frac{1}{\psi} \left[\mathbf{v} \mathbf{u}^{\mathrm{T}} - (\mathbf{u}^{\mathrm{T}} \mathbf{v}) \mathbf{u} \mathbf{u}^{\mathrm{T}}\right]
+ \left(1 - \frac{\sin \psi}{\psi}\right) \frac{1}{\psi} \left[\mathbf{u} \mathbf{v}^{\mathrm{T}} - 2 (\mathbf{u}^{\mathrm{T}} \mathbf{v}) \mathbf{u} \mathbf{u}^{\mathrm{T}} + (\mathbf{u}^{\mathrm{T}} \mathbf{v}) \mathbf{I}\right]$$
(4.108)

with the vector \mathbf{v} maintained constant during the differentiation.

Thus, \mathbf{K}_{v1} and \mathbf{K}_{v2} are evaluated from equation (4.108) with $\mathbf{\Psi} = \mathbf{\Psi}_{1}^{g}$ and $\mathbf{\Psi} = \mathbf{\Psi}_{2}^{g}$, respectively and $\mathbf{v} = [f_{g_4} f_{g_5} f_{g_6}]^{\mathrm{T}}$, $\mathbf{v} = [f_{g_{10}} f_{g_{11}} f_{g_{12}}]^{\mathrm{T}}$, respectively.

With this new parameterisation, the rotational variables are additive and the iterative updates are performed according to

$$\mathbf{\Psi}_n^g = \mathbf{\Psi}_o^g + \delta \mathbf{\Psi}^g \qquad \mathbf{R}_n^g = \exp(\mathbf{\Psi}_n^g) \tag{4.109}$$

The main drawback of a parameterisation based on the rotation vector lies in the fact that it cannot be retained globally. As implied by equation (4.13), the linear operator \mathbf{T}_s becomes singular if the magnitude of the rotation vector reaches 2π . This undesirable feature is then passed over to the tangent stiffness matrix computed according to equation (4.106). In order to remove this drawback, a parameterisation based on the incremental rotation vector $\mathbf{\Theta}^g$ and its iterative increment $\delta\mathbf{\Theta}^g$, cf. subsection 4.1.2, will be discussed in the next subsection.

Change of variables: $\delta \theta^g \longrightarrow \delta \Theta^g$

The transformation matrices required in this second case are constructed on the basis of equation (4.18) which provides the connection between $\delta \boldsymbol{\theta}^g$ and $\delta \boldsymbol{\Theta}^g$. Following a procedure entirely similar to that used in the preceding subsection, the vector \mathbf{p}_r^g is now defined as

$$\mathbf{p}_r^g = \begin{bmatrix} \mathbf{u}_1^{g \, \mathrm{T}} & \mathbf{\Theta}_1^{g \, \mathrm{T}} & \mathbf{u}_2^{g \, \mathrm{T}} & \mathbf{\Theta}_2^{g \, \mathrm{T}} \end{bmatrix}^{\mathrm{T}}$$
(4.110)

where Θ_i^g denotes the spatial form of the incremental rotation vector at node *i*. Note that in order to avoid singularities in the expression of T_s , the magnitude of Θ^g should be restricted to values less than 2π . Since Θ^g now represents an incremental rotation between two consecutive equilibrium states, this restriction is of no practical consequence.

The transformation equations for the internal force vector and the tangent stiffness matrix are formally identical to equations (4.105)–(4.108), by replacing Ψ_i^g by Θ_i^g .

Using the incremental rotation vector, additive updates apply only within an increment at the level of the iterative corrections. Thus, the updating of the nodal rotations is performed according to

$$\Theta_n^g = \Theta_o^g + \delta \Theta^g \qquad \mathbf{R}_n^g = \exp(\Theta_n^g) \, \mathbf{R}_{n-1}^g$$
(4.111)

where \mathbf{R}_{n-1}^g is the rotational matrix obtained at the end of the previous increment. The transformation matrices required for this second type of parameterisation are essentially constructed using the same linear operators as before, which considerably simplifies the implementation.

4.2.6 Formulation with warping

In order to include warping effects, additional (warping) degrees of freedom α_i are introduced at both nodes i = 1, 2 of the element. The local displacement vector will

thus become

$$\mathbf{p}_{l}^{*} = \begin{bmatrix} \bar{u} & \bar{\boldsymbol{\vartheta}}_{1}^{\mathrm{T}} & \bar{\boldsymbol{\vartheta}}_{2}^{\mathrm{T}} & \alpha_{1} & \alpha_{2} \end{bmatrix}^{\mathrm{T}}$$

$$(4.112)$$

However, since the warping is in itself a deformational quantity, these additional degrees of freedom remain constant during the sequence of transformations previously defined. Hence, referring for instance to equation (4.59), the variations $\delta \mathbf{p}_a$ and $\delta \mathbf{p}_g^g$ are rewritten as

$$\delta \mathbf{p}_{a}^{*} = \begin{bmatrix} \delta \bar{u} & \delta \bar{\boldsymbol{\theta}}_{1}^{\mathrm{T}} & \delta \bar{\boldsymbol{\theta}}_{2}^{\mathrm{T}} & \delta \alpha_{1} & \delta \alpha_{2} \end{bmatrix}^{\mathrm{T}}$$

$$(4.113a)$$

$$\delta \mathbf{p}_{g}^{g*} = \begin{bmatrix} \delta \mathbf{u}_{1}^{g \, \mathrm{T}} & \delta \boldsymbol{\theta}_{1}^{g \, \mathrm{T}} & \delta \mathbf{u}_{2}^{g \, \mathrm{T}} & \delta \boldsymbol{\theta}_{2}^{g \, \mathrm{T}} & \delta \alpha_{1} & \delta \alpha_{2} \end{bmatrix}^{\mathrm{T}}$$
(4.113b)

and the corresponding connection is defined by

$$\delta \mathbf{p}_a^* = \mathbf{B}_g^* \, \delta \mathbf{p}_g^{g*} \qquad \mathbf{B}_g^* = \begin{bmatrix} \mathbf{B}_g & \mathbf{0}_2 \\ \mathbf{0}_2 & \mathbf{I}_2 \end{bmatrix}$$
(4.114)

with \mathbf{B}_g as given in (4.59) and \mathbf{I}_2 denoting a 2×2 identity matrix. Including warping effects, the global internal force vector and tangent stiffness matrix are given by

$$\mathbf{f}_{g}^{*} = \mathbf{B}_{g}^{*T} \mathbf{f}_{a}^{*} \qquad \mathbf{K}_{g}^{*} = \mathbf{B}_{g}^{*T} \mathbf{K}_{a}^{*} \mathbf{B}_{g}^{*} + \mathbf{K}_{m}^{*} \qquad \mathbf{K}_{m}^{*} = \begin{bmatrix} \mathbf{K}_{m} & \mathbf{0}_{2} \\ \mathbf{0}_{2} & \mathbf{0}_{2} \end{bmatrix}$$
 (4.115)

with \mathbf{K}_m as defined in equation (4.94). The two other transformations are modified in a similar way.

4.3 Local element formulation in elasticity

The purpose of this section is to define the internal force vector \mathbf{f}_l (\mathbf{f}_l^* if warping effects are considered) and tangent stiffness matrix \mathbf{K}_l (\mathbf{K}_l^*) in local coordinates. Assuming elastic material behaviour, \mathbf{f}_l and \mathbf{K}_l can be derived from the strain energy Φ expressed as a function of the local displacements \mathbf{p}_l (or alternatively \mathbf{p}_l^*), through successive differentiations

$$\mathbf{f}_{l} = \frac{\partial \Phi}{\partial \mathbf{p}_{l}} \qquad \mathbf{K}_{l} = \frac{\partial^{2} \Phi}{\partial \mathbf{p}_{l}^{2}} \tag{4.116}$$

For all element types presented in this section, the differentiations involved in equation (4.116) have been performed using the Maple symbolic software package. For this reason, explicit expressions for \mathbf{f}_l and \mathbf{K}_l will not be provided here. The remainder of this section will instead focus on the strain energy expression which is the keystone in constructing the necessary Maple subroutines. To complete the element definition, the Maple codes are given in Appendix A.

In order to provide an explicit expression for $\Phi(\mathbf{p}_l)$, a certain definition of the local strains must be adopted. As the main interest of the co-rotational formulation lies

in the fact that the geometrical non-linearity is embedded in the motion of the local element frame, the local strains can be expressed in a simple manner. In fact, most of the co-rotational elements found in the literature are based on local linear strain assumptions. However, as the numerical tests presented in this thesis will show, such elements can give inaccurate results for problems where the torsion effects are important. For these reasons, in the present work a second order approximation of the Green-Lagrange strains is constructed at the level of the local element frame. The resulting expressions are subsequently simplified by neglecting certain second order terms. The effects of these simplifications are then carefully examined in the numerical examples.

4.3.1 Local beam kinematics, strain energy

As a general rule, all kinematic quantities introduced in this subsection are referred to the local element frame \mathbf{r}_i , i=1,2,3, as defined in equations (4.25), (4.27) and (4.28). The origin of the local system is taken at node 1 with \mathbf{r}_1 directed along the line of centroids. Note however that \mathbf{r}_2 and \mathbf{r}_3 are not necessarily directed along the principal axes of the cross-section.

With respect to the local system, the Green-Lagrange strain components which contribute to the strain energy of the beam are given by

$$\begin{array}{rcl} \varepsilon_{11} & = & \bar{u}_{1,1} + \frac{1}{2}\,\bar{u}_{1,1}^2 + \frac{1}{2}\,\bar{u}_{2,1}^2 + \frac{1}{2}\,\bar{u}_{3,1}^2 \\ 2\,\varepsilon_{12} & = & \bar{u}_{1,2} + \bar{u}_{2,1} + \bar{u}_{1,1}\,\bar{u}_{1,2} + \bar{u}_{2,1}\,\bar{u}_{2,2} + \bar{u}_{3,1}\,\bar{u}_{3,2} \\ 2\,\varepsilon_{13} & = & \bar{u}_{1,3} + \bar{u}_{3,1} + \bar{u}_{1,1}\,\bar{u}_{1,3} + \bar{u}_{2,1}\,\bar{u}_{2,3} + \bar{u}_{3,1}\,\bar{u}_{3,3} \end{array} \tag{4.117}$$

where $\bar{u}_1, \bar{u}_2, \bar{u}_3$ are the local (deformational) displacements of the current point P. In the above equation, a comma followed by an index denotes differentiation with respect to the corresponding variable.

In order to obtain a consistent second order approximation of the strain expressions in equation (4.117), a second order approximation of the displacement field is needed. Within the settings of classical beam theory, cf. e.g. [4], bending is defined around the centroid G while torsion is referred to the shear center C. Consequently, whenever C and G are not coincident, the derivation of a non-linear displacement field is not an easy task since rotations are not defined around the same point. An attempt can be found in [60], but the approach presented there lacks consistency. In fact, with the classical beam theory, only a linearised displacement field, obtained by superposition of linear stretching, bending and torsional effects can be derived.

In order to avoid such problems, the kinematic model proposed by Gruttmann et al. [41] is adopted, see Figure 4.3. Thus, let $\mathbf{x}_P^o(x_1, x_2, x_3)$ denote the position vector of point P in the initial (i.e. rotated but still undeformed) configuration and let $\mathbf{x}_P(x_1, x_2, x_3)$ denote the position vector of P in the current configuration. These

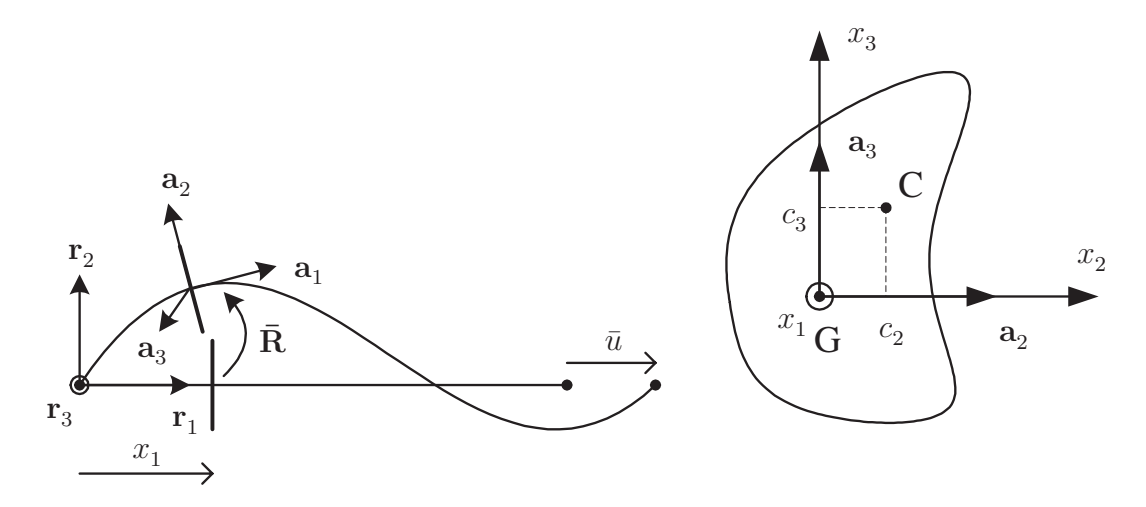


Figure 4.3: Local beam configuration.

two vectors are given by

$$\mathbf{x}_{P}^{o}(x_{1}, x_{2}, x_{3}) = \mathbf{x}_{G}^{o}(x_{1}) + x_{2} \mathbf{r}_{2} + x_{3} \mathbf{r}_{3}$$

$$\mathbf{x}_{P}(x_{1}, x_{2}, x_{3}) = \mathbf{x}_{G}(x_{1}) + x_{2} \mathbf{a}_{2}(x_{1}) + x_{3} \mathbf{a}_{3}(x_{1}) + \alpha(x_{1}) \bar{\omega}(x_{2}, x_{3}) \mathbf{a}_{1}(x_{1})$$

$$(4.118)$$

with \mathbf{x}_G^o and \mathbf{x}_G denoting the position vectors of G in the initial and current configurations, respectively. The warping function $\bar{\omega}(x_2, x_3)$ is defined within Saint-Venant torsion theory and refers to the centroid G, i.e.

$$\bar{\omega} = \omega - c_2 x_3 + c_3 x_2 \tag{4.119}$$

where ω refers to the shear center C of coordinates c_2, c_3 . Note that in connection with ω , the following normality conditions hold

$$\int_{A} \omega \, \mathrm{d}A = 0 \qquad \int_{A} \omega \, x_2 \, \mathrm{d}A = 0 \qquad \int_{A} \omega \, x_3 \, \mathrm{d}A = 0 \qquad (4.120)$$

The orhonormal triad \mathbf{a}_i , i = 1, 2, 3 which specifies the orientation of the current cross-section, is given by

$$\mathbf{a}_i = \bar{\mathbf{R}} \, \mathbf{r}_i \qquad i = 1, 2, 3 \tag{4.121}$$

where the orthogonal matrix $\bar{\mathbf{R}}$ defines a rotation relative to the local element axes, see (4.30). Using (4.4), a second order approximation of $\bar{\mathbf{R}}$ can be constructed as

$$\bar{\mathbf{R}} = \mathbf{I} + \tilde{\bar{\boldsymbol{\vartheta}}} + \frac{1}{2}\tilde{\bar{\boldsymbol{\vartheta}}}^2 \qquad \tilde{\bar{\boldsymbol{\vartheta}}} = \begin{bmatrix} 0 & -\vartheta_3 & \vartheta_2 \\ \vartheta_3 & 0 & -\vartheta_1 \\ -\vartheta_2 & \vartheta_1 & 0 \end{bmatrix}$$
(4.122)

Introducing equation (4.122) into (4.118), a second order approximation of the displacement vector $\bar{\mathbf{u}}_P = [\bar{u}_1 \ \bar{u}_2 \ \bar{u}_3]^{\mathrm{T}} = \mathbf{x}_P - \mathbf{x}_P^o$ can be evaluated as

$$\bar{u}_{1} = u_{1} - x_{2} \vartheta_{3} + x_{3} \vartheta_{2} + \frac{1}{2} x_{2} \vartheta_{1} \vartheta_{2} + \frac{1}{2} x_{3} \vartheta_{1} \vartheta_{3} + \bar{\omega} \alpha$$

$$\bar{u}_{2} = u_{2} - x_{3} \vartheta_{1} - \frac{1}{2} x_{2} (\vartheta_{1}^{2} + \vartheta_{3}^{2}) + \frac{1}{2} x_{3} \vartheta_{2} \vartheta_{3} + \bar{\omega} \alpha \vartheta_{3}$$

$$\bar{u}_{3} = u_{3} + x_{2} \vartheta_{1} - \frac{1}{2} x_{3} (\vartheta_{1}^{2} + \vartheta_{2}^{2}) + \frac{1}{2} x_{2} \vartheta_{2} \vartheta_{3} - \bar{\omega} \alpha \vartheta_{2}$$

$$(4.123)$$

where u_1, u_2, u_3 are the displacements of the centroid G, i.e. the components of the vector $\mathbf{x}_G - \mathbf{x}_G^o$.

Using equations (4.119), (4.120) and (4.123), a second order approximation of the Green-Lagrange strains defined in (4.117) can be evaluated. At this level, two additional simplifications are introduced. First, the term $1/2 \bar{u}_{1,1}^2$ in the expression of ε_{11} is neglected. Second, the non-linear strain components generated by warping are omitted since warping effects are rationally taken into account in a linearised way only [42]. Using these simplifications gives

$$\varepsilon_{11} = \varepsilon_c + x_2 k_2 + x_3 k_3 + \frac{1}{2} r^2 \vartheta_{1,1}^2 + \omega \alpha,_1
2 \varepsilon_{12} = \gamma_{12} + \bar{\omega},_2 \alpha - x_3 k_1
2 \varepsilon_{13} = \gamma_{13} + \bar{\omega},_3 \alpha + x_2 k_1$$
(4.124)

with

$$r^{2} = x_{2}^{2} + x_{3}^{2}$$

$$\varepsilon_{c} = u_{1,1} + \frac{1}{2} \left(u_{2,1}^{2} + u_{3,1}^{2} \right)$$

$$k_{2} = -\vartheta_{3,1} + \frac{1}{2} \left(\vartheta_{1,1} \vartheta_{2} + \vartheta_{1} \vartheta_{2,1} \right) + u_{3,1} \vartheta_{1,1} + c_{3} \alpha_{,1}$$

$$k_{3} = \vartheta_{2,1} + \frac{1}{2} \left(\vartheta_{1,1} \vartheta_{3} + \vartheta_{1} \vartheta_{3,1} \right) - u_{2,1} \vartheta_{1,1} - c_{2} \alpha_{,1}$$

$$k_{1} = \vartheta_{1,1} + \frac{1}{2} \left(\vartheta_{2,1} \vartheta_{3} - \vartheta_{2} \vartheta_{3,1} \right)$$

$$\gamma_{12} = u_{2,1} - \vartheta_{3} + \frac{1}{2} \vartheta_{1} \vartheta_{2} + u_{3,1} \vartheta_{1} - u_{1,1} \vartheta_{3}$$

$$\gamma_{13} = u_{3,1} + \vartheta_{2} + \frac{1}{2} \vartheta_{1} \vartheta_{3} - u_{2,1} \vartheta_{1} + u_{1,1} \vartheta_{2}$$

$$(4.125)$$

The strain energy can then be evaluated from

$$\Phi = \int_{l_0} \Phi_A \, \mathrm{d}x_1 = \int_{l_0} \left(\frac{1}{2} E \int_A \varepsilon_{11}^2 \, \mathrm{d}A + \frac{1}{2} G \int_A \left[(2\varepsilon_{12})^2 + (2\varepsilon_{13})^2 \right] \, \mathrm{d}A \right) \, \mathrm{d}x_1 \quad (4.126)$$

Integration through the cross-section gives

$$\int_{A} \varepsilon_{11}^{2} dA = A \varepsilon_{c}^{2} + I_{22} k_{2}^{2} + I_{33} k_{3}^{2} + \frac{1}{4} I_{rr} \vartheta_{1,1}^{4} + I_{\omega} \alpha_{,1}^{2} + I_{o} \varepsilon_{c} \vartheta_{1,1}^{2} \quad (4.127)^{2} + 2 I_{23} k_{2} k_{3} + I_{2r} k_{2} \vartheta_{1,1}^{2} + I_{3r} k_{3} \vartheta_{1,1}^{2} + I_{\omega r} \alpha_{,1} \vartheta_{1,1}^{2}$$

$$\int_{A} \left[(2\varepsilon_{12})^{2} + (2\varepsilon_{13})^{2} \right] dA = A \left(\gamma_{12}^{2} + \gamma_{13}^{2} \right) + I_{o} k_{1}^{2} + (I_{o} - J) \alpha^{2}$$

$$- 2 \left(I_{o} - J \right) \alpha k_{1}$$

$$(4.128)$$

where J denotes the Saint-Venant torsion modulus

$$J = \int_{A} \left[x_2(\bar{\omega}_{,3} + x_2) - x_3(\bar{\omega}_{,2} - x_3) \right] dA$$
 (4.129)

and the other section quantities are defined by

$$I_{22} = \int_{A} x_{2}^{2} dA \qquad I_{33} = \int_{A} x_{3}^{2} dA \qquad I_{23} = \int_{A} x_{2} x_{3} dA$$

$$I_{2r} = \int_{A} x_{2} r^{2} dA \qquad I_{3r} = \int_{A} x_{3} r^{2} dA \qquad I_{rr} = \int_{A} (x_{2}^{2} + x_{3}^{2})^{2} dA \qquad (4.130)$$

$$I_{\omega} = \int_{A} \omega^{2} dA \qquad I_{\omega r} = \int_{A} \omega r^{2} dA \qquad I_{o} = \int_{A} (x_{2}^{2} + x_{3}^{2}) dA$$

In deriving equations (4.128) and (4.129), the following relations have been used (cf. the proof in [41])

$$\int_{A} \bar{\omega}_{,2} \, dA = \int_{A} \bar{\omega}_{,3} \, dA = 0 \tag{4.131}$$

$$\int_{A} (\bar{\omega}_{,2}^{2} + \bar{\omega}_{,3}^{2}) dA = -\int_{A} (\bar{\omega}_{,3} x_{2} - \bar{\omega}_{,2} x_{3}) dA = I_{o} - J$$
(4.132)

Bernoulli assumption

The bending shear strains γ_{12} and γ_{13} in equation (4.125) are neglected, which gives

$$\vartheta_2 = -u_{3,1} + \frac{1}{2}u_{2,1}\vartheta_1 + u_{1,1}u_{3,1} \qquad \vartheta_3 = u_{2,1} + \frac{1}{2}u_{3,1}\vartheta_1 - u_{1,1}u_{2,1} \qquad (4.133)$$

By introducing the above equations into (4.125), the bending curvatures and torsional twist can be rewritten as

$$k_{1} = \vartheta_{1,1} + \frac{1}{2} \left(u_{3,1} u_{2,11} - u_{2,1} u_{3,11} \right)$$

$$k_{2} = -u_{2,11} + u_{1,11} u_{2,1} + u_{1,1} u_{2,11} - u_{3,11} \vartheta_{1} + c_{3} \alpha_{,1}$$

$$k_{3} = -u_{3,11} + u_{1,11} u_{3,1} + u_{1,1} u_{3,11} + u_{2,11} \vartheta_{1} - c_{2} \alpha_{,1}$$

$$(4.134)$$

Since the bending shear stresses are neglected, it appears logical to neglect the bi-shear F_{ω} also. Thus

$$F_{\omega} = \frac{\partial \Phi_A}{\partial \alpha} = 0 \tag{4.135}$$

where Φ_A is defined in equation (4.126). Introducing (4.127) and (4.128) into the above expression, gives

$$\alpha = k_1 \tag{4.136}$$

The integral (4.128) is then simplified under the form

$$\int_{A} \left[(2\varepsilon_{12})^2 + (2\varepsilon_{13})^2 \right] dA = J k_1^2$$
(4.137)

In order to avoid membrane locking, ε_{11} in equation (4.124) is rewritten as

$$\varepsilon_{11} = \varepsilon_{av} + x_2 k_2 + x_3 k_3 + \frac{1}{2} \left(r^2 - \frac{I_o}{A} \right) \vartheta_{1,1}^2 + \omega \alpha_{1,1}$$
 (4.138)

where the "average" value ε_{av} is given by

$$\varepsilon_{av} = \frac{1}{l_o} \int_{l_o} \left[u_{1,1} + \frac{1}{2} \left(u_{2,1}^2 + u_{3,1}^2 + \frac{I_o}{A} \vartheta_{1,1}^2 \right) \right] dx_1 \tag{4.139}$$

This gives

$$\int_{A} \varepsilon_{11}^{2} dA = A \varepsilon_{av}^{2} + I_{22} k_{2}^{2} + I_{33} k_{3}^{2} + \frac{1}{4} \left(I_{rr} - \frac{I_{o}^{2}}{A} \right) \vartheta_{1,1}^{4} + I_{\omega} \alpha_{,1}^{2}
+ 2 I_{23} k_{2} k_{3} + I_{2r} k_{2} \vartheta_{1,1}^{2} + I_{3r} k_{3} \vartheta_{1,1}^{2} + I_{\omega r} \alpha_{,1} \vartheta_{1,1}^{2} \quad (4.140)$$

4.3.2 Element types

Both Timoshenko and Bernoulli elements were developed in the present work. The Timoshenko elements are based on equations (4.125), (4.127) and (4.128), whereas the Bernoulli elements are based on (4.134), (4.137), (4.139) and (4.140). Both element types have been implemented by neglecting the nonlinear terms in the expressions of the curvatures k_1, k_2, k_3 and bending shear strains γ_{12}, γ_{13} . Extensive numerical testing has shown that this simplification has no effect whatsoever on the accuracy of the results; i.e. including these terms generates differences of less than 0.01% in the final results. On the other hand, certain tests have shown that the Wagner term $\frac{1}{2} r^2 \vartheta_{1,1}^2$ in the expression of ε_{11} can not be neglected or even be replaced by its average value $(\frac{1}{2} \frac{I_o}{A} \vartheta_{1,1}^2)$ over the cross-section.

4.3.3 Beams with thin-walled or open cross-sections

For beams with thin-walled or open cross-sections, warping effects are introduced through an additional degree of freedom at each node. The vector of local displacements is then given by

$$\mathbf{p}_{l}^{*} = \begin{bmatrix} \bar{u} & \bar{\boldsymbol{\vartheta}}_{1}^{\mathrm{T}} & \bar{\boldsymbol{\vartheta}}_{2}^{\mathrm{T}} & \alpha_{1} & \alpha_{2} \end{bmatrix}^{\mathrm{T}} \qquad \bar{\boldsymbol{\vartheta}}_{i}^{\mathrm{T}} = \begin{bmatrix} \vartheta_{1} & \vartheta_{2} & \vartheta_{3} \end{bmatrix}_{i} \quad i = 1, 2$$
(4.141)

The Timoshenko element tw3d, is implemented using linear interpolations for all variables, including the warping parameter α . The integrals in the strain energy expression are computed using a one point Gauss rule in order to avoid shear locking. Note that a linear interpolation scheme gives $u_2 \equiv u_3 \equiv 0$ since these displacements have zero values at the nodes of the beam due to the particular choice of the local system. Moreover, $u_{2,1} \equiv u_{3,1} \equiv 0$ and the only non-linear term in the expression of ε_{11} is the so-called Wagner term.

For the Bernoulli element bw3d, Vlasov's assumption is adopted, i.e.

$$\alpha_{,1} = \vartheta_{1,11} \tag{4.142}$$

which, since the non-linear terms in the expression of the curvatures are neglected, is the direct consequence of equation (4.136). Linear interpolation is used for the

axial displacement u, whereas Hermitian interpolations are used for u_2 and u_3 and for the axial rotation ϑ_1 . Note that in this case, the shallow arch terms $u_{2,1}^2$ and $u_{3,1}^2$ in the expression of ε_{11} , are non-zero.

4.3.4 Beams with solid or closed cross-sections

For such beams, the vector of local displacements is given by

$$\mathbf{p}_{l} = \begin{bmatrix} \bar{u} & \bar{\boldsymbol{\vartheta}}_{1}^{\mathrm{T}} & \bar{\boldsymbol{\vartheta}}_{2}^{\mathrm{T}} \end{bmatrix}^{\mathrm{T}} \tag{4.143}$$

The cross-section is assumed to be bi-symmetric, with \mathbf{r}_2 and \mathbf{r}_3 directed along the principal axes of the cross-section (see Figure 4.3). These assumptions give

$$I_{23} = I_{2r} = I_{3r} = I_{\omega r} = c_2 = c_3 = 0 (4.144)$$

The warping stresses are neglected and consequently the bi-shear F_{ω} and the bi-moment M_{ω} are set to zero

$$F_{\omega} = \frac{\partial \Phi_A}{\partial \alpha} = 0 \qquad M_{\omega} = \frac{\partial \Phi_A}{\partial \alpha_{,1}} = 0$$
 (4.145)

Introducing equations (4.127) and (4.128) in the above expressions, gives

$$\alpha = k_1 \qquad I_{\omega} \, \alpha,_1 = 0 \tag{4.146}$$

which are further substituted in the corresponding expressions of the strain energy. It should be noted here that if the cross-section is not bi-symmetric, the second of equation (4.146) is not valid; a more complicated equation is obtained.

The Timoshenko element t3d is implemented using linear interpolations for all variables and a one point Gauss rule. The element t3dl is obtained by keeping only linear terms in the strain expressions. This element is the classical two-node linear Timoshenko element.

The Bernoulli element b3d is implemented using linear interpolations for the axial displacement u and the axial rotation ϑ_1 and Hermitian interpolations for u_2 and u_3 . The classical linear Bernoulli element b3dl is obtained by considering only linear terms in the strain expressions.

4.4 Local element formulation in elasto-plasticity

The purpose of this section is to define the internal force vector \mathbf{f}_l (\mathbf{f}_l^* if warping effects are considered) and tangent stiffness matrix \mathbf{K}_l (\mathbf{K}_l^*) in local coordinates in case of elasto-plasticity. Assuming a von Mises material with isotropic hardening, Timoshenko elements are developed. Due to the material non-linearity, numerical integration over the cross-section is required, see the introduction of Chapter 3. The

constitutive equations are solved at each integration point by including interaction between the normal and shear stresses.

Assuming elasto-plastic material, \mathbf{f}_l and \mathbf{K}_l can be derived from the virtual work principle. If no volume or surface loads are acting on the element, this is written as

$$V = \int_{v} \delta \boldsymbol{\varepsilon}^{\mathrm{T}} \cdot \boldsymbol{\sigma} \, \mathrm{d}v = \delta \mathbf{p}_{l}^{\mathrm{T}} \, \mathbf{f}_{l}$$
 (4.147)

4.4.1 Strain definition

The strain definition and displacement field are the same as in the elastic case, see equations (4.117) and (4.118). However, in elasto-plasticity, the notion of shear center does not have any meaning, and the warping function $\bar{\omega}$ is not replaced by ω , see equation (4.119). As a matter of fact, due to the material non-linearity, the normality conditions (4.120) do not introduce any simplifications, as it was the case in elasticity. Equation (4.124) is then rewritten as

$$\varepsilon_{11} = \varepsilon_c + x_2 k_2 + x_3 k_3 + \frac{1}{2} r^2 \vartheta_{1,1}^2 + \bar{\omega} \alpha_{,1}
2 \varepsilon_{12} = \gamma_{12} + \bar{\omega}_{,2} \alpha - x_3 k_1
2 \varepsilon_{13} = \gamma_{13} + \bar{\omega}_{,3} \alpha + x_2 k_1$$
(4.148)

with

$$r^{2} = x_{2}^{2} + x_{3}^{2}$$

$$\varepsilon_{c} = u_{1,1} + \frac{1}{2} (u_{2,1}^{2} + u_{3,1}^{2})$$

$$k_{2} = -\vartheta_{3,1} + \frac{1}{2} (\vartheta_{1,1} \vartheta_{2} + \vartheta_{1} \vartheta_{2,1}) + u_{3,1} \vartheta_{1,1}$$

$$k_{3} = \vartheta_{2,1} + \frac{1}{2} (\vartheta_{1,1} \vartheta_{3} + \vartheta_{1} \vartheta_{3,1}) - u_{2,1} \vartheta_{1,1}$$

$$k_{1} = \vartheta_{1,1} + \frac{1}{2} (\vartheta_{2,1} \vartheta_{3} - \vartheta_{2} \vartheta_{3,1})$$

$$\gamma_{12} = u_{2,1} - \vartheta_{3} + \frac{1}{2} \vartheta_{1} \vartheta_{2} + u_{3,1} \vartheta_{1} - u_{1,1} \vartheta_{3}$$

$$\gamma_{13} = u_{3,1} + \vartheta_{2} + \frac{1}{2} \vartheta_{1} \vartheta_{3} - u_{2,1} \vartheta_{1} + u_{1,1} \vartheta_{2}$$

$$(4.149)$$

The warping function $\bar{\omega}(x_2, x_3)$ is defined within Saint-Venant torsion theory and refers to the centroid G. For arbitrary cross-section, $\bar{\omega}$ is determined numerically in a separate finite element analysis. The theoretical aspects of this computation are given in Appendix B. In the numerical examples presented in this thesis, isoparametric quadratic plane elements with four Gauss points are used to discretise cross-sections. It must be noted that within the Saint-Venant torsion theory, warping effects are assumed to be small and are therefore taken into account in a linearised way only [42]. Consequently, the warping function is determined by considering an elastic material and linear deformations. Although frequently used, this assumption is certainly debatable. However, even if the influence of plastic deformations

or finite displacements can be introduced by updating at each step the warping function [2, 103], in practice, this operation requires too much computational time.

4.4.2 Finite element formulation

A finite element formulation can be easily derived from equations (4.148) and (4.149). However, the numerical tests performed in the elastic range have shown that these expressions can be simplified without affecting the results by neglecting the non-linear terms in the expressions of the curvatures k_1, k_2, k_3 and bending shear strains γ_{12}, γ_{13} . With these simplifications, the strains can be rewritten as

$$\begin{array}{rcl} \varepsilon_{11} & = & u_{1,1} + \frac{1}{2} \left(u_{2,1}^2 + u_{3,1}^2 \right) - x_2 \, \vartheta_{3,1} + x_3 \, \vartheta_{2,1} + \frac{1}{2} \, r^2 \, \vartheta_{1,1}^2 + \bar{\omega} \, \alpha_{,1} \\ 2 \, \varepsilon_{12} & = & u_{2,1} - \vartheta_3 + \bar{\omega}_{,2} \, \alpha - x_3 \, \vartheta_{1,1} \\ 2 \, \varepsilon_{13} & = & u_{3,1} + \vartheta_2 + \bar{\omega}_{,3} \, \alpha + x_2 \, \vartheta_{1,1} \end{array} \tag{4.150}$$

which leads to a simple and computationally efficient local element.

The Bernoulli assumption $\alpha = \vartheta_1$, see section 4.3.1, can be introduced in equations (4.150), leading to elements based on the same hypotheses as bw3d and b3d (see Sections 4.3.3 and 4.3.4). However, the formulation of such elements in elasto-plasticity is computationally expensive and only Timoshenko elements will be considered in the remainder of this section.

4.4.3 Beams with thin-walled or open cross-sections

Based on the same assumptions as the elastic element tw3d, see Section 4.3.3, a Timoshenko element, called ptw3d is implemented. Thus, linear interpolations are used for all variables, including the warping parameter α . Note that a linear interpolation scheme gives $u_2 \equiv u_3 \equiv 0$ (and consequently $u_{2,1} \equiv u_{3,1} \equiv 0$) since these displacements have zero values at the nodes of the beam due to the particular choice of the local system. Consequently, the only geometrical non-linear term in the strain definition is the Wagner term $\frac{1}{2}r^2\vartheta_{1,1}^2$.

Differentiation of equation (4.150) gives

$$\delta \boldsymbol{\varepsilon} = \mathbf{A} \, \delta \hat{\boldsymbol{\varepsilon}} \qquad \hat{\boldsymbol{\varepsilon}} = \begin{bmatrix} u_{1,1} & \vartheta_3 & \vartheta_2 & \vartheta_{1,1} & \vartheta_{2,1} & \vartheta_{3,1} & \alpha & \alpha_{1} \end{bmatrix}^{\mathrm{T}} \tag{4.151}$$

with

$$\mathbf{A} = \begin{bmatrix} 1 & 0 & 0 & r^2 \vartheta_{1,1} & x_3 & -x_2 & 0 & \bar{\omega} \\ 0 & -1 & 0 & -x_3 & 0 & 0 & \bar{\omega}_{,2} & 0 \\ 0 & 0 & 1 & x_2 & 0 & 0 & \bar{\omega}_{,3} & 0 \end{bmatrix}$$
(4.152)

The virtual internal work in equation (4.147) can be rewritten as

$$V = \int_{v} \delta \boldsymbol{\varepsilon}^{\mathrm{T}} \cdot \boldsymbol{\sigma} \, \mathrm{d}v = \int_{l_{o}} \delta \hat{\boldsymbol{\varepsilon}}^{\mathrm{T}} \cdot \hat{\boldsymbol{\sigma}} \, \mathrm{d}x_{1}$$
 (4.153)

where l_o is the initial length of the element and $\hat{\sigma}$ is the vector of stress resultants defined by

$$\hat{\boldsymbol{\sigma}} = \int_{A} \mathbf{A}^{\mathrm{T}} \boldsymbol{\sigma} \, \mathrm{d}A \tag{4.154}$$

To avoid shear locking, the second integral in equation (4.153) is evaluated by one Gauss point integration. This gives

$$\int_{l_0} \delta \hat{\boldsymbol{\varepsilon}}^{\mathrm{T}} \cdot \hat{\boldsymbol{\sigma}} \, \mathrm{d}x_1 = \delta \mathbf{p}_l^{*\mathrm{T}} \, \mathbf{G}^{\mathrm{T}} \, \hat{\boldsymbol{\sigma}}$$
(4.155)

where \mathbf{p}_{l}^{*} is given in (4.141) and \mathbf{G} is defined by

$$\delta \hat{\boldsymbol{\varepsilon}} = \mathbf{G} \, \delta \mathbf{p}_l^* \tag{4.156}$$

From the choice of the interpolations, the matrix **G** is given as

The vector of internal forces \mathbf{f}_l^* in local coordinates is then given by

$$\mathbf{f}_{l}^{*} = \mathbf{G}^{\mathrm{T}} \,\hat{\boldsymbol{\sigma}} \tag{4.158}$$

where $\hat{\sigma}$ is the vector of stress resultants for the section at the middle of the element.

The local tangent stiffness matrix defined by $\delta \mathbf{f}_l^* = \mathbf{K}_l^* \delta \mathbf{p}_l^*$ can be calculated by differentiation of equation (4.158), which gives

$$\mathbf{K}_{l}^{*} = \mathbf{G}^{\mathrm{T}} \,\hat{\mathbf{D}} \,\mathbf{G} \qquad \delta \hat{\boldsymbol{\sigma}} = \hat{\mathbf{D}} \,\delta \hat{\boldsymbol{\varepsilon}} \tag{4.159}$$

The matrix $\hat{\mathbf{D}}$ can be obtained by taking the variations of (4.154)

$$\delta \hat{\boldsymbol{\sigma}} = \int_{A} \left[\mathbf{A}^{\mathrm{T}} \, \delta \boldsymbol{\sigma} + \delta (\mathbf{A}^{\mathrm{T}} \, \boldsymbol{\sigma}) \right] \, \mathrm{d}A = \int_{A} \left[\mathbf{A}^{\mathrm{T}} \, \mathbf{C}_{ct} \, \mathbf{A} + \mathbf{L} \right] \, \mathrm{d}A \, \, \delta \hat{\boldsymbol{\varepsilon}}$$
(4.160)

where \mathbf{C}_{ct} is the consistent tangent operator defined by $\delta \boldsymbol{\sigma} = \mathbf{C}_{ct} \, \delta \boldsymbol{\varepsilon}$ and \mathbf{L} is obtained from $\delta(\mathbf{A}^T \boldsymbol{\sigma})$ with $\boldsymbol{\sigma}$ maintained constant during the differentiation. Hence, the only non zero term in the matrix \mathbf{L} is

$$\mathbf{L}_{4,4} = r^2 \,\sigma_{11} \tag{4.161}$$

Finally, $\hat{\sigma}$ and $\hat{\mathbf{D}}$ are calculated trough a numerical integration over the cross-section, by using the same mesh as for the determination of the warping function. Hence, the cross-section is discretised using isoparametric quadratic elements and integration over each of these elements is performed using 4 Gauss points. At each point, the constitutive equations are solved iteratively using a backward Euler scheme [23], which allows the generation of a consistent tangent operator \mathbf{C}_{ct} .

The constitutive equations for a 3D beam are derived from the von Mises equations in three dimensions [23] by setting

$$\sigma_{22} = \sigma_{33} = \sigma_{23} = 0 \tag{4.162}$$

By performing a similar work as in Section 3.4.4 for the 2D beam case, it can be shown that the Backward-Euler algorithm and consistent tangent operator are similar to those given in Figure 3.4 and equation (3.93) with

$$\boldsymbol{\varepsilon} = \begin{bmatrix} \varepsilon_{11} \\ 2 \varepsilon_{12} \\ 2 \varepsilon_{13} \end{bmatrix} \qquad \boldsymbol{\sigma} = \begin{bmatrix} \sigma_{11} \\ \sigma_{12} \\ \sigma_{13} \end{bmatrix} \qquad \mathbf{C} = \begin{bmatrix} E & 0 & 0 \\ 0 & G & 0 \\ 0 & 0 & G \end{bmatrix}$$
(4.163)

$$f = (\sigma_{11}^2 + 3\sigma_{12}^2 + 3\sigma_{13}^2)^{1/2} - \sigma_o(\varepsilon_{ps}) = \sigma_e - \sigma_o(\varepsilon_{ps})$$
(4.164)

$$\mathbf{a} = \frac{1}{\sigma_e} \begin{bmatrix} \sigma_{11} \\ 3\sigma_{12} \\ 3\sigma_{13} \end{bmatrix} \qquad \frac{\partial \mathbf{a}}{\partial \boldsymbol{\sigma}} = \frac{3}{\sigma_e^3} \begin{bmatrix} \sigma_{12}^2 + \sigma_{13}^2 & -\sigma_{11}\sigma_{12} & -\sigma_{11}\sigma_{13} \\ -\sigma_{11}\sigma_{12} & \sigma_{11}^2 + 3\sigma_{13}^2 & -3\sigma_{12}\sigma_{13} \\ -\sigma_{11}\sigma_{13} & -3\sigma_{12}\sigma_{13} & \sigma_{11}^2 + 3\sigma_{12}^2 \end{bmatrix}$$
(4.165)

4.4.4 Beams with solid or closed cross-section

For beams with solid or closed cross-sections, warping stresses can be neglected. Assuming a bi-symmetric cross-section, it has been shown in Section 4.3.4 that the local finite element formulation is obtained by introducing in equations (4.150) to (4.157) the constraints

$$\alpha = \vartheta_{1,1} \qquad \alpha_{1} = 0 \tag{4.166}$$

Hence, $\hat{\boldsymbol{\varepsilon}}$ and \mathbf{A} , see equations (4.151) and (4.152), are rewritten as

$$\hat{\boldsymbol{\varepsilon}} = \begin{bmatrix} u_{1,1} & \vartheta_3 & \vartheta_2 & \vartheta_{1,1} & \vartheta_{2,1} & \vartheta_{3,1} \end{bmatrix}^{\mathrm{T}}$$

$$(4.167)$$

and

$$\mathbf{A} = \begin{bmatrix} 1 & 0 & 0 & r^2 \vartheta_{1,1} & x_3 & -x_2 \\ 0 & -1 & 0 & \bar{\omega}_{,2} - x_3 & 0 & 0 \\ 0 & 0 & 1 & \bar{\omega}_{,3} + x_2 & 0 & 0 \end{bmatrix}$$
(4.168)

The internal force vector \mathbf{f}_l and tangent stiffness matrix \mathbf{K}_l are then obtained by a procedure similar to the one described in Section 4.4.3. This element is called pt3d.

4.5 Applied loads

The aim of the present section is to discuss two aspects related to the applied external loads. The first one refers to the modelling of eccentrically applied forces. The second refers to the applied external moments, in the context of the re-parameterisation of finite rotations advocated in Section 4.2.5.

4.5.1 Eccentric forces

Assume that the vector of external forces \mathbf{f}_{ex1} is applied at node I, and that node I is rigidly connected to node 1 through the eccentricity vector \mathbf{v}_o , defined by

$$\mathbf{x}_{1}^{g} = \mathbf{x}_{1}^{g} + \mathbf{v}_{o} \qquad \mathbf{u}_{1}^{g} = \mathbf{u}_{1}^{g} + (\mathbf{R}_{1}^{g} - \mathbf{I}) \ \mathbf{v}_{o} \qquad \mathbf{R}_{1}^{g} = \mathbf{R}_{1}^{g}$$
 (4.169)

where \mathbf{x}_1^g and \mathbf{x}_I^g denote the position vectors of nodes 1 and I in the original undeformed configuration.

The modelling of such a situation can be performed in two ways. The first one consists of a change of variables from \mathbf{u}_{1}^{g} to \mathbf{u}_{1}^{g} , as developed in Section 4.2.4. The second one requires a transformation of \mathbf{f}_{ex1} into \mathbf{f}_{ex1} , which can be obtained by considering that both forces must perform the same virtual external work

$$\delta \mathbf{p}_{\mathbf{I}}^{g \, \mathrm{T}} \, \mathbf{f}_{ex \, \mathbf{I}} = \delta \mathbf{p}_{\mathbf{I}}^{g \, \mathrm{T}} \, \mathbf{f}_{ex \, \mathbf{I}} \tag{4.170}$$

with

$$\delta \mathbf{p}_{\mathrm{I}}^{g} = \left[\delta \mathbf{u}_{\mathrm{I}}^{g \, \mathrm{T}} \, \delta \boldsymbol{\theta}_{1}^{g \, \mathrm{T}} \right]^{\mathrm{T}} \qquad \delta \mathbf{p}_{1}^{g} = \left[\delta \mathbf{u}_{1}^{g \, \mathrm{T}} \, \delta \boldsymbol{\theta}_{1}^{g \, \mathrm{T}} \right]^{\mathrm{T}} \tag{4.171}$$

Similar calculations as in Section 4.2.4 give

$$\mathbf{f}_{ex\,1} = \mathbf{B}_{ef}^{\mathrm{T}} \mathbf{f}_{ex\,\mathrm{I}} \qquad \mathbf{B}_{ef} = \begin{bmatrix} \mathbf{I} & -\tilde{\mathbf{v}} \\ \mathbf{0} & \mathbf{I} \end{bmatrix} \qquad \mathbf{v} = \mathbf{R}_{1}^{g} \mathbf{v}_{o}$$
 (4.172)

In addition, differentiation of equation (4.170) gives the stiffness correction

$$\mathbf{K}_{ef} = \begin{bmatrix} \mathbf{0} & \mathbf{0} \\ \mathbf{0} & \tilde{\mathbf{n}}_{\mathrm{I}} \tilde{\mathbf{v}} \end{bmatrix} \qquad \mathbf{f}_{ex\,\mathrm{I}} = \begin{bmatrix} \mathbf{n}_{\mathrm{I}} \\ \mathbf{m}_{\mathrm{I}} \end{bmatrix}$$
(4.173)

which must be subtracted from the tangent stiffness matrix of the structure. It should also be noted here that, equations (4.172) and (4.173) are consistent with spatial angular variations. A different choice of finite rotation parameters will then require a further transformation of these equations, cf. Section 4.2.5.

4.5.2 External moments

Consider that at node i, an external moment \mathbf{m}_{θ} performs the virtual work $\delta \boldsymbol{\theta}_{i}^{g \mathrm{T}} \mathbf{m}_{\theta}$, with $\delta \boldsymbol{\theta}_{i}^{g}$ representing spatial angular variations. This means that if a parameterisations in terms of the total rotational vector $\boldsymbol{\Psi}_{i}^{g}$ is adopted, \mathbf{m}_{θ} should be accordingly

transformed into \mathbf{m}_{Ψ} in order to represent the same physical problem. By considering that both moments must perform the same virtual external work, it is obtained

$$\delta \boldsymbol{\theta}_{i}^{g \, \mathrm{T}} \, \mathbf{m}_{\theta} = \delta \boldsymbol{\Psi}_{i}^{g \, \mathrm{T}} \, \mathbf{m}_{\Psi} \tag{4.174}$$

which, by using equation (4.11) leads to

$$\mathbf{m}_{\Psi} = \mathbf{T}_{s}^{\mathrm{T}}(\Psi) \,\mathbf{m}_{\theta} \tag{4.175}$$

Differentiating the above equation gives the stiffness correction

$$\mathbf{K}_{\Psi} = \frac{\partial}{\partial \mathbf{\Psi}} \left[\mathbf{T}_{s}^{\mathrm{T}}(\mathbf{\Psi}) \, \mathbf{m}_{\theta} \right] \tag{4.176}$$

which must be subtracted from the tangent stiffness matrix. The expression of \mathbf{K}_{Ψ} is given in equation (4.108). If a parameterisation in terms of the incremental rotation vector is adopted, the required transformations are obtained by replacing Ψ_i^g with Θ_i^g in equations (4.175) and (4.176). These aspects will be further discussed in connection with one of the numerical examples where it is shown that if the above transformations are not applied, the three parameterisations discussed in the paper will produce totally different results. Note however that, if the moment is applied at a point which is constrained to rotate around a fixed axis, \mathbf{T}_s reduces to the identity matrix and the above transformations are no longer necessary.

Chapter 5

Path following techniques

Concerning non-critical paths, the Newton-Raphson method, preceded by an Euler forward predictor is chosen to solve the equilibrium equations at each step. In most of commercial codes, the length of the step is defined by adding an arc-length equation (see e.g. [23]) to the equilibrium equations. In this thesis, a displacement or load control strategy has been adopted. The procedure for computing non-critical paths is described at both structural and element levels in Section 5.1.

Since the purpose of the elements described in this thesis is the study of elastic and elasto-plastic instability phenomena, special procedures are needed in order to first detect and isolate bifurcation points along fundamental equilibrium paths and then to perform branch-switching to secondary paths.

This approach is different to the one usually adopted in commercial finite element codes. In these programs, the bifurcation loads are often evaluated by a linearised buckling analysis based on the equation

$$(\mathbf{K}_1 + \omega \,\Delta \mathbf{K}) \,\boldsymbol{\phi}_{cr} = \mathbf{0} \qquad \Delta \mathbf{K} = \mathbf{K}_2 - \mathbf{K}_1 \tag{5.1}$$

where \mathbf{K}_1 and \mathbf{K}_2 are the tangent stiffness matrices of two known equilibrium points on the fundamental path of the perfect structure. The buckling load factor λ_{cr} is then calculated by

$$\lambda_{cr} = \lambda_1 + \omega \, \Delta \lambda \qquad \Delta \lambda = \lambda_2 - \lambda_1 \tag{5.2}$$

where λ_1 , λ_2 are the load factors of the two known equilibrium points.

This approach assumes a linear relation between the increment of the geometric stiffness matrix (assumed to be $\Delta \mathbf{K}$) and the increment of the load factor $\Delta \lambda$. This assumption is satisfied when the pre-buckling displacements are sufficiently small so that the shape of the stress distribution remains unchanged and only the stress levels change with the factor λ . If this condition is not respected, a linearised buckling analysis gives more or less inaccurate results.

As regard the post-bifurcation behaviour, this is normally investigated in commercial codes by introducing small imperfections in the geometry or the loading of the structure. However, apart from the difficulties related to the choice of the form and

the magnitude of these imperfections, such an approach does not allow a complete understanding of the instability phenomenon.

Thus, the main purpose of the procedures developed in this chapter is to isolate bifurcation points and to study post-critical behaviour of the perfect structure, i.e. without introducing any imperfections.

In elasticity, branch-switching is performed classically, using the mode injection method. This procedure consists of taking as predictor for the secondary path the eigenvector associated to the zero eigenvalue of the tangent stiffness matrix at the bifurcation point. The main innovation of this thesis resides in a new numerical approach for the direct computation of critical points. This procedure, which can also handle limit points, is explained in detail in Section 5.2.

In elasto-plasticity, numerical analyses of buckling problems are not so common in the literature. This is probably due to the fact that the instability phenomenon in itself is more complicated. Taking as starting point the theoretical bases presented in Chapter 2, the purpose of Section 5.3 is to describe and discuss the advantages and drawbacks of two different branch-switching procedures.

5.1 Non-critical equilibrium path

5.1.1 Procedure at the structural level

The discretised structure has n degrees of freedom. The values of the n components of the displacement vector \mathbf{d} and the load factor λ have to be calculated.

The n non-linear equilibrium equations can be written as

$$\mathbf{f}\left(\mathbf{d},\mathcal{H}\right) - \mathbf{f}_{ex}\left(\lambda\right) = \mathbf{0} \tag{5.3}$$

where \mathbf{f} are the internal forces. In case of elasto-plasticity, \mathbf{f} depends on the history of the deformations, which is represented by the parameter \mathcal{H} . The external load vector \mathbf{f}_{ex} is assumed to be conservative and proportional (dead loading) and can be written in the form

$$\mathbf{f}_{ex}(\lambda) = \lambda \,\mathbf{p} + \mathbf{p}^{\,p} \tag{5.4}$$

where \mathbf{p} and \mathbf{p}^p are two constant vectors. \mathbf{p} represents the main load while \mathbf{p}^p stands for a small constant perturbation load which can be applied in order to introduce imperfections.

Under load control, a load increment $\Delta \bar{\lambda} = \lambda - \bar{\lambda}$ is applied at each step and the auxiliary equation

$$g(\lambda) = \lambda - \bar{\lambda} = 0 \tag{5.5}$$

is added to the system (5.3). Under displacement control, a displacement increment $\Delta \bar{d}_i = d_i - \bar{d}_i$ is applied at each step and the auxiliary equation becomes

$$q\left(\mathbf{d}\right) = d_i - \bar{d}_i = 0 \tag{5.6}$$

which implies that the value of the i th displacement d_i is constrained to \bar{d}_i .

In order to simplify the notations, the auxiliary equations (5.5) and (5.6) are expressed in the same form as

$$q\left(\mathbf{d},\lambda\right) = 0\tag{5.7}$$

The system of equations (5.3) and (5.7) is solved by Newton-Raphson iterations preceded by an Euler forward step.

The differential matrix required in this procedure is given by

$$\begin{bmatrix} \mathbf{K} & -\mathbf{p} \\ g, \mathbf{d} & g, \lambda \end{bmatrix} \begin{bmatrix} \Delta \mathbf{d} \\ \Delta \lambda \end{bmatrix} = - \begin{bmatrix} \mathbf{f} (\mathbf{d}, \mathcal{H}) - \mathbf{f}_{ex} (\lambda) \\ g (\mathbf{d}, \lambda) \end{bmatrix}$$
(5.8)

where \mathbf{K} is the tangent stiffness matrix.

The vector t tangent to the path at a non-critical equilibrium point is given by

$$\mathbf{t} = \begin{bmatrix} \mathbf{K}^{-1} \, \mathbf{p} \\ 1 \end{bmatrix} \tag{5.9}$$

The Euler forward predictor is defined under displacement control by

$$\begin{bmatrix} \Delta \mathbf{d} \\ \Delta \lambda \end{bmatrix} = \frac{\Delta \bar{d}_i}{t_i} \mathbf{t} \tag{5.10}$$

and under load control by

$$\begin{bmatrix} \Delta \mathbf{d} \\ \Delta \lambda \end{bmatrix} = \Delta \bar{\lambda} \mathbf{t} \tag{5.11}$$

Remarks

- In order to avoid numerical problems during the iteration process, the magnitude of the vector \mathbf{p} is chosen such that $\Delta \lambda$ has the same order of magnitude as the Δd_i , i = 1..n.
- To calculate the whole equilibrium path, it is often necessary to switch between different controls (e.g. in case of snap-throughs or snap-backs). An automatic solution is to take as control parameter in each step the largest component of the tangent vector **t**.

5.1.2 Procedures at the element level

The purpose of this section is to summarise the procedure for computing at the level of the element the internal force vector \mathbf{f}_g and tangent stiffness matrix \mathbf{K}_g in global coordinates. These procedures have been described in detail in Chapters 3 and 4.

Elastic case

- 1. The local displacements \mathbf{p}_l are extracted from the global ones \mathbf{p}_g .
- 2. The local internal force vector \mathbf{f}_l and tangent stiffness matrix \mathbf{K}_l are functions of the local displacements \mathbf{p}_l and are computed using the Maple subroutines given in Appendix A.
- 3. Finally, the global internal force vector \mathbf{f}_g and tangent stiffness matrix \mathbf{K}_g are obtained using the transformation matrices.

Elasto-plastic case

Steps 1 and 3 are identical in elasticity and elasto-plasticity. As a matter of fact, these steps depend only on the definition of the co-rotational framework and are independent on the deformations. The difference between the two material cases lies in the computation of \mathbf{f}_l and \mathbf{K}_l . In elasto-plasticity, due to the non-linear relationship between the strains and the stresses, \mathbf{f}_l and \mathbf{K}_l cannot be calculated only from the current local displacements \mathbf{p}_l . A more complicated procedure, taking into account the history of the deformation process, has to be implemented.

In the following the subscript o refers to old known values at the last equilibrium state while the subscript n refers to new values at the current iteration.

Step 2.

• The current strains ε_n are calculated at each integration point from the local displacements \mathbf{p}_l . In order to avoid spurious numerical unloading, an incremental strategy is adopted. This means that the strains increment $\Delta\varepsilon$ at each integration point is defined by reference to the last converged equilibrium state and is calculated using the strains at the beginning of the increment ε_o by

$$\Delta \varepsilon = \varepsilon_n - \varepsilon_o \tag{5.12}$$

• The current stresses σ_n , equivalent plastic strain ε_{psn} and consistent tangent operator \mathbf{C}_{ct} (\hat{E} for 2D Bernoulli elements) are calculated at each integration point by solving the constitutive equations

$$(\boldsymbol{\sigma}_n, \varepsilon_{psn}, \mathbf{C}_{ct}) = f(\boldsymbol{\sigma}_o, \varepsilon_{pso}, \Delta \boldsymbol{\varepsilon})$$
 (5.13)

• \mathbf{f}_l and \mathbf{K}_l are then computed through numerical integration over the element.

Remark

This procedure requires to save at each integration point the stresses σ_o , the strains ε_o and the equivalent plastic strain ε_{pso} obtained at the last equilibrium state. However, in order to save memory space, it has been chosen to save the local displacements \mathbf{p}_l at the beginning of the step and to recalculate at each iteration the strains ε_o , which is a simple operation. This is particularly interesting for 3D beam elements for which an important number of integration points are required.

5.2 Direct computation of elastic critical points

The simplest and most general method to isolate critical points along an equilibrium path is to perform successive bisections by monitoring the number of negative eigenvalues of the tangent stiffness matrix at each equilibrium point. However, this approach is not efficient since it requires the calculation of many intermediate equilibrium points. A more efficient method can be developed on the basis of an extended system obtained by augmenting the equilibrium equations with a criticality condition which forces the Newton-Raphson iterations to converge to the critical point. Thus, once a critical point has been detected along an equilibrium path within a load increment, its isolation is performed in only one step. Following the work of Wriggers et al. [104, 105], a vectorial form of the criticality condition is the most popular choice in this context.

The alternative presented in this section is based on two new ideas. First, following Eriksson [32–34], the criticality condition is expressed by a scalar equation, thus keeping the size of the extended system to a minimum. The main problem of the direct computation of critical points based on extended systems is that convergence is not assured in all cases, specially if the pre-buckling deformations are non-linear. Then, in order to improve the convergence properties, a second modification is introduced. This consists of combining iterations based on the extended system with iterations based on equilibrium equations under load or displacement control.

The outline of this section is as follows. First, the classical method of Wriggers et al. [104, 105] is briefly summarised. Next the alternative extended system and its solution is presented. Finally, the whole procedure and its initialisation is described.

5.2.1 Classical approach

The purpose of this section is to briefly summarise the classical approach developed by Wriggers et al. [104, 105].

Using the property that the tangent stiffness matrix **K** possesses a zero eigenvalue at a critical point, the vectorial critical condition $\mathbf{K} \phi = \mathbf{0}$ is added to the equilibrium

equations. The system of non-linear equations becomes

$$\begin{pmatrix} \mathbf{f}(\mathbf{d}) - \lambda \mathbf{p} \\ \mathbf{K}(\mathbf{d}) \boldsymbol{\phi} \\ \|\boldsymbol{\phi}\| - 1 \end{pmatrix} = \mathbf{0}$$
 (5.14)

where \mathbf{f} denotes the vector of internal forces, \mathbf{d} the displacement vector, λ the load factor, \mathbf{p} the reference load vector and $\boldsymbol{\phi}$ the critical eigenvector. Note, once again, that in the above system and in all this chapter, the reference load vector \mathbf{p} is assumed constant (dead loading).

The solution to the extended system (5.14) is obtained through a full Newton-Raphson procedure. The differential matrix required in this procedure is given by

$$\begin{bmatrix} \mathbf{K} & -\mathbf{p} & \mathbf{0} \\ (\mathbf{K}\boldsymbol{\phi}),_{\mathbf{d}} & \mathbf{0} & \mathbf{K} \\ \mathbf{0} & 0 & \boldsymbol{\phi}^{\mathrm{T}}/\|\boldsymbol{\phi}\| \end{bmatrix} \begin{bmatrix} \Delta \mathbf{d} \\ \Delta \lambda \\ \Delta \boldsymbol{\phi} \end{bmatrix} = - \begin{bmatrix} \mathbf{f}(\mathbf{d}) - \lambda \mathbf{p} \\ \mathbf{K}\boldsymbol{\phi} \\ \|\boldsymbol{\phi}\| - 1 \end{bmatrix}$$
(5.15)

The above systems contains 2n + 1 equations and unknowns (n is the number of active degrees of freedom). However, due to its particular form, it can be shown (see e.g. [105]) that its solution can be performed by factorising only the tangent stiffness matrix \mathbf{K} . Consequently, compared to a classical iteration of the equilibrium equations with n unknowns, only a small increase of computational time is needed.

5.2.2 Alternative extended system

The procedure for the direct computation of critical points based on an alternative extended system is now presented. This approach, developed by Eriksson [32–34] in the context of fold line evaluation algorithms, makes use of a scalar criticality condition.

Extended system

The vectorial criticality condition $\mathbf{K} \phi = \mathbf{0}$ is replaced by the scalar equation

$$g(\mathbf{d}) = \boldsymbol{\phi}^{\mathrm{T}} \mathbf{K} \, \boldsymbol{\phi} = 0 \tag{5.16}$$

in which g represents the lowest (in absolute value) eigenvalue of the tangent stiffness matrix \mathbf{K} and $\boldsymbol{\phi}$ its associated eigenvector. At a critical point, \mathbf{K} is singular and the condition g=0 is obtained. The eigenvector $\boldsymbol{\phi}$ is normalised according to

$$\boldsymbol{\phi}^{\mathrm{T}} \, \boldsymbol{\phi} = 1 \tag{5.17}$$

g and ϕ are determined in a separate procedure, based on the iterative sequence

$$\begin{bmatrix} \boldsymbol{\phi}^{(i+1)} \\ g^{(i+1)} \end{bmatrix} = \begin{bmatrix} -\mathbf{K} & \boldsymbol{\phi}^{(i)} \\ \boldsymbol{\phi}^{(i)} & 0 \end{bmatrix}^{-1} \begin{bmatrix} \mathbf{0} \\ 1 \end{bmatrix}$$
 (5.18)

This system, which is obtained from equations (5.16) and (5.17), can be viewed as one step of an inverse subspace iteration. Note that any random vector can be used to initiate the process and convergence is usually obtained in very few iterations.

Using equation (5.16), the extended system can be written as

$$\begin{pmatrix} \mathbf{f}(\mathbf{d}) - \lambda \mathbf{p} \\ g(\mathbf{d}) \end{pmatrix} = \mathbf{0} \tag{5.19}$$

The solution to the extended system (5.19) is obtained through a full Newton-Raphson procedure. The differential matrix required in this procedure is given by

$$\begin{bmatrix} \mathbf{K} & -\mathbf{p} \\ g, \mathbf{d} & 0 \end{bmatrix} \begin{bmatrix} \Delta \mathbf{d} \\ \Delta \lambda \end{bmatrix} = - \begin{bmatrix} \mathbf{f}(\mathbf{d}) - \lambda \mathbf{p} \\ g(\mathbf{d}) \end{bmatrix}$$
 (5.20)

The vector $g_{,\mathbf{d}}$ is evaluated numerically by using a finite difference formula (for details see [32, 104])

$$g_{,\mathbf{d}} \approx \frac{\boldsymbol{\phi}^{\mathrm{T}}}{\gamma} \left[\mathbf{K} (\mathbf{d} + \gamma \, \boldsymbol{\phi}) - \mathbf{K} (\mathbf{d}) \right]$$
 (5.21)

where γ is a numerical parameter taken as

$$\gamma = \max_{1 < i < n} ||d_i|| \times 10^{-6} \tag{5.22}$$

with d_i denoting the *i* th component of **d**. Numerical tests have shown that the procedure is not sensitive to the choice of the exponent coefficient in equation (5.22), i.e. any values in the interval $[10^{-8} \ 10^{-3}]$ can also be chosen.

In some works [52, 105], the directional derivative of the tangent stiffness matrix in equation (5.21) is performed analytically. For the co-rotational elements, this approach seems difficult to apply and would require additional developments.

Efficient numerical scheme

The numerical approach described in this section requires the solution of two sets of equations: at each iteration of the extended system (5.20), the system (5.18) must be solved in order to compute g. The solution procedures for these two systems are given in Tables 5.1 and 5.2. As it can be seen, the only matrix which needs to be factorised is \mathbf{K} . Consequently, compared to a classical iteration involving only the equilibrium equations, just a small increase in computational work is required. The additional expense is due to one loop over the elements for the evaluation of g, one back substitution step for the computation of $\Delta \mathbf{d}_2$ and one or two back substitution steps for the solution of (5.18). Hence, compared to the classical approach in [52,105], the solution of the present system requires about the same computational time.

Table 5.1: Solution of system (5.18).

Solve
$$\mathbf{K}\,\boldsymbol{\psi} = \boldsymbol{\phi}^{(i)}$$
 Calculate new values
$$g = \frac{1}{\boldsymbol{\phi}^{(i)\,\mathrm{T}}\,\boldsymbol{\psi}} \quad \boldsymbol{\phi}^{(i+1)} = \boldsymbol{\psi}\,g$$

Table 5.2: Solution of system (5.20).

Solve
$$\mathbf{K} \Delta \mathbf{d}_1 = \mathbf{p} \quad \mathbf{K} \Delta \mathbf{d}_2 = -(\mathbf{f}(\mathbf{d}) - \lambda \mathbf{p})$$

Calculate $g_{,\mathbf{d}}$ within a loop over all elements

Calculate new values $\Delta \lambda = -\frac{g + g_{,\mathbf{d}} \Delta \mathbf{d}_2}{g_{,\mathbf{d}} \Delta \mathbf{d}_1} \quad \Delta \mathbf{d} = \Delta \mathbf{d}_1 \Delta \lambda + \Delta \mathbf{d}_2$

5.2.3 Modified algorithm

The main problem of the direct computation of critical points based on extended systems is that convergence is not assured if the non-linearity between the starting equilibrium point for the iterations and the critical one is too high. As a matter of fact, during the iterative process, the matrix K does not correspond to an equilibrium point and it may not be reliable to use the properties of K in order to reach the critical point.

In this context, the numerical tests performed by the author have shown that the classical approach of Wriggers (Section 5.2.1) has better performances than the alternative presented in Section 5.2.2. As a matter of fact, in the original formulation, the critical condition is depending on both \mathbf{d} and $\boldsymbol{\phi}$, which means that at each iteration both \mathbf{d} and $\boldsymbol{\phi}$ are iteratively updated. On the contrary, in the alternative proposed in this thesis, the critical condition depends only on \mathbf{d} and $\boldsymbol{\phi}$ is recalculated at each iteration as the eigenvector associated to the lowest eigenvalue of \mathbf{K} . This constraint on $\boldsymbol{\phi}$, not present in the original approach, makes the procedure more sensitive to the variations of \mathbf{K} .

It has also been observed numerically that the first iteration of the extended systems (5.15) or (5.20), based on a \mathbf{K} corresponding to an equilibrium point, often gives very good approximations to the bifurcation load factors. On the contrary, the following iterations, based on a \mathbf{K} which does not correspond to an equilibrium point, give less accurate approximations to the bifurcation load factors, specially in case of high non-linearity.

Following these considerations, the algorithm presented in the previous section has been modified in order to improve its convergence properties. For that, a distinction

between bifurcation and limit points is required.

Bifurcation points

The idea of this new approach, whose algorithm is given in Table 5.3, is to evaluate at the end of each iteration g_{new} , the absolutely lowest eigenvalue of the tangent stiffness matrix. If $||g_{\text{new}}||$ is lower than the previous value $||g_{\text{old}}||$ or if the current point is in equilibrium, then the next iteration will use the extended system (5.20). In the opposite case, the information given by the critical condition may not be reliable. It is then better to perform an iteration using the equilibrium equations under load control in order to obtain a point nearer an equilibrium state, and consequently, a more reliable \mathbf{K} matrix for expressing the critical condition.

Another effect of this modification is that some iterations performed using the extended system (5.20) are replaced by pure equilibrium iterations which require less computational work.

Limit points

The procedure described in Table 5.3 is not suitable for the isolation of limit points since the equilibrium iterations based on a load control may fail in the neighbourhood of a limit point. The solution, see Table 5.4, is then to perform equilibrium iterations under displacement instead of load control. The degree of freedom corresponding to the largest component of the tangent vector (computed by $\mathbf{K}^{-1}\mathbf{p}$) at the starting equilibrium point for the procedure is taken as control.

This method can also be used for the isolation of bifurcation points. However, the numerical tests performed by the author have shown that the convergence properties of the procedure are better if a load control is adopted. It can also be noted that the author has also tested different arc-length procedures as substitution of the load and displacement controls, without obtaining better results for the tested examples.

It appears then judicious, but not absolutely necessary, to have two different isolation procedures, one for bifurcation points and one for limit points. In practice, this is scarcely a problem since such a distinction is also required at the level of the initial values of the procedure. This issue will be addressed in the next subsection.

5.2.4 Initialisation

Along a solution branch, the detection of critical points is performed by monitoring at each converged equilibrium state the number of negative eigenvalues of \mathbf{K} . This can e.g. be performed efficiently by a $\mathbf{LDL}^{\mathrm{T}}$ -factorisation. Once a critical point has been detected within an increment, it is isolated by taking as starting point the left or right bound of the increment. For that point, initial values g_o and ϕ_o are needed.

Table 5.3: Modified algorithm – bifurcation points.

initial values :
$$\mathbf{d} \ \lambda \ \mathbf{K} \ g_o \ \phi_o$$
 first iteration : solve $(5.20) \rightarrow \mathbf{d} = \mathbf{d} + \Delta \mathbf{d} \quad \lambda = \lambda + \Delta \lambda$ assemble \mathbf{K} and $\mathbf{r} = \mathbf{f}(\mathbf{d}) - \lambda \mathbf{p}$ solve $(5.18) \rightarrow g_{\text{new}} \ \phi_{\text{new}}$ $g_{\text{old}} = g_o \ \phi_{\text{old}} = \phi_o$ loop : while $\|g_{\text{new}}\| > tol$ or $\|\mathbf{r}\| > tol$ if $\|g_{\text{new}}\| < \|g_{\text{old}}\|$ or $\|\mathbf{r}\| < tol$ $g_{\text{old}} = g_{\text{new}} \ \phi_{\text{old}} = \phi_{\text{new}}$ solve $(5.20) \rightarrow \mathbf{d} = \mathbf{d} + \Delta \mathbf{d} \ \lambda = \lambda + \Delta \lambda$ else solve $\mathbf{K} \Delta \mathbf{d} = -\mathbf{r} \ \rightarrow \mathbf{d} = \mathbf{d} + \Delta \mathbf{d}$ end assemble \mathbf{K} and $\mathbf{r} = \mathbf{f}(\mathbf{d}) - \lambda \mathbf{p}$ solve $(5.18) \rightarrow g_{\text{new}} \ \phi_{\text{new}}$ end

Table 5.4: Partial modified algorithm – limit points.

else solve
$$\begin{cases} \mathbf{K} \Delta \mathbf{d} - \Delta \lambda \mathbf{p} = -\mathbf{r} \\ \Delta d_i = 0 \end{cases} \rightarrow \begin{cases} \mathbf{d} = \mathbf{d} + \Delta \mathbf{d} \\ \lambda = \lambda + \Delta \lambda \end{cases}$$
 end

If a bifurcation point is expected, g_o is given by the $\mathbf{LDL}^{\mathrm{T}}$ -factorisation and is taken as the lowest negative or positive eigenvalue, depending on the choice of the starting point. Usually, only one critical point is situated in the neighbourhood of the initial point and g_o is the lowest absolute eigenvalue. ϕ_o , which is the eigenvector associated

to g_o , can then be computed using the system (5.18). For that, any random vector can be used to initiate the iterations and convergence is usually obtained in two or three iterations, due to the favourable spectral properties of \mathbf{K} close to the critical point. However, if several critical points are situated in the neighbourhood of the initial point, g_o may not be the lowest absolute eigenvalue, and ϕ_o must be calculated using a more elaborate method.

If a limit point is expected, the lowest negative or positive eigenvalue and its associated eigenvector may not be a judicious choice for g_o and ϕ_o , especially if the initial point is far from the critical one. A better choice is to take for ϕ_o the tangent vector to the equilibrium path, which gives

$$\phi_o = \mathbf{K}^{-1} \mathbf{p} \qquad g_o = \phi_o^{\mathrm{T}} \mathbf{K} \phi_o$$
 (5.23)

5.3 Branch-switching in elasto-plasticity

The physical and theoretical aspects of plastic instability phenomena have been discussed in Chapter 2 (particularly in Section 2.4) and can be summarised as follow:

- In elasto-plastic situations, a continuous range of bifurcation points can be obtained and the notion of stability of an equilibrium point normally used in elasticity must be replaced by the notion of stability of a deformation path.
- Only the secondary path branching out at the lowest bifurcation point has a physical meaning and needs to be computed.
- \bullet At the lowest bifurcation point, the tangent stiffness matrix **K** ceases to be positive definite and becomes indefinite.

Using these properties, this section presents and discusses the advantages and draw-backs of two different branch-switching procedures.

5.3.1 Mode injection method

This procedure is similar to the one used in elasticity. Using the property of the tangent stiffness matrix, the lowest bifurcation point is isolated by successive one side bisections and the branch-switching to the secondary path is performed by taken as predictor the eigenvector \mathbf{v} associated to the zero eigenvalue of \mathbf{K} at the bifurcation point. The expression "one side bisections" means that, due to the history aspect of the deformations, the intermediate equilibrium states during the process are always calculated by reference to the left (lower) limit.

This approach presents two drawbacks. First, contrary to the elastic case, the eigenvector may not be a good predictor and it is not certain that the Newton-Raphson iterations will converge on the secondary path. This is in particular the case when the secondary path is tangent to the fundamental one [98].

Second, it can happen that the bifurcation is induced by a discontinuous drop of the incremental stiffness of the material so that the tangent stiffness matrix along the fundamental path becomes indefinite without being singular. One such example is the Euler beam when $A \sigma_Y > P_t$, see Section 2.3. The lowest bifurcation point is then $A \sigma_Y$ and the tangent stiffness matrix along the fundamental path is discontinuous at this point. As a matter of fact, the bifurcation is induced by the sudden change of E to E_t in the beam. In such cases, the bifurcation point can still be isolated by successive bisections, but the notion of critical eigenvalue or eigenvector has no meaning and the choice of a predictor for the branch-switching is not evident. An alternative [26, 101] is to take the eigenvector associated to the negative eigenvalue of K. However, it is not certain that this vector corresponds to the buckling mode and the convergence on the secondary path is therefore not obvious.

In order to force the Newton-Raphson iterations to converge to the secondary path, an alternative is to adopt a displacement control procedure and to choose a displacement or a rotation which is zero along the fundamental path. Thus, if the Newton-Raphson iterations converge, it will necessarily be on the secondary path. However, if an arc-length procedure is adopted, this solution fails. Then, in order to maximise the possibility of converging on the secondary path and not on the fundamental one, a predictor ${\bf w}$ perpendicular to the tangent vector to the fundamental path ${\bf u}$ can be chosen [26, 101]. In this case, ${\bf w}$ is computed by

$$\mathbf{w} = \mathbf{u} + \beta \mathbf{v} \qquad \beta = -\frac{\mathbf{u}^{\mathrm{T}} \mathbf{u}}{\mathbf{u}^{\mathrm{T}} \mathbf{v}}$$
 (5.24)

where \mathbf{v} is the eigenvector associated to the negative eigenvalue.

This previously described procedure has been implemented in the following way. The bifurcation point is isolated by successive bisections until

$$\frac{\lambda_r - \lambda_l}{\lambda_r + \lambda_l} < tol \tag{5.25}$$

where λ_l and λ_r are the left (lower) and right (upper) approximations of the critical load factor and tol is taken as 10^{-4} . Branch-switching is performed by taking as predictor the eigenvector associated to the negative eigenvalue for the right point. Switching to the secondary path is forced by choosing as displacement control a degree of freedom which is zero on the fundamental path.

5.3.2 Minimisation procedure

The second approach, developed by Petryk [76–81], avoids the problems related to the definition of the critical eigenvector and the choice of the predictor. This method, for which the theoretical background has been given in Section 2.4, is based on the fact that along a stable deformation path, the displacement vector \mathbf{d} corresponds to an absolute minimum of the functional J defined in equation (2.90). With the notations introduced in Section 5.1.1, the potential J can be rewritten as

$$J = \frac{1}{2} \mathbf{d}^{\mathrm{T}} \mathbf{K} \mathbf{d} - \mathbf{d}^{\mathrm{T}} \mathbf{f}_{ex}$$
 (5.26)

Using this property, the branch-switching procedure is performed by finding an incremental solution to the equilibrium equations (5.3) which minimises J. Thus, the unstable fundamental path is rejected and the stable secondary path is automatically selected. This method is therefore based on the implicit assumption that, at least in a neighbourhood of the critical point, the post-buckling path is stable.

The bifurcation point is detected and isolated by classical one side bisections. In fact, the isolation is not essential for this method. However, due to the historical aspect of plastic deformations, it is important to initiate the secondary path from a point which is close to the bifurcation point. The first point of the secondary path is computed by minimising J. In order to ensure that the minimisation procedure will not terminate on a saddle point corresponding to the fundamental path, the predictor is constructed by adding a perturbation vector to the tangent vector at the fundamental path \mathbf{u} . Any random perturbation vector can be taken. However, if an eigenvalue analysis has already been performed at the bifurcation point, it can be judicious to take the eigenvector \mathbf{v} associated to the negative eigenvalue of \mathbf{K} . In that case, the predictor \mathbf{w} is computed by

$$\mathbf{w} = \mathbf{u} + \alpha \mathbf{v} \qquad \alpha = \frac{1}{100} \frac{\|\mathbf{u}\|}{\|\mathbf{v}\|}$$
 (5.27)

The minimisation procedure which has been implemented [36] consists of solving at each iteration k the system

$$(\mathbf{K}^{(k)} + \beta \mathbf{I}) \Delta \mathbf{d} = -\mathbf{r}^{(k)} \tag{5.28}$$

where \mathbf{r} is the residual vector of the equilibrium equations and \mathbf{I} the identity matrix. The coefficient β is taken to 0 if \mathbf{K} is positive definite and to 1.1 λ_{\min} otherwise (λ_{\min} is the lowest eigenvalue of \mathbf{K}). The displacements are then updated by

$$\mathbf{d}^{(k+1)} = \mathbf{d}^{(k)} + \mu \,\Delta \mathbf{d} \tag{5.29}$$

where μ is calculated by a line search procedure [57]. However, the tests performed by the author have shown that the line search procedure was not essential and that $\mu = 1$ could be taken without affecting the convergence property of the procedure.

The following points along the secondary path are then computed by classical Newton-Raphson iterations under displacement control.

As already pointed out, this minimisation procedure assumes that the bifurcation is stable and is therefore not suited for elastic problems. For elasto-plastic instability problems where buckling is induced by compressive forces, material non-linearity prevails over the geometric one in the vicinity of the bifurcation point and a stable post-buckling path is usually observed (cf. the study of the Hutchinson's model in Section 2.1.2). However, there is no guarantee that this is always the case. As an example, unstable secondary path can be obtained if materials with very low hardening are used. It can also happen that the stable region of the secondary path is restricted to a small neighbourhood of the bifurcation point and thus is difficult to catch numerically. All these cases will be illustrated by numerical applications in Chapters 6 and 9.

Chapter 6

2D examples in elasto-plasticity

Three main objectives motivate the selection of the numerical examples included in this chapter. The first one is to verify the ability of the element formulations introduced in Chapter 3 in handling large displacement problems in the presence of material non-linearity. Two classical problems, widely used as benchmark tests in the literature, have been chosen for this purpose. These are a cantilever beam under tip load and Lee's frame.

The second objective of these examples is to test the two branch-switching procedures presented in Section 5.3 and to compute elasto-plastic post-bifurcation paths for structures exhibiting different types of instabilities in elasticity. Thus, the third, fourth and fifth examples are characterised in elasticity by symmetric stable, asymmetric and symmetric unstable bifurcations, respectively.

For these three examples, both the minimisation procedure and the mode injection method worked very well and convergence to the first point on the secondary path was obtained within 4–7 iterations. However, as expected, the minimisation procedure failed for the case in the third example which presents an unstable bifurcation.

The third objective of these numerical applications is to examine comparatively the three local element formulations, and especially test the differences between the two Bernoulli elements. In addition, the influence of the number of Gauss points in the cross-section is also analysed. All these comparisons are performed through the study of the three first examples.

6.1 Example 1: cantilever beam

The purpose of this classical example, described in Figure 6.1, is to test and compare the elements based on the Bernoulli assumption. The load–displacement diagrams computed with ten linear elements and fifteen Gauss points along the beam depth are presented in Figures 6.2 and 6.3. As shown in these figures, the results are in excellent agreement with those obtained by Kondoh and Atluri [54].

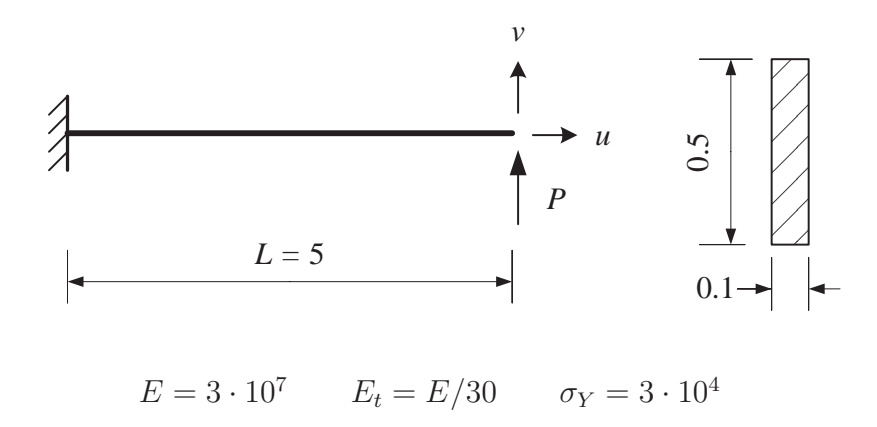


Figure 6.1: Cantilever beam.

This example has also been tested with twenty linear elements and ten shallow arch elements and the same load–displacement curves were obtained. This indicates that convergence is already reached with ten linear elements. In the same way, no significant difference was noted between results obtained with seven and fifteen integration points.

It can also be noted that computation using ten Timoshenko elements (with $\nu = 0.3$) gave the same load–displacement diagram as the one obtained with Bernoulli elements. Consequently, the effect of shear deformations can be neglected, which was not obvious since the height to length ratio is not small.

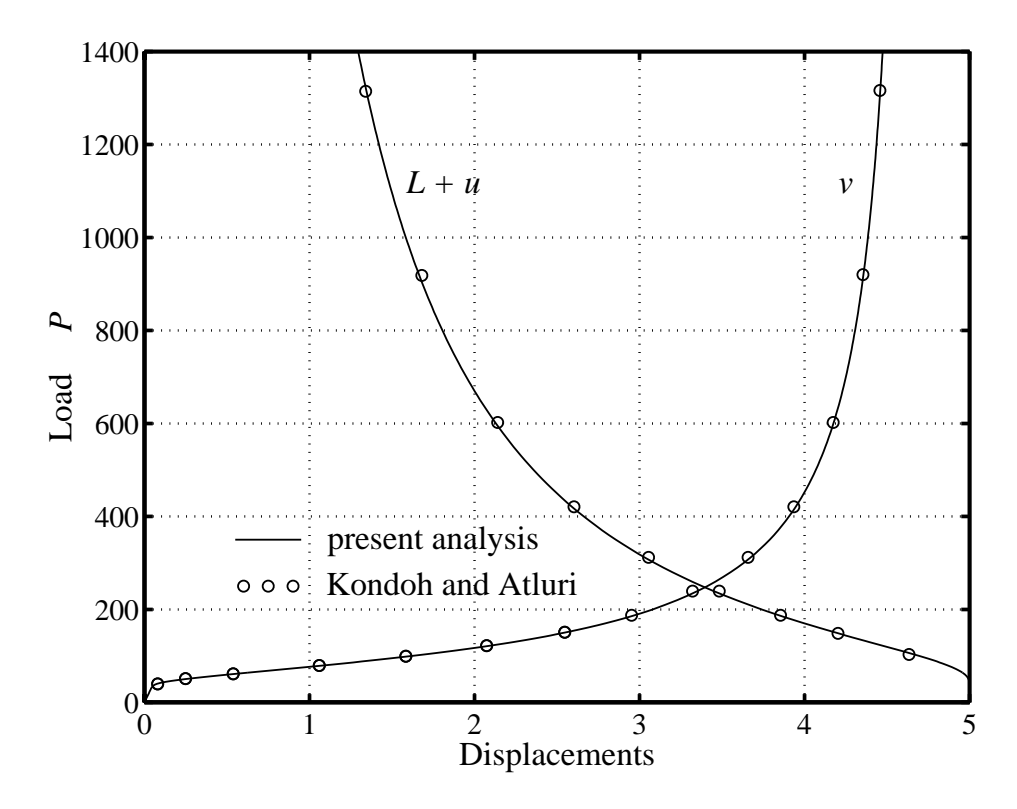


Figure 6.2: Cantilever beam: load-displacements diagram.

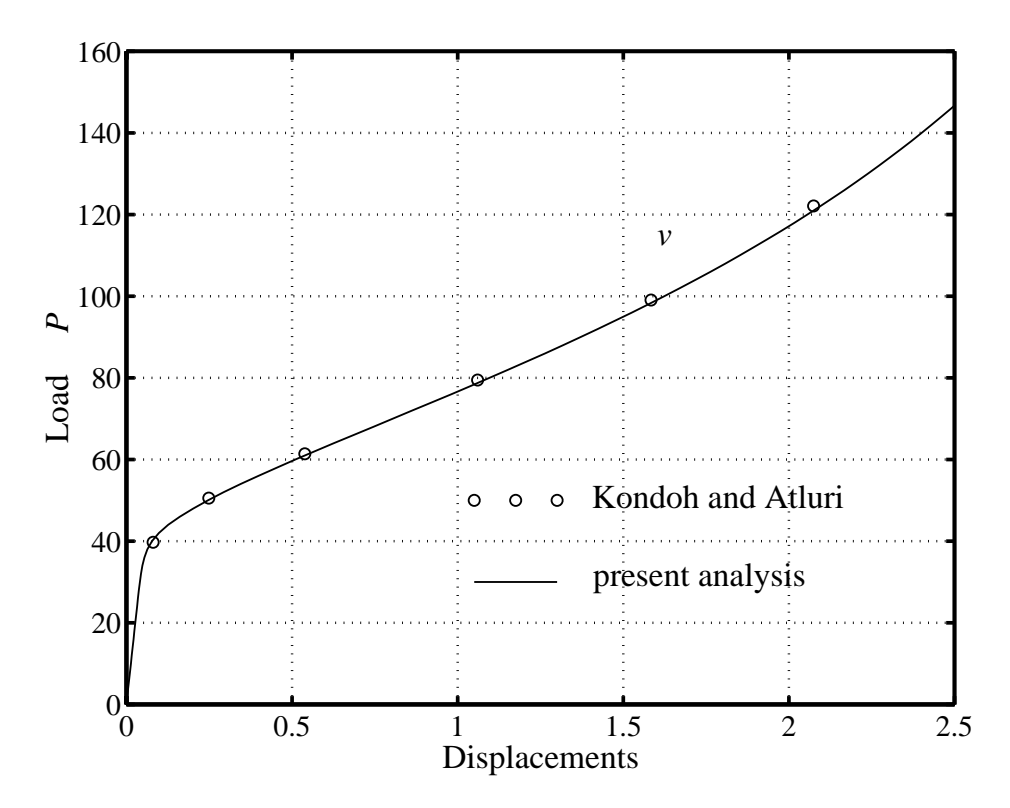


Figure 6.3: Cantilever beam: partial load-displacements diagram.

6.2 Example 2: Lee's frame

The second example is depicted in Figure 6.4. This structure exhibits a snap-through behaviour and a limit point in the load–deflection diagram is obtained.

Several discretisations have been used, for comparative purposes in the analysis of this problem. Thus, the results computed with twenty Timoshenko elements and seven Gauss points in the cross-section are presented in Figure 6.5 for both elastic and elasto-plastic cases. For the elasto-plastic analysis, deformed configurations at typical load steps are shown in Figure 6.6. As noted from Figure 6.5, a very good agreement with the results obtained by Park and Lee [74] and Cichon [17] is found.

The influence of the number of integration points along the beam depth has been studied for the Timoshenko element. As shown in Figure 6.7, the difference between results obtained with seven and fifteen Gauss points is very small.

Load—deflection curves have also been computed using the two types of Bernoulli elements. Comparison with Timoshenko elements (Figure 6.8) shows that the effect of shear deformations is almost negligible, which was expected since the two beams are very slender. Moreover, it is shown in Figure 6.9 that results obtained with ten shallow arch elements and twenty linear elements are almost identical.

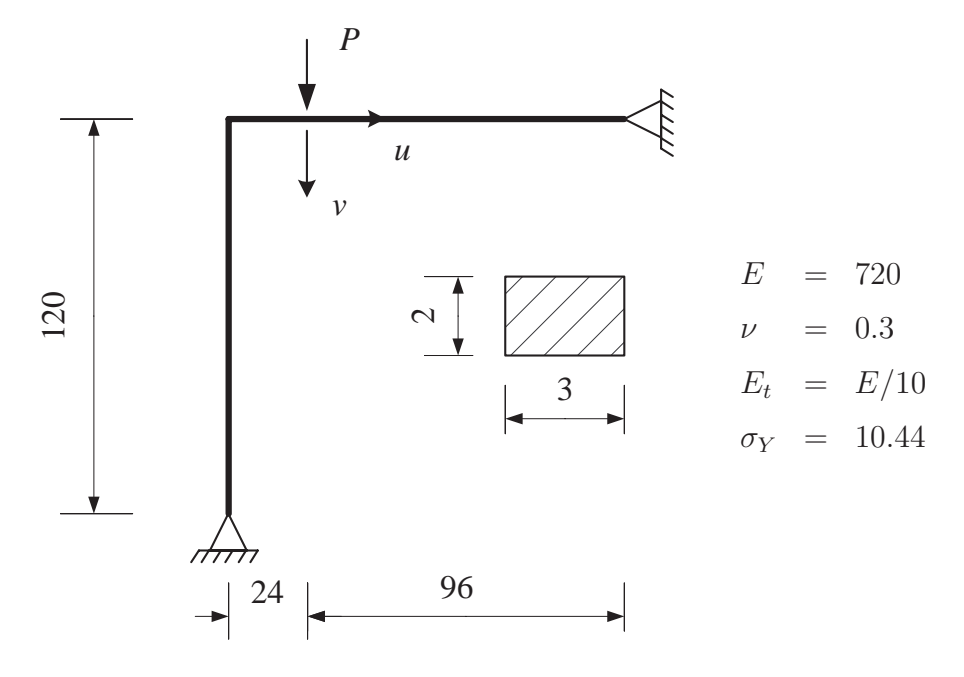


Figure 6.4: Lee's frame.

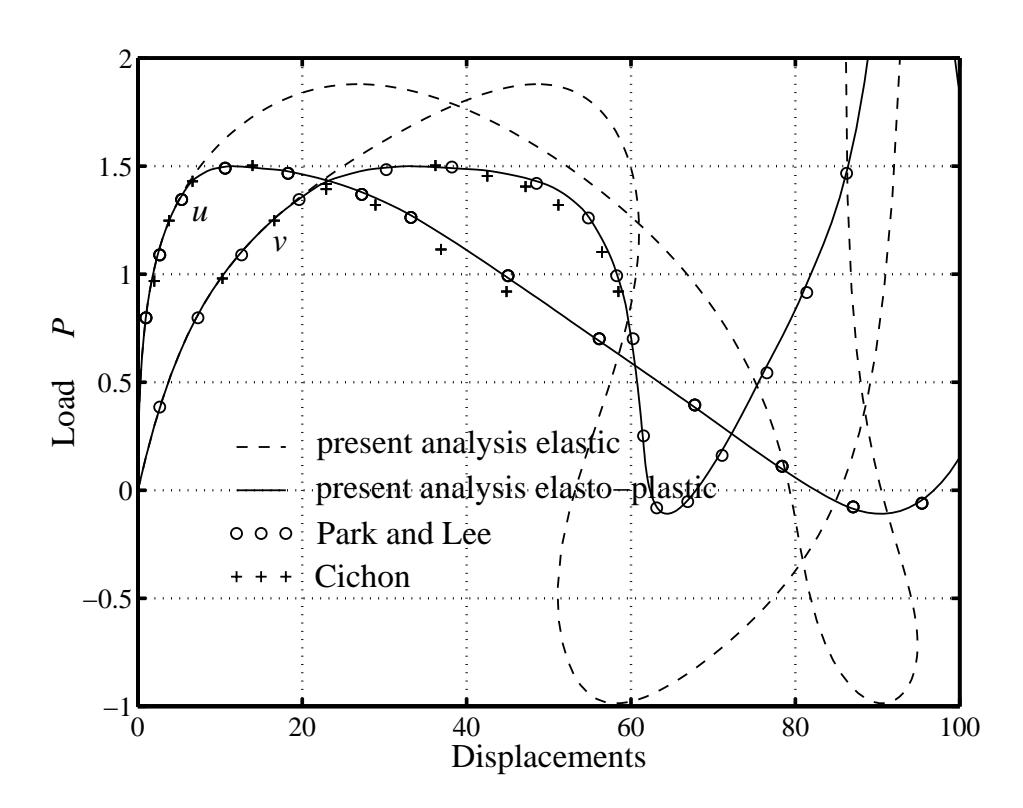


Figure 6.5: Lee's frame: diagram with 20 Timoshenko elements and 7 Gauss points.

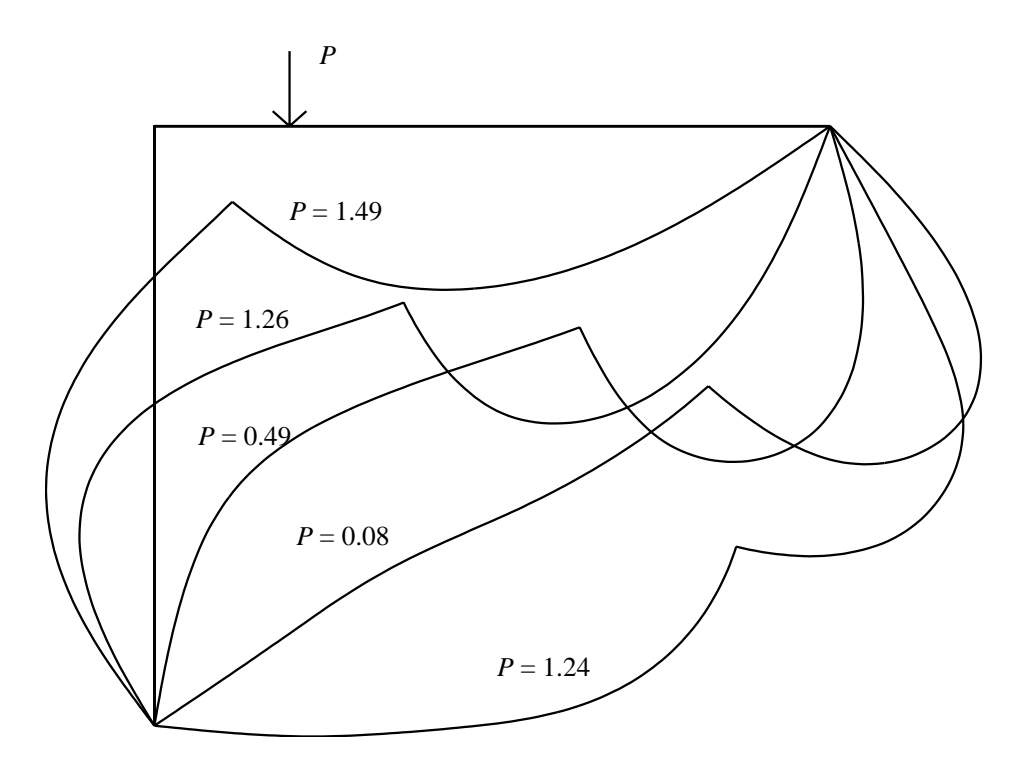


Figure 6.6: Lee's frame: elasto-plastic deformed profiles.

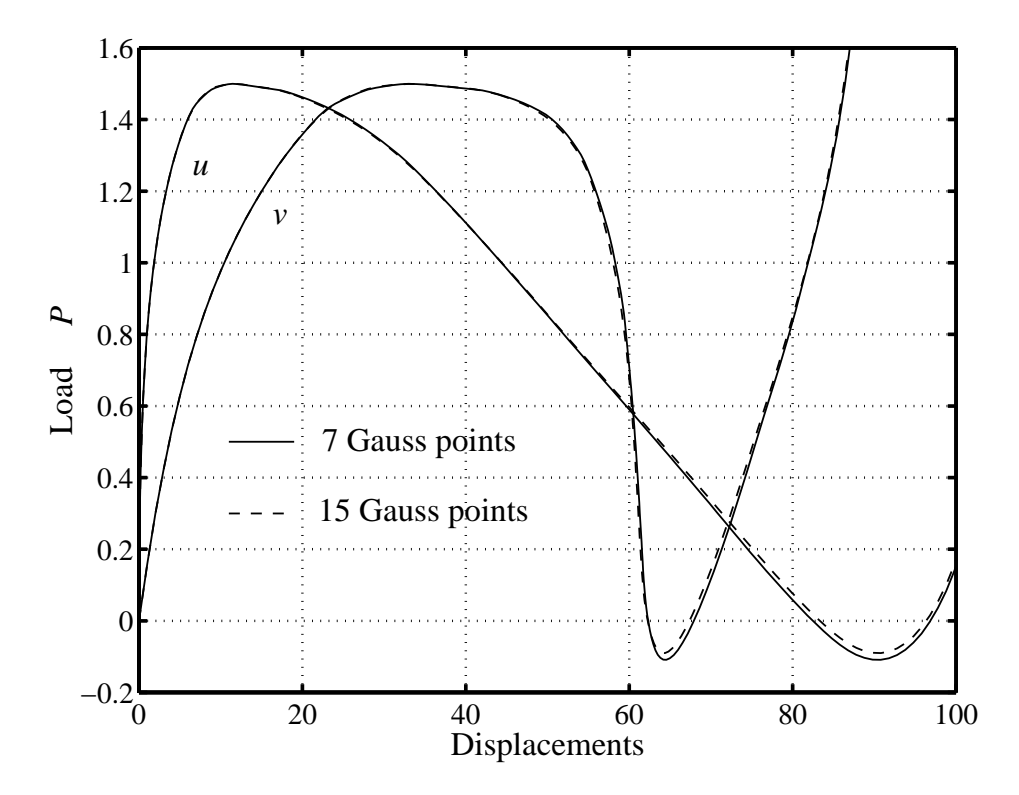


Figure 6.7: Lee's frame: diagram with 20 Timoshenko elements.

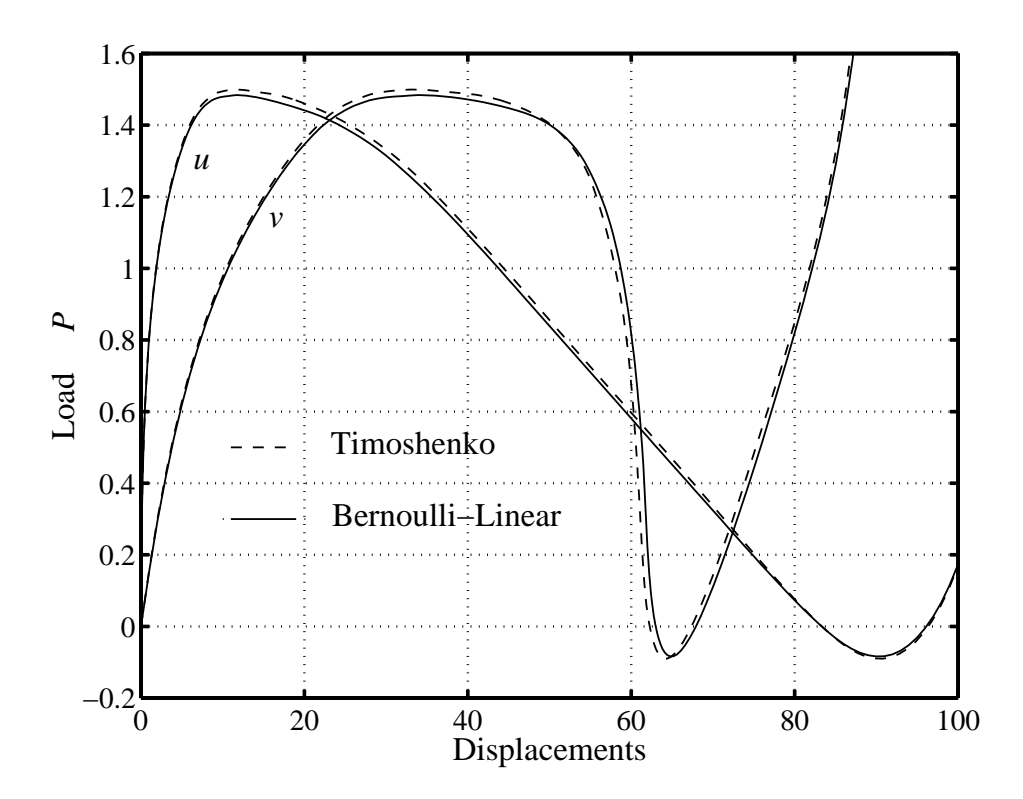


Figure 6.8: Lee's frame: diagram with 20 elements and 7 Gauss points.

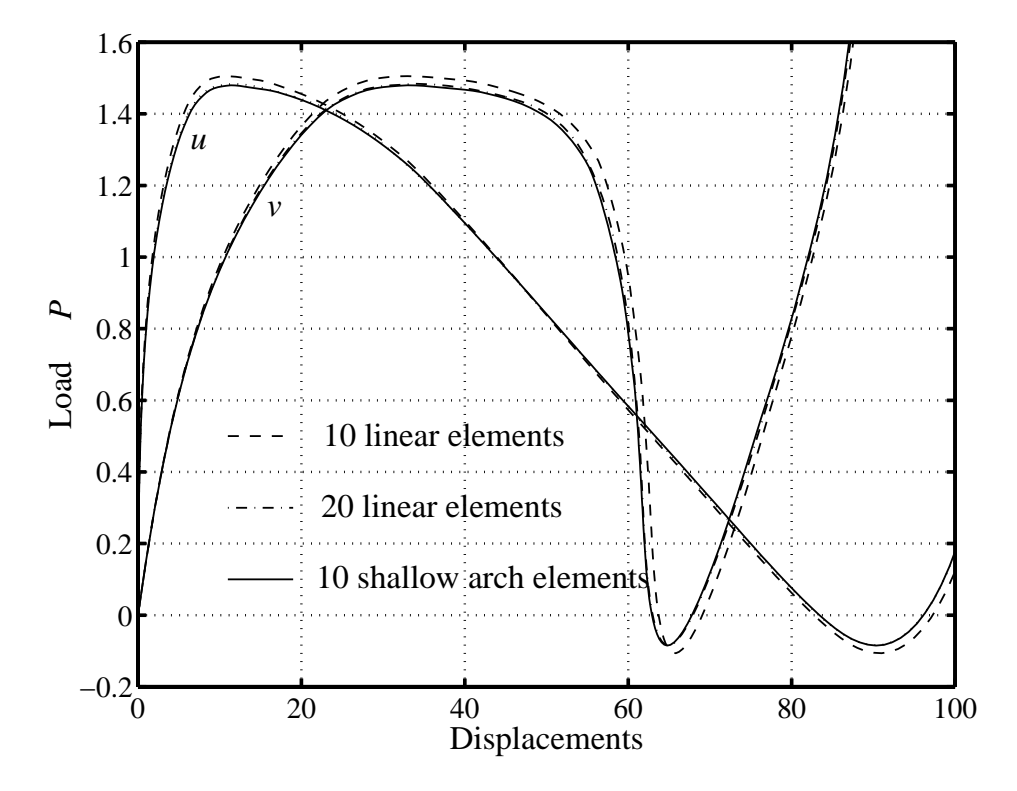


Figure 6.9: Lee's frame: diagram with Bernoulli elements and 15 Gauss points.

6.3 Example 3: Euler beam

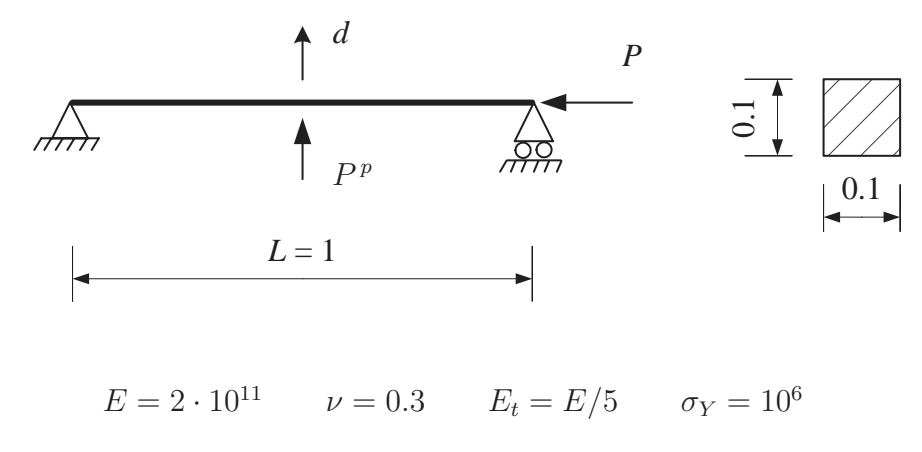


Figure 6.10: Euler beam.

The third example is an Euler beam with the geometrical and material parameters presented in Figure 6.10. In order to study the imperfection sensitivity, a small perturbing force P^p , acting at the midpoint of the beam is introduced. The load factor λ and the force P^p are defined by

$$\lambda = \frac{P}{P_t} \qquad P_t = \frac{\pi^2 E_t I}{L^2} \qquad P^p = \frac{P_t}{s}$$

where s is varied to give different imperfection magnitudes.

Load–displacement curves computed using Timoshenko and Bernoulli shallow arch elements are shown in Figures 6.11 and 6.12. As expected, the equilibrium paths computed with imperfections tend to the path branching at the lowest bifurcation point when the perturbation force P^p tends to zero. This confirms the theoretical conclusions of Petryk that only the secondary path branching at the lowest bifurcation point is stable in an energetic sense and has a physical meaning. Here also, computations performed with seven and fifteen integration points along the beam depth gave almost the same results, as shown in Figure 6.13.

A comparison between the two Bernoulli elements is presented in Table 6.1, where the bifurcation and maximum loads have been computed using fifteen Gauss points. It can be noted that results obtained with ten shallow arch elements, twenty linear elements and forty linear elements are almost identical.

The two asymptotic expansions (2.79) and (2.80) presented in Section 2.3.3 are compared in Figure 6.14 with the results obtained with ten shallow arch elements and fifteen Gauss points. Very good agreement between expression (2.79) and finite element calculations is observed up to $\lambda = 1.3$, where the two curves begin to diverge. Expression (2.80) diverges from numerical calculation at $\lambda = 1.1$ and therefore the validity of the term $\lambda_3 \xi^{9/5}$ should be seriously questioned.

A number of reasons why asymptotic expressions should be considered with great caution have already been discussed in Section 2.3.3. The examination of the growing zone of elastic unloading, which appears at bifurcation, gives an additional argument. The zones of elastic deformations at several increments are shown in Figure 6.16. Calculations have been performed with forty shallow arch elements in order to get an accurate representation of the zone of elastic unloading, but the load–displacement curve is similar to the one depicted in Figure 6.14. It is shown in Figure 6.16 that a zone of plastic reversal stresses is developing before the occurrence of the maximal load. This zone is not considered in the derivation of the asymptotic expansions [49,58]. The same phenomenon has been observed with different values for the yield limit σ_Y and the tangent modulus E_t . Another consequence is that the characteristic of the hardening cannot be neglected. The present method is based on isotropic hardening. Similar computations with kinematic hardening would certainly give different load–displacement diagrams.

Finally, the structure has been tested when $P_t < A \sigma_Y$ by taking $\sigma_Y = 5 \cdot 10^8$. In this case, the lowest bifurcation point is $A \sigma_Y$ and the tangent stiffness matrix along the fundamental path becomes negative at this point without being singular. The secondary paths computed with two different hardening parameters are presented Figure 6.15. It can be observed that depending on the value of E_t , the bifurcation can be stable or unstable.

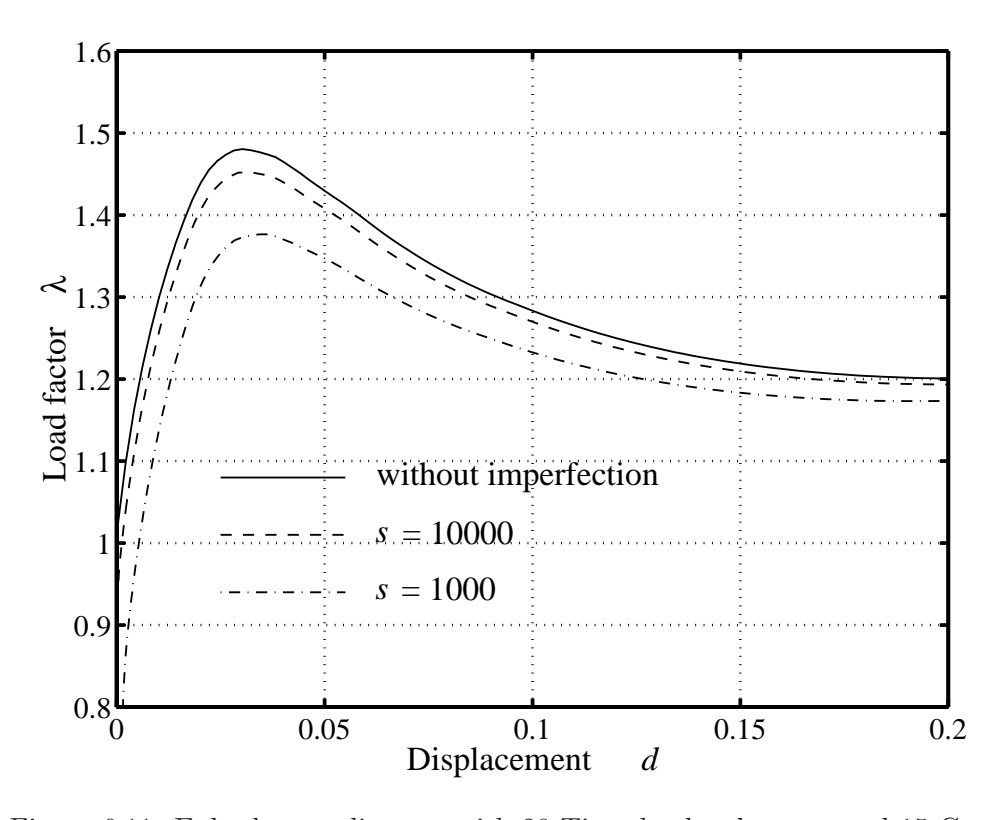


Figure 6.11: Euler beam: diagram with 20 Timoshenko elements and 15 G.p.

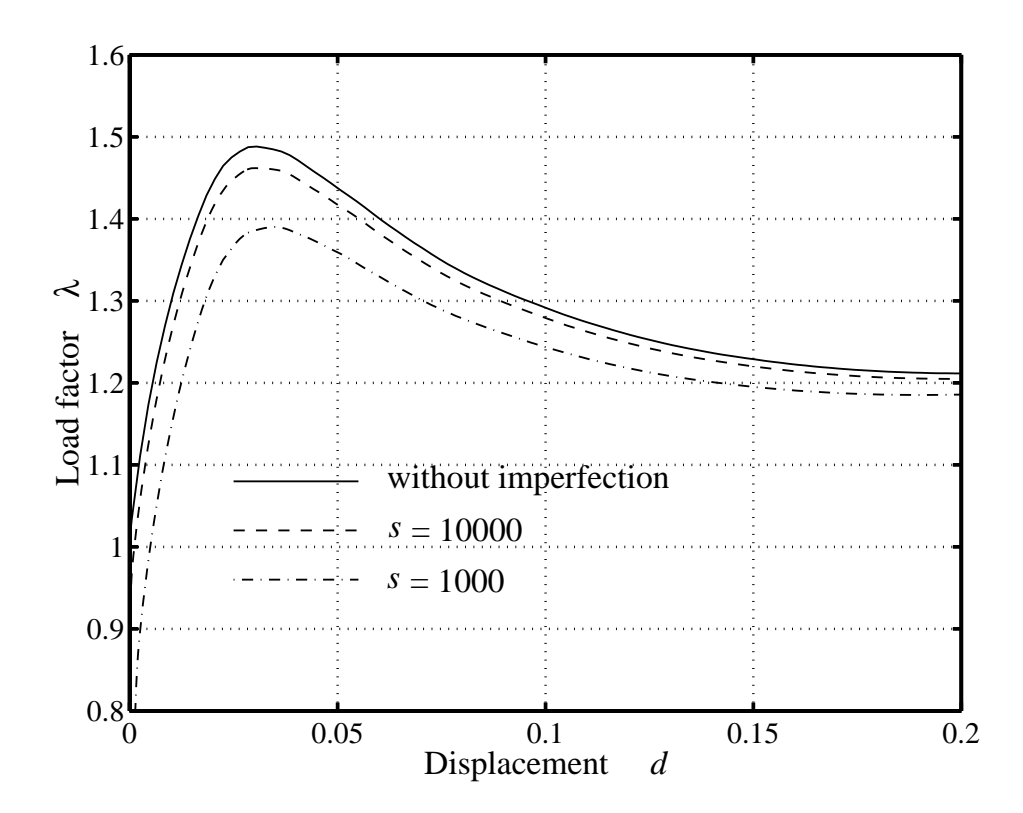


Figure 6.12: Euler beam: diagram with 10 shallow arch elements and 15 G.p.

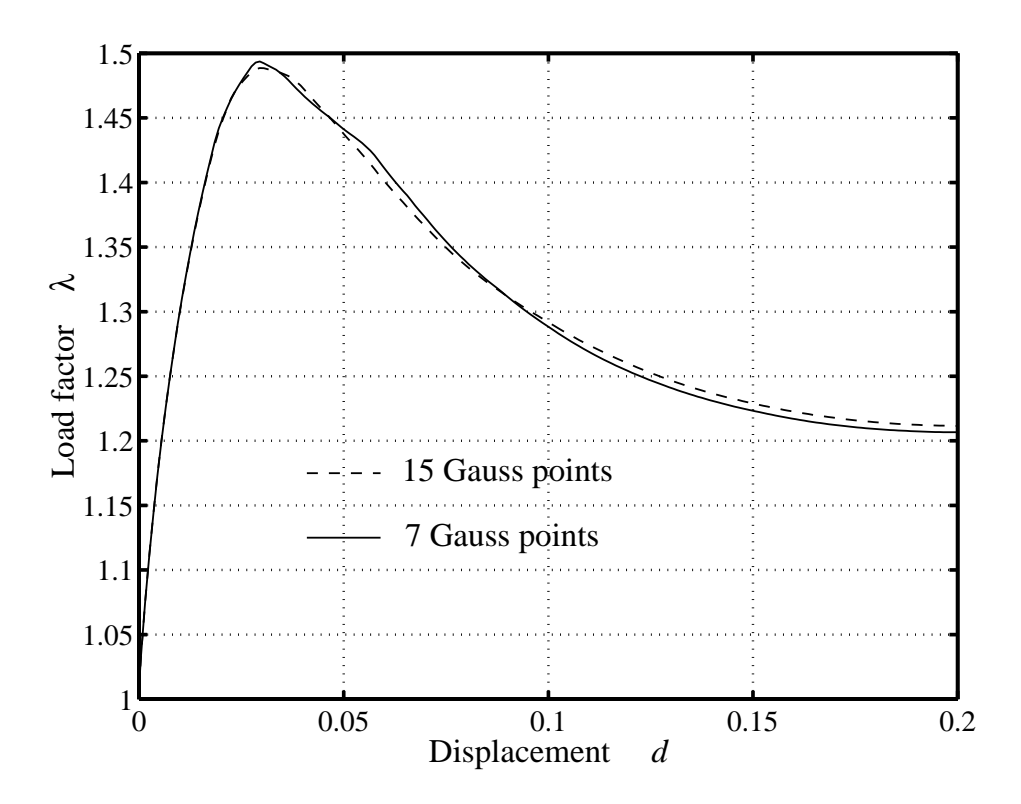


Figure 6.13: Euler beam: diagram with 10 shallow arch elements.

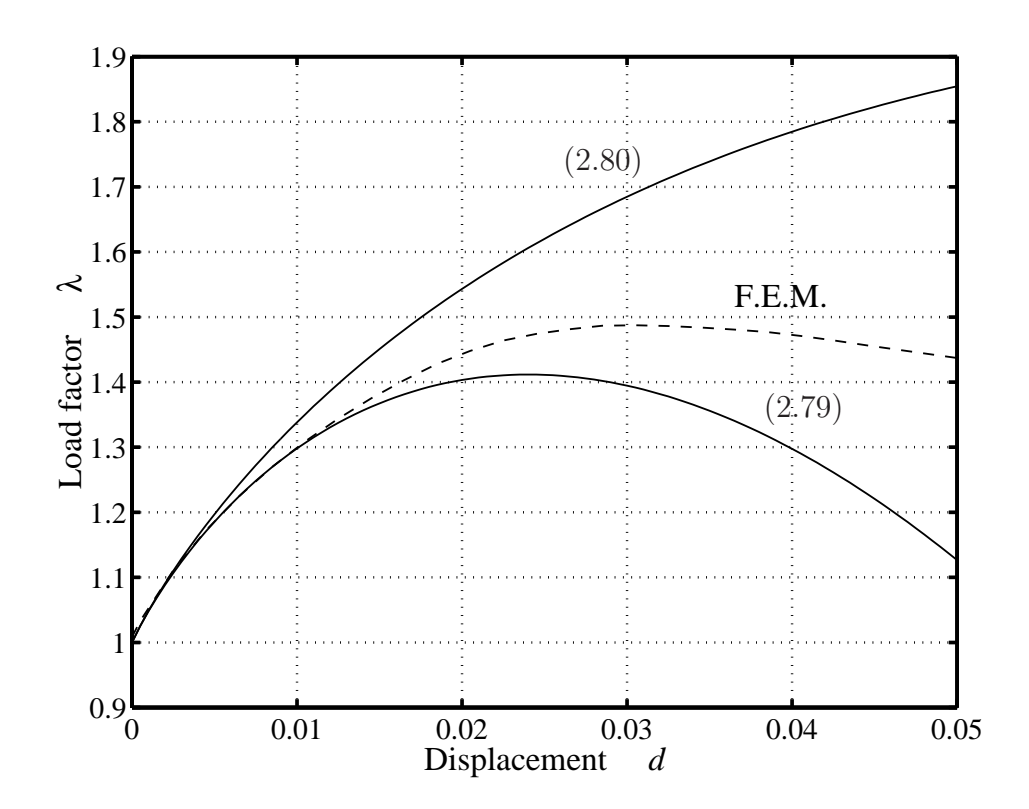


Figure 6.14: Euler beam: comparison between asymptotic expressions and numerical calculations.

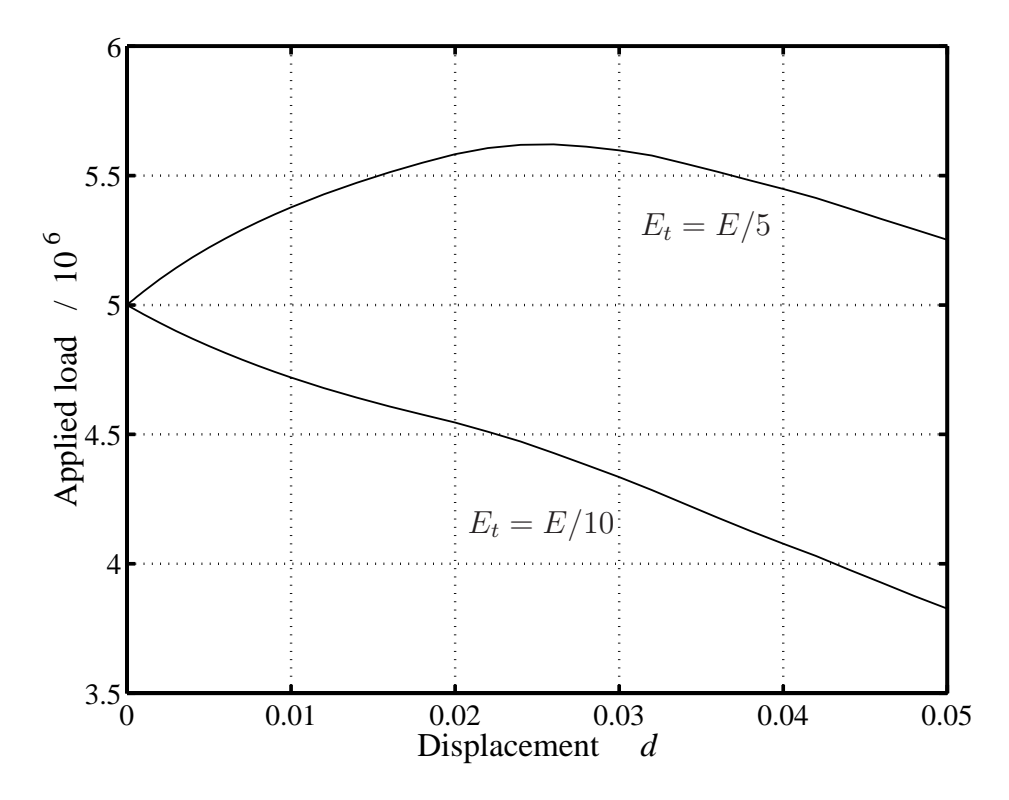


Figure 6.15: Euler beam: diagram when $P_t < A \sigma_Y$.

Table 6.1: Euler beam: comparison of Bernoulli elements.

Number and type of elements	$\lambda_{ m cr}$	λ_{max}
10 linear elements	1.017	1.501
20 linear elements	1.010	1.491
40 linear elements	1.009	1.488
10 shallow arch elements	1.008	1.489
20 shallow arch elements	1.008	1.488

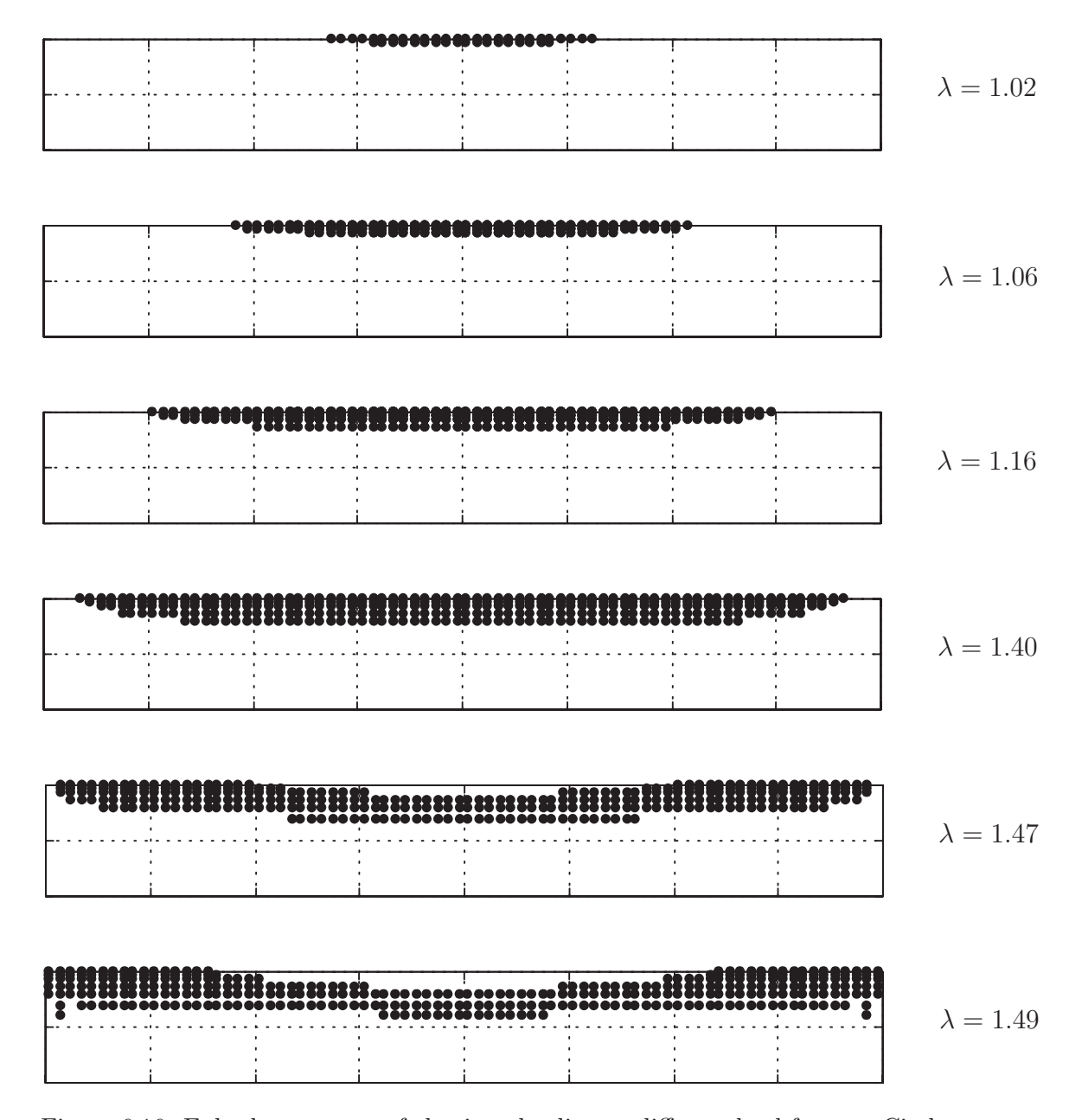


Figure 6.16: Euler beam: zone of elastic unloading at different load factors. Circles represent Gauss points where elastic deformation occurs.

6.4 Example 4: asymmetrical frame

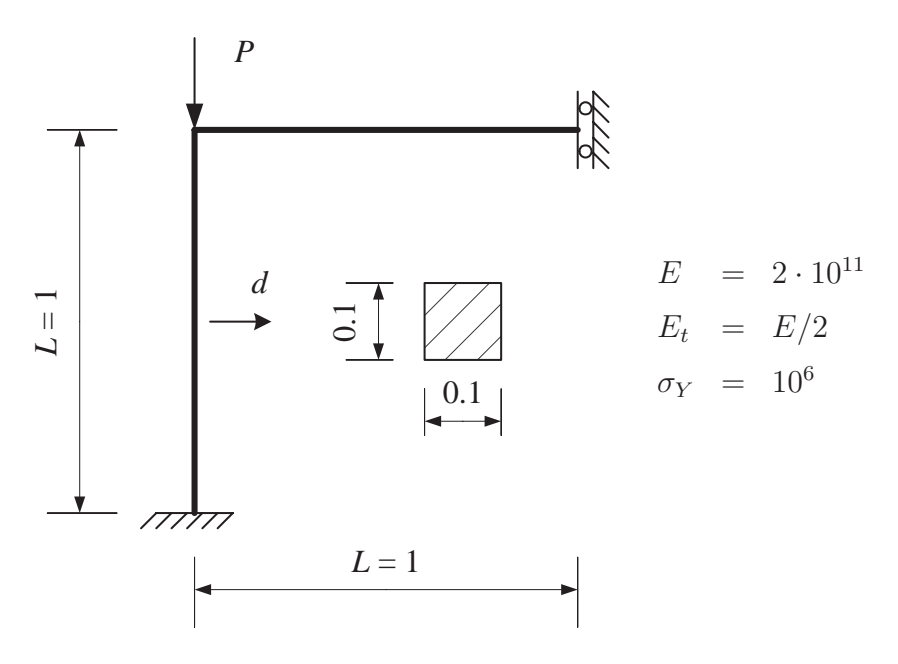


Figure 6.17: Asymmetrical frame.

The frame described in Figure 6.17 exhibits an asymmetrical bifurcation for the case of elastic behaviour, as shown in Figure 6.18. The load factor λ is defined by

$$P = \lambda \frac{4\pi^2 E I}{L^2} \qquad \text{in elasticity} \tag{6.1}$$

and

$$P = \lambda \frac{4\pi^2 E_t I}{L^2} \qquad \text{in elasto-plasticity} \tag{6.2}$$

The purpose of this example is to investigate the phenomenon of bifurcation in elasto-plasticity. Sixteen shallow arch elements and fifteen Gauss points have been used. The results are shown in Figure 6.19. Both post-bifurcation secondary paths present a stable part before a limit point is reached. These results confirm the conclusion derived from the analysis of Hutchinson's model (Section 2.1.2) that in the vicinity of the bifurcation, material non-linearity prevails over the geometric one and, consequently, a stable path is usually obtained.

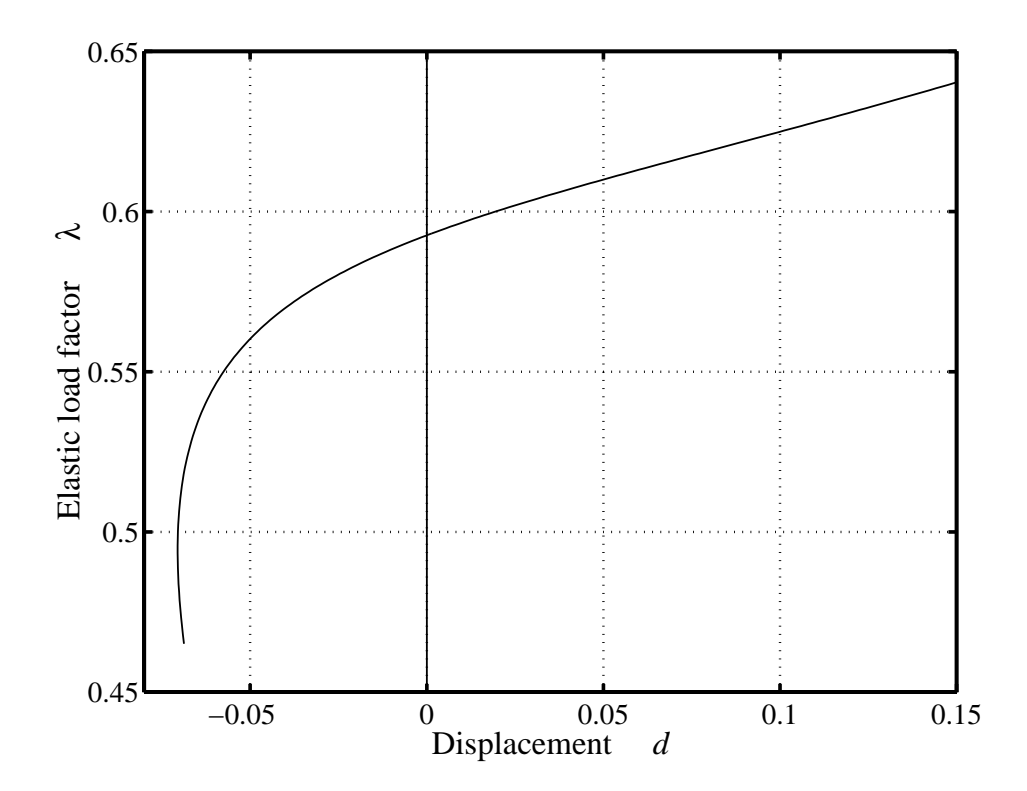


Figure 6.18: Asymmetrical frame: post-bifurcation paths in elasticity.

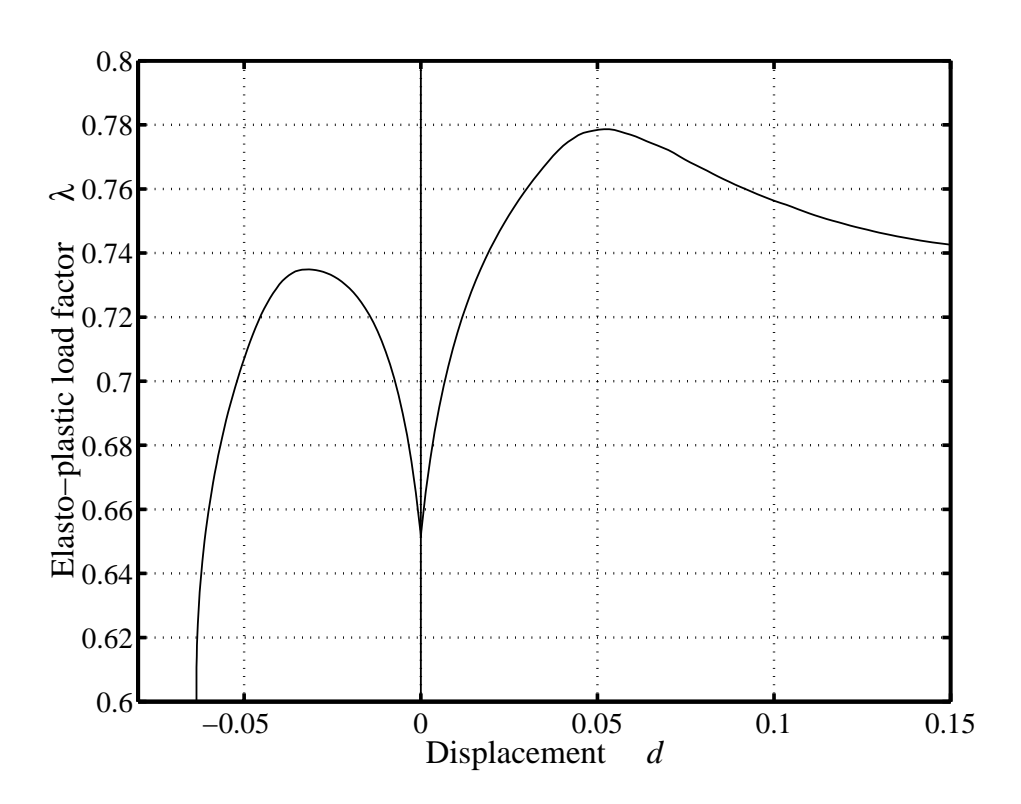


Figure 6.19: Asymmetrical frame: post-bifurcation paths in elasto-plasticity.

6.5 Example 5: toggle frame

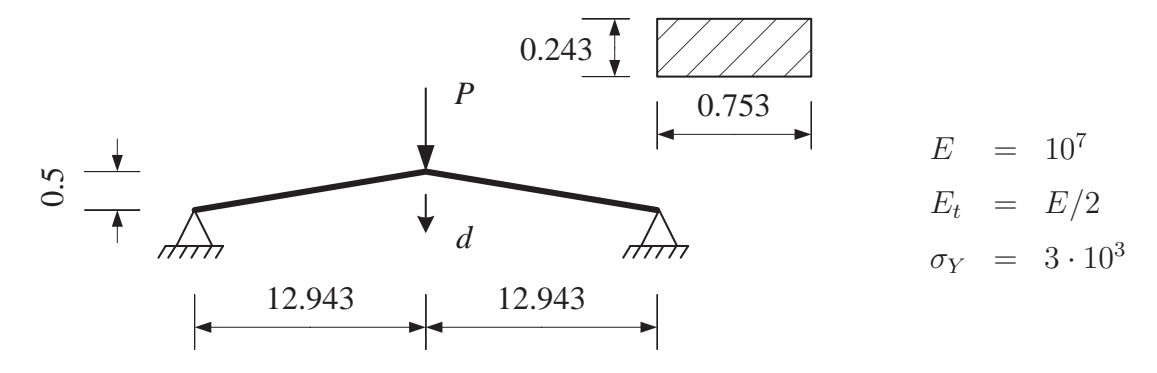


Figure 6.20: Toggle frame.

The toggle frame, described in Figure 6.20 has been analysed using a discretisation with eight linear Bernoulli elements and seven Gauss points along the beam height. The equilibrium paths for the elastic and elasto-plastic situations are shown in Figures 6.21 and 6.22. In the elastic case, the structure exhibits a symmetric unstable bifurcation while in the elasto-plastic case, a stable bifurcation is observed. However, it must be noted that the stable part of the secondary path is very short and a limit point is quickly reached. This observation confirms once again the conclusion that in the vicinity of the bifurcation point, material non-linearity prevails over the geometric one and a stable path is usually obtained.

Moreover, the results plotted in Figure 6.22 suggest that the structure presents a tangent bifurcation in the elasto-plastic case. The existence of such a bifurcation has been proved theoretically by Leger and Potier-Ferry [58] and an example has been studied by Triantafyllidis [98]. According to these authors, a tangent bifurcation can occur when the structure is only partially plasticised along the fundamental path and is characterised by the apparition of a zone of elastic reloading. The analysis of Figures 6.23 and 6.24 shows that along the fundamental path, a zone of plasticisation is developing on the concave side of the two beams while the rest of the structure deforms elastically. In addition, a zone of elastic unloading ($\dot{\varepsilon} < 0$) appears on the convex side of the two beams. Along the secondary path, the zone of plasticisation continues to grow in the left beam while it decreases and disappears in the right beam. At the same time, the zone of elastic unloading disappears on the convex side of the right beam. Consequently, the conditions for a tangent bifurcation stated in [58] seem to be respected, but a rigorous proof of such a phenomenon cannot be performed in a discretised and numerical context.

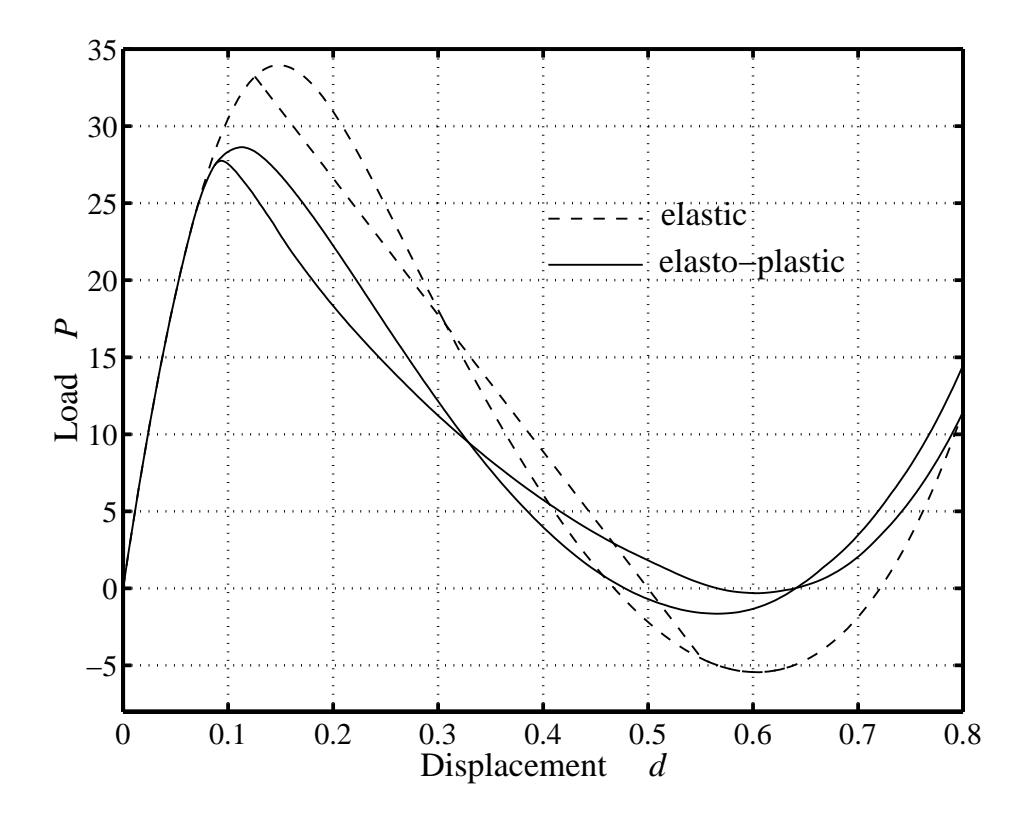


Figure 6.21: Toggle frame: elastic and elasto-plastic diagrams.

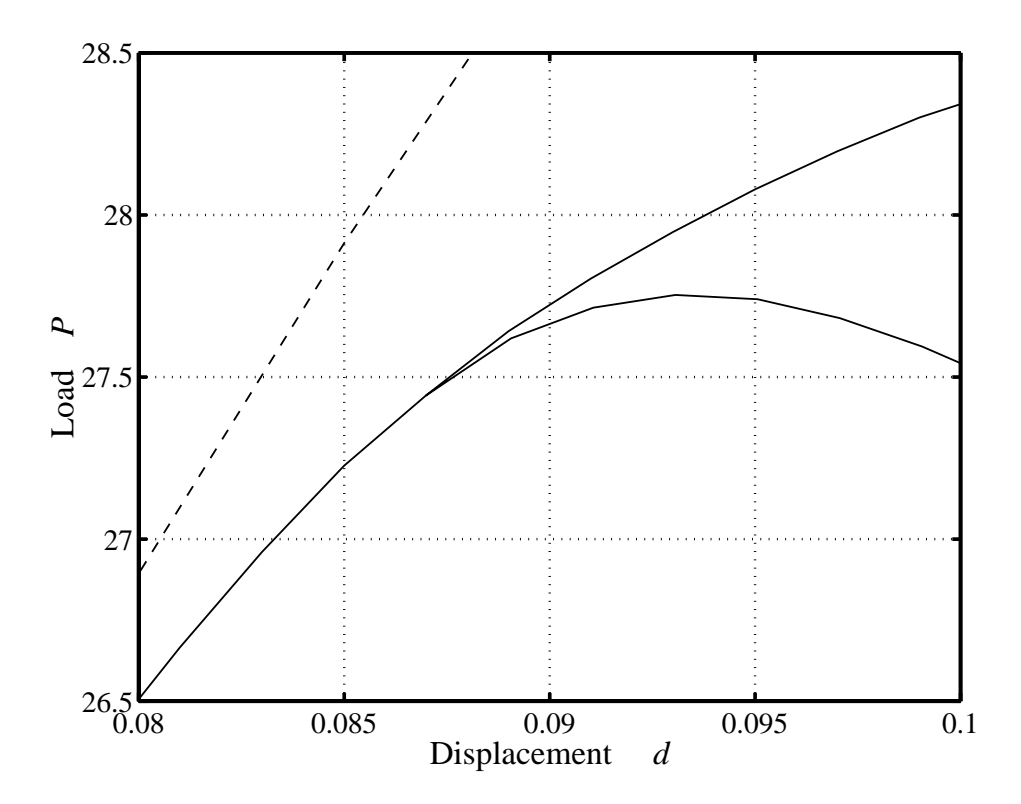


Figure 6.22: Toggle frame: tangent bifurcation in elasto-plasticity.

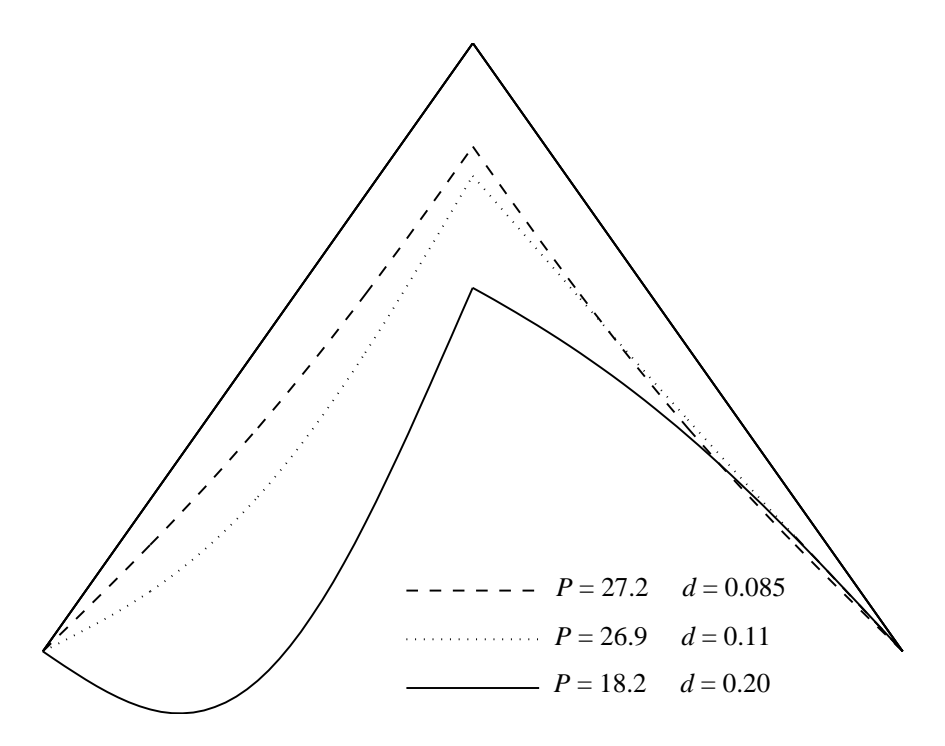


Figure 6.23: Toggle frame: deformed profiles before and after bifurcation.

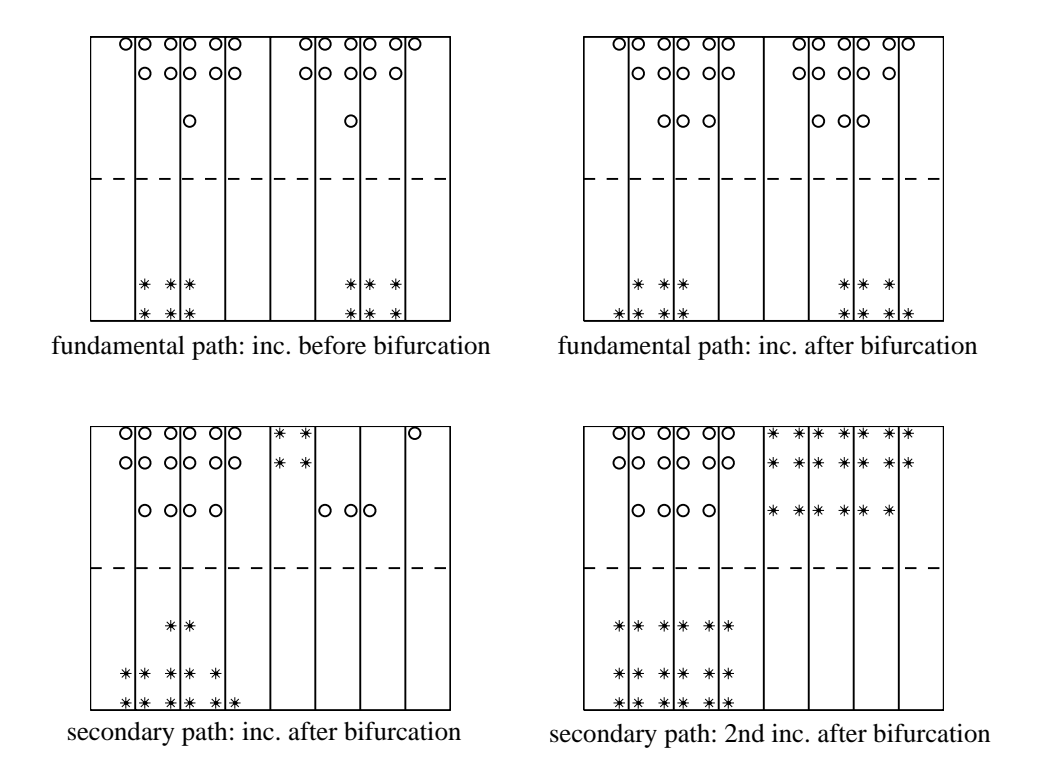


Figure 6.24: Toggle frame: zone of plastic deformations at different increments. Circles represent Gauss points where plastic deformation occurs. Stars represent Gauss points where elastic unloading occurs.

Chapter 7

3D examples in elasticity

The test problems included in this chapter have two objectives. The first one is to test the ability of the elements in handling problems involving large 3D rotations. As a general rule, the parameterisation in terms of the incremental rotation vector is used throughout the whole set of test problems. However, for the first two examples, the parameterisation based on the total rotation vector together with the more traditional "intrinsic" parameterisation (see Section 4.2.5) were also included in order to discuss the relative merits of the three possible choices. The second objective is to test the ability of the elements to deal with problems involving coupling between axial, bending and torsional-warping effects. For this purpose several examples exhibiting pure torsional or flexural-torsional buckling were also included.

For all the instability problems included in this chapter, the procedure of direct isolation of bifurcation points presented in Section 5.2 was used. Convergence to the bifurcation point was obtained within 4–6 iterations. The performances of this procedure will be investigated in more detail in Chapter 8.

For certain problems, the results obtained from the beam models have been compared with results obtained using shell models. The shell models were constructed using the flat facet triangular element developed by Pacoste [68,71].

The characteristics of the cross-sections have been either taken from the literature or determined with the finite element program presented in Appendix B.

7.1 Example 1, deployable ring

This first example, introduced by Goto [38], refers to the ring depicted in Figure 7.1. The ring is fully clamped at one end and loaded at the other end by a twisting moment. At the loaded end, the center point of the section (point A) is restricted to move along and rotate around the x axis.

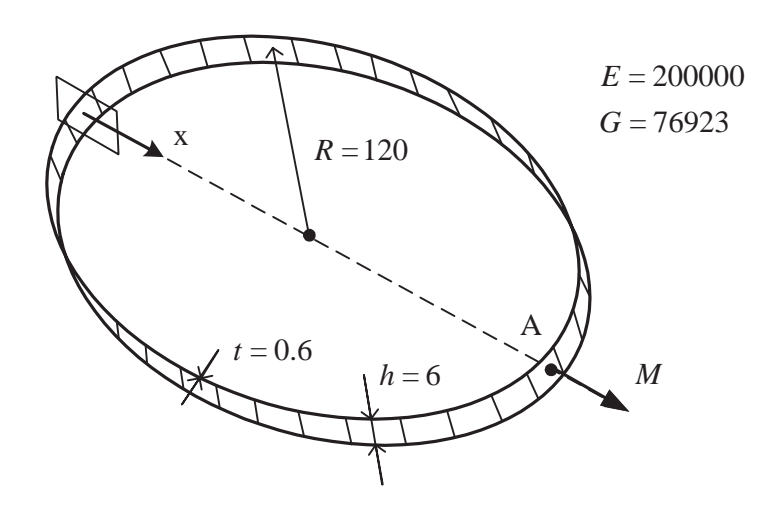


Figure 7.1: Deployable ring.

The ring shows a very interesting behaviour under increasing rotation at A. Thus, after a complete rotation cycle, i.e. $\Theta_{\rm A}=2\pi$ the ring is wrapped around itself and transformed into a smaller ring with a radius of only one third of the original one. One more cycle, i.e. $\Theta_{\rm A}=4\pi$, will bring the ring back to the original configuration. This example is therefore ideally suited in order to test the ability of the formulation to handle large rotations.

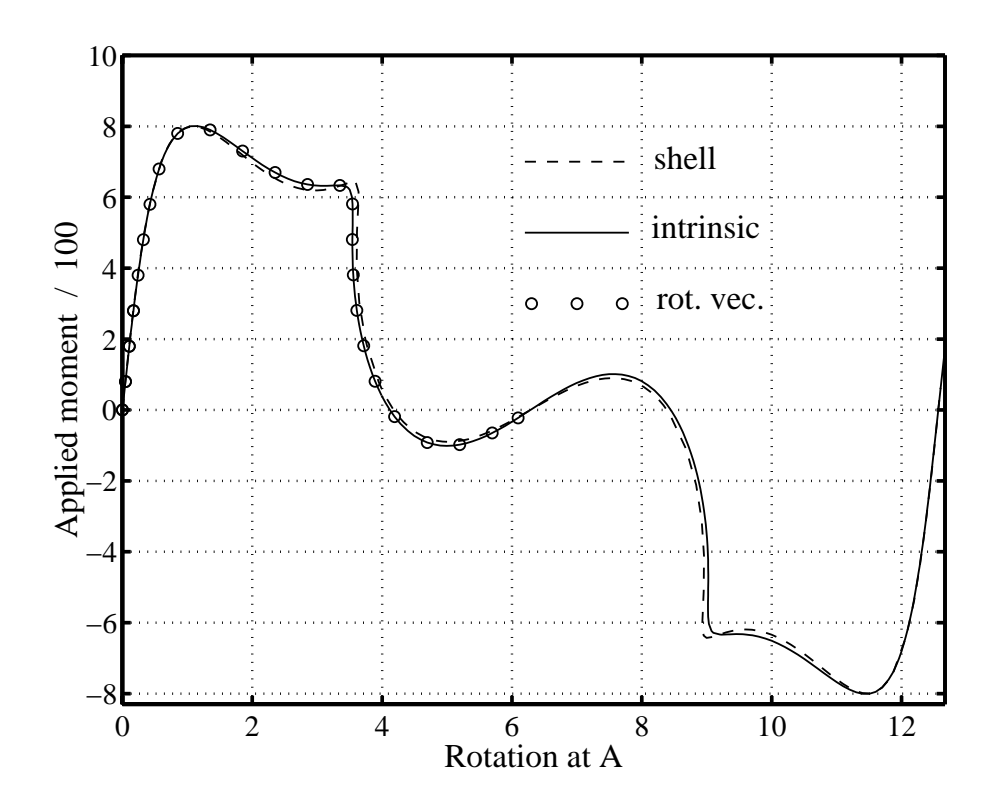


Figure 7.2: Deployable ring: load–displacement curves.

The results shown in Figure 7.2 were obtained using 128 t3dl elements (with J=0.432). The analysis included all three parameterisations of finite 3D rotations discussed in Section 4.2.5. Thus, for the total rotational vector, a quadratic convergence rate was observed for values $\Theta_{\rm A}<2\pi$. In the vicinity of 2π , the tangent stiffness matrix became ill-conditioned (see Section 4.1.1), the quadratic convergence was gradually lost and ultimately, the iterations failed to converge. In contrast, the parameterisation based on the incremental rotation vector as well as the usual "intrinsic" parameterisation, were unaffected and the computations were continued up to $\Theta_{\rm A}=4\pi$. A quadratic convergence rate was maintained for the whole range of the equilibrium path.

Note that since the point A is restrained to rotate around the x axis, all three types of parameterisation produce identical results, regardless of whether the transformation of the external moment is performed or not. Finally, note the excellent agreement between the present solution and the results from the shell analyses presented in [71].

7.2 Example 2, helical beam

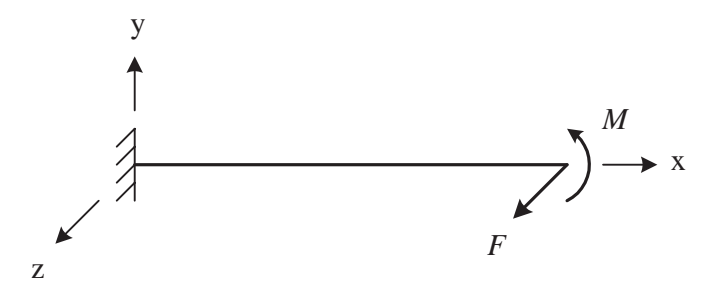


Figure 7.3: Helical beam.

This example was introduced by Ibrahimbegovic [51]. Its purpose is to illustrate the effects of the transformations in equations (4.175) and (4.176) on the outcome of the analysis, for problems involving concentrated moment loading. Thus, the beam shown in Figure 7.3 is subjected to a concentrated moment M and an out-of-plane force F, applied at its free end. Both M and F are increased proportionally up to the values $M_{\text{max}} = 120\pi$ and $F_{\text{max}} = 30$. The beam is modelled with 60 t3dl elements. The geometric and sectional properties of the beam are

$$L=10 \qquad EA=GA=10^4 \qquad EI_{22}=EI_{33}=GJ=10^2$$

The simultaneous application of a concentrated moment and a force, bends the beam into a helical shape. At the end of the loading process, the beam is wrapped around in six concentric circles. The results, obtained using the "intrinsic" parameterisation of finite rotations are shown in Figure 7.4. Note that the out of plane z-displacement oscillates around a zero value. Each passing through zero corresponds to a deformed shape which is entirely situated in the plane xy.

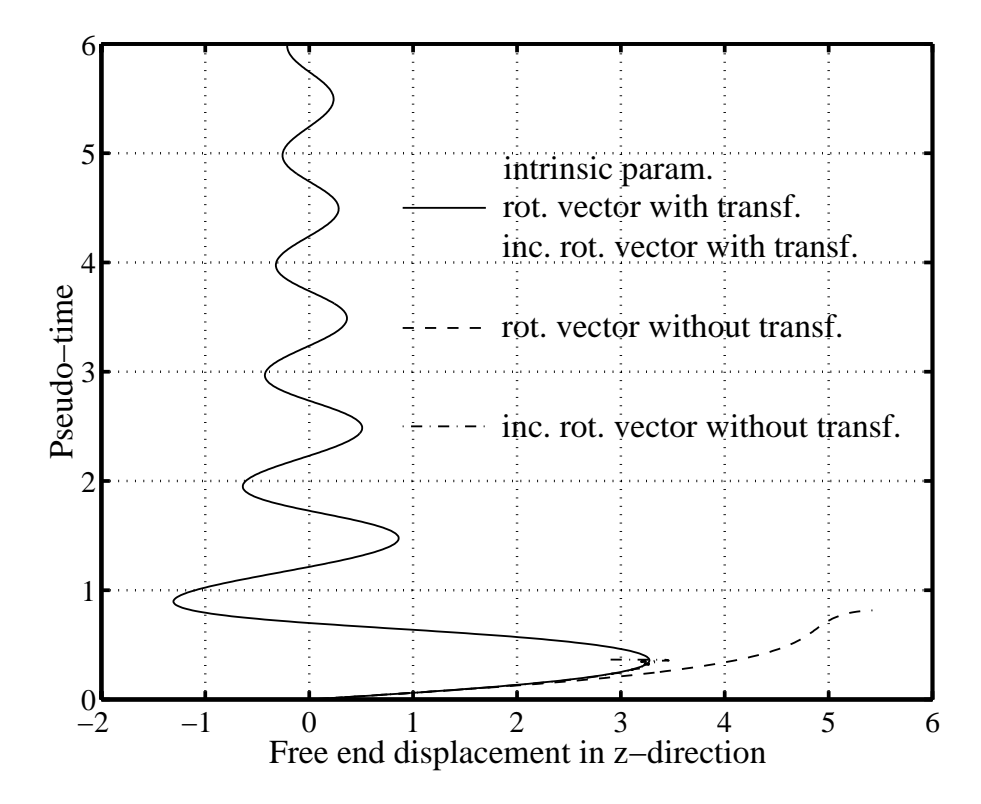


Figure 7.4: Helical beam: load-displacement curves.

Changing the type of parameterisation should not affect the outcome of the analysis since the physical problem does not change. Thus, absolutely identical results should be obtained using either the total rotational or the incremental rotational vector. However, as shown in Figure 7.4, this is the case only if the transformations described in Section 4.5.2 are applied on the external moment M. Without such a transformation, a different parameterisation will imply a different physical definition of M. As a consequence, the results obtained using different types of parameterisation will be completely different.

7.3 Example 3, right angle frame

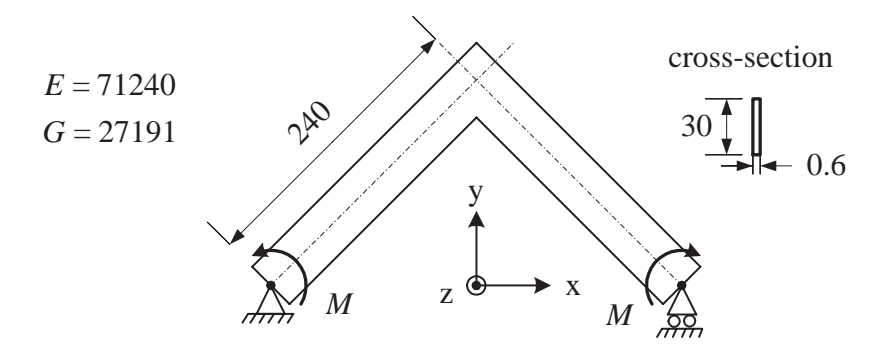


Figure 7.5: Right angle frame.

This classical example (see Figure 7.5), has often been used in order to check the ability of various beam formulations to properly account for torsional-bending coupling [40,44,64,73,92,93]. Due to the symmetry, only half of the frame is modelled. At the support only translation along x and rotation around z are allowed. The loading is given by a pair of concentrated moments applied at the support. The non-trivial cross sectional characteristics are J=2.133 and $I_{\omega}=40.43$.

The problem is typical for situations where a local linear strain definition will lead to an incorrect solution. Thus, the results obtained using $10 \ t3dl$ elements are shown in Figure 7.6. As the moment increases, an unstable bifurcation point is reached. These results are in excellent agreement with those found in the literature [40, 44, 64, 73, 92, 93].

A qualitatively different behaviour is predicted by the models using $10 \ tw3d$ or t3d elements, as shown in Figure 7.7. A stable bifurcation point is now reached at a slightly higher value of the critical moment. The secondary path loses its stability at a limit point, for a value of the moment of about $1.20M_{cr}$. In order to confirm these results, the analysis was repeated using a model with 576 triangular shell elements for one half of the frame. A good agreement with the beam model is observed up to a value of the apex displacement of about one half of the frame height. Over this value the quantitative differences are more pronounced. According to the author's opinion, these differences originate from the very large height to thickness ratio of the cross-section. As a result, in the large displacement regime, the cross-section can no longer be assumed as undeformable in its plane and a beam analysis is not appropriate. Finally, it can be noted that similar results were obtained by Sauer [86].

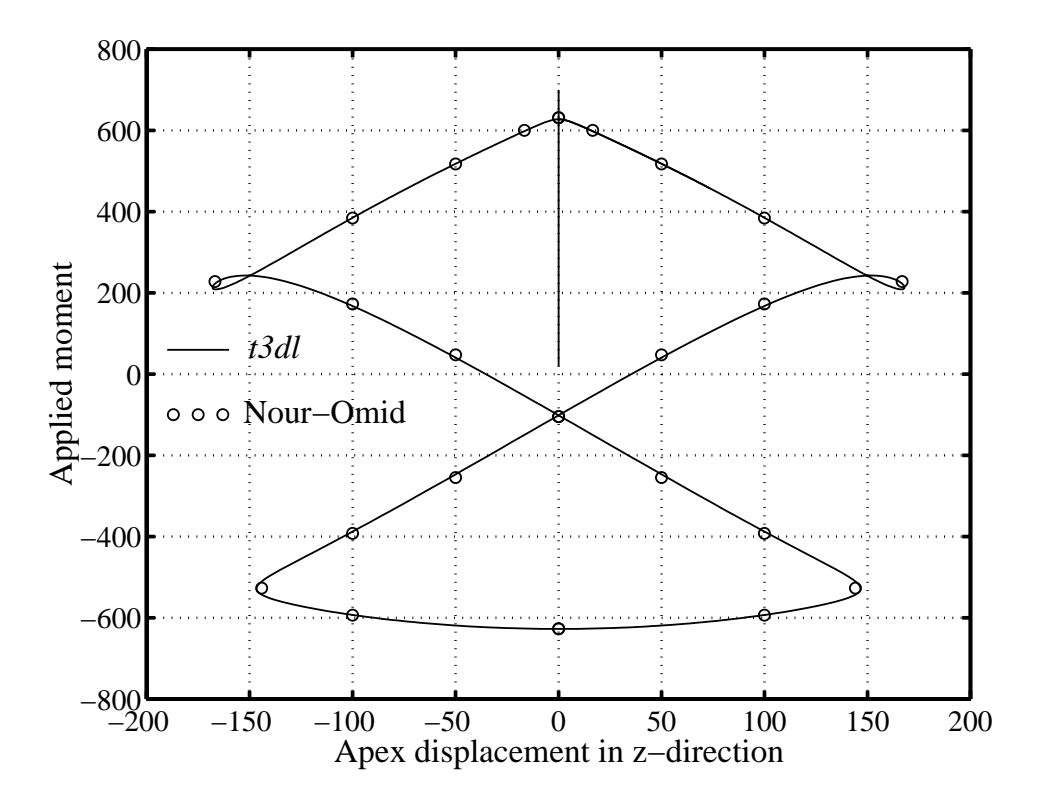


Figure 7.6: Right angle frame: post-buckling behaviour; t3dl element.

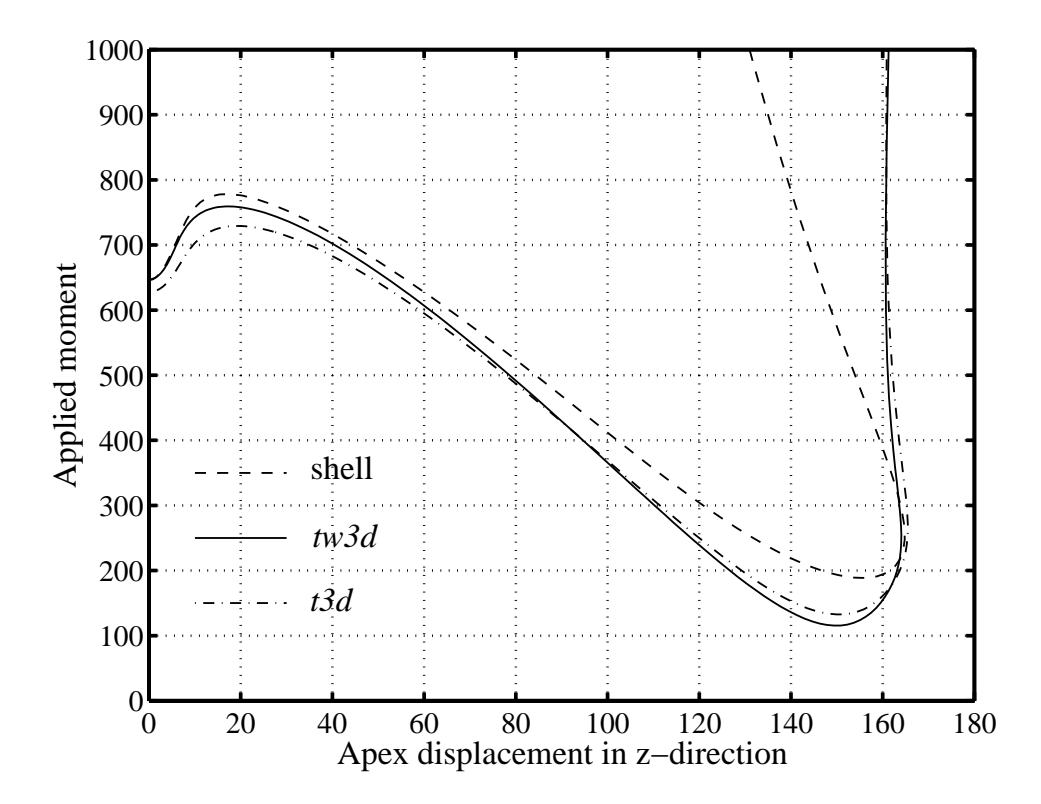


Figure 7.7: Right angle frame: post-buckling behaviour; tw3d and t3d elements.

7.4 Example 4, non-linear torsion

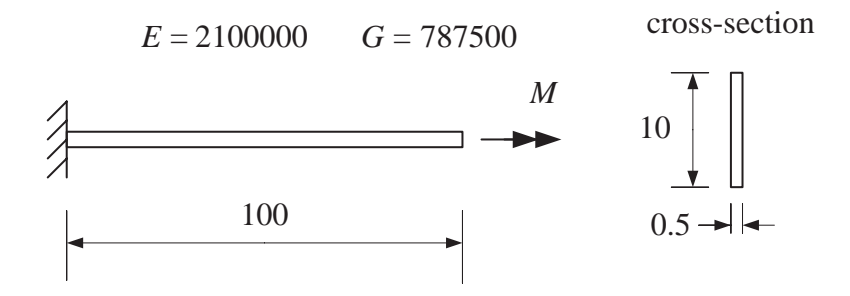


Figure 7.8: Non-linear torsion of a cantilever.

The non-linear torsion of the cantilever beam, depicted in Figure 7.8, was investigated. The non-trivial cross sectional characteristics are J=0.40433 and $I_{\omega}=0.85976$. The results obtained using 20 tw3d elements are shown in Figure 7.9 and compared with the analytical solution [27] based on Vlasov's beam theory. Very good agreement between the two solutions is observed.

Note that for a beam subjected to pure torsion, the only non-zero nodal displacements are the translations along and rotations around the longitudinal axis of the beam. Consequently, the co-rotational framework in itself will not introduce any

non-linearity. The non-linear character of the solution shown in Figure 7.9, is entirely generated by the so-called Wagner term included in the local element definition. The absence of this term, as in the case of the t3dl or b3dl elements, will result in a purely linear solution.

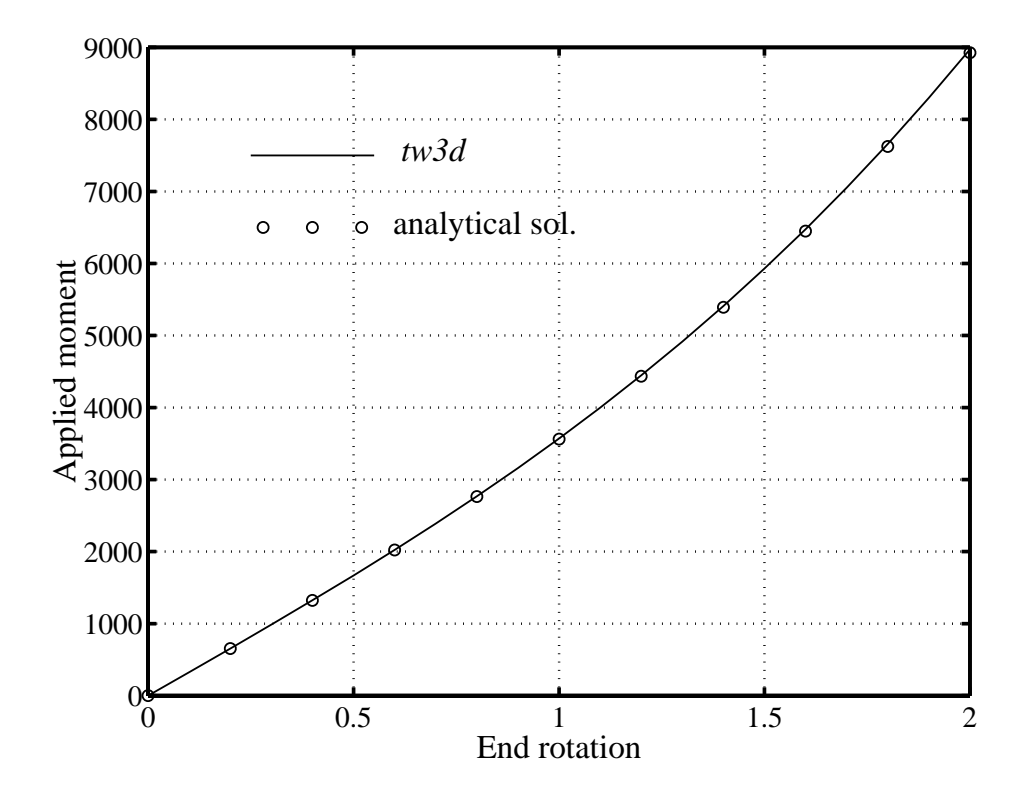


Figure 7.9: Non-linear torsion of a cantilever: moment versus end-rotation.

7.5 Example 5, channel-section beam

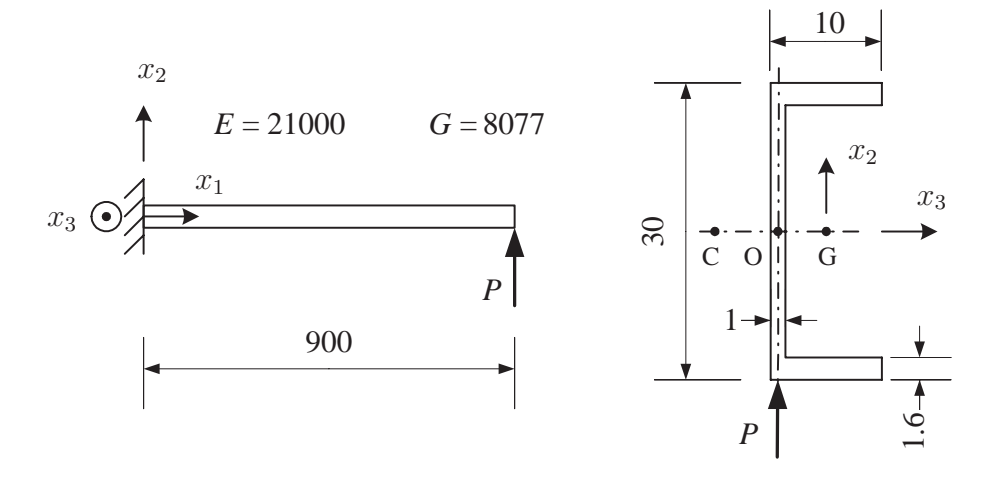


Figure 7.10: Channel-section beam.

The example presented in Figure 7.10 was introduced by Gruttmann et al. [40,41]. It refers to a channel-section beam, clamped at one end and subjected to a tip force at the free end. The parameters of the cross-section are

$$A = 58.8 \qquad J = 34.994 \qquad I_{22} = 8063.4 \qquad I_{33} = 564.25 \qquad I_{2r} = 0$$

$$I_{3r} = 10827 \qquad I_{rr} = 1676005 \qquad I_{\omega} = 79917 \qquad {\rm OG} = 2.449 \qquad {\rm OC} = 3.567$$

The results, obtained using 20~bw3d elements, are shown in Figure 7.11. Very similar results were obtained using 20~tw3d elements. These results are in excellent agreement with those obtained in [41] using beam elements and with the results provided by a shell element model. The shell model used a $(4+12+4) \times 180$ mesh with 7200 triangular elements.

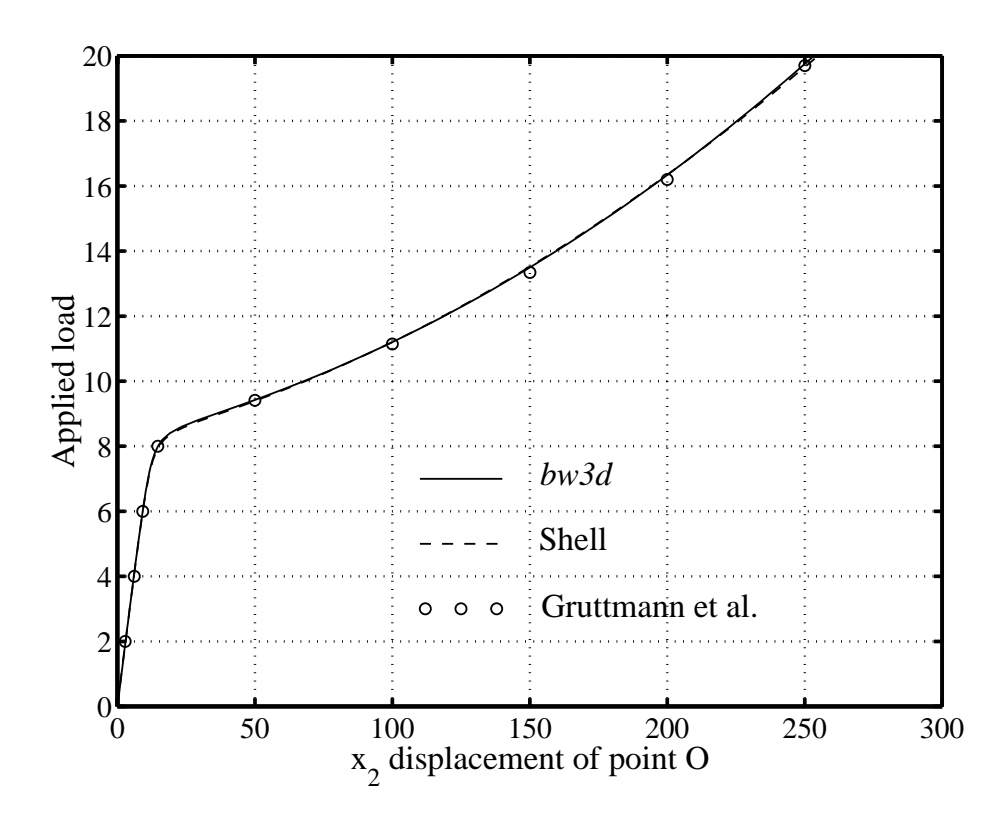


Figure 7.11: Channel-section beam: load-displacement diagram.

7.6 Example 6, torsional buckling

The torsional buckling of the beam depicted in Figure 7.12 was analysed. The parameters of the cross-section are

$$A = 12.8 \qquad J = 0.683 \qquad I_{22} = I_{33} = 136.62 \qquad I_{rr} = 10493 \qquad I_{\omega} = 3.641$$

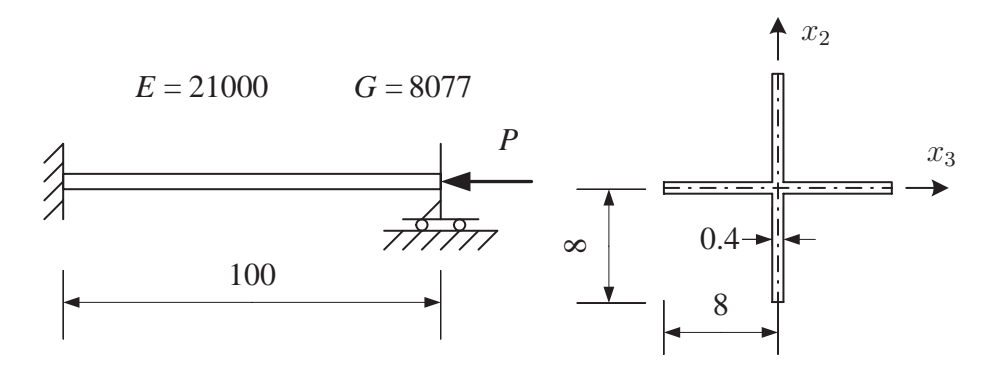


Figure 7.12: Torsional buckling.

All degrees of freedom including warping, are set to zero at the left end and only the axial displacement is permitted at the other end. Since the cross-section is bisymmetrical and the axial load is applied at the centroid of the cross-section, the bending and torsional buckling modes are uncoupled.

The analysis was initiated by isolating the first three critical points on the fundamental path of the beam. The critical modes are torsional modes with 1,2 and 3 half-waves, respectively. The corresponding critical loads, obtained using a mesh with $10 \ bw3d$ elements, are listed in Table 7.1. These results are in excellent agreement with the analytical solutions given by Timoshenko and Gere [97] based on Bernoulli beam theory with Vlasov warping. Rigorously speaking, only the bw3d element matches these assumptions. However, since for the present problem the effects of the bending shear strains on the torsional buckling modes are negligible, the tw3d element was also included in the comparison. Note that a finer mesh of tw3d elements is needed in order to obtain the same level of accuracy as for bw3d, especially for the higher buckling modes. This situation originates from the fact that tw3d is defined using linear interpolation functions.

No.	Theory [97]	10 bw3d	10 tw3d	20 tw3d	mode
1	272.57	272.57	273.55	272.80	torsional (1h-w)
2	287.35	287.38	291.99	288.40	torsional (2h-w)
3	314.99	315.17	334.00	318.89	torsional (3h-w)

Table 7.1: Torsional buckling: critical loads.

Using a model with 20 bw3d elements, a post-buckling analysis was also performed. The results, plotted in Figure 7.13, are in excellent agreement with those obtained from a shell model with 1600 triangular elements.

Finally note that for the present problem, an analysis using a linear local strain definition will completely miss the torsional modes. This comes from the fact that the only non-zero displacements on the fundamental path are the axial ones. In such a situation, as also shown in example 4, the co-rotational framework does not induce any coupling between the axial and torsional effects.

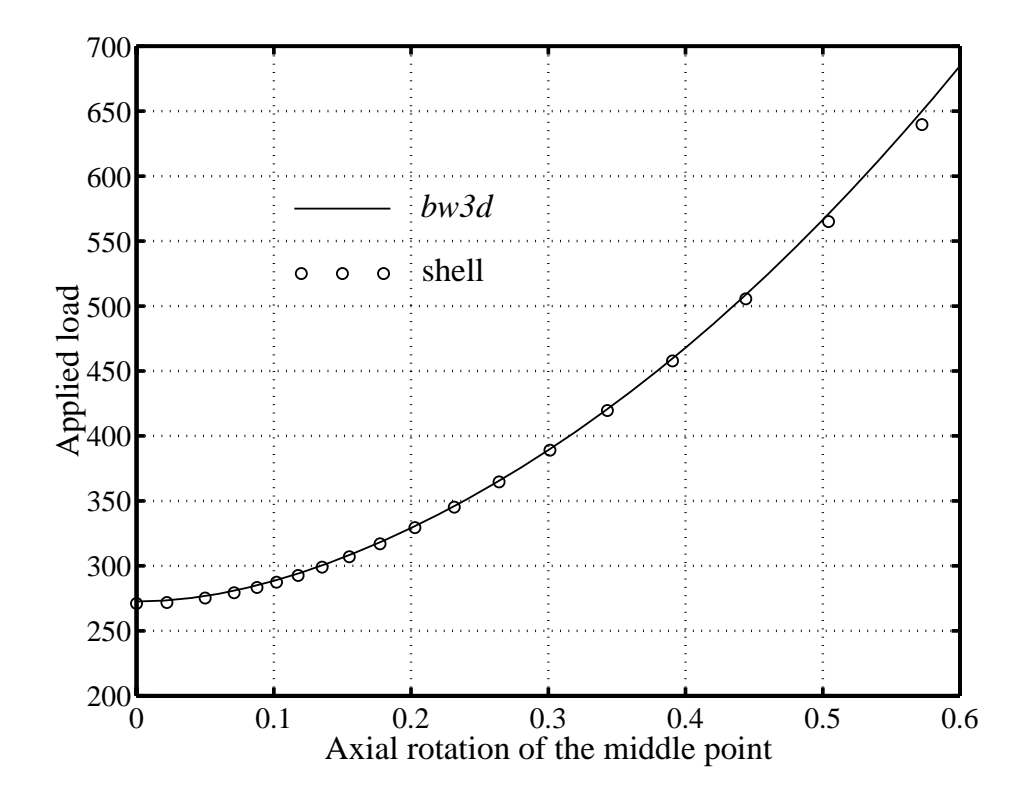


Figure 7.13: Torsional buckling: post-bifurcation behaviour.

7.7 Example 7, lateral torsional buckling

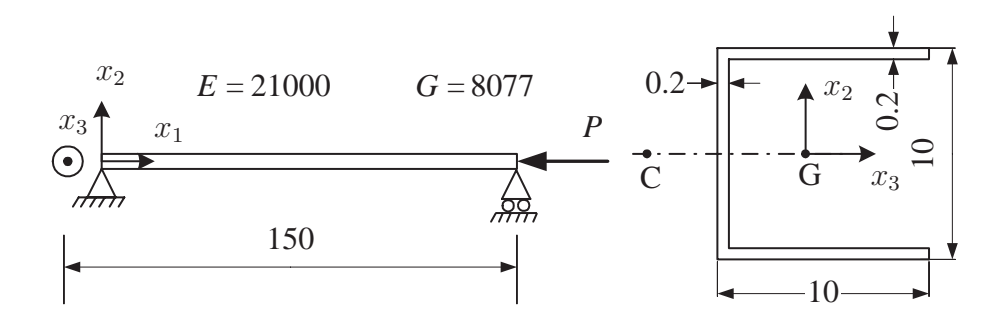


Figure 7.14: Lateral torsional buckling.

This example, taken from [41], concerns the lateral torsional buckling of the beam depicted in Figure 7.14. The characteristics of the cross-section are

$$A=5.92 \qquad J=0.0792 \qquad I_{22}=110.8 \qquad I_{33}=64.49 \qquad I_{2r}=0$$

$$I_{3r}=209.06 \qquad I_{rr}=6182.9 \qquad I_{\omega}=1108.2 \qquad \mathrm{GC}=7.55$$

The axial load is applied at the centroid of the cross-section. The beam is assumed as simply supported. The rotation around the axis of the beam is set to zero at

both supports. Warping deformations are however permitted. Since the cross-section is not bi-symmetrical, both bending and torsional effects are included in the buckling mode. The buckling loads, obtained using different discretisations are listed in Table 7.2. Very good agreement with the theoretical solution given in [97] is obtained.

Table 7.2: Lateral torsional buckling loads.

Theory [97]	10 <i>bw3d</i>	10 tw3d	20 tw3d
115.54	115.62	117.18	115.81

7.8 Example 8, lateral buckling of a cantilever

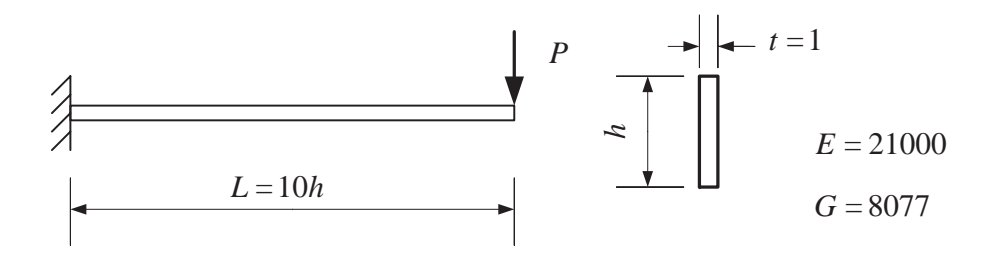


Figure 7.15: Lateral buckling of a cantilever.

This example concerns the lateral buckling of the narrow rectangular cantilever beam shown in Figure 7.15. At the free end, a transversal load is applied at the centroid of the cross-section. The load is described as $P = \lambda P_o$ with P_o given by

$$P_o = \frac{1}{L^2} \sqrt{EIGJ} \qquad I = \frac{ht^3}{12} \qquad J = \frac{ht^3}{3}$$
 (7.1)

The buckling loads were evaluated for various t/h ratios. The obtained buckling load factors λ_{cr} are listed in Table 7.3. Both the b3d and b3dl elements were used in the analysis (10 elements meshes). For comparison purposes the theoretical buckling loads according to Timoshenko and Gere [97], are also listed in the table. Note that for low values of the t/h ratio, significant pre-buckling deflections occur. Varying this parameter will thus illustrate the influence of pre-buckling displacements on the critical load.

Table 7.3: Lateral buckling of a cantilever: λ_{cr} for various heights h.

h	Theory [97]	10 <i>b3dl</i>	10 <i>b3d</i>
50	4.013	4.039	4.039
10	4.085	4.099	4.099
5	4.324	4.313	4.314
3	5.030	5.072	5.077

One particularly relevant parameter for this problem refers to the specific point of application of the force P. Thus, Table 7.4 lists the results obtained for three different cases: P applied at the centroid, top and bottom of the end cross-section. A very good agreement with the theoretical solutions given in [97] can be noted.

Table 7.4: Lateral buckling of cantilever: λ_{cr} for various load positions (h = 50).

position	Theory [97]	10 <i>b3dl</i>	10 <i>b3d</i>
centroid	4.013	4.039	4.039
bottom	4.175	4.198	4.198
top	3.851	3.859	3.859

The post-buckling behaviour of the cantilever was also investigated with the load applied at the centroid of the end cross-section. Two cases were considered. For the first one, h=10. All three Bernoulli elements, i.e. bw3d, b3d and b3dl, were considered in the analysis. The Saint-Venant torsion modulus and the warping constant were taken as J=3.123 and $I_{\omega}=6.643$. The results depicted in Figure 7.16 were obtained using 20 element meshes. The results obtained with the element bw3d are in excellent agreement with those provided by a shell model using a mesh with 720 triangular elements. The results obtained with the elements b3d and b3dl are a little bit different, which shows that warping has some minor effect.

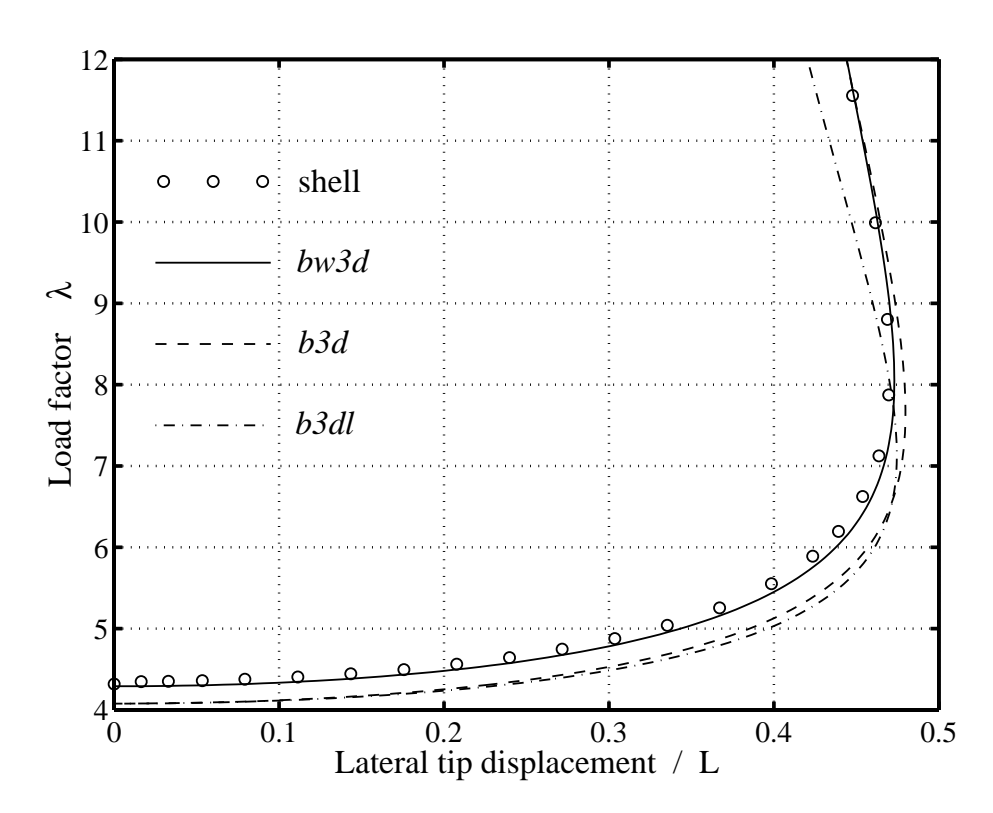


Figure 7.16: Lateral buckling of a cantilever: post-buckling behaviour h/t = 10.

The numerical data for the second case were taken from the literature [55, 73]. Referring to the notations in Figure 7.15, the following values of the geometrical, mechanical and cross-sectional parameters were used

$$L = 240 \qquad h = 30 \qquad t = 0.6 \qquad J = 2.133$$

$$I_{\omega} = 40.43 \qquad E = 71.24 \cdot 10^6 \qquad G = 27.19 \cdot 10^6$$

The results shown in Figure 7.17, were obtained using the same mesh and element types as before. In addition, the results from a shell model with 576 triangular elements, are also plotted in the figure. For the bw3d element, good agreement with the shell results is obtained up to a lateral displacement of about 0.45L. The situation is very similar to that in example 3. For very high h/t ratios, in the large displacement regime, a beam analysis is not appropriate due to significant inplane deformations of the cross-section. This explanation is also supported by the results obtained in the previous case h/t = 10 which showed an excellent agreement between the shell and beam models. It is worth mentioning here, that the results obtained using the bw3d and shell elements are significantly different from those of Kouhia [55]. According to the author's opinion, the differences are due to the fact that in the cited reference, an averaged form of the Wagner term (see Section 4.3.2) is used in the definition of the element.

Finally note that the b3dl element (which is also used in [73]) appears to be too crude in order to model correctly the post-buckling behaviour of the cantilever beam, especially when the ratio h/t is high.

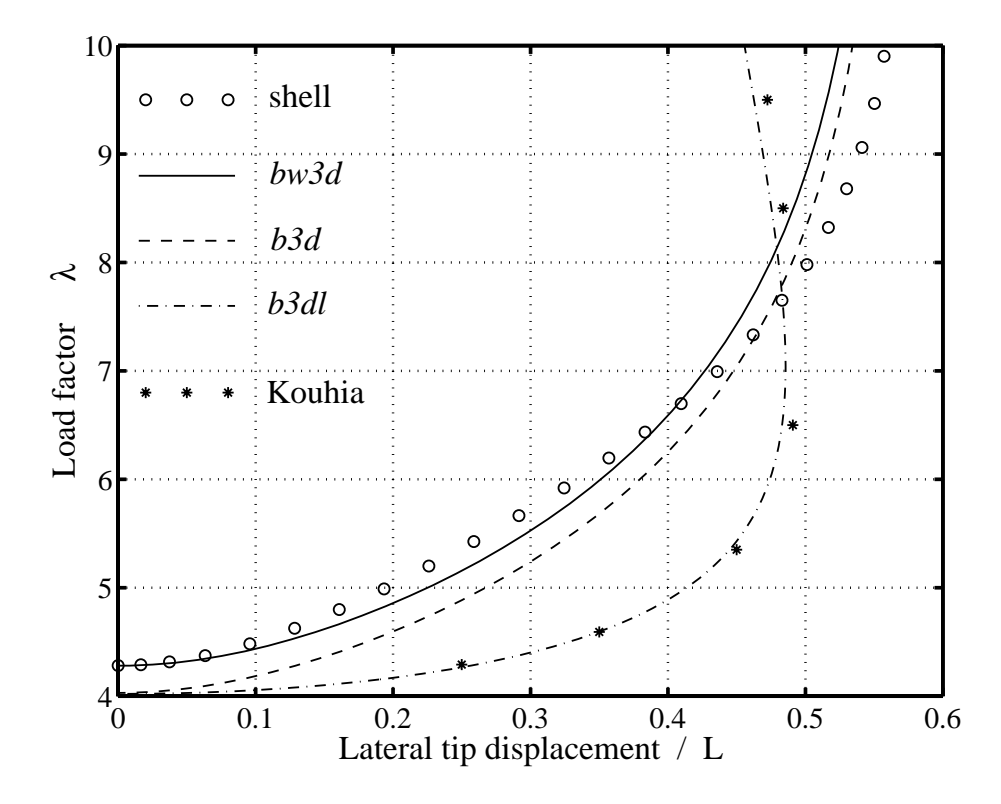


Figure 7.17: Lateral buckling of a cantilever: post-buckling behaviour h/t = 50.

7.9 Example 9, lateral buckling with warping

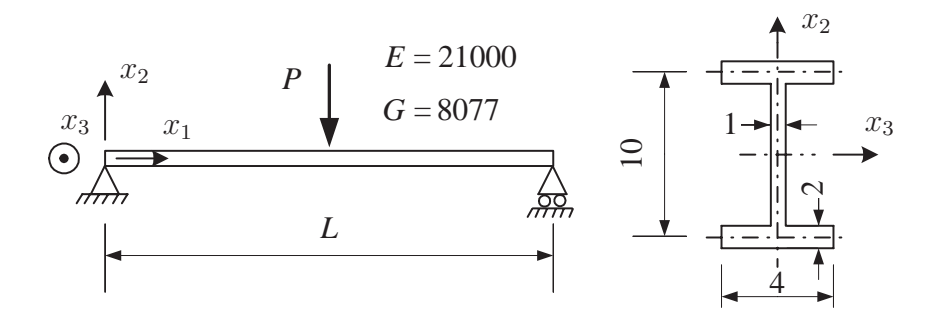


Figure 7.18: Lateral buckling with warping.

This example concerns the lateral buckling of the simply supported I beam shown in Figure 7.18. The characteristics of the cross-section are

$$A = 24 \qquad J = 24.67 \qquad I_{22} = 448 \qquad I_{33} = 22 \qquad I_{rr} = 12352 \qquad I_{\omega} = 533.3$$

A transversal load P is applied at the centroid of the midsection. The load is described as $P = \lambda P_o$ with P_o given by

$$P_o = \frac{1}{L^2} \sqrt{EI_{33}GJ} (7.2)$$

A theoretical solution to this problem was given by Timoshenko and Gere [97]. This solution takes into account the effect of warping but neglects the effect of prebuckling bending deformations. Thus, in order to enable a comparison with the numerical results, the value of I_{22} was multiplied by a factor of 100. The buckling load factors λ_{cr} , obtained using a discretisation with 20 bw3d elements, are listed in Table 7.5 for different values of the length L. An excellent agreement with the theoretical solutions can be noted.

Table 7.5: Lateral buckling with warping: critical load factors λ_{cr} .

$\frac{L^2GJ}{EI_{\omega}}$	L	Theory [97]	20 bw3d
80	67.1	18.1	18.1
160	94.8	17.5	17.6
320	134.1	17.2	17.3

7.10 Example 10, L frame

The final example concerns the post-buckling behaviour of the L frame shown in Figure 7.19. The non trivial characteristics of the cross-section are J=2.133 and $I_{\omega}=40.43$. The frame is loaded by a horizontal force P applied at the centroid

of the end cross-section. Two different modelling alternatives were tested in the analysis. The first one disregards the finite dimensions of the connection and uses beam elements for the whole length of the frame members. For the second one, the connection area is modelled using rigid links, as shown in Figure 7.19. In both cases, a discretisation with $10 \ tw3d$ elements per member was used. The obtained results are shown in Figure 7.20. The rigid link model gives a reasonably good fit with shell results obtained using a mesh with 512 triangular elements. Note that the use of rigid links amounts to assuming the connection area as infinitely rigid, which is certainly not the case. This explains the slightly overstiff behaviour of the rigid link beam model.

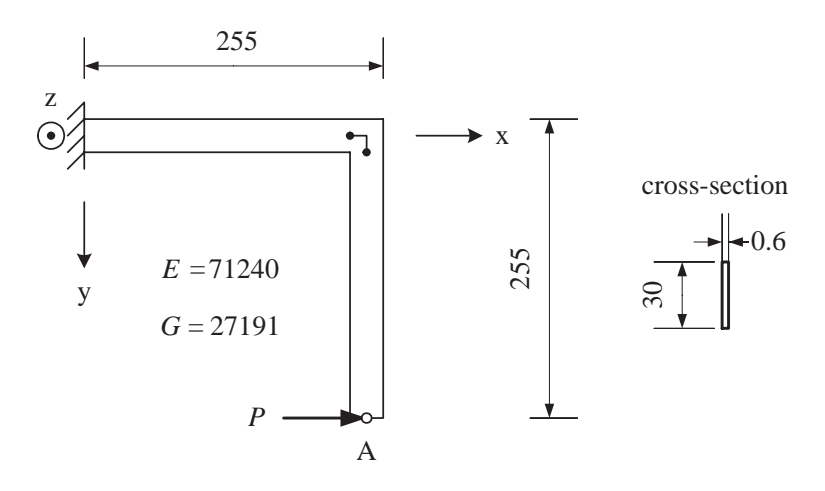


Figure 7.19: L frame.

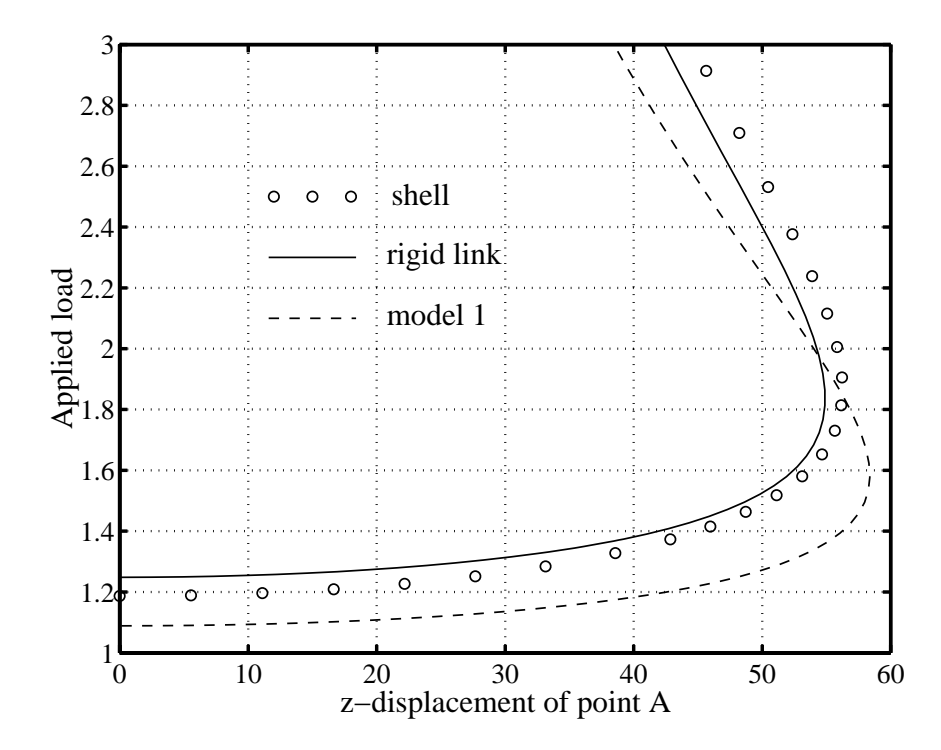


Figure 7.20: L frame: post-buckling behaviour.

Chapter 8

Elastic isolation – examples

The purpose of the eight problems included in this chapter is to compare the performances of the procedure presented in Section 5.2 with the classical approach of Wriggers et al. [104, 105]. For that, the number of iterations required for convergence is given in tables. Note that for the present method, both the total number of iterations and the number of the iterations which used the extended system (in parenthesis) are given. In order to allow a better comparison, for each structure, the isolation procedure was initiated from several equilibrium points.

The tolerance, tol, is given for each example. For the classical approach, this refers to the norm of the residual of the extended system. For the present method, its definition is given in Table 5.3.

The 2D numerical examples were solved by using a local linear Timoshenko element, while the 3D examples were computed using the local Timoshenko element t3d presented in Section 4.3.4.

8.1 Example 1, 2D clamped arch

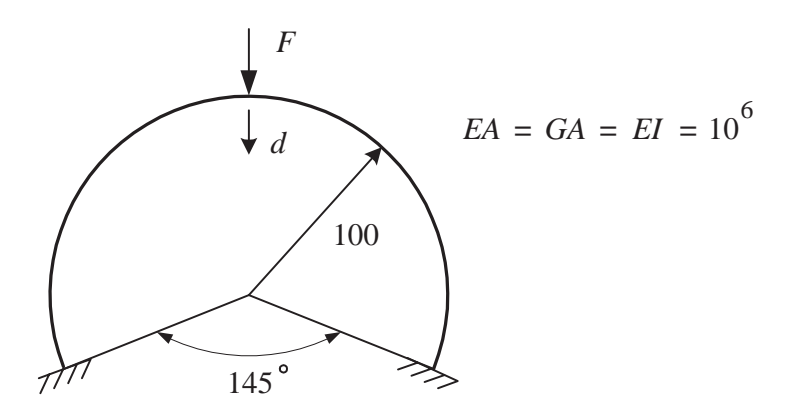


Figure 8.1: 2D clamped arch.

This example, introduced by Wriggers and Simo [104] is depicted in Figure 8.1. The arch is discretised into 20 elements. The tolerance is set to $tol = 10^{-6}$. As shown in Figure 8.2, the structure exhibits a limit point at a load $F_{cr} = 972.9$ and for a displacement $d_{cr} = 72.13$. The isolation procedure was initiated from five different points. The results, presented in Table 8.1, show that if the starting point is far from the critical one, the present method is more reliable than the classical approach.

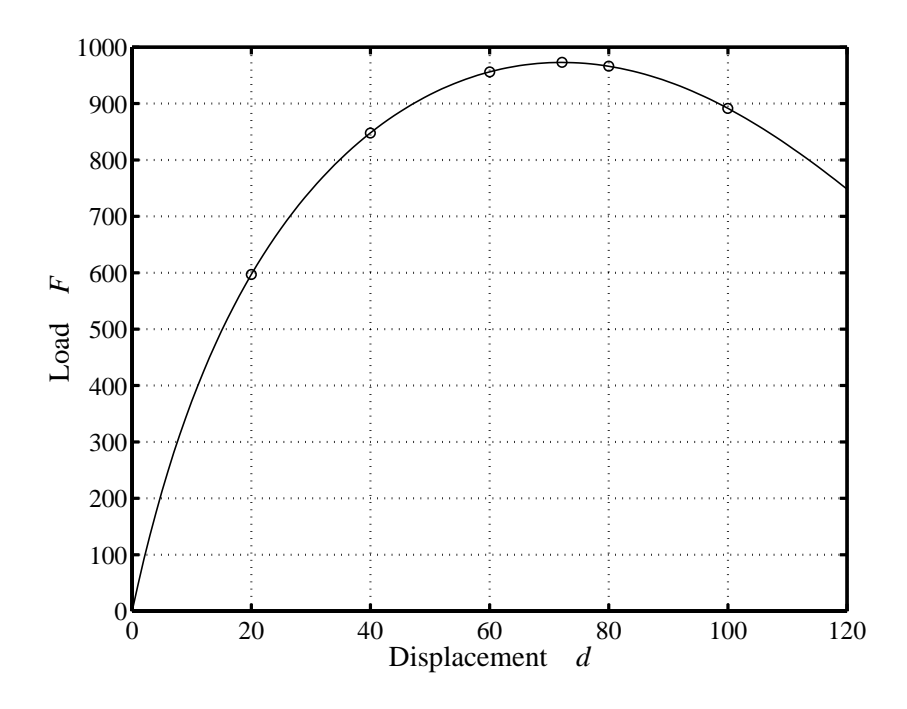


Figure 8.2: 2D clamped arch: equilibrium path.

Table 8.1: 2D clamped arch: isolation – $d_{cr} = 72.13$

Starting point	d = 20	d = 40	d = 60	d = 80	d = 100
Classical approach	no	8	5	5	no
Present method	11 (6)	9 (4)	6 (4)	5 (4)	9 (4)

8.2 Example 2, 2D simply supported arch

This example, shown in Figure 8.3, is similar to the previous one, except that the arch is simply supported at both ends. With these new boundary conditions, a bifurcation point is obtained on the fundamental path for a force $F_{cr} = 334.9$, as shown in Figure 8.4. The convergence properties of the two procedures, given in Table 8.2 are very similar. In order to illustrate the switching between the extended system and pure equilibrium iterations under load control, the details of the present approach are given in Table 8.3 for the lowest starting point. Along the secondary path, a limit point is obtained at $F_{cr} = 423.1$, $d_{cr} = 86.65$. The results of its

isolation, presented in Table 8.4, show that the present method is better if the starting point is far from the limit one.

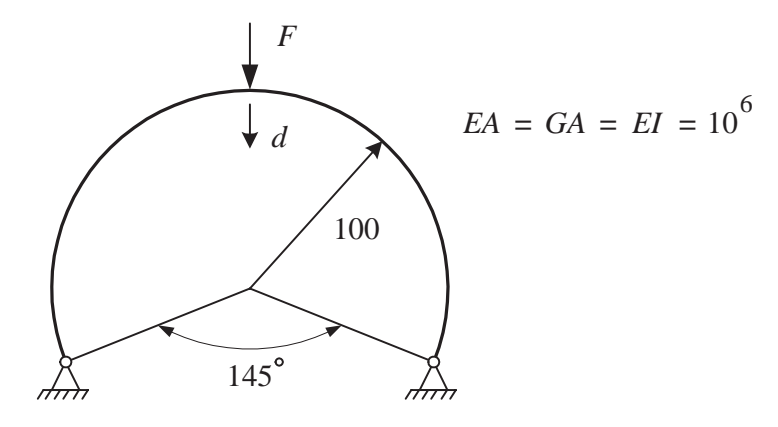


Figure 8.3: 2D simply supported arch.

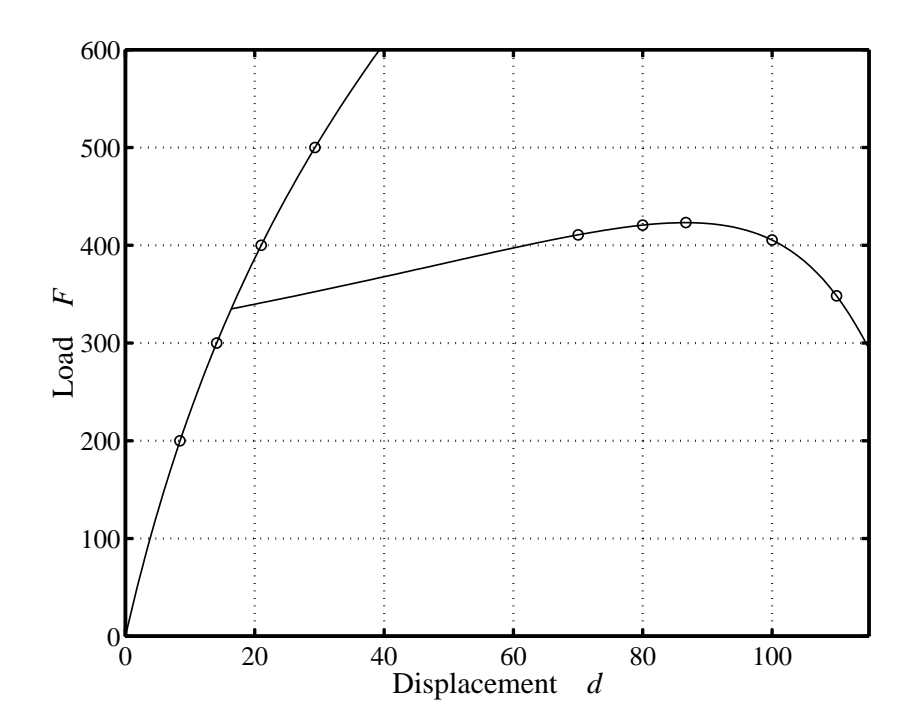


Figure 8.4: 2D simply supported arch: equilibrium paths.

Table 8.2: 2D simply supported arch: isolation of the bifurcation pt – $F_{cr}=334.9$

Starting point	F = 200	F = 300	F = 400	F = 500
Classical approach	5	4	5	6
Present method	6 (4)	4 (3)	6 (3)	7 (4)

Table 8.3: 2D simply supported arch: details of the present approach.

Iter.	Residual norm	Lowest eigenvalue	Force	Type of the next iteration
0	$1.192 \cdot 10^{-9}$	$1.164 \cdot 10^{-1}$	200.00	extended system
1	$1.176 \cdot 10^4$	$2.408 \cdot 10^{0}$	331.56	equilibrium equations only
2	$3.209 \cdot 10^2$	$5.631 \cdot 10^{-3}$	331.56	extended system
3	$7.804 \cdot 10^{1}$	$3.224 \cdot 10^{-2}$	334.89	equilibrium equations only
4	$1.786 \cdot 10^{-1}$	$1.738 \cdot 10^{-5}$	334.89	extended system
5	$3.372 \cdot 10^{-4}$	$1.525 \cdot 10^{-7}$	334.91	extended system
6	$3.100 \cdot 10^{-9}$	$1.226 \cdot 10^{-10}$	334.91	

Table 8.4: 2D simply supported arch: isolation of the limit point – $d_{cr} = 86.65$

Starting point	d = 70	d = 80	d = 100	d = 110
Classical approach	no	9	10	16
Present method	21 (5)	8 (4)	11 (5)	20 (5)

8.3 Example 3, 2D shallow arch

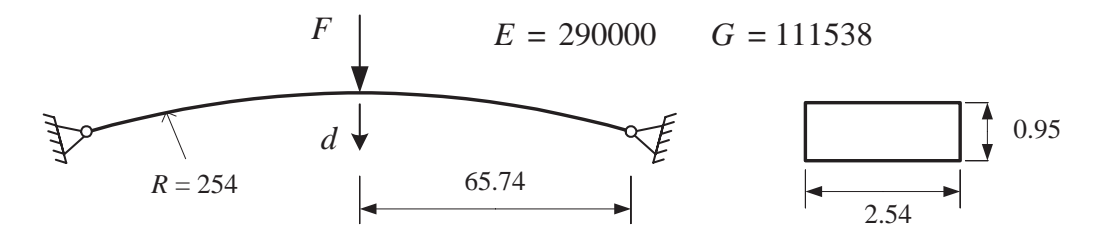


Figure 8.5: 2D shallow arch.

The structure presented Figure 8.5 is discretised into 40 elements. The tolerance is set to $tol = 10^{-6}$. The load–displacement diagram in Figure 8.6 shows that a limit point is reached at the values $d_{cr} = 2.917$, $F_{cr} = 45.82$. The results concerning the isolation are given in Table 8.5. For this structure, both methods worked very well. This is probably due to the fact that the deformations are relatively small.

Table 8.5: 2D shallow arch: isolation – $d_{cr} = 2.917$

Starting point	d = 0.5	d = 1.0	d = 2.0	d = 4.0
Classical approach	8	7	6	6
Present method	8 (8)	8 (6)	6 (5)	8 (5)

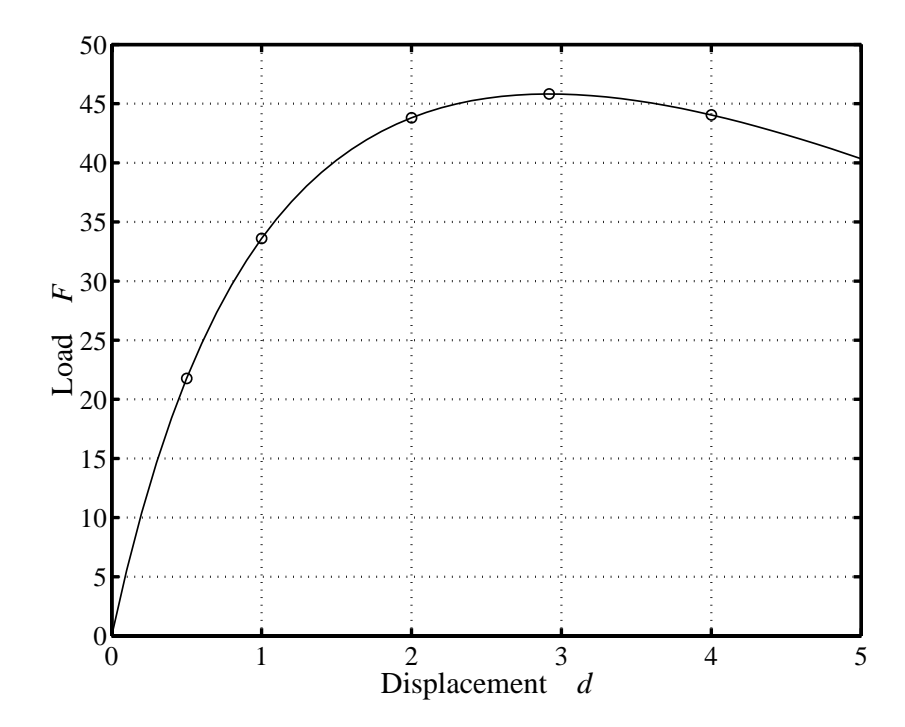


Figure 8.6: 2D shallow arch: equilibrium path.

8.4 Example 4, deep circular arch

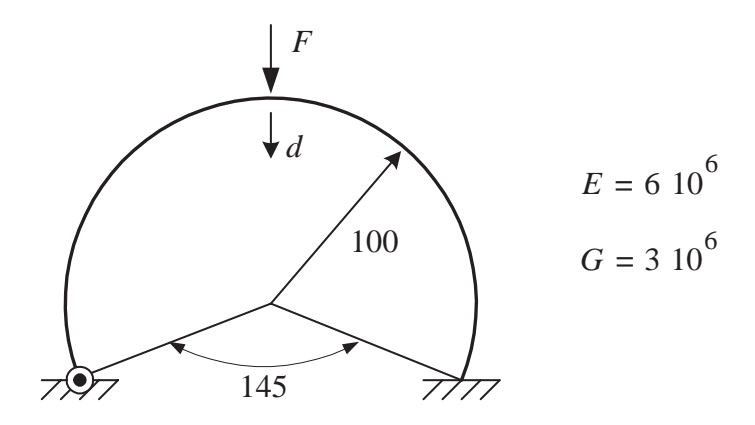


Figure 8.7: Deep circular arch.

This example, shown in Figure 8.7 has been introduced by Cardona and Huespe [12]. The arch is fully clamped at one end and only the in plane rotation is permitted at the other end. The tolerance is set to $tol = 10^{-6}$. The structure is discretised using 40 elements. The characteristics of the square cross-section are

$$A = 1.414 \qquad I_{22} = I_{33} = 0.1667 \qquad J = 0.4741 \qquad I_{rr} = 0.1100$$

The structure (see Figure 8.8) presents a bifurcation point at a load value $F_{cr} = 256.7$, corresponding to an out of plane bifurcation mode. For this problem (see Table 8.6), both isolation methods give almost similar results.

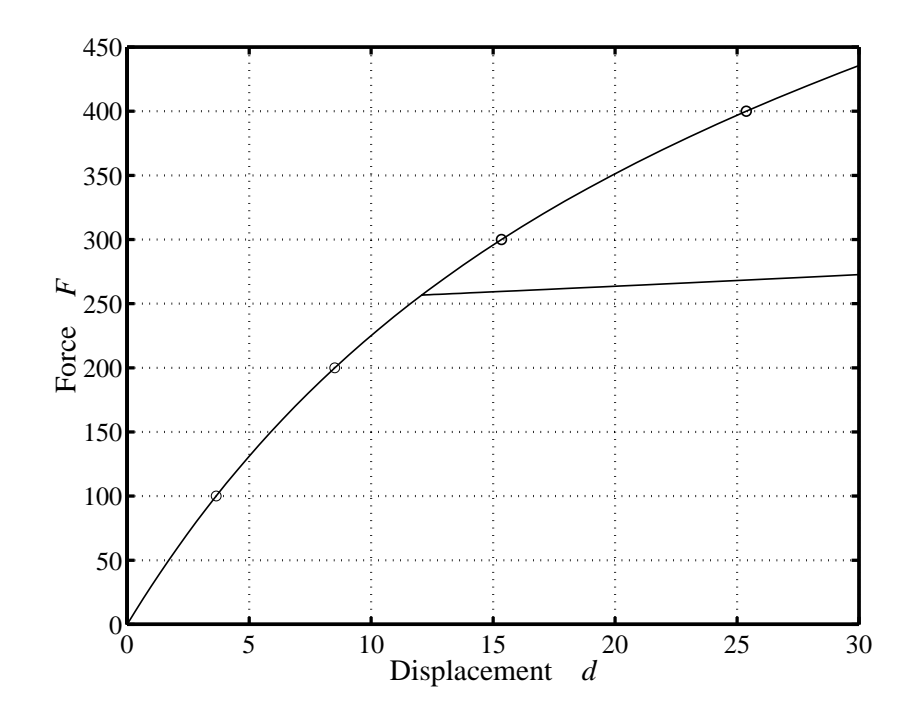


Figure 8.8: Deep circular arch: equilibrium paths.

Table 8.6: Deep circular arch: isolation – $F_{cr} = 256.7$

Starting point	F = 100	F = 200	F = 300	F = 400
Classical approach	6	6	6	12
Present method	8 (4)	6 (2)	6 (2)	9 (3)

8.5 Example 5, narrow cantilever

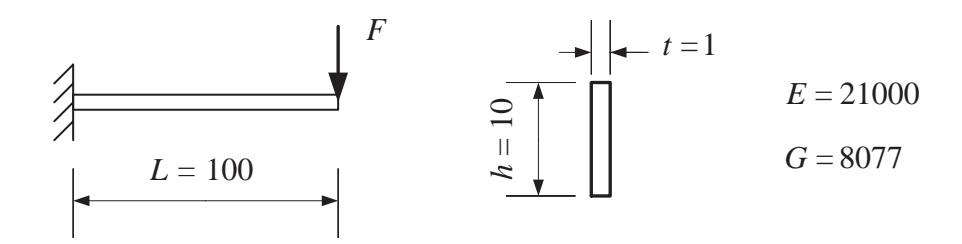


Figure 8.9: Narrow cantilever.

This example concerns the lateral buckling of the narrow rectangular cantilever beam shown in Figure 8.9. At the free end, a transversal load is applied at the centroid of the cross-section. The load is described as $F = \lambda F_o$ with F_o given by:

$$F_o = \frac{1}{L^2} \sqrt{EIGJ} \qquad I = \frac{ht^3}{12} \qquad J = \frac{ht^3}{3}$$
 (8.1)

The beam is discretised into 20 elements and the tolerance is set to $tol = 10^{-8}$. The load–displacement diagram is given in Figure 8.10 and the convergence properties of the isolation procedures are listed in Table 8.7. The lateral buckling is obtained for a load factor $\lambda_{cr} = 4.083$, which is very close to the analytical result (4.085) obtained by Timoshenko and Gere [97]. For this example, the pre-buckling deformations are linear and very small, and both methods converge rapidly.

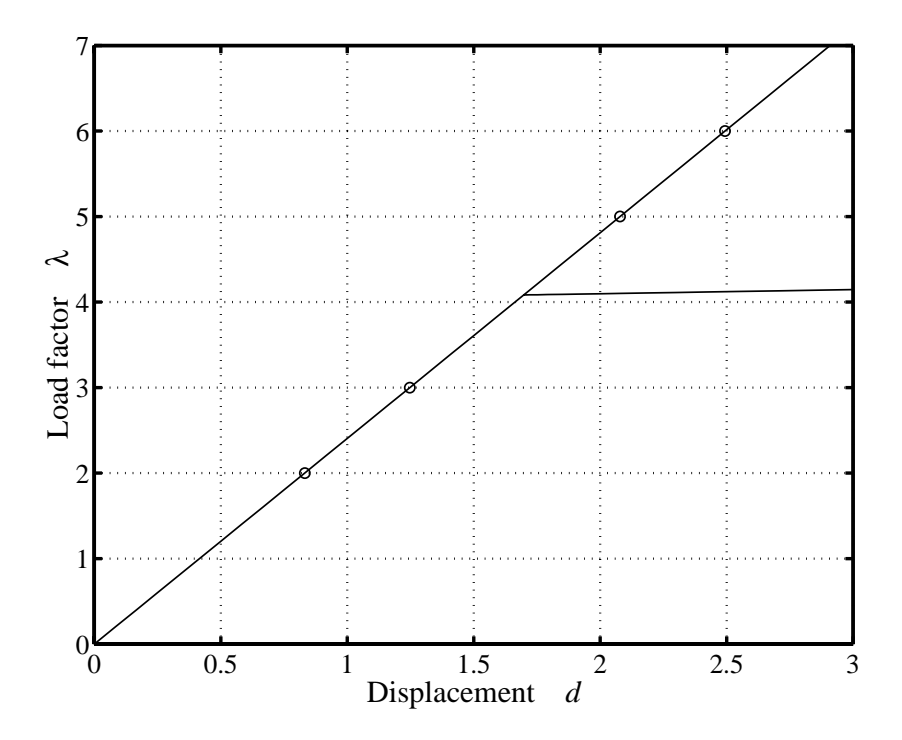


Figure 8.10: Narrow cantilever: equilibrium paths.

Table 8.7: Narrow cantilever: isolation – $\lambda_{cr} = 4.083$

Starting point	$\lambda = 2$	$\lambda = 3$	$\lambda = 5$	$\lambda = 6$
Classical approach	no	5	5	6
Present method	no	6 (5)	6 (4)	6 (6)

8.6 Example 6, L frame

This example, depicted in Figure 8.11, is also taken from Cardona and Huespe [12]. The frame is modelled by 16 elements. The tolerance is set to $tol = 10^{-7}$. As shown in Figure 8.12, the structure develops very large pre-buckling deformations before the bifurcation point ($F_{cr} = 1.243$) is reached. For this structure (see Table 8.8), the present method gives better results than the classical approach.

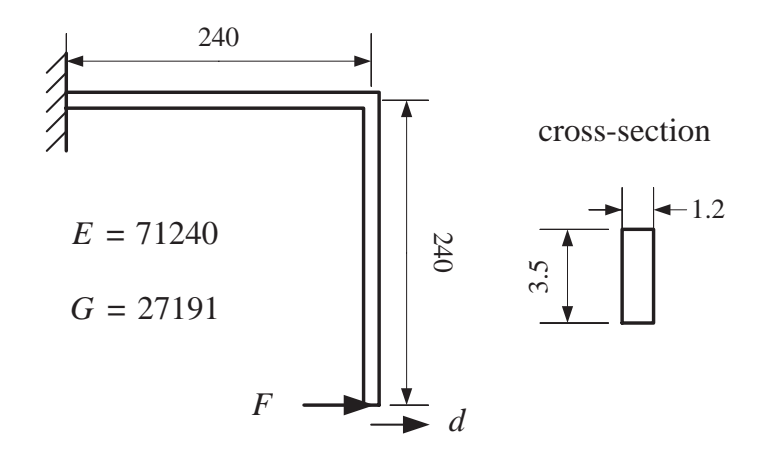


Figure 8.11: L frame.

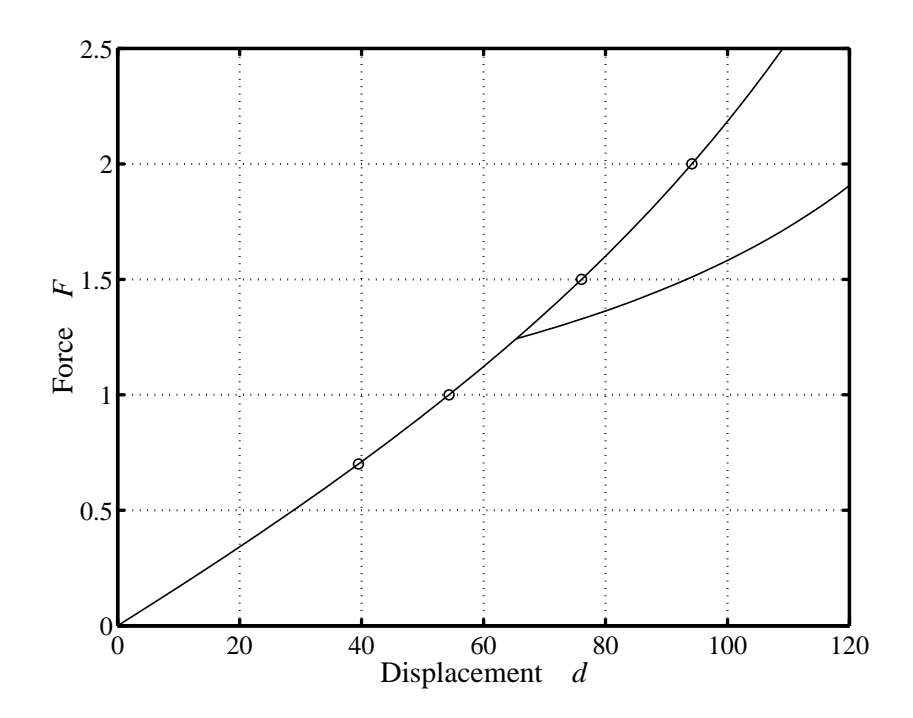


Figure 8.12: L frame: equilibrium paths.

Table 8.8: L frame: isolation – $F_{cr}=1.243$

Starting point	F = 0.7	F = 1.0	F = 1.5	F = 2.0
Classical approach	no	21	7	13
Present method	no	6 (3)	6 (3)	8 (4)

8.7 Example 7, cable hockling

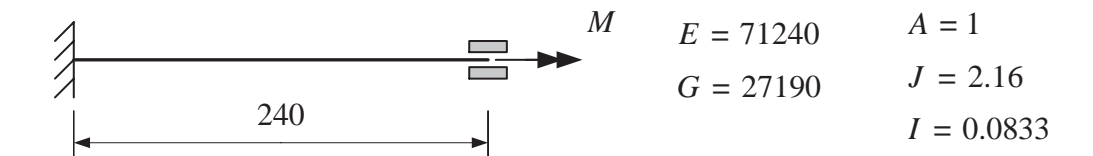


Figure 8.13: Cable hockling.

This classical example, see e.g. [52,64], is described in Figure 8.13. It concerns an initially straight cable built in at one end and submitted to a concentrated axial moment at the other end. At the loaded end, only the axial displacement and axial rotation are permitted. The finite element model consists of 20 elements. The tolerance is set to $tol = 10^{-6}$. The load–displacement diagram is plotted in Figure 8.14. The fundamental path corresponds to a pure torsion while the secondary path, initiated at a value of the applied moment $M_{cr} = 225.4$, is characterised by bending deformations. The results, given in Table 8.9, show that also for this structure, the present method performs better than the classical approach.

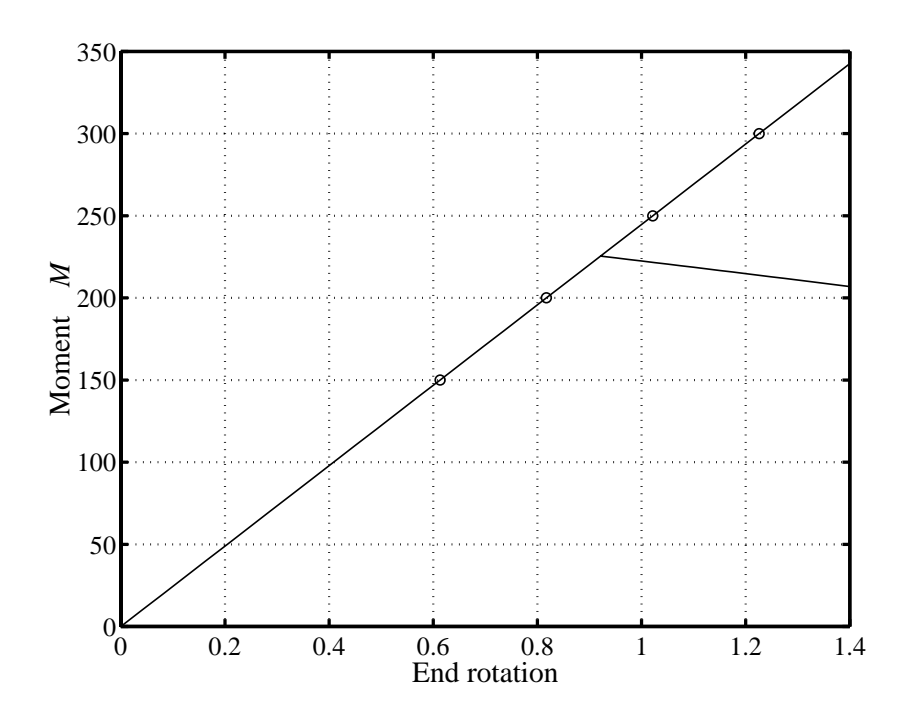


Figure 8.14: Cable hockling: equilibrium paths.

Table 8.9: Cable hockling: isolation – $M_{cr} = 225.4$

Starting point	M = 150	M = 200	M = 250	M = 300
Classical approach	11	26	14	26
Present method	4 (4)	3 (3)	3 (3)	4 (4)

8.8 Example 8, spatial frame

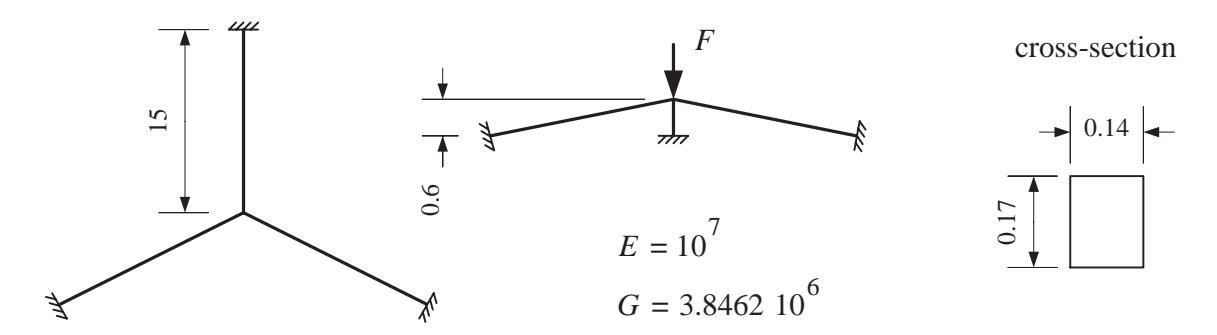


Figure 8.15: Spatial frame.

The last example concerns the spatial dome structure depicted in Figure 8.15. The structure is composed of three beams placed symmetrically with respect to the vertical axis and is loaded by a vertical force applied at its top. Each beam is discretised by 8 elements. The tolerance is set to $tol = 10^{-7}$.

As shown in Figure 8.16, several bifurcation points are present along the fundamental path. These points are relatively close to each other, which generates difficulties for the initialisation and convergence of the isolation procedures. This situation is illustrated in Figure 8.17. The fundamental path was computed using displacement control by imposing at each step a vertical displacement increment $\Delta d = 0.05$ at the top. Hence, at the equilibrium point corresponding to d = 0.1, the first bifurcation point was detected by the appearance of a negative eigenvalue λ_1 , see Table 8.10. However, due to the proximity of the second bifurcation point, λ_1 is not the lowest one in absolute value. Consequently, in order to isolate the first bifurcation point, ϕ_o , which is the eigenvector associated to λ_1 , cannot be evaluated using the iterative scheme (5.18). As a matter of fact, this system converges to λ_2 and both isolation procedures will then converge to the second bifurcation point. In this case, ϕ_o must be evaluated using a different numerical method. This operation may take some time, particularly for systems with large number of degrees of freedom.

A similar problem occurs at the equilibrium point corresponding to d=0.15. The second and third bifurcation points, are detected by the appearance of two additional negative eigenvalues, see Table 8.10. Note that λ_2 and λ_3 are double eigenvalues. In order to isolate the third bifurcation point, λ_3 and its associated eigenvector must be taken for g_o and ϕ_o . Since λ_3 is the lowest absolute eigenvalue, the iterative process (5.18) can be used to compute ϕ_o . However, in order to converge to the second bifurcation point, λ_2 and its associated eigenvector must be taken as initial values. In this case, ϕ_o must be calculated using a different numerical method.

The convergence characteristics for the isolation of the first three bifurcation points are reported in Table 8.11. For this example, the pre-buckling deformations are small, and both methods work very well.

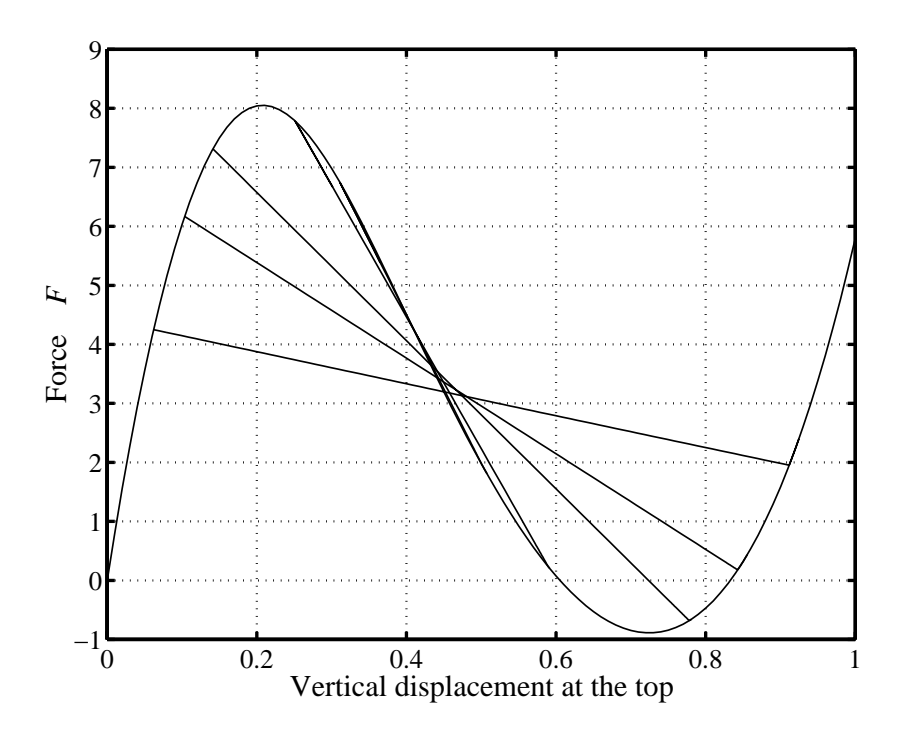


Figure 8.16: Spatial frame: equilibrium paths.

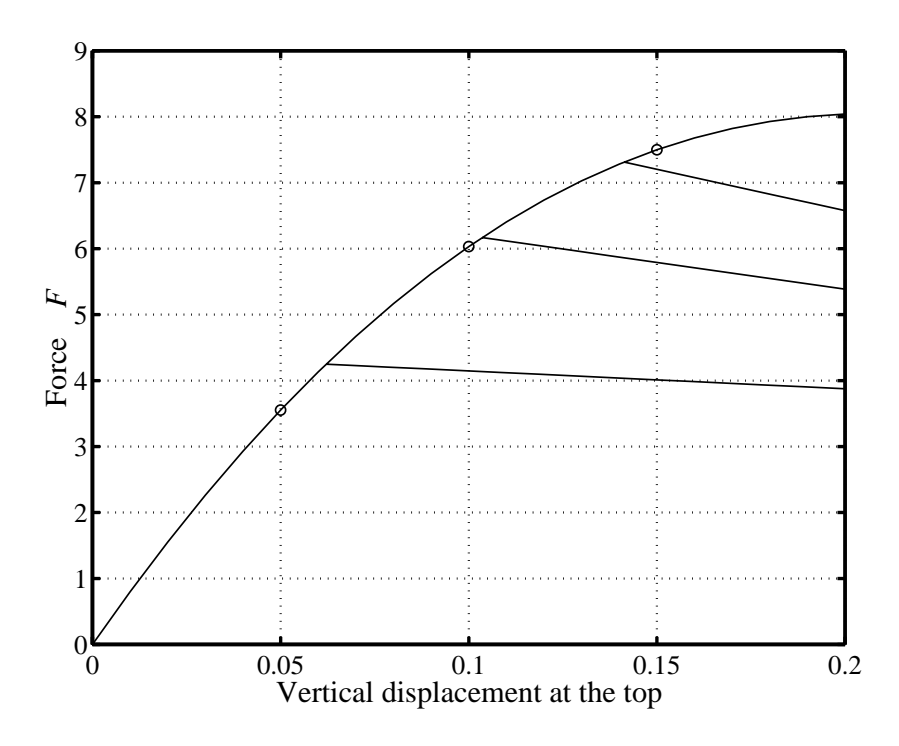


Figure 8.17: Spatial frame: near bifurcation points.

Table 8.10: Spatial frame: lowest eigenvalues of $\boldsymbol{K}.$

eq. pt.	λ_1	λ_2	λ_3
d = 0.10	-1.850(1)	+0.191 (2)	+1.892 (2)
d = 0.15	-4.174(1)	-1.883(2)	-0.359(2)

Table 8.11: Spatial frame: isolation.

Bifurcation point	$F_{cr} = 4.249$	$F_{cr} = 6.169$	$F_{cr} = 7.313$
Starting point	d = 0.10	d = 0.15	d = 0.15
Classical approach	4	4	3
Present method	4 (3)	4 (4)	3 (3)

Chapter 9

3D examples in elasto-plasticity

The test problems included in this chapter have two objectives. The first one is to test the ability of the element to deal with elasto-plastic problems involving coupling between axial, bending and torsional warping effects. For this purpose, examples exhibiting lateral and flexural-torsional buckling were also included. The second objective was to test and compare the two branch-switching procedures presented in Section 5.3. For all instability problems included in the present set of examples, the mode injection method worked very well and convergence to the first point on the secondary path was obtained within 4–7 iterations. The minimisation procedure also worked very well for all cases presenting a stable bifurcation. In these cases, convergence to the secondary path was also obtained within few iterations. However, as expected, the minimisation procedure failed for cases presenting an unstable bifurcation.

In order to obtain converged results, the cross-sections have been discretised using large numbers of integration points. For many examples, fewer points would certainly have given the same numerical results. No attempt of optimising the discretisation of the cross-sections has been performed. However, the tests performed by the author have shown that in order to capture accurately the spreading of the plasticity and get converged load—displacements curves, a large number of points is often needed.

9.1 Example 1, channel-section beam

The example presented in Figure 9.1 was introduced by Gruttmann et al. [41]. It refers to a channel-section beam, clamped at one end and subjected to a tip force at the free end. An ideal elasto-plastic material with yield stress $\sigma_Y = 36$ is considered.

The results obtained using 30 ptw3d elements and 336 integration points in the cross-section are shown in Figure 9.2. These results are in very good agreement with those presented in [41] based on shell elements.

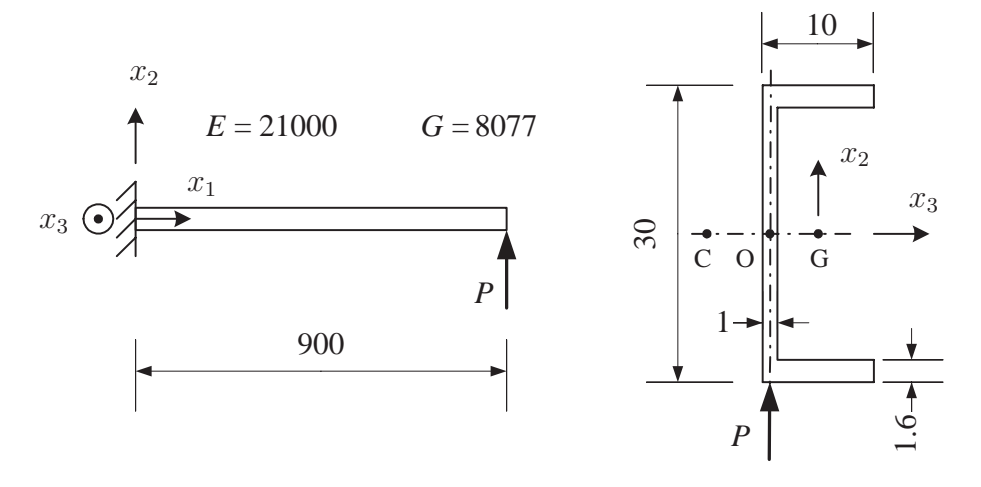


Figure 9.1: Channel-section beam.

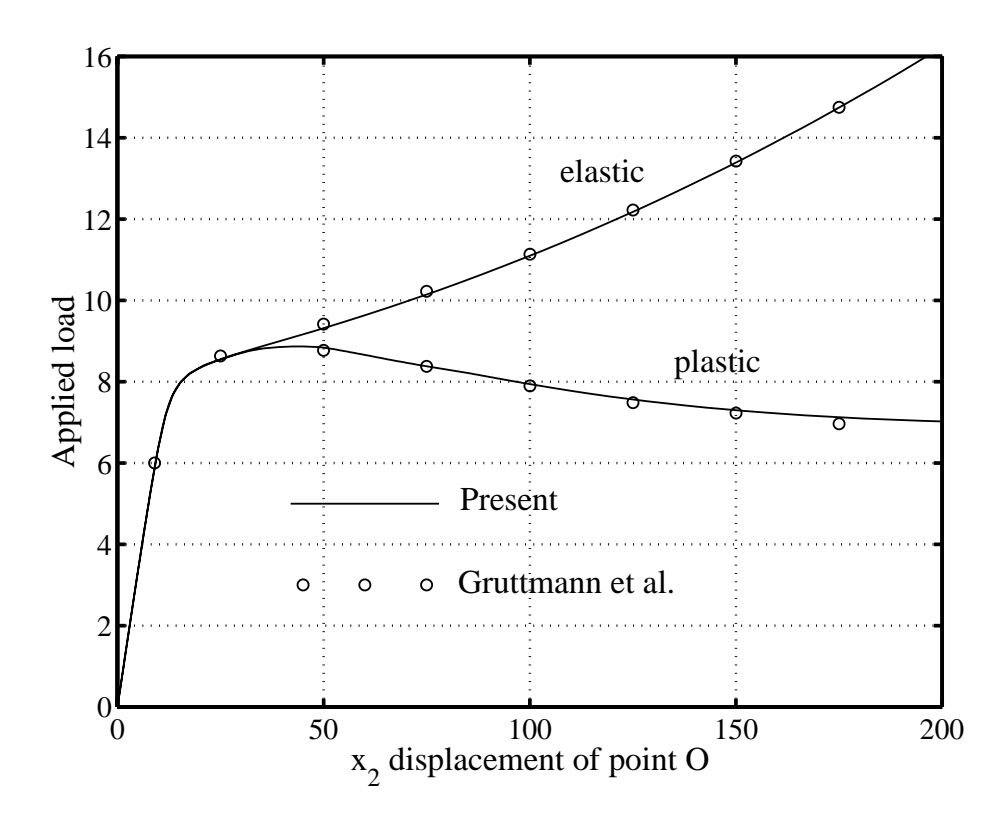


Figure 9.2: Channel-section beam: load-displacement diagram.

9.2 Example 2, framed dome

The instability of the framed dome shown in Figure 9.3 was analysed. Two different load cases were considered. Case 1 consisted of a single vertical force applied at the top of the dome while case 2 consisted of seven vertical loads of equal magnitude placed at the top and at the end points of horizontal members. The dome was modelled using N pt3d elements for each member, i.e. totally $18 \times N$ elements.

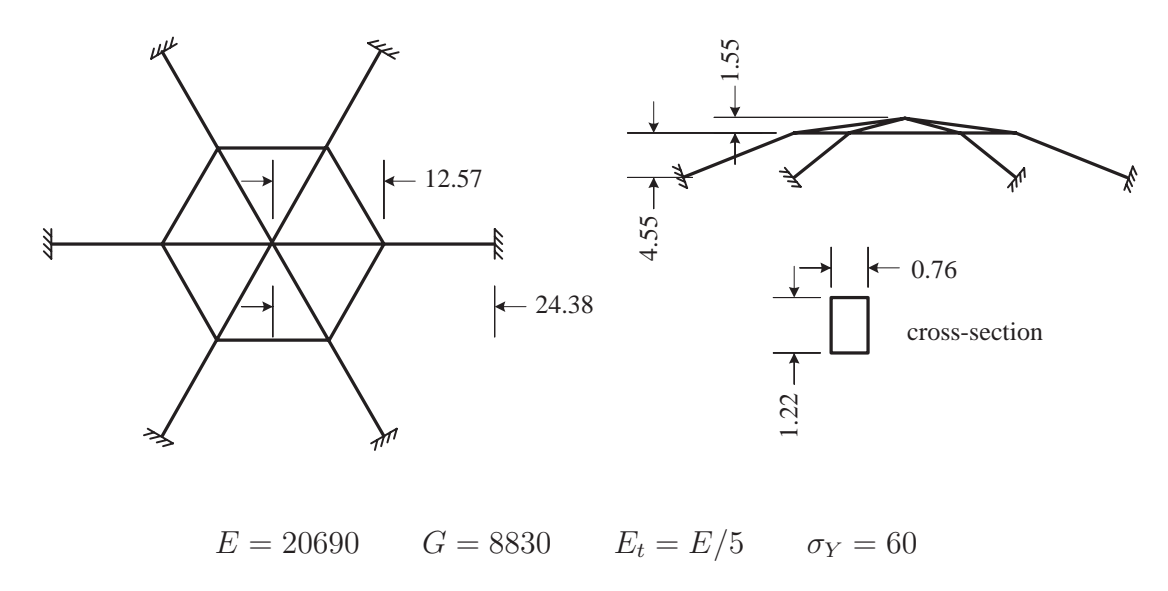


Figure 9.3: Framed dome.

For the elastic material, the results computed with N=5 and N=8 are presented in Figures 9.4 and 9.5. Very good agreement with Kouhia [56], who used N=5, is observed. It can be noted that there are several bifurcation points along the fundamental paths. In Figures 9.4 and 9.5, only the fundamental path and the secondary path branching out at the lowest bifurcation point are represented. For both loadings, the buckling mode is a rotation around a vertical axis, see Figure 9.6.

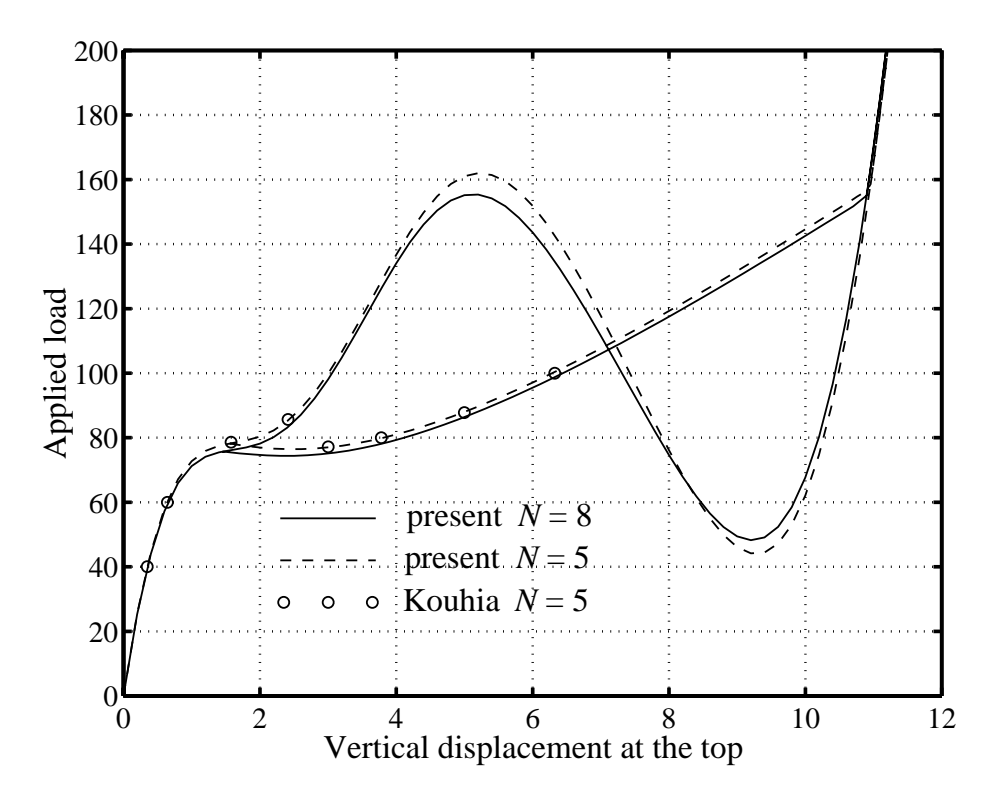


Figure 9.4: Framed dome: elastic material – case 1.

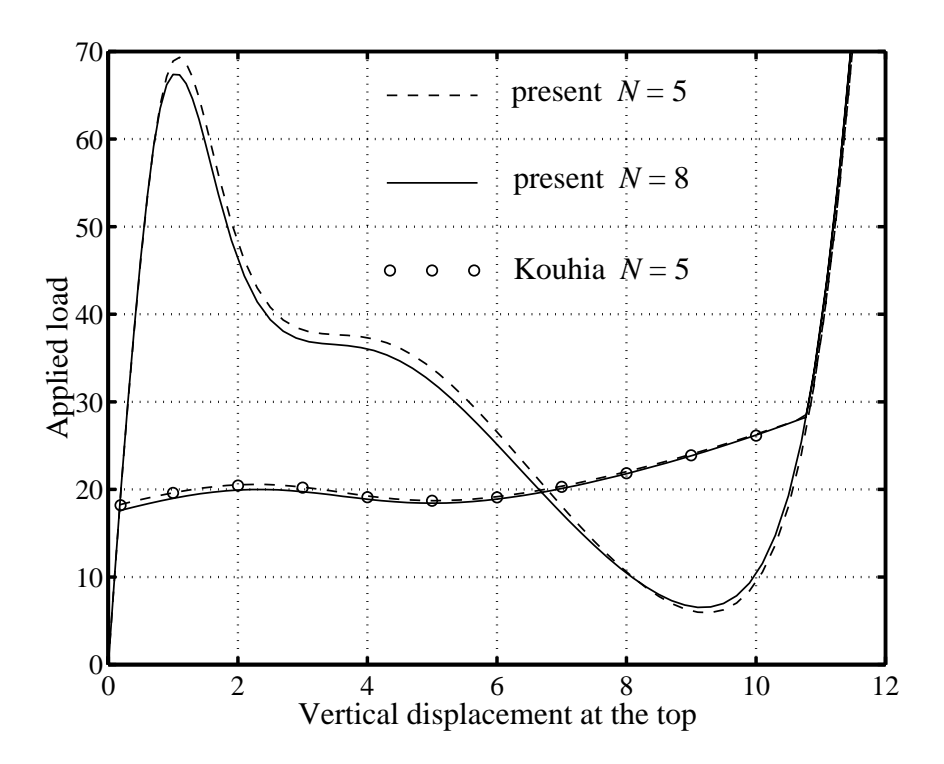


Figure 9.5: Framed dome: elastic material – case 2.

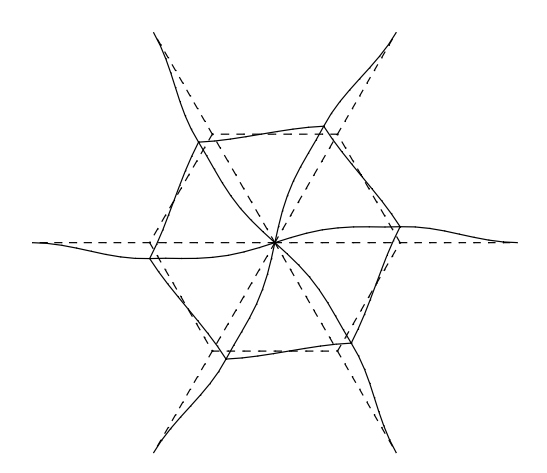


Figure 9.6: Framed dome: elastic material – first buckling mode.

For the elasto-plastic material, the results computed with N=8 and 10×16 integration points in the cross-section are shown in Figures 9.7 and 9.8. For case 1, the deformations are first concentrated in the upper part of the dome and a limit point is reached. After that, the load increases again and a bifurcation point is observed. For case 2, a bifurcation point is quickly reached. In both cases, the buckling mode is, as in the elastic case, a rotation around a vertical axis. For case 2, see Figure 9.9, the bifurcation is stable. However, the stable part of the secondary path is so short that very small increments must be taken in order to catch it numerically. Consequently, the minimisation procedure is not well suited to perform branch-switching in that case since it requires a very small load increment.

The mode injection method avoids this problem. In order to assure convergence on the secondary path, this method was implemented by taken as control the rotation around a vertical axis of the top of the structure. It can also be noted that Figure 9.9 suggests that the structure exhibits a tangent bifurcation.

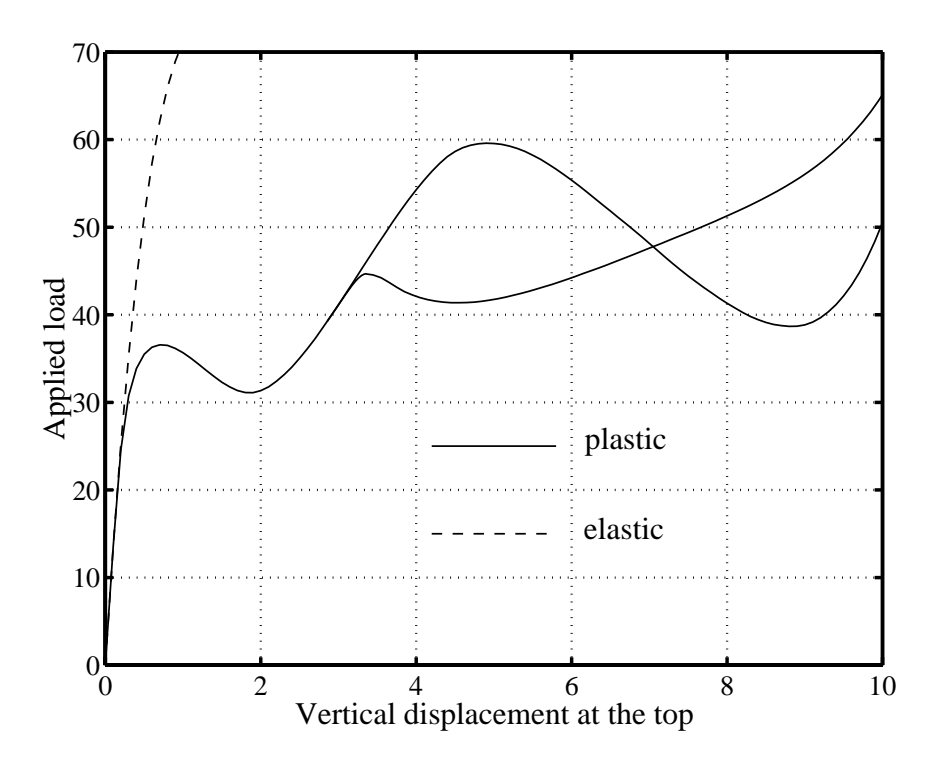


Figure 9.7: Framed dome: elasto-plastic material – case 1.

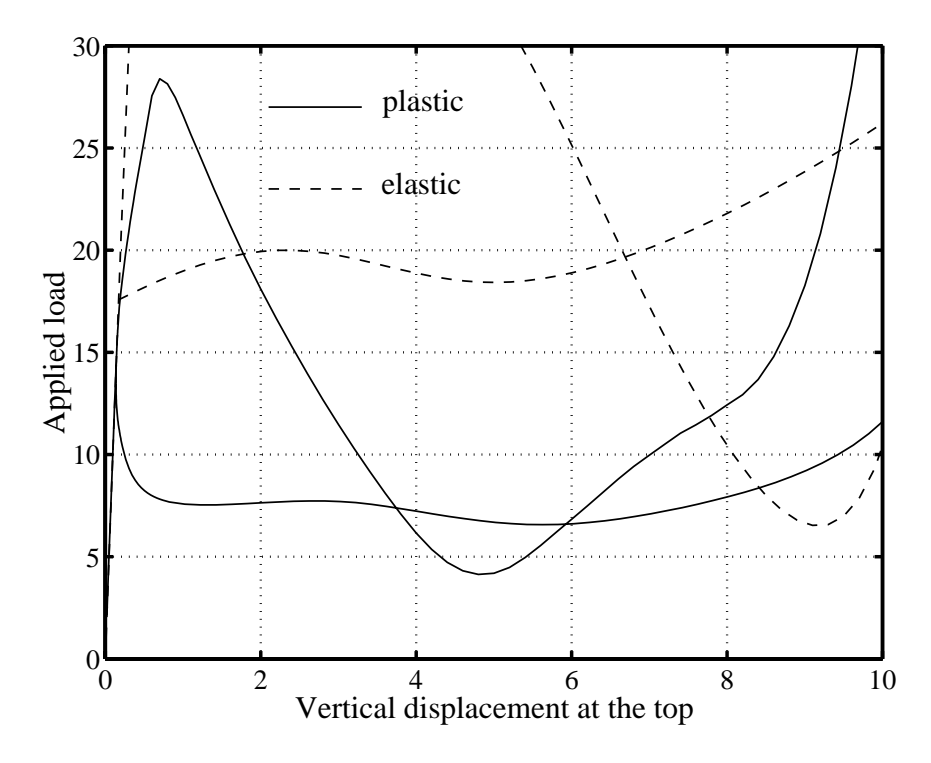


Figure 9.8: Framed dome: elasto-plastic material – case 2.

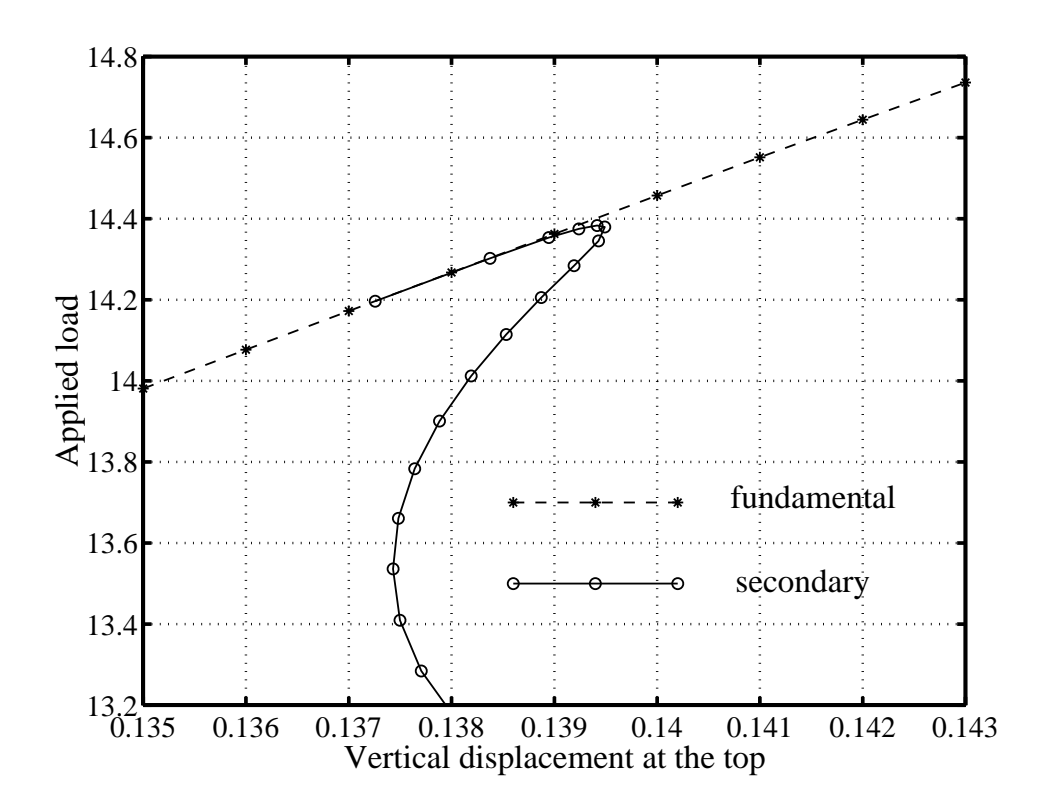


Figure 9.9: Framed dome: elasto-plastic material – bifurcation for case 2.

9.3 Example 3, lateral buckling of an I beam

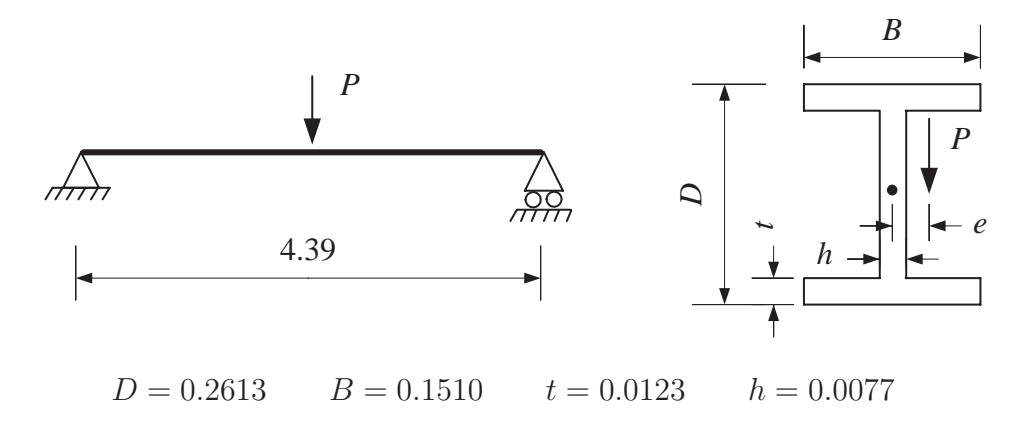


Figure 9.10: Lateral buckling of an I beam.

This example, introduced by Pi and Trahair [82], concerns the elasto-plastic lateral buckling of the simply supported I beam depicted in Figure 9.10. The rotation around the axis of the beam is set to zero at both supports, but warping deformations are permitted. The trilinear elastic-plastic stress-strain relationship shown in Figure 9.11 is used.

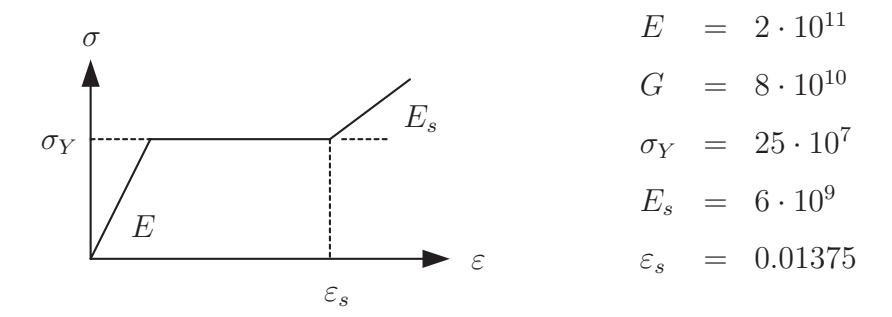


Figure 9.11: Lateral buckling of an I beam: material parameters.

The results shown in Figure 9.12 were computed with 20 ptw3d elements and 168 integration points in the cross-section. Very good agreement with Reference [82] is obtained. It can be noted that, due to the absence of hardening, the perfect structure (e = 0) presents an unstable bifurcation.

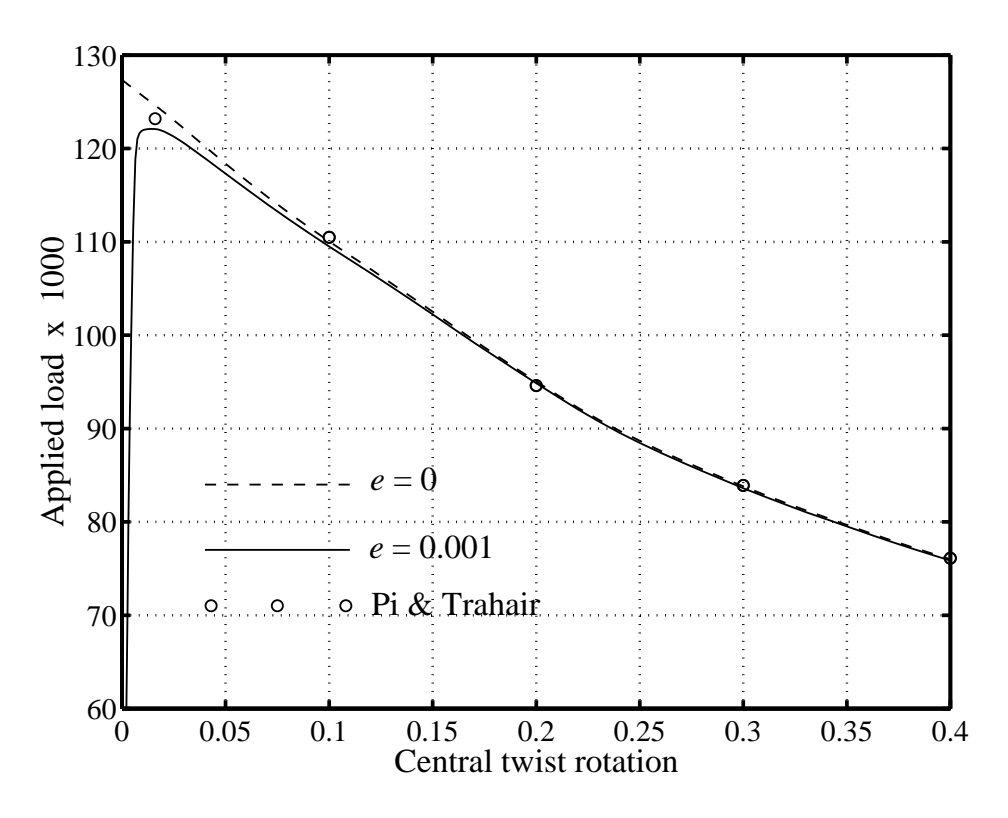


Figure 9.12: Lateral buckling of an I beam: post-buckling behaviour.

9.4 Example 4, lateral buckling of a T cantilever

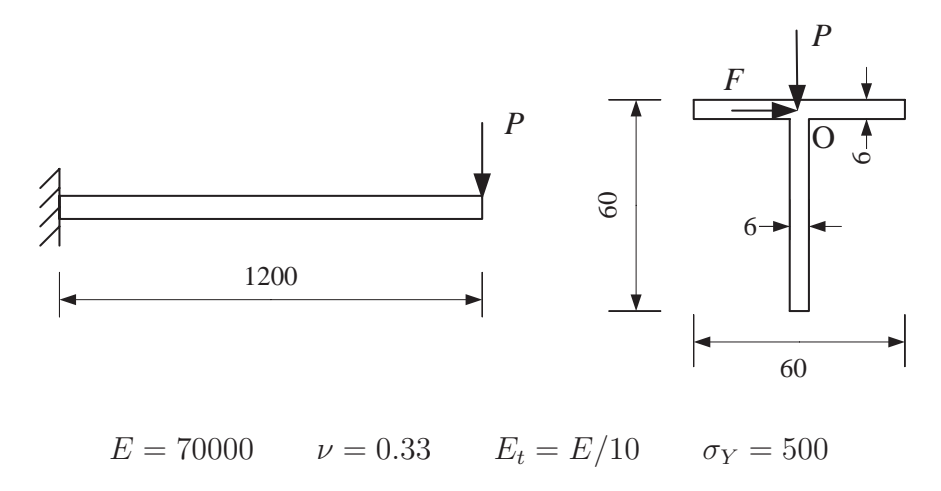


Figure 9.13: Lateral buckling of a T cantilever.

The lateral buckling of the T cantilever depicted in Figure 9.13 were analysed. Imperfections were introduced through a small lateral force F = P/1000. The beam was modelled using 30 ptw3d elements and 288 integration points in the cross-section. For this example, elastic shell and solid analyses were also performed. The elastic shell model was constructed using the flat facet triangular co-rotational element developed by Pacoste [68,71]. A $(10+10) \times 150$ mesh with 6000 triangular elements has been used. The solid analysis was performed with the finite element package SOLVIA. The mesh consisted of $(8+8) \times 60 = 960$ isoparametric 20 noded elements.

The bifurcation loads obtained with the different models are listed in Table 9.1. For the solid analysis, the critical loads were calculated by applying very small load increments and by checking the number of negative eigenvalues of the tangent stiffness matrix at each converged state. The post-bifurcation paths for elastic and elasto-plastic materials are presented in Figures 9.14 to 9.17.

With regard to the bifurcation loads, very good agreement between beam and solid analyses is obtained. It can also be noted that the values obtained with elastic and the elasto-plastic materials are almost similar. This unusual result can be explained by the fact that at the bifurcation, the zone of plastic deformations, situated at the lower part of the left end of the beam, is very small. Therefore, these plastic deformations have almost no influence on the lateral buckling of the beam. Their effect is, compared to the elastic case, to increase the bending pre-buckling deflections. However, it can be observed that in elasto-plasticity, a limit point is rapidly reached along the secondary path. This shows that the elasto-plastic structure has, as expected, a lower load carrying capacity than the elastic one.

The elasto-plastic post-bifurcation behaviours obtained with the beam and 3D models are similar up to a load of 3500. After this point, the curves diverge, which indicates that the structure does no longer deform as a beam. This is confirmed by Figure 9.18 which shows that although the structure is very slender, the deformations are concentrated in the first third part, near the clamped end. It can also be noted that the beam analysis gives an accurate estimate of the maximum load (2% difference from the solid model), which, from an engineering point of view, is of first importance.

For the elastic case, the results obtained with the shell model are within a 4% difference from those obtained using the beam or solid models. The reason for such a difference is that using shell elements for modelling a T connection leads to an overestimation of the cross-section. Consequently, the behaviour of the structure in pure bending (fundamental path) is stiffer than in reality, see Figure 9.14.

Table 9.1: Lateral buckling of a T cantilever: bifurcation loads.

material	beam	3D	shell
elastic	3390	3375	3258
elasto-plastic	3400	3395	

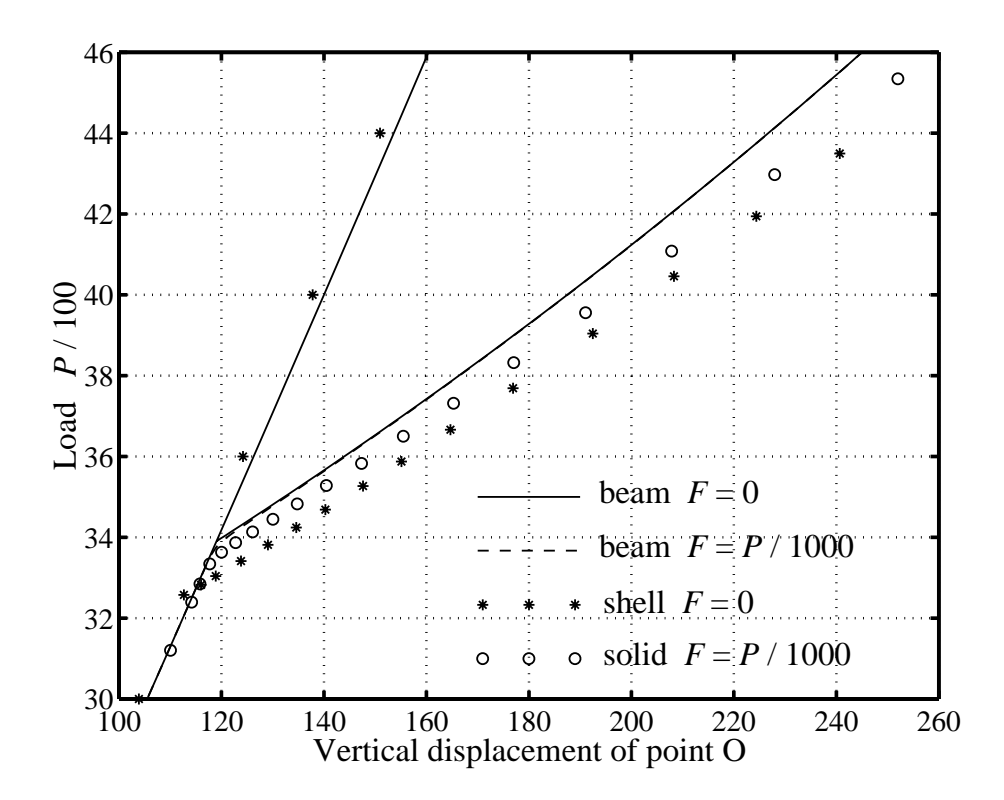


Figure 9.14: Lateral buckling of a T cantilever: elastic case.

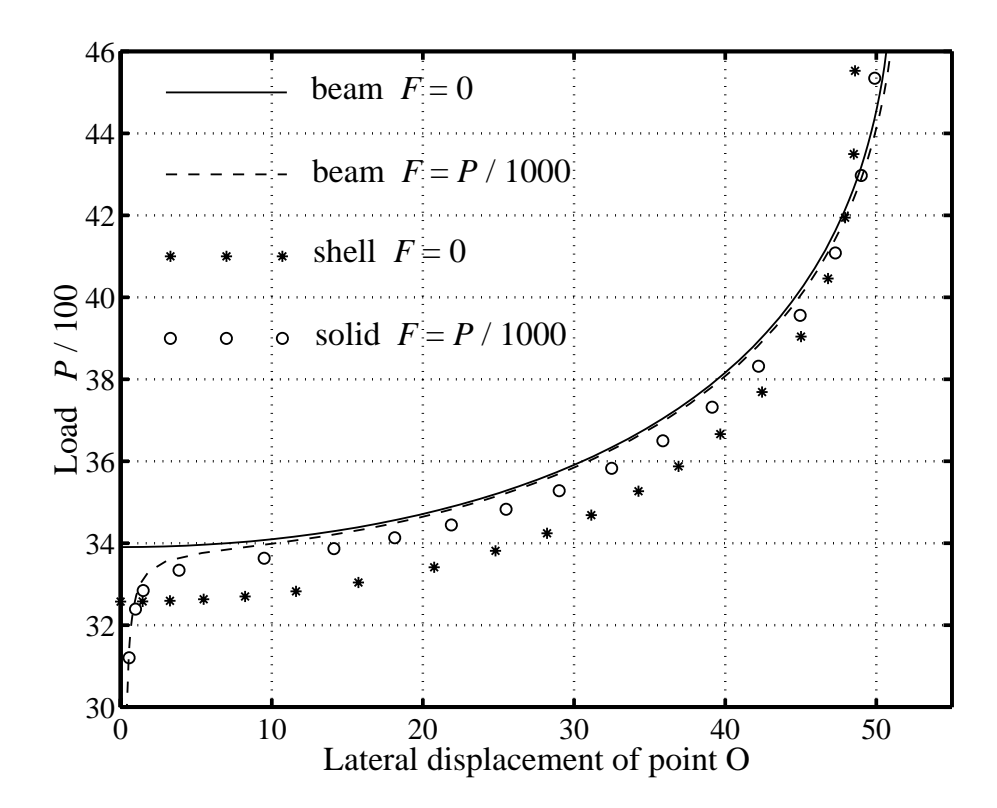


Figure 9.15: Lateral buckling of a T cantilever: elastic case.

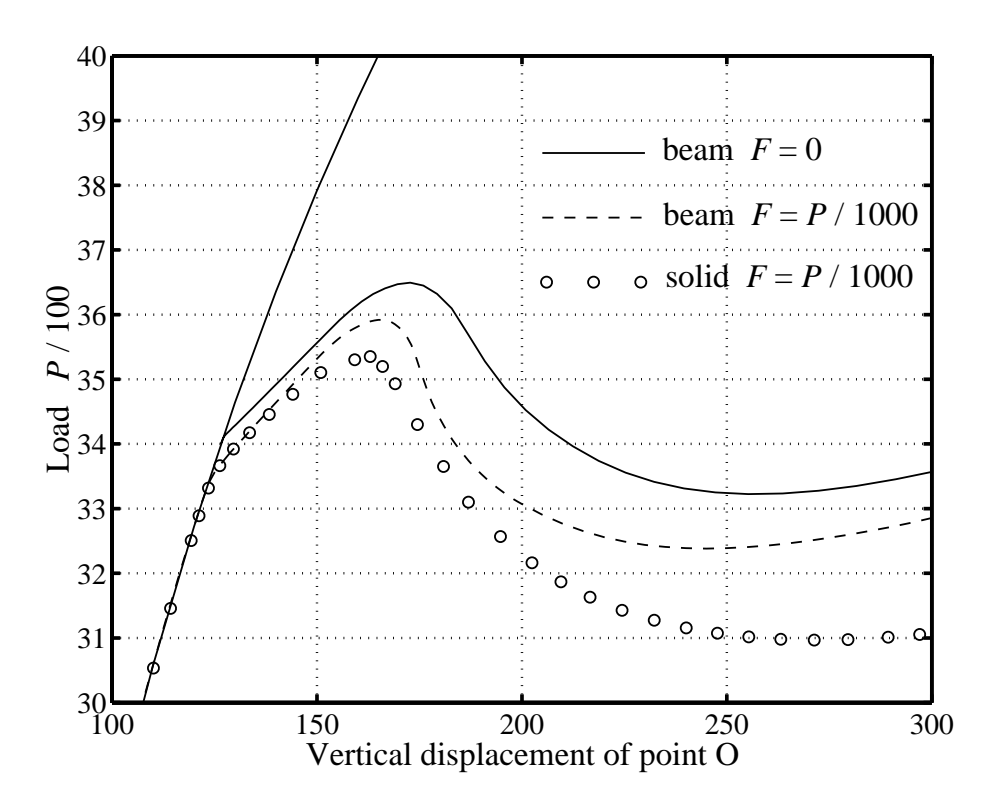


Figure 9.16: Lateral buckling of a T cantilever: elasto-plastic case.

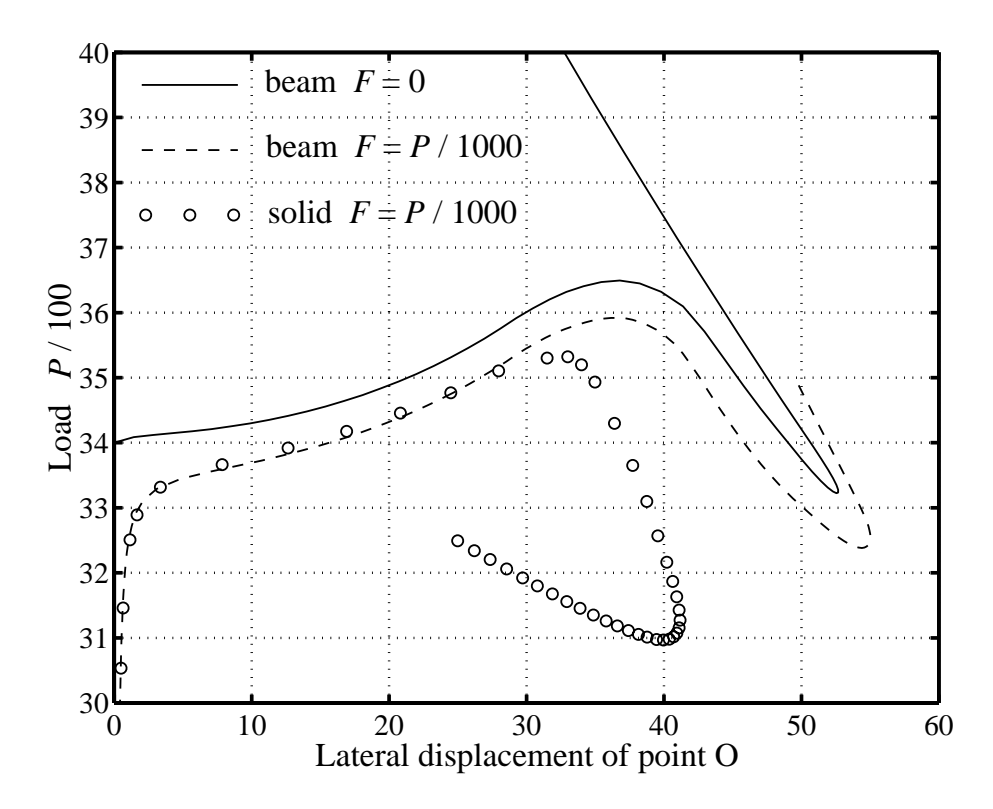


Figure 9.17: Lateral buckling of a T cantilever: elasto-plastic case.

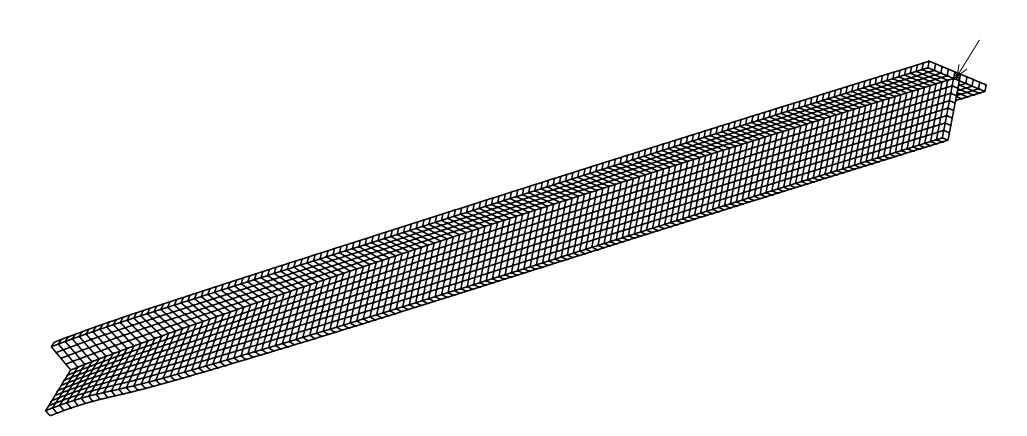


Figure 9.18: Lateral buckling of a T cantilever: elasto-plastic case – deformations for P=3500.

9.5 Example 5, buckling by torsion and flexure

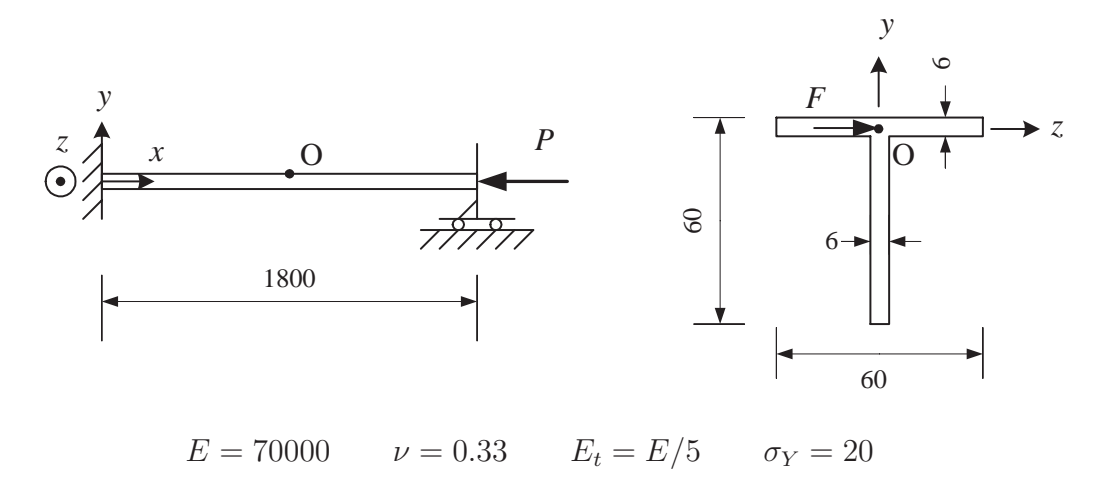


Figure 9.19: Buckling by torsion and flexure.

The buckling by torsion and flexure of the beam depicted in Figure 9.19 was analysed. All degrees of freedom including warping are set to zero at the left end and only the axial displacement is permitted at the right end. In order to introduce imperfections, a small lateral force F = P/1000 is applied in the midspan. The beam model consists of 40 ptw3d elements and 288 integration points in the cross-section. Elastic shell and solid analyses have also been performed, using the same discretisations as in the previous example.

The bifurcation loads obtained with the different models are listed in Table 9.2. It can be observed that the critical loads obtained using the different models differ by less than 1%.

The load–displacement curves for elastic and elasto-plastic materials are presented in Figures 9.20 to 9.24. In elasticity, good agreement between the three models is obtained until a displacement in the z-direction of about 220. After that, due to the apparition of local deformations, see Figure 9.22, the shell and solid load–displacement curves present limit points. In the elasto-plastic case, the post-buckling behaviour is dominated by the bending mode, and very good agreement between beam and solid models is obtained.

Table 9.2: Buckling by torsion and flexure: bifurcation loads/10000.

material	theory [97]	beam	3D	shell
elastic	8.452	8.444	8.405	8.482
elasto-plastic		1.834	1.845	

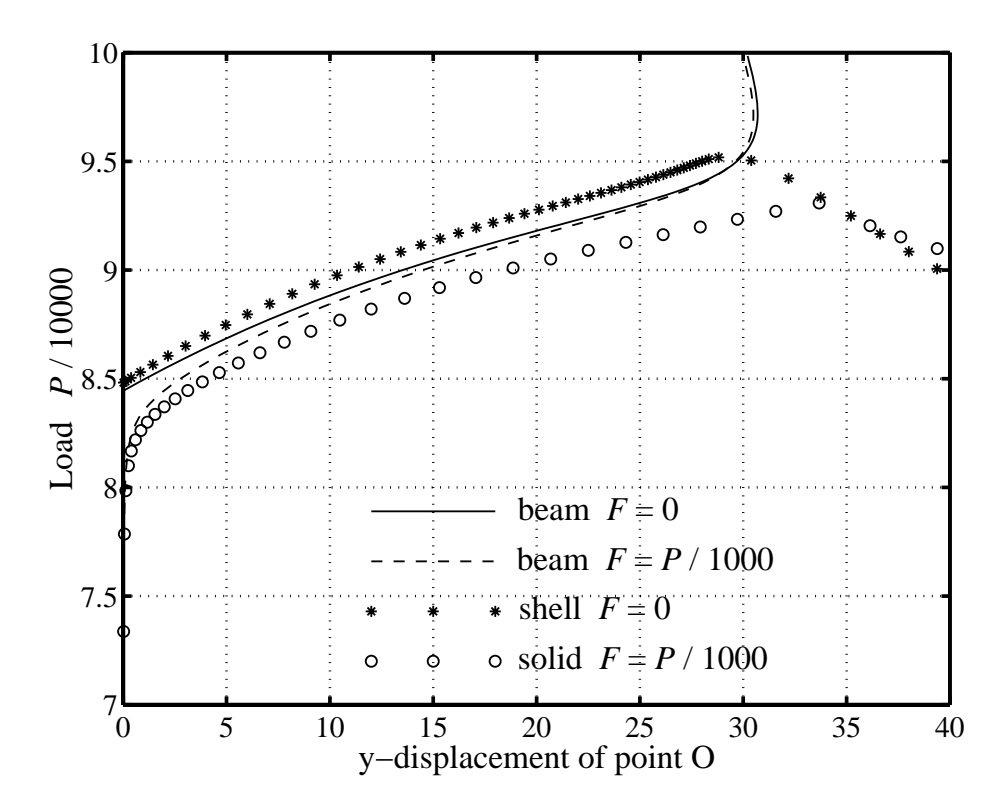


Figure 9.20: Buckling by torsion and flexure: elastic case.

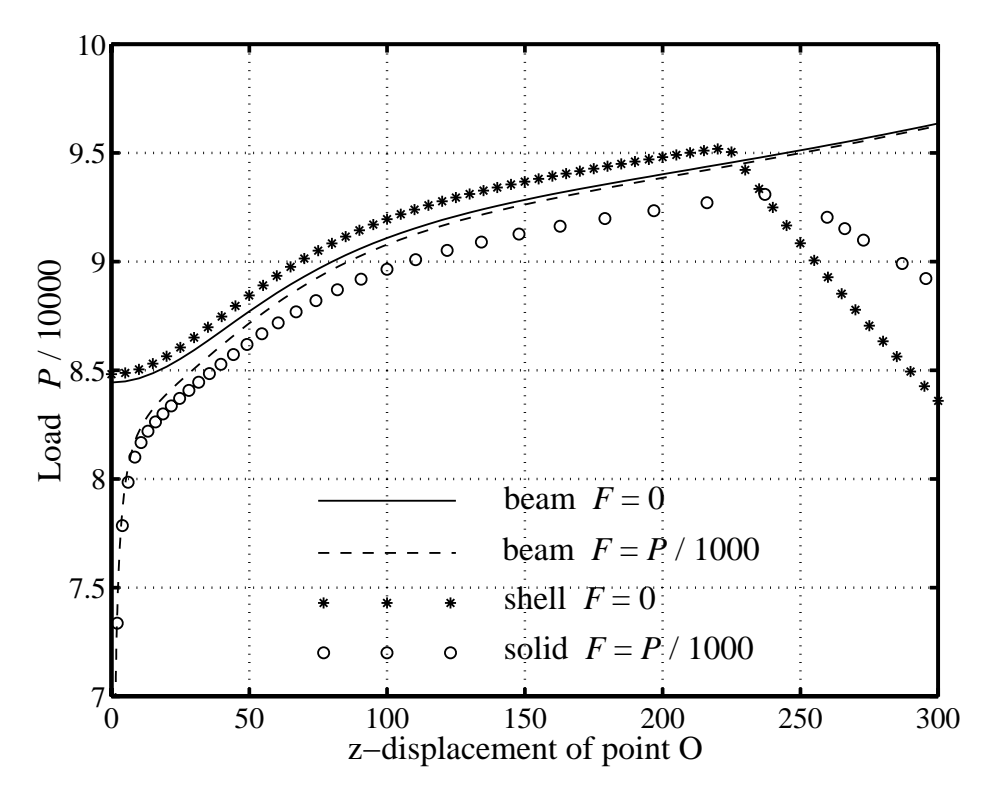


Figure 9.21: Buckling by torsion and flexure: elastic case.

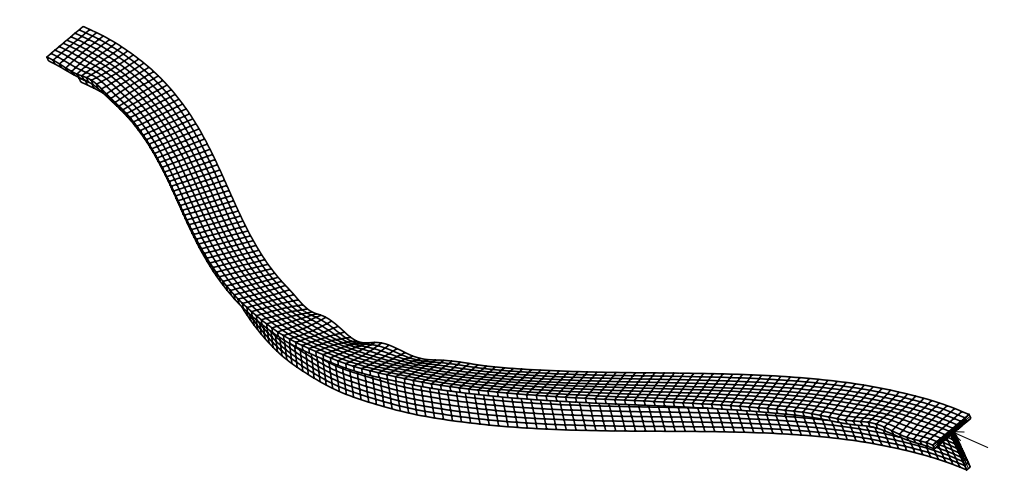


Figure 9.22: Buckling by torsion and flexure: elastic case – deformations after the limit point (P=91000) – solid analysis.

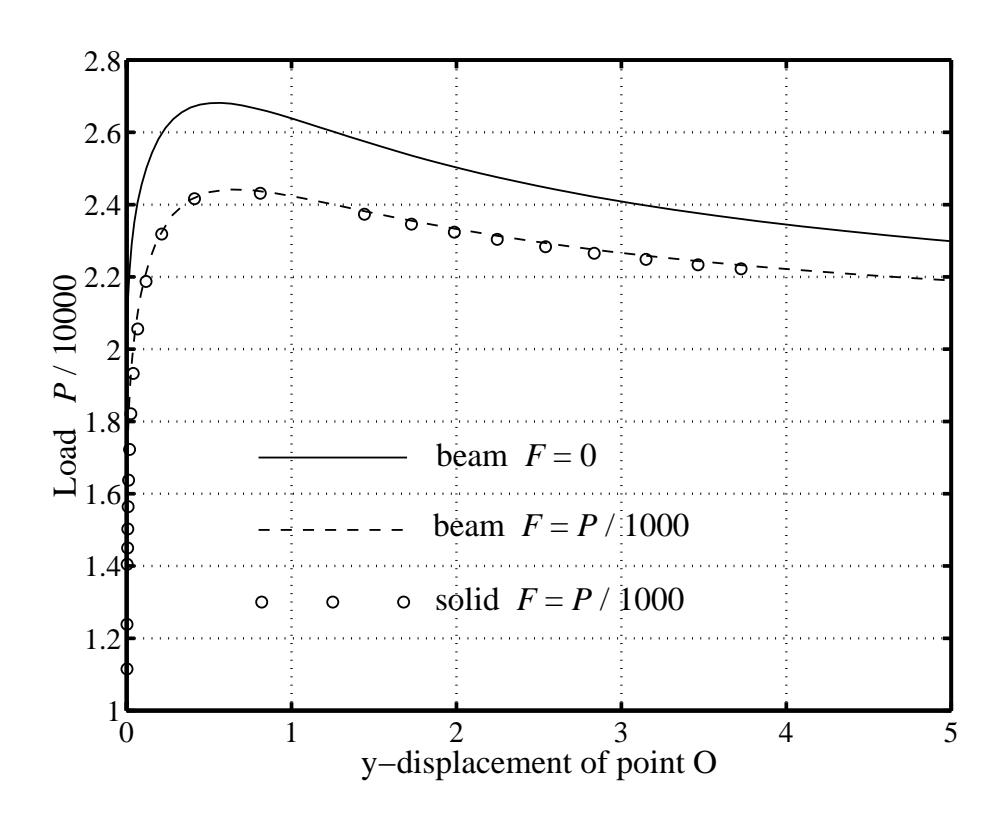


Figure 9.23: Buckling by torsion and flexure: elasto-plastic case.

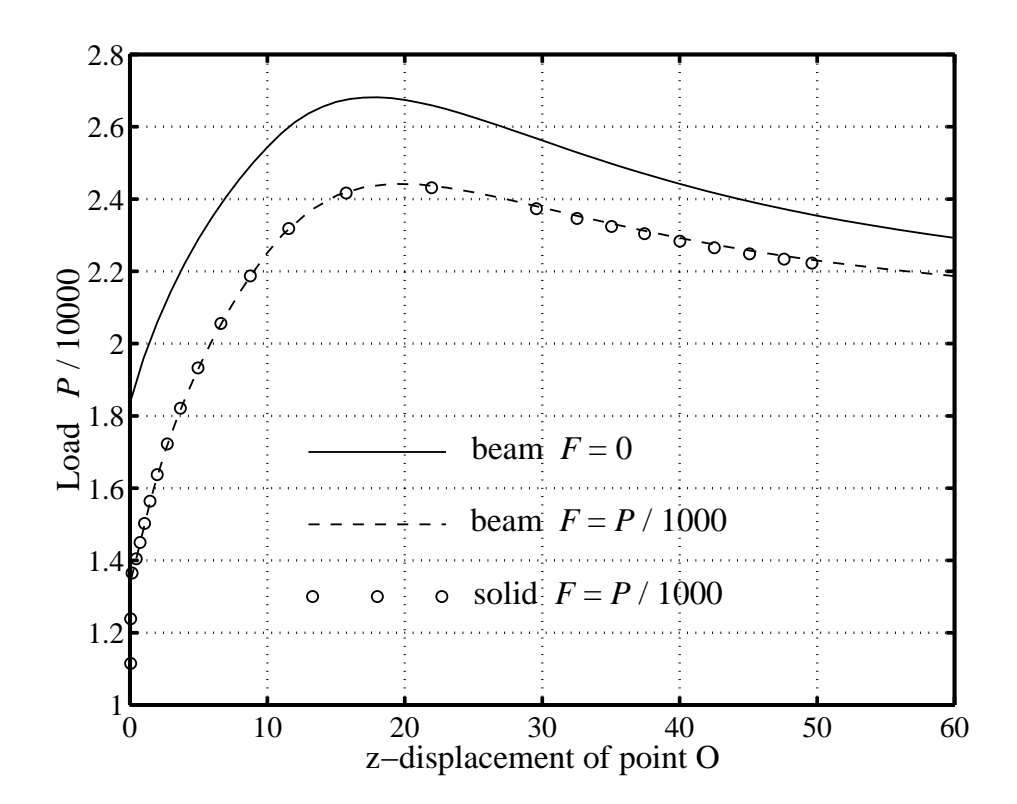


Figure 9.24: Buckling by torsion and flexure: elasto-plastic case.

Chapter 10

Conclusions and future research

In this last chapter, conclusions about the numerical computations performed in Chapters 6 to 9 and suggested directions for future research are presented.

10.1 Conclusions

The purpose of this thesis was to implement efficient co-rotational beam elements and branch-switching procedures in order to study elastic and elasto-plastic instability problems. These elements and procedures, presented in details in Chapters 3 to 5 have been tested through a large numbers of examples in Chapters 6 to 9. From the analysis of these numerical applications, several conclusions can be stated.

2D beam element formulation

The co-rotational approach for 2D beam elements is a well known topic and the objective of the present work was to compare three local elasto-plastic elements.

Both Timoshenko and Bernoulli elements gave close numerical results for frames consisting of slender beams. This observation was expected since in such cases the shear deformations can be neglected. It is therefore recommended to use Bernoulli elements for these structures since the resolution of the constitutive equations at each Gauss point does not require any implicit process.

Only small variations have been observed between load—displacement diagrams computed with seven and fifteen integration points along the beam depth. From an engineering point of view, these differences are negligible and a small number of Gauss points should be used for the analysis of large structures.

Concerning Bernoulli elements, the shallow arch approach should be preferred to the linear one since identical numerical results can be obtained with fewer elements. This point, already observed in [73] for elastic structures, was not evident in elastoplasticity: by decreasing the number of elements, the number of sections in the structure where Gauss integrations are performed is also reduced, and consequently, zones of plastification or elastic unloading are modelled with lower accuracy. However, this does not seem to have any significant effect on load–displacement diagrams.

3D beam element formulation

Compared to Pacoste and Eriksson [73], the 3D co-rotational formulation developed in Chapter 4 presents new items concerning the parameterisation of the rotations, the definition of the local frame, the inclusion of warping effects through the introduction of a seventh nodal degree of freedom and the consideration of rigid links. All these improvements have been tested in a large number of examples in Chapters 7 and 9. The present results have been compared with results found in the literature and also with analyses performed using shell and solid elements. It can then be concluded that the elements developed in this thesis can be used to study any large displacements and rotations problems involving non-linear coupling between axial, bending and torsional-warping effects. In addition, any cross-section shape can be considered. In fact, concerning the element formulation, the only restriction resides in the small strain assumption.

One of the main properties of the co-rotational formulation adopted in this thesis, is its independence of the local strains assumptions used to derive local internal force vectors and tangent stiffness matrices. Using this property most authors use linear strains at the level of the local element definition. However, as shown by several of the numerical examples included in Chapter 7, this type of elements may give incorrect results for problems where torsional effects are important.

For these reasons, the displacement field proposed by Gruttmann et al. [41] has been adopted and used to construct a consistent second order approximation to the Green-Lagrange strains, at the level of the local element frame. The resulting expressions have been further simplified by neglecting the non-linear terms in the expression of shear strains ε_{12} and ε_{13} and in the bending curvatures. In fact it appears that the only important non-linear term is the Wagner term, i.e. $\frac{1}{2} r^2 \vartheta_{1,1}^2$, in the expression of ε_{11} . Some authors (see e.g. [55]) replace this term by its average value over the cross-section. The tests performed by the author have shown that this simplification is not acceptable.

Another characteristic of the co-rotational approach is that the material non-linearity is only present at the level of the local deformations and does not affect the co-rotational framework. Hence, due to the simplicity of the local strains expression, the derivation of elasto-plastic local elements is rather easy. Using linear interpolations, Timoshenko elements have been developed. Based on the work done in Section 4.3.1, Bernoulli elements can also be derived without difficulties.

Branch-switching in elasto-plasticity

Two methods of branch-switching in elasto-plasticity have been presented in Section 5.3. In the first one, the bifurcation point is isolated by successive bisections and the branch-switching is operated by using the eigenvector associated to the negative

eigenvalue. In the second one, introduced by Petryk [76–81], an energy approach is used to select automatically the stable post-bifurcation path.

In most studied examples in Chapters 6 and 9, both methods work very well and convergence to the first point of the secondary path is obtained after 4–7 iterations. However, if the bifurcation is unstable (examples 6.3 and 9.3) or if the stable part of the secondary path is very small (example 9.2), the minimisation procedure can not be employed. On the other hand, if an arc-length procedure is used, the mode injection method does not ensure convergence to the secondary path, in particular for structures exhibiting a tangent bifurcation (examples 6.5 and 9.2). The conclusion of the author is that the best alternative is to use the mode injection method together with a displacement control procedure and to take as control a displacement or a rotation which is zero along the fundamental path.

Direct computation of elastic critical points

In Section 5.2, a new procedure for the direct computation of elastic critical points has been presented. Compared to the approach of Wriggers et al. [104, 105], two new ideas have been introduced. First, the condition of criticality is expressed by a scalar equation. Next, the present method combines iterations based on the extended system obtained by the equilibrium equations and the criticality condition with iterations based only on the equilibrium equations under load or displacement control.

The performances of the present method and the classical approach [104,105] have been compared through eight numerical examples in Chapter 8. In most of the cases, both approaches give similar results. However, if the non-linearity between the initial point and the critical one is important, as in examples 8.1, 8.6 and 8.7, the convergence properties of the present method are better. It can then be concluded that the numerical procedure presented in this thesis is an interesting alternative for the direct computation of critical points.

10.2 Future research

The work done in this thesis can be extended in three directions which are now briefly presented.

Element formulation

The co-rotational formulation presented in this thesis is based on a spatial representation of the rotations, see Section 4.1. Another possibility is to derive elements using a material representation. As pointed out by Ibrahimbegovic [51], a material approach is more suitable in the context of dynamics and time-stepping schemes.

For a certain class of problems, the small strains hypothesis may not be correct and local elements based on large strains should be developed. Concerning co-rotational 2D beams and shells elements, such an approach was adopted by Kolahi [53].

Elasto-plastic models

The elasto-plastic model adopted in this thesis is based on an incremental flow theory, a von-Mises yield criterion, a bilinear uniaxial stress-strain relation and an isotropic hardening. However, a bilinear law is too crude to model correctly the real behaviour of materials, in particular metals. A better approach, common in finite elements codes, is to represent the plastic uniaxial behaviour by a succession of segments. Such a modification would allow a more accurate description of the post-buckling behaviour. As a matter of fact, the analysis of Hutchinson's model in Section 2.1.2 has shown that the decreasing stiffness in the plastic range has destabilising effects and a significant influence on the post-bifurcation.

In order to model correctly plastic reversal deformations, kinematical and mixed hardening should also be incorporated. The extension to other yield criteria such as Tresca or Mohr-Coulomb can also be considered. However, it is not certain that the bifurcation procedure based on the minimisation procedure holds in such cases. Since these criteria are not characterised by a smooth yield surface, the condition (2.97) must be investigated, which may be difficult.

Finally, the main interesting development would probably be to develop elements based on a plastic deformation theory and to compare their performances with the performances of the present elements in predicting elasto-plastic buckling loads.

New finite elements

The present work can also be extended to composite beam or shell elements. Concerning shell elements, a co-rotational approach, similar to the one adopted for beam elements, has been developed by Pacoste [68,71]. The main challenge concerns then the local formulation. Many alternatives are available and the choice of an efficient local strain definition is open. It would also be interesting to test the two elastoplastic branch-switching methods and the new procedure for the direct computation of elastic critical points in a shell context.

Bibliography

- [1] J.H. Argyris, B. Boni, U. Hindenlang, and M. Kleiber. Finite element analysis of two- and three-dimensional elasto-plastic frames—the natural approach. *Comput. Methods Appl. Mech. Engrg.*, 35:221–248, 1982.
- [2] S. Baba and T. Kajita. Plastic analysis of torsion of a prismatic beam. *Int. J. Numer. Meth. Engng.*, 18:927–944, 1982.
- [3] J.L. Batoz and G. Dhatt. *Modélisation Des Structures Par Eléments Finis, Volume 1: Solides Elastiques.* Hermès, Paris, 1990. In French.
- [4] J.L. Batoz and G. Dhatt. *Modélisation Des Structures Par Eléments Finis, Volume 2: Poutres et Plaques.* Hermès, Paris, 1990. In French.
- [5] J.-M. Battini. Plastic Instability Analysis of Plane Frames Using a Co-Rotational Approach. Licentiate Thesis, Department of Structural Engineering, KTH, Stockholm, 1999.
- [6] J.-M. Battini and C. Pacoste. Co-rotational beam elements with warping effects in instability problems. *Accepted by Comput. Methods Appl. Mech. Engrg.*
- [7] J.-M. Battini and C. Pacoste. Eléments poutres co-rotationels avec gauchissement. *Proceedings CSMA 5ème colloque national en calcul des structures, Giens 2001.* In French.
- [8] J.-M. Battini and C. Pacoste. Minimal augmentation procedure for the direct computation of critical points. Submitted to Comput. Methods Appl. Mech. Engrg.
- [9] J.-M. Battini and C. Pacoste. Plastic instability of beam structures using co-rotational elements. Submitted to Comput. Methods Appl. Mech. Engrg.
- [10] Z.J. Bazant. Stability of Structures. Oxford University Press, 1991.
- [11] B. Budianski. A reassessment of deformation theories of plasticity. *J. Appl. Mech.*, 26:259–264, 1959.
- [12] A. Cardona and A. Huespe. Evaluation of simple bifurcation points and post-critical path in large finite rotation problems. *Comput. Methods Appl. Mech. Engrg.*, 175:137–156, 1999.

- [13] C.N. Chen. Study on the reliability of Shanley's plastic buckling model by using the finite element method. *Proceedings of the 1994 Pressure Vessels and Piping Conference*, 277:127–134, 1994.
- [14] N.C. Chen. A finite element study on Shanley's plastic buckling theory of short columns. *Computers and Structures*, 59(5):975–982, 1996.
- [15] Y. Cheng, H. Fang, and W. Lu. Imperfection sensitivity analysis of a rectangular column compressed into the plastic range. *Applied Mathematics and Mechanics*, 19(1):9–14, 1998.
- [16] Y. Cheng, W. Lu, and H. Fang. Plastic post-buckling of a simply supported column with a rectangular cross-section. *Applied Mathematics and Mechanics*, 16(8):713–722, 1995.
- [17] C. Cichon. Large displacements in-plane analysis of elastic-plastic frames. Computers and Structures, 19:737–745, 1984.
- [18] A. Cimetière, A. Elkoulani, and A. Léger. Buckling and post-buckling of an elastic-plastic simple model. *Comptes rendus de l'académie des sciences, Paris*, 319:1263–1269, 1994.
- [19] A. Cimetière and A. Léger. Some problems about elastic-plastic post-buckling. *Int. J. Solids Structures*, 33(10):1519–1533, 1996.
- [20] A. Considère. Résistance des pièces comprimées. In Paris Librairie Polytechnique, editor, Congrès International Des Procédés de Construction, 1891. In French.
- [21] R.D. Cook, D.S. Malkus, and M.E. Plesha. *Concepts and Applications of Finite Element Analysis*. Wiley, Chichester, third edition, 1989.
- [22] M.A. Crisfield. A consistent co-rotational formulation for non-linear, three-dimensional, beam-elements. Comput. Methods Appl. Mech. Engrg., 81:131–150, 1990.
- [23] M.A. Crisfield. Non-Linear Finite Element Analysis of Solids and Structures, Volume 1: Essentials. Wiley, Chichester, 1991.
- [24] M.A. Crisfield. Non-Linear Finite Element Analysis of Solids and Structures, Volume 2: Advanced Topics. Wiley, Chichester, 1997.
- [25] M.A. Crisfield and D. Tan. A low-order large-strain quadrilateral shell element. In European Congress on Computational Methods in Applied Sciences and Engineering, Barcelona, 11-14 September 2000. ECCOMAS 2000.
- [26] R. de Borst. Computation of post-bifurcation and post-failure behavior of strain-softening solids. *Computers and Structures*, 25(2):211–224, 1987.
- [27] V. de Ville de Goyet. L'analyse Statique Non Linéaire Par la Méthode Des Éléments Finis Des Structures Spatiales Formées de Poutres a Section Non Symétrique. PhD thesis, Université de Liège, 1988-1989.

- [28] R.H. Dodds. Numerical techniques for plasticity computations in finite element analysis. *Computers and Structures*, 26:767–779, 1987.
- [29] M.S. El Naschie. Stress, Stability and Chaos in Structural Engineering: An Energy Approach. McGraw-Hill, 1990.
- [30] A. Eriksson. Fold lines sensitivity analyses in structural instability. *Comput. Methods Appl. Mech. Engrg.*, 114:77–101, 1994.
- [31] A. Eriksson. Equilibrium subsets for multi-parametric structural analysis. Comput. Methods Appl. Mech. Engrg., 140:305–327, 1997.
- [32] A. Eriksson. Structural instability analyses based on generalised pathfollowing. *Comput. Methods Appl. Mech. Engrg.*, 156:45–74, 1998.
- [33] A. Eriksson and C. Pacoste. Solution surfaces and generalised paths in non-linear structural mechanics. *Int. J. Struct. Stability and Dynamic*, 1(1), 2001.
- [34] A. Eriksson, C. Pacoste, and A. Zdunek. Numerical analysis of complex instability behaviour using incremental-iterative strategies. *Comput. Methods Appl. Mech. Engrg.*, 179:265–305, 1999.
- [35] C.A. Felippa. A systematic approach to the element-independent corotational dynamics of finite elements. In *Int. Conf. Computational Methods for Shell and Spatial Structures*, Papadrakakis, M., Samartin, A. and Onate, E. (Eds.) ISASR-NTUA, Athens, Greece 2000. IASS-IACM 2000.
- [36] R. Fletcher. Practical Methods of Optimization. Wiley, second edition, 1987.
- [37] K. Forsell. *Instability Analyses of Structures under Dynamic Loads*. PhD thesis, Department of Structural Engineering, KTH, Stockholm, 2000.
- [38] Y. Goto, T. Yoshimitsu, and M. Obata. Elliptic integral solutions of plane elastica with axial and shear deformations. *Int. J. Solids Structures*, 26(4):375–390, 1990.
- [39] F. Gruttmann, R. Sauer, and W. Wagner. Shear stresses in prismatic beams with arbitrary cross-sections. *Int. J. Numer. Meth. Engng.*, 45:865–889, 1999.
- [40] R. Gruttmann, R. Sauer, and W. Wagner. A geometrical nonlinear eccentric 3d-beam element with arbitrary cross-section. Comput. Methods Appl. Mech. Engrg., 160:383–400, 1998.
- [41] R. Gruttmann, R. Sauer, and W. Wagner. Theory and numerics of three-dimensional beams with elastoplastic behaviour. *Int. J. Num. Meth. Engng.*, 48:1675–1702, 2000.
- [42] W. Guggenberger. Nonlinear analysis of space frame structures—large rotation formulations and their consistent approximations for moderate rotations. In European Congress on Computational Methods in Applied Sciences and Engineering, Barcelona, 11-14 September 2000. ECCOMAS 2000.

- [43] B. Haugen and C.A. Felippa. A unified formulation of co-rotational finite elements: I. theory. Technical Report CU-CAS-95-06, Center for Aerospace Structures, Dept of Aerospace Engineering, U. Colorado, Boulder.
- [44] B. Haugen and C.A. Felippa. A unified formulation of co-rotational finite elements: II. applications. Technical Report CU-CAS-95-06, Center for Aerospace Structures, Dept of Aerospace Engineering, U. Colorado, Boulder.
- [45] R. Hill. A general theory of uniqueness and stability in elastic-plastic solids. J. Mech. Phys. Solids, 6:236–249, 1958.
- [46] R. Hill and M. J. Sewell. A general theory of inelastic column failure. *J. Mech. Phys. Solids*, 8:105–111, 1960.
- [47] K.M. Hsiao and W.Y. Lin. A co-rotational finite element formulation for buckling and postbuckling analyses of spatial beams. Comput. Methods Appl. Mech. Engrg., 188:567–594, 2000.
- [48] J.W. Hutchinson. Imperfection sensitivity in the plastic range. J. Mech. Phys. Solids, 21:191–204, 1973.
- [49] J.W. Hutchinson. Post-bifurcation behaviour in the plastic range. *J. Mech. Phys. Solids*, 21:163–190, 1973.
- [50] J.W. Hutchinson. Plastic buckling. Advances in Appl. Mech., 14:67–144, 1974.
- [51] A. Ibrahimbegovic. On the choice of finite rotation parameters. *Comput. Methods Appl. Mech. Engrg.*, 149:49–71, 1997.
- [52] A. Ibrahimbegovic and M. Al Mikad. Quadratically convergent direct calculation of critical points for 3d structures undergoing finite rotations. *Comput. Methods. Appl. Mech. Engrg.*, 189:107–120, 2000.
- [53] A.S. Kolahi. Co-Rotational Methods for Small and Large Strain Beams, Sheets and Shells. PhD thesis, Dept. of Aeronautics, Imperial College, London, 1998.
- [54] K. Kondoh and N. Atluri. Large-deformation, elasto-plastic analysis of frames under nonconservative loading, using explicitly derived tangent stiffness based on assumed stresses. *Comp. Mech.*, 2:1–25, 1987.
- [55] R. Kouhia. On kinematical relations of spatial framed structures. *Computers and Structures*, 40(5):1185–1191, 1991.
- [56] R. Kouhia and M. Tuomala. Static and dynamic analysis of space frames using simple Timoshenko type elements. *Int. J. Num. Meth. Engng.*, 36:1189–1221, 1993.
- [57] S.H. Lee. Rudimentary considerations for effective line search method in non-linear finite element analysis. *Computers and Structures*, 32(6):1287–1301, 1989.

- [58] A. Léger and M. Potier-Ferry. Sur le flambage plastique. *J. Mécanique Théor.* Appl., 7:819–857, 1988. In French.
- [59] T. Lidström. Computational Methods for Finite Element Instability Analyses. PhD thesis, Department of Structural Engineering, KTH, Stockholm, 1996.
- [60] K. Moon-Young, C. Sung-Pil, and K. Sung-Bo. Spatial stability analysis of thin-walled space frames. *Int. J. Num. Meth. Engng.*, 39:499–525, 1996.
- [61] A. Needleman and V. Tvergaard. An analysis of the imperfection sensitivity of square elastic-plastic plates under compression. *Int. J. Solids Structures*, 12:185–201, 1976.
- [62] Q.S. Nguyen. Bifurcation and postbifurcation analysis in plasticity and brittle fracture. J. Mech. Phys. Solids, 33:303–324, 1987.
- [63] Q.S. Nguyen. Bifurcation and stability of time-independent standard dissipative systems. In Q.S. Nguyen, editor, CISM Courses and Lectures No. 327: Bifurcation and Stability of Dissipative Systems. Springer-Verlag, 1993.
- [64] B. Nour-Omid and C.C. Rankin. Finite rotation analysis and consistent linearization using projectors. Comput. Methods Appl. Mech. Engrg., 93:353–384, 1991.
- [65] A. Olsson. Object-Oriented Finite Element Algorithms. Licenciate Thesis, Department of Structural Engineering, KTH, Stockholm, 1997.
- [66] M. Ortiz and E. P. Popov. Accuracy and stability of integration algorithms for elastoplastic constitutive relations. *Int. J. Num. Meth. Engng.*, 21:1561–1576, 1985.
- [67] D.R.J. Owen and E. Hinton. Finite Elements in Plasticity: Theory and Practice. Pineridge Press Limited, Swansea UK, 1980.
- [68] C. Pacoste. Co-rotational flat facet triangular elements for shell instability analysis. *Comput. Methods Appl. Mech. Engrg.*, 156:75–110, 1998.
- [69] C. Pacoste and J.-M. Battini. Calcul des chemins d'équilibres post-critiques. Proceedings CSMA 5ème colloque national en calcul des structures, Giens 2001. In French.
- [70] C. Pacoste, J.-M. Battini, and A. Eriksson. Parameterisation of rotations in co-rotational elements. *Proceedings Euromech 2000, Metz.*
- [71] C. Pacoste and A. Eriksson. Element formulation and numerical techniques for stability problems in shells. *Accepted by Comput. Methods Appl. Mech. Engrg.*
- [72] C. Pacoste and A. Eriksson. Element behaviour in post-critical plane frame analysis. *Comput. Methods Appl. Mech. Engrg.*, 125:319–343, 1995.

- [73] C. Pacoste and A. Eriksson. Beam elements in instability problems. *Comput. Methods Appl. Mech. Engrg.*, 144:163–197, 1997.
- [74] M.S. Park and B.C. Lee. Geometrically non-linear and elastoplastic threedimensional shear flexible beam element of von-Mises-type hardening material. *Int. J. Num. Meth. Engng.*, 39:383–408, 1996.
- [75] U. Perego. Explicit backward difference operators and consistent predictors for linear hardening elastic-plastic constitutive laws. SM Archives, 13(2):65–102, 1988.
- [76] H. Petryk. The energy criteria of instability in time-independent inelastic solids. Arch. Mech., 43:519–545, 1991.
- [77] H. Petryk. Theory of bifurcation and instability in time-independent plasticity. In Q.S. Nguyen, editor, CISM Courses and Lectures No. 327—Bifurcation and Stability of Dissipative Systems, pages 95–152. Springer-Verlag, 1993.
- [78] H. Petryk. Instability of plastic deformation processes. In T. Tatsumi et Al., editor, *Theoretical and Applied Mechanics, Proc.XIXth IUATAM Congress, Kyoto*, pages 497–516. Elsevier, Amsterdam, 1997.
- [79] H. Petryk and K. Thermann. Second-order bifurcation in elastic-plastic solids. J. Mech. Phys. Solids, 33(6):577–593, 1985.
- [80] H. Petryk and K. Thermann. On discretized plasticity problems with bifurcations. *Int. J. Solids Structures*, 29(6):745–765, 1992.
- [81] H. Petryk and K. Thermann. On post-bifurcation paths in plastic deformation process. In D.R.J. Owen, editor, *Computational Plasticity. Fundamentals and Applications—Part I. Proceedings of the Third Int. Conf.*, pages 593–604. Pineridge Press, 1992.
- [82] Y.L. Pi and N.S. Trahair. Nonlinear inelastic analysis of steel beam-columns: II: Applications. *Journal of Structural Engineering*, 120(7):2062–2085, 1994.
- [83] C.C. Rankin and F.A. Brogan. An element-independent co-rotational procedure for the treatment of large rotations. ASME J. Pressure Vessel Tchn., 108:165–174, 1986.
- [84] C.C. Rankin and B. Nour-Omid. The use of projectors to improve finite element performance. *Computers and Structures*, 30:257–267, 1988.
- [85] M. Ristinmaa and J. Tryding. Exact integration of constitutive equations in elasto-plasticity. *Int. J. Num. Meth. Engng.*, 36:2525–2544, 1993.
- [86] R. Sauer. Eine Einheitliche Finite-Element-Formulierung Für Stab- und Schalentragwerke mit Endlichen Rotationen. PhD thesis, Bericht Nr. 4, Institut für Baustatik, Universität Karlsruhe, 1998. In German.
- [87] M.J. Sewell. A Survey of Plastic Buckling. Solid Mechanics Division, University of Waterloo, Waterloo, Ontario, Canada, 1972.

- [88] F.R. Shanley. Inelastic column theory. J. Aero. Science, 14:261–267, 1947.
- [89] J.C. Simo, J.G. Kennedy, and S. Govindjee. Non-smooth multisurface plasticity and viscoplasticity. Loading/unloading conditions and numerical algorithms. *Int. J. Num. Meth. Engng.*, 26:2161–2185, 1988.
- [90] J.C. Simo and R.L. Taylor. Consistent tangent operators for rate-independent elastoplasticity. *Comput. Methods Appl. Mech. Engrg.*, 48:101–118, 1985.
- [91] J.C. Simo and R.L. Taylor. A return mapping algorithm for plane stress elastoplasticity. *Int. J. Num. Meth. Engng.*, 22:649–670, 1986.
- [92] J.C. Simo and L. Vu-Quoc. A three-dimensional finite-strain rod model. part II: Computational aspects. Comput. Methods Appl. Mech. Engrg., 58:79–116, 1986.
- [93] J.C. Simo and L. Vu-Quoc. A geometrically-exact rod model incorporating shear and torsion-warping deformation. *Int. J. Solids Structures*, 27(3):371–393, 1991.
- [94] X.M. Su and W. Lu. Postbuckling and imperfection sensitivity analysis of structures in the plastic range—part 1: Model analysis. *Thin-Walled Structures*, 10:263–275, 1990.
- [95] J.G. Teigen. Nonlinear Analysis of Concrete Structures Based on a 3D Shear-Beam Element Formulation. PhD thesis, Department of Mathematics, Mechanics Division, University of Oslo, Norway, 1994.
- [96] J.M.T. Thompson and G.W. Hunt. *Elastic Instability Phenomena*. Wiley, Chichester, 1984.
- [97] S.P. Timoshenko and J.M. Gere. *Theory of Elastic Stability*. Second Edition, McGraw-Hill, Tokyo, 1961.
- [98] N. Triantafyllidis. On the bifurcation and postbifurcation analysis of elastic-plastic solids under general prebifurcation conditions. *J. Mech. Phys. Solids*, 31(6):499–510, 1983.
- [99] A.M.A. van der Heijden. A study of Hutchinson's plastic buckling model. *J. Mech. Phys. Solids*, 27:441–464, 1979.
- [100] H. van der Veen. The Significance and Use of Eigenvalues and Eigenvectors in the Numerical Analysis of Elasto-Plastic Soils. PhD thesis, Faculty of Civil Engineering and Geosciences, Delft University of Technology, Netherlands, 1998.
- [101] H. van der Veen, K. Vuik, and R. de Borst. Branch switching techniques for bifurcation in soil deformation. Comput. Methods Appl. Mech. Engrg., 190:707-719, 2000.
- [102] T. von Karman. Untersuchungen über Knickfestigkeit. In Verein Deutscher Ingenieure, editor, *Mitteilungen über Forschungsarbeiten*, 1910. In German.

- [103] W. Wagner and F. Gruttmann. Finite element analysis of Saint-Venant torsion problem with exact integration of the elastic-plastic constitutive equations. Comput. Methods Appl. Mech. Engrg., 190:3831–3848, 2001.
- [104] P. Wriggers and J.C. Simo. A general procedure for the direct computation of turning and bifurcation points. *Int. J. Num. Meth. Engrg.*, 30:155–176, 1990.
- [105] P. Wriggers, W. Wagner, and C. Miehe. A quadratically convergent procedure for the calculation of stability points in finite element analysis. *Comput. Methods Appl. Mech. Engrg.*, 70:329–347, 1988.

Appendix A

3D elastic local formulation

This appendix presents the Maple procedures necessary in order to generate the Fortran code for the 3D local elastic elements. These elements have been developed in Section 4.3.

A.1 t3d element

```
with(linalg):
du:=u12/L:
t1:=(t11+t12)/2:
t2:=(t21+t22)/2:
t3:=(t31+t32)/2:
dt1:=(t12-t11)/L:
dt2:=(t22-t21)/L:
dt3:=(t32-t31)/L:
g12:=-t3:
g13:=t2:
k1:=dt1:
k2:=-dt3:
k3:=dt2:
Phi1:=A*du^2+I22*k2^2+I33*k3^2+Irr/4*dt1^4+Io*du*dt1^2:
Phi2:=A*(g12^2+g13^2)+J*k1^2:
Phi:=1/2*L*(E*Phi1+G*Phi2):
fl:=grad(Phi,[u,t11,t21,t31,t12,t22,t32]):
kl:=hessian(Phi,[u,t11,t21,t31,t12,t22,t32]):
fortran(fl,optimized);
fortran(kl,optimized);
```

A.2 tw3d element

```
with(linalg):
du:=u12/L:
a:=(a1+a2)/2:
da:=(a2-a1)/L:
t1:=(t11+t12)/2:
t2:=(t21+t22)/2:
t3:=(t31+t32)/2:
dt1:=(t12-t11)/L:
dt2:=(t22-t21)/L:
dt3:=(t32-t31)/L:
g12:=-t3:
g13:=t2:
k1:=dt1:
k2:=-dt3+c3*da:
k3:=dt2-c2*da:
Phi1:=A*du^2+I22*k2^2+I33*k3^2+Irr/4*dt1^4+Iw*da^2+Io*du*dt1^2:
Phi2:=2*I23*k2*k3+I2r*k2*dt1^2+I3r*k3*dt1^2+Iwr*da*dt1^2:
Phi3:=A*(g12^2+g13^2)+Io*k1^2+(Io-J)*a^2-2*(Io-J)*k1*a:
Phi:=1/2*L*(E*Phi1+E*Phi2+G*Phi3):
fl:=grad(Phi,[u,t11,t21,t31,t12,t22,t32,a1,a2]):
kl:=hessian(Phi,[u,t11,t21,t31,t12,t22,t32,a1,a2]):
fortran(fl,optimized);
fortran(kl,optimized);
```

A.3 b3d element

```
with(linalg):
u21:=0:
u31:=0:
u22:=0:
u32:=0:
f1:=1-3*(x/L)^2+2*(x/L)^3:
f2:=x*(1-x/L)^2:
f3:=1-f1:
f4:=x^2*(x/L-1)/L:
u2:=f1*u21+f2*t31+f3*u22+f4*t32:
du2:=diff(u2,x):
ddu2:=diff(du2,x):
u3:=f1*u31-f2*t21+f3*u32-f4*t22:
du3:=diff(u3,x):
ddu3:=diff(du3,x):
t1:=(1-x/L)*t11+x/L*t12:
```

```
dt1:=diff(t1,x):
k1:=dt1:
k2:=-ddu2:
k3:=-ddu3:
eav:=u12/L+1/2/L*int(du2^2+du3^2+Io/A*dt1^2,x=0..L):
Phi1:=A*eav^2+I22*k2^2+I33*k3^2+1/4*(Irr-Io^2/A)*dt1^4:
Phi:=1/2*int(E*Phi1+G*J*k1^2,x=0..L):
f1:=grad(Phi,[u,t11,t21,t31,t12,t22,t32]):
k1:=hessian(Phi,[u,t11,t21,t31,t12,t22,t32]):
fortran(f1,optimized);
fortran(k1,optimized);
```

A.4 bw3d element

```
with(linalg):
u21:=0:
u31:=0:
u22:=0:
u32:=0:
f1:=1-3*(x/L)^2+2*(x/L)^3:
f2:=x*(1-x/L)^2:
f3:=1-f1:
f4:=x^2*(x/L-1)/L:
u2:=f1*u21+f2*t31+f3*u22+f4*t32:
du2:=diff(u2,x):
ddu2:=diff(du2,x):
u3:=f1*u31-f2*t21+f3*u32-f4*t22:
du3:=diff(u3,x):
ddu3:=diff(du3,x):
t1:=f1*t11+f2*a1+f3*t12+f4*a2:
dt1:=diff(t1,x):
ddt1:=diff(dt1,x):
k1:=dt1:
k2:=-ddu2+c3*ddt1:
k3:=-ddu3-c2*ddt1:
eav:=u12/L+1/2/L*int(du2^2+du3^2+Io/A*dt1^2,x=0..L):
Phi1:=A*eav^2+I22*k2^2+I33*k3^2+1/4*(Irr-Io^2/A)*dt1^4+Iw*ddt1^2:
Phi2:=2*I23*k2*k3+I2r*k2*dt1^2+I3r*k3*dt1^2+Iwr*ddt1*dt1^2:
Phi3:=G*J*k1^2:
Phi:=1/2*int(E*Phi1+E*Phi2+G*Phi3,x=0..L):
fl:=grad(Phi,[u,t11,t21,t31,t12,t22,t32,a1,a2]):
kl:=hessian(Phi,[u,t11,t21,t31,t12,t22,t32,a1,a2]):
fortran(fl,optimized);
fortran(kl,optimized);
```

Appendix B

Warping function

The purpose of this appendix is to describe the theoretical and numerical aspects related to the computation of the warping function $\bar{\omega}$ and cross-section quantities introduced in equation (4.130). The theoretical aspects are taken from Batoz and Dhatt [3] and Gruttmann et al. [39]. Concerning the finite element implementation, the description of isoparametric quadratic plane elements can be found e.g. in [21].

B.1 Basic equations

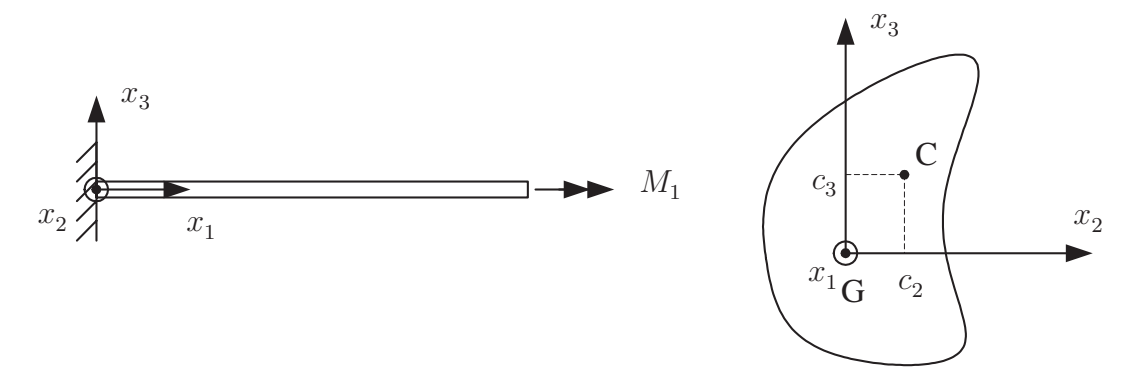


Figure B.1: Prismatic cantilever beam.

A prismatic cantilever beam, see Figure B.1 with reference axis x_1 and section coordinates x_2 and x_3 is considered. Following the hypotheses of Section 4.3.1, x_2 and x_3 intersect at the centroid G and are not necessarily directed along the principal axes of the cross-section. The displacements of a current point are noted u_1, u_2, u_3 .

The linear strain-displacement relations are

$$\varepsilon_{11} = u_{1,1} \qquad \gamma_{12} = u_{1,2} + u_{2,1} \qquad \gamma_{13} = u_{1,3} + u_{3,1}$$
 (B.1)

Assuming a linear elastic material, the stress-strain relations read

$$\sigma_{11} = E \,\varepsilon_{11} \qquad \tau_{12} = G \,\gamma_{12} \qquad \tau_{13} = G \,\gamma_{13}$$
 (B.2)

Finally, the stress resultants are defined by

$$N = \int_{A} \sigma_{11} \, dA \qquad M_1 = \int_{A} (\tau_{13} \, x_2 - \tau_{12} \, x_3) \, dA \qquad (B.3a)$$

$$M_2 = \int_A \sigma_{11} x_3 dA$$
 $M_3 = -\int_A \sigma_{11} x_2 dA$ (B.3b)

B.2 Saint-Venant torsion

A torque M_1 is applied at the free end of the cantilever, as shown in Figure B.1. Assuming the torsion angle θ_1 small, the displacements of a current point are

$$u_1 = \omega \,\theta_{1,1}$$
 $u_2 = -(x_3 - c_3) \,\theta_1$ $u_3 = (x_2 - c_2) \,\theta_1$ (B.4)

where the warping function ω refers to the shear center C of coordinates c_2, c_3 . Using equations (B.1), the strains can be rewritten as

$$\varepsilon_{11} = \omega \, \theta_{1,11} \qquad \gamma_{12} = (\omega,_2 - x_3 + c_3) \, \theta_{1,1} \qquad \gamma_{13} = (\omega,_3 + x_2 - c_2) \, \theta_{1,1} \qquad (\text{B.5})$$

The cantilever is free of normal forces and bending moments. This is inserted into equations (B.3), which gives the normality conditions

$$\int_{A} \omega \, \mathrm{d}A = 0 \qquad \int_{A} \omega \, x_2 \, \mathrm{d}A = 0 \qquad \int_{A} \omega \, x_3 \, \mathrm{d}A = 0 \tag{B.6}$$

B.3 Determination of the warping function

Since the position of the shear center is a priori unknown, the following transformation is applied

$$\bar{\omega} = \omega - c_2 x_3 + c_3 x_2 \tag{B.7}$$

Introducing the above equation into the first of equations (B.6) gives the constraint

$$\int_{A} \bar{\omega} \, \mathrm{d}A = 0 \tag{B.8}$$

The shear deformations in equations (B.5) can then be rewritten as

$$\gamma_{12} = (\bar{\omega}_{,2} - x_3) \,\theta_{1,1} \qquad \gamma_{13} = (\bar{\omega}_{,3} + x_2) \,\theta_{1,1}$$
(B.9)

The problem is free of external volume or surface forces. The principle of virtual work, per unit length, can be written as

$$\int_{A} (\tau_{12} \, \delta \gamma_{12} + \tau_{13} \, \delta \gamma_{13}) \, dA = 0$$
 (B.10)

with

$$\delta \gamma_{12} = \theta_{1,1} \, \delta \bar{\omega}_{,2} \qquad \delta \gamma_{13} = \theta_{1,1} \, \delta \bar{\omega}_{,3} \tag{B.11}$$

By introducing equations (B.2), (B.9) and (B.11) into (B.10), it is obtained

$$\int_{A} (\bar{\omega}_{,2} \, \delta \bar{\omega}_{,2} + \bar{\omega}_{,3} \, \delta \bar{\omega}_{,3}) \, \mathrm{d}A = \int_{A} (x_3 \, \delta \bar{\omega}_{,2} - x_2 \, \delta \bar{\omega}_{,3}) \, \mathrm{d}A \tag{B.12}$$

This equation is solved numerically by a finite element approach. Isoparametric quadratic plane elements, see Figure B.2, are used to discretise the cross-section. This means that the coordinates x_2 , x_3 and the unknown warping function $\bar{\omega}$ are interpolated within an element using the same shape functions

$$x_2 = \sum_{I=1}^{8} N_I(\xi, \eta) \ x_{2I} \qquad x_3 = \sum_{I=1}^{8} N_I(\xi, \eta) \ x_{3I} \qquad \bar{\omega} = \sum_{I=1}^{8} N_I(\xi, \eta) \ \bar{\omega}_I \quad (B.13)$$

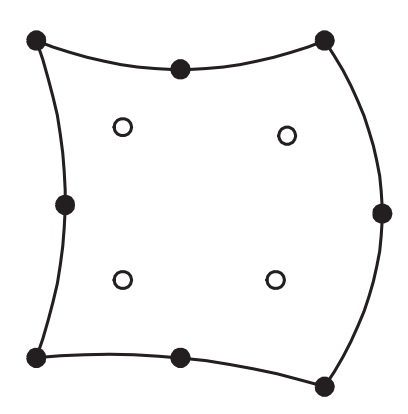


Figure B.2: Isoparametric quadratic plane element.

The element stiffness matrix and load vector are given by

$$K_{IJ} = \int_{A_e} (N_{I,2} N_{J,2} + N_{I,3} N_{J,3}) dA_e \qquad f_I = \int_{A_e} (N_{I,2} x_3 - N_{I,3} x_2) dA_e \quad (B.14)$$

Using the isoparametric transformation, the integrals over each element are performed numerically with four Gauss points. After assembly, the system

$$\mathbf{K} \mathbf{d} = \mathbf{f} \tag{B.15}$$

is solved by setting arbitrarily a nodal value of $\bar{\omega}$ to zero. This provides the vector **d** which contains the nodal values of $\bar{\omega}$. The vector **d** is next transformed using

$$\bar{\omega} := \bar{\omega} - \frac{1}{A} \int_{A} \bar{\omega} \, \mathrm{d}A \tag{B.16}$$

in order to fulfill the constraint (B.8).

B.4 Cross-section quantities

The cross-section quantities defined in equations (4.130), and those introduced in the present section, are integrated numerically using 4 Gauss points for each isoparametric elements.

The coordinates of the shear center are derived from the two last (B.6) equations, which gives after some work

$$c_2 = -\frac{I_{\bar{\omega}3} I_{22} - I_{\bar{\omega}2} I_{23}}{I_{22} I_{33} - I_{23}^2} \qquad c_3 = \frac{I_{\bar{\omega}2} I_{33} - I_{\bar{\omega}3} I_{23}}{I_{22} I_{33} - I_{23}^2}$$
(B.17)

with

$$I_{\bar{\omega}2} = \int_{A} \bar{\omega} \, x_2 \, \mathrm{d}A \qquad I_{\bar{\omega}3} = \int_{A} \bar{\omega} \, x_3 \, \mathrm{d}A \tag{B.18}$$

The Saint-Venant torsion modulus, defined in equation (4.129), can be calculated directly by

$$J = I_{22} + I_{33} - \mathbf{d}^{\mathrm{T}} \mathbf{f} \tag{B.19}$$

with \mathbf{d} and \mathbf{f} defined in (B.15).

Finally, I_{ω} and $I_{\omega r}$ are rewritten with the help of equation (B.7) as

$$I_{\omega} = \int_{A} \bar{\omega}^{2} dA - I_{33} c_{2}^{2} - I_{22} c_{3}^{2} + 2 I_{23} c_{2} c_{3}$$
 (B.20a)

$$I_{\omega r} = \int_{A} \bar{\omega} r^2 \, dA + I_{3r} \, c_2 - I_{2r} \, c_3 \tag{B.20b}$$